



HAL
open science

Proximity Effect in High-Tc d-wave Superconductor/2D Materials Heterostructures

Kévin Seurre

► **To cite this version:**

Kévin Seurre. Proximity Effect in High-Tc d-wave Superconductor/2D Materials Heterostructures. Superconductivity [cond-mat.supr-con]. Université Paris-Saclay, 2024. English. NNT : 2024UP-ASP002 . tel-04452744

HAL Id: tel-04452744

<https://theses.hal.science/tel-04452744v1>

Submitted on 12 Feb 2024

HAL is a multi-disciplinary open access archive for the deposit and dissemination of scientific research documents, whether they are published or not. The documents may come from teaching and research institutions in France or abroad, or from public or private research centers.

L'archive ouverte pluridisciplinaire **HAL**, est destinée au dépôt et à la diffusion de documents scientifiques de niveau recherche, publiés ou non, émanant des établissements d'enseignement et de recherche français ou étrangers, des laboratoires publics ou privés.

Proximity Effect in High- T_c d -wave Superconductor/2D Materials Heterostructures

*Effet de proximité dans les hétérostructures supraconducteur onde d à
haute température critique/matériaux 2D*

Thèse de doctorat de l'université Paris-Saclay

École doctorale n°564, physique en Île-de-France (PIF)

Spécialité de doctorat : Physique

Graduate School : Physique. Référent : Faculté des sciences d'Orsay

Thèse préparée dans l'unité de recherche

Laboratoire Albert Fert (Université Paris-Saclay, CNRS, Thales)

sous la direction de **Javier VILLEGAS**, Directeur de recherche,

la co-direction de **Pierre SENEOR**, Professeur des universités.

Thèse soutenue à Paris-Saclay, le 18 janvier 2024, par

Kévin SEURRE

Composition du Jury

Membres du jury avec voix délibérative

Jean-Christophe CHARLIER Professeur des universités, Université Catholique de Louvain	Président
Wolfgang LANG Professeur des universités, Universität Wien	Rapporteur & Examineur
Miguel ORTUNO Professeur des universités, Universidad de Murcia	Rapporteur & Examineur
Claire MARRACHE-KIKUCHI Maître de conférences HDR, Université Paris-Saclay	Examinatrice

Titre : Effet de proximité dans les hétérostructures supraconducteurs à onde d à haute température critique/matériaux 2D

Mots clés : supraconductivité, matériaux 2D, effet de proximité, réflexion d'Andreev, onde d , YBCO

Résumé : L'émergence des matériaux bidimensionnels (2D), associée aux supraconducteurs *onde d* à haute température critique (HT_c), étudiés de longue date, permet le développement de dispositifs aux nouvelles fonctionnalités. Cependant, il est d'abord nécessaire de comprendre le couplage entre ces matériaux.

Cette thèse, qui englobe à la fois des expériences et leur description théorique, est dédiée à cette exploration avec pour objectif principal la compréhension de la physique à l'interface des supraconducteurs *onde d* et des matériaux 2D, en modulant des paramètres externes tels que la température, le champ magnétique et la tension de grille.

Le point central de la thèse tourne autour de l'interface entre $\text{YBa}_2\text{Cu}_3\text{O}_{7-x}$ (YBCO), un oxyde supraconducteur *onde d* à haute température critique, et d'autres matériaux, examinée à la fois de manière théorique et expérimentale. L'aspect théorique comprend une revue approfondie de la théorie Blonder-Tinkham-Klapwijk (BTK) dans le cas des supraconducteurs *onde d* , accompagnée de calculs numériques concrets que j'ai réalisés pour des publications. La composante expérimentale implique l'étude de jonctions SN utilisant de l'YBCO et des métaux. L'analyse, employant à la fois la théorie BTK et le formalisme d'Usadel, révèle que, bien que la supraconductivité *onde d* soit induite dans la fine couche en proximité de YBCO, l'interface entre le métal et le YBCO supraconducteur/isolant génère des corrélations supraconductrices de type s qui rivalisent avec les corrélations de type d et s'étendent sur une grande partie du métal. Ces premiers résultats offrent une base solide pour l'étude des hétérostructures YBCO/2D.

J'ai ensuite étudié des jonctions YBCO/graphène/YBCO, dont la magnétorésistance a révélé une modulation de la résistance différentielle. L'étude systématique de la dépendance au champ magnétique circonscrit les principales caractéristiques de cet effet. L'origine de ces effets oscillatoires dans les jonctions supraconductrices est largement discutée, suggérant l'effet Al'tshuler-Aronov-Spivak; ces oscillations cohérentes résultent des interférences entre les particules normalement et Andreev réfléchies en présence d'un champ magnétique.

Cette exploration du couplage entre les supraconducteurs *onde d* et les matériaux 2D est étendue à l'étude des jonctions YBCO/MoS₂. Alors que les jonctions planaires similaires à celles déjà mentionnées nécessitent des développements ultérieurs, j'ai mis au point une nouvelle méthode pour aborder la croissance délicate des matériaux 2D directement au-dessus des oxydes supraconducteurs. Les détails d'optimisation et une analyse approfondie des mesures de transport des dispositifs supraconducteurs fabriqués avec cette méthode démontrent un excellent couplage entre l'YBCO et MoS₂, offrant des perspectives prometteuses pour de futurs dispositifs de proximité.

Title : Proximity Effect in High- T_c *d-wave* Superconductor/2D Materials Heterostructures

Keywords : superconductivity, 2D materials, proximity effect, Andreev reflexion, *d-wave*, YBCO

Abstract : The emergence of innovative bidimensional materials (2D), coupled with the long-studied High- T_c *d-wave* superconductors, allows for the development of devices with new functionalities. It however first requires to understand the coupling between these media.

This thesis, which encompasses both experiments and their theoretical description, is dedicated to this exploration with the primary objective of understanding the physics at the interface of *d-wave* superconductors and 2D materials, by modulating external parameters such as temperature, magnetic field, and gate voltage.

The central focus of the thesis revolves around the interface between $\text{YBa}_2\text{Cu}_3\text{O}_{7-x}$ (YBCO), a High- T_c *d-wave* superconducting oxide, and other materials, examined both theoretically and experimentally. The theoretical aspect encompasses a comprehensive review of the Blonder-Tinkham-Klapwijk (BTK) theory for *d-wave* superconductors, accompanied by concrete numerical calculations I carried out for publications. The experimental component involves the investigation of SN junctions using YBCO and metals. The analysis, employing both the BTK theory and Usadel's framework, reveals that while *d-wave* superconductivity is induced in the thin layer in proximity of YBCO, the interface between the metal and the superconducting/insulating YBCO generates *s-wave* superconducting correlations that compete with *d-wave* correlations and extend over a large portion of the metal. These first results offer a strong ground for the study of YBCO/2D materials heterostructures.

I subsequently studied YBCO/graphene/YBCO junctions, in which magnetoresistance revealed modulation in the differential resistance. The systematic investigation of the magnetic field dependence circumscribes the main features of this effect. The origin of these oscillatory effects in superconducting junctions is widely discussed, pointing toward the Al'tshuler-Aronov-Spivak effect; these coherent oscillations result from interferences between normally and Andreev reflected particles in the presence of a magnetic field.

This exploration of the coupling between *d-wave* superconductors and 2D materials is extended to the study of YBCO/ MoS_2 junctions. While planar junctions similar to the ones already mentioned require further developments, I developed a new method for addressing the challenging growth of 2D materials directly atop superconducting oxides. The optimization details and a thorough analysis of transport measurements of superconducting devices fabricated with this method demonstrate excellent coupling between YBCO and MoS_2 , holding promise for future proximity devices.

TABLE OF CONTENTS

Table of contents.....	4
1 Résumé étendu en français	9
1.1 Introduction et aperçu de la thèse	9
1.2 Effet de proximité, théorie BTK et applications concrètes.....	10
1.3 Effet de proximité entre un supraconducteur a onde d et un film métallique fin	12
1.4 Effet de proximité dans les jonctions YBCO/Graphene	14
1.5 Un nouveau matériau à l'étude, MoS ₂	15
2 Introduction.....	17
2.1 Superconductors.....	17
2.1.1 Basic properties of superconductors and microscopic theory	17
2.1.2 More exotic superconductivity and YBCO	21
2.1.3 Applications of superconductors	23
2.2 2D-materials	28
2.2.1 Graphene and its properties	28
2.2.2 The wave of new 2D materials and their variety	34
2.2.3 New growth methods for more applications.....	39
2.3 Motivations and state-of-the-art	42
2.3.1 Proximity effect in normal metal thin films	42
2.3.2 Proximity effect in graphene.....	46
2.3.3 Proximity effect in MoS ₂	51
2.4 Structure of the thesis.....	55
3 Superconducting proximity effect and transport at the interface with a superconductor ...	58
3.1 Andreev reflection and superconducting proximity effect	58
3.1.1 Superconducting proximity effect.....	58
3.1.2 Single-particle density of states and Andreev reflection mechanism	59
3.1.3 Bogoliubov-de Gennes formalism.....	61
3.2 Blonder-Tinkham-Klapwijk theory	62
3.2.1 BTK Model and generic resolution method	62
3.2.2 Josephson effect.....	65
3.2.3 Limitations and improvements of the BTK model	66
3.3 Applications to d-wave superconductors	68
3.3.1 <i>d-wave</i> superconductors.....	68
3.3.2 Simulation of the temperature dependence	70
3.3.3 Demonstration of superconductivity in La ₅ SrCu ₆ O ₁₅	73
3.3.4 Quasiparticle density of states and spin-injection in YBCO	75
3.4 Conclusive remarks	78
4 General fabrication, characterization, and measurement methods	80
4.1 Fabrication of planar superconducting devices.....	80
4.1.1 Step 1: Growth of the superconducting thin films.....	81
4.1.2 Step 2: Electronic lithography patterning of irradiation mask.....	83
4.1.3 Step 3: Oxygen ion irradiation.....	84
4.1.4 Step 4: 2D material transfer.....	85
4.1.5 Step 5: Optical lithography of the 2D material	88
4.1.6 Step 6: Plasma etching of the 2D material	88
4.1.7 Step 7: Top gate fabrication	88

4.2	Fabrication of vertical superconducting devices	90
4.2.1	Two-steps lithography of resist apertures	91
4.2.2	Sputtering of the top electrode	91
4.2.3	Specificities of the wire bonding in the case of the vertical junctions	92
4.3	Materials characterization	93
4.3.1	Atomic force microscopy (AFM)	93
4.3.2	Raman spectroscopy	94
4.4	Transport measurements	95
4.4.1	Cryogenic system and magnetic field control	95
4.4.2	Electrical measurements	97
4.5	Conclusive remarks	99
5	<i>Proximity effect in YBCO/Metal Planar devices</i>	100
5.1	Study of SN junctions	100
5.1.1	Geometry of the samples	100
5.1.2	Differential conductance and symmetry of the gap	101
5.1.3	BTK-inspired model	110
5.1.4	Numerical resolution using Usadels equation	116
5.2	Study of SNS junctions	121
5.2.1	Comments on the chosen geometries	121
5.2.2	Results	122
5.2.3	Discussion	124
5.3	Conclusive remarks	125
6	<i>Planar YBCO/Graphene junctions</i>	127
6.1	Previous works on d-wave superconductors/graphene junctions	127
6.1.1	Fabricating high-quality interfaces and measurement configuration	128
6.1.2	Differential conductance at low temperature	129
6.1.3	Model	130
6.1.4	Tunability with a back gate voltage	130
6.2	Coherent transport of Andreev d-wave pairs	131
6.2.1	Geometry of the junctions and measurements	132
6.2.2	Modelization of the system	133
6.3	Magnetic field effect on short junctions	138
6.3.1	Physical description of the oscillations in the magnetoresistance	138
6.3.2	Discussion	146
6.4	Conclusive remarks	158
7	<i>A new material under study, MoS₂</i>	159
7.1	Attempts with CVD MoS₂	159
7.2	New growth method and characterization of the materials	162
7.2.1	Presentation of the setup	163
7.2.2	Growth parameters and their effects	163
7.2.3	Characterization of the 2D material	166
7.3	Transport measurements of vertical junctions	171
7.3.1	Device fabrication	171
7.3.2	Junction's differential conductance	172
7.3.3	Josephson regime	177
7.3.4	Overall discussion	183
7.4	Conclusive remarks	184

8	Conclusion	185
8.1	Summary of the main results	185
8.1.1	Numerical studies within the BTK framework	185
8.1.2	Proximity effect between <i>d-wave</i> superconductor/metal thin films	186
8.1.3	Proximity effect in graphene	188
8.1.4	Proximity effect in MoS ₂	189
8.2	Broad perspectives.....	190
8.2.1	Transferring Van der Waals materials.....	190
8.2.2	Direct growth of VdW materials with specific properties onto YBCO	191
8.3	Conclusive remarks	192
9	Bibliography	193
10	Appendix.....	209
10.1	Lithography recipes	209
10.1.1	Electronic lithography	209
10.1.2	Optical lithography	210
10.2	Numerical calculation.....	211

Avant de parler sciences dans tout le reste de ce manuscrit, j'aimerais ici m'exprimer plus personnellement et aborder l'aspect humain de ma thèse. Une thèse n'est pas faite que de travail, de mesures et de résultats mais aussi et surtout de rencontres, de discussions et de liens avec les personnes. J'ai eu la chance pendant ma thèse de multiplier ses interactions.

Je tiens tout d'abord à remercier mes directeurs de thèse. Javier et Pierre, secondés respectivement par Vincent et Bruno. Vous m'avez accordé l'autonomie dont j'avais besoin tout en veillant à ce que je ne me perde pas. Au-delà de votre rôle de « chefs », vous avez toujours été là pour moi lors des moments de doutes ou d'inquiétudes. Vous savez aussi entretenir une ambiance conviviale d'entraide et d'amitié autour de vous. Je n'oublierai jamais les facéties du groupe 2D ni les supra-bières ou supra-BBQ. Si je deviens un jour « manager », il y aura forcément un peu de chacun de vous en moi. Je voudrais aussi remercier Christian Ulysse pour ses conseils et tout le temps qu'il a consacré à optimiser la lithographie électronique de mes échantillons. Anke, Santiago et Javier ont aussi beaucoup œuvré pour me fournir les films de YBCO dont j'avais besoin. Je ne peux pas oublier ici Florian qui m'a accompagné de très nombreuses fois à la PLD (ou à l'évaporateur) pour optimiser les paramètres de croissance de mes échantillons et avec qui il était toujours plaisant de passer du temps. Je remercie Julian pour son aide avec la station pick up qu'il a développée (quel travail !) mais aussi Victor qui m'a transmis son savoir-faire en transfert humide de matériaux 2D. Enfin, je souhaite remercier Nicolas, Juan et Salvatore pour leur aide quand la bondeuse ou la smartprint ne marchaient pas comme je le voulais. Merci aussi à Fayçal, Sophie, Cécile, Aymeric, Anne et Florence pour leur aide et leur bonne humeur. Concernant la compréhension des phénomènes, je dois beaucoup à Denis ainsi que Sebastian Bergeret et Tim Kokkeler.

Maintenant, j'aimerais remercier l'ensemble de mes collègues durant ces quatre années au laboratoire. Je pense notamment à mes camarades de promotion (et celles d'avant ou d'après) avec qui j'ai partagé le contexte difficile des confinements mais aussi et surtout tellement de bons moments comme l'escalade (et la descente qui suivait) ou les social events. J'ai aussi eu la chance de pouvoir me mêler à différents groupes comme celui des footeux, des nageurs, des coureurs jusqu'aux joueurs d'échecs ! Pendant ma thèse, plus que des collègues, je me suis fait de véritables amis comme Jack, Santiago, Aurélien, Nicolas, Carol, David, Meghan, Enzo,... et bien sûr Sarah et Vincent.

Dans ce dernier paragraphe, je tiens à remercier mes amis les plus fidèles, Félix, Marie et Jérémy, qui n'ont cessé de me soutenir même dans les moments plus compliqués. Je remercie aussi Marin, Joris, Germain et Ganaël. Pendant ma thèse, j'ai aussi eu la chance de rencontrer ma principale source de bonheur, Margaux. Ta présence (et celle de Mimi) auprès de moi change tout (moi inclus) et transforme le négatif en positif. Enfin, je pense à ma mamie, partie au début de ma thèse ainsi qu'à mes parents. Vous êtes là pour moi depuis toujours, vous m'avez inculqué une grande partie de mes valeurs, vous m'avez toujours soutenu et aimé inconditionnellement. J'ai de la chance de vous avoir.

Lecteur.rice, je vous remercie et vous laisse désormais avec les aspects techniques de ma thèse, œuvre d'un homme heureux et bien entouré.

À mamie,

1 RESUME ETENDU EN FRANÇAIS

1.1 INTRODUCTION ET APERÇU DE LA THESE

La supraconductivité, découverte il y a déjà plus d'un siècle par Onnes [1] est toujours l'objet d'intenses recherches. Ce phénomène se manifeste par une résistance nulle d'un matériau supraconducteur en dessous d'une certaine température critique (T_c) qui lui est propre. Bien que les propriétés électromagnétiques des supraconducteurs ont vite été établies par les frères London notamment [2], il a fallu d'avantage de temps pour comprendre la transition supraconductrice, grâce à Ginzburg et Landau [3] et encore plus pour identifier l'origine microscopique de la supraconductivité avec la théorie BCS [4], élaborée par Bardeen, Cooper et Schrieffer. Leur théorie permet d'expliquer la supraconductivité par la présence d'une force attractive entre électrons au niveau de Fermi qui, à suffisamment faible température, permet la formation de paires d'électrons de spins opposés, les fameuses paires de Cooper. La mer de Fermi étant instable face à la formation de paires, un condensat de paires de Cooper se crée. Il forme alors un objet quantique macroscopique représenté par une fonction d'onde complexe. A la fin des années 80, de nouveaux matériaux supraconducteurs ont été découverts, avec des températures critiques bien supérieures et une anisotropie du paramètre d'ordre supraconducteur, ne rentrant pas dans l'explication de théorie BCS. Le supraconducteur utilisé dans l'ensemble de cette thèse est $\text{YBa}_2\text{Cu}_3\text{O}_{7-\delta}$ (YBCO) et il appartient à cette catégorie avec une T_c à 92K, visible sur la Figure 1a et un paramètre d'ordre dit « onde d » représenté dans la Figure 1b.

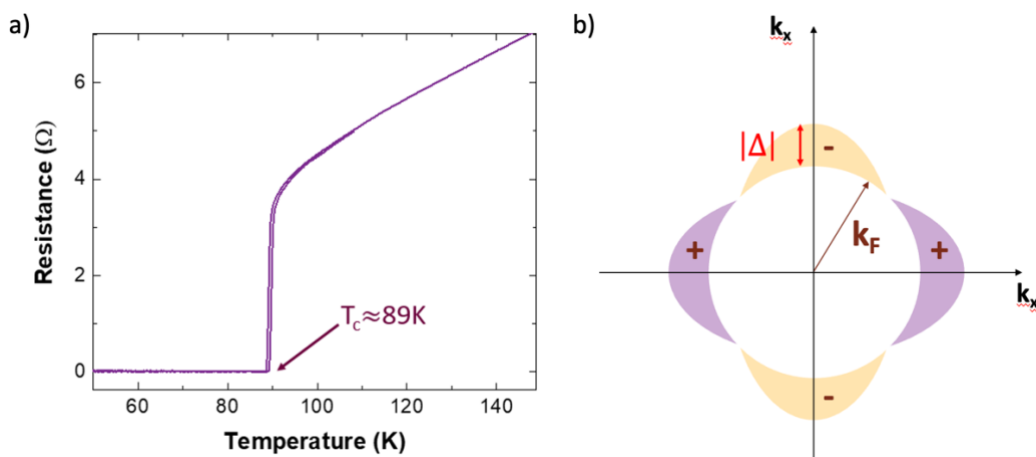


Figure 1 a) Resistance en fonction de la température d'un film d'YBCO. b) Paramètre d'ordre onde-d. Celui n'est pas isotrope mais son amplitude ainsi que sa phase dépend de la direction.

Cependant, de nombreux matériaux ne deviennent jamais supraconducteurs aussi basse soit la température. Le but de cette thèse est d'étudier comment un matériau, en particulier des matériaux bidimensionnels (2D), peut acquérir des corrélations supraconductrices s'il est en contact avec un supraconducteur, dans cette thèse $\text{YBa}_2\text{Cu}_3\text{O}_{7-x}$ (YBCO). Après une introduction à la physique des supraconducteurs et des matériaux 2D, ainsi qu'un état de l'art des systèmes dits proximités entre des supraconducteurs « onde s » et des films

métalliques, du graphène et du MoS₂. Ensuite, j'aborde la théorie de l'effet de proximité et en particulier la très utilisée théorie BTK pour Blonder-Tinkham-Klapwijk [5] dans le cas d'onde *s* (isotropique) puis *d*. Cette étude théorique m'a permis de reproduire numériquement les mesures de conductance différentielle réalisées au sein de mon laboratoire ou dans le cadre de collaborations [6–8]. Le chapitre suivant présente les techniques expérimentales utiliser pour fabriquer, caractériser et mesurer les dispositifs. Les chapitres suivants sont consacrés à l'étude de l'effet de proximité dans différents matériaux. Le premier se concentre sur des dispositifs planaires réalisés à partir d'un film fin d'or crû *in situ* sur un film d'YBCO. Des jonctions supraconductrices sont étudiées dans deux configurations différentes. Le chapitre suivant s'intéresse à des dispositifs avec une géométrie proche à la différence près que le matériau proximisé est du graphène et non de l'or. Dans ce chapitre, j'analyse l'évolution de la résistance en fonction du champ magnétique qui permet de sonder l'effet de proximité supraconducteur. Enfin, le troisième chapitre aborde l'étude d'un nouveau matériau 2D semiconducteur, MoS₂. Si la première section du chapitre reprend la même géométrie que celle du précédent chapitre, la suite se consacre à une nouvelle méthode de croissance direct de MoS₂ et l'étude de jonctions supraconductrices verticales. Finalement, je conclue et présente quelques-uns des multiples axes ouverts par ses travaux de thèses. Dans ce résumé étendu, nous allons synthétiser ce qui a été vu plus en détails dans le manuscrit.

1.2 EFFET DE PROXIMITE, THEORIE BTK ET APPLICATIONS CONCRETES

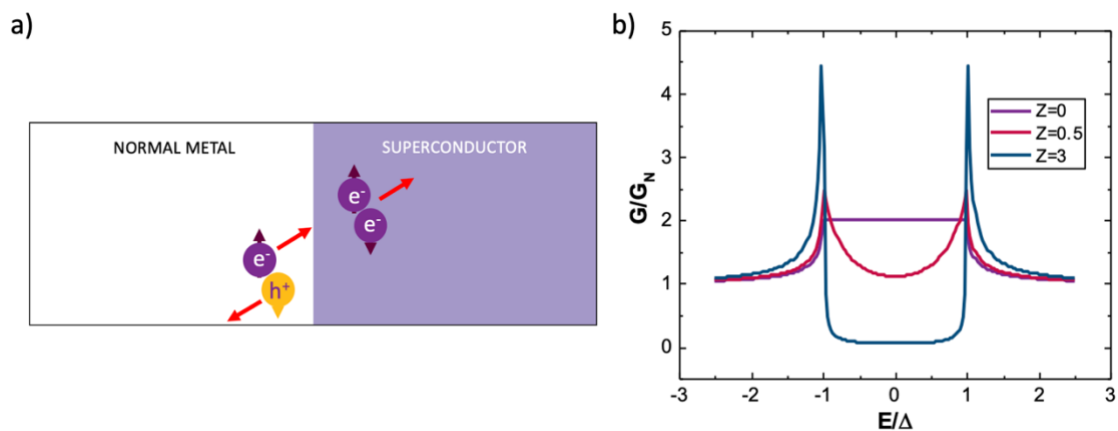


Figure 2 a) Schéma d'une réflexion d'Andreev : un électron incident dans le métal vers le supraconducteur avec une énergie situé dans le gap supraconducteur ne peut pénétrer directement dans le supraconducteur car il ne présente pas d'état à un électron. Le seul moyen pour lui de traverser est de trouver un autre électron pour former une paire de Cooper. Un trou de spin opposé est alors rétro-réfléchi. b) Simulations de la conductance différentielle normalisée en fonction de l'énergie normalisée par le gap supraconducteur pour trois paramètres de diffusion à l'interface.

L'effet de proximité supraconducteur a fait l'objet de nombreuses études depuis les travaux de de Gennes [9]. Lorsqu'un métal est en contact avec un supraconducteur, le paramètre d'ordre du supraconducteur se propage localement dans le métal à l'échelle de la longueur de cohérence de phase du métal. Plus précisément, comme illustré Figure 2a, si l'interface

entre les deux matériaux est suffisamment transparente, lorsqu'un électron du métal à l'intérieur du gap se propage vers l'interface, celui-ci ne peut pénétrer seul dans le supraconducteur puisqu'il n'y a pas d'état à un électron dans celui-ci. Cependant, il peut former une paire de Cooper avec un autre électron à l'interface. Un trou se propageant en direction opposé est alors créé. On appelle ce phénomène la réflexion d'Andreev. Elle a été quantifiée par Blonder, Tinkham et Klapwijk [5]. Je vais ici rappeler les principales hypothèses et les résultats sous la forme de simulations que j'ai réalisées et présentées en Figure 2b.

Dans leur modèle, les charges se déplacent de manière balistique et l'interface est modélisée par un potentiel de Dirac, la qualité de l'interface est quantifiée par un unique paramètre Z allant de 0 (parfaitement transparente) à $+\infty$ (tunnel). Lorsque l'interface est parfaitement transparente, la conductance différentielle dans le gap supraconducteur est le double de la conductance normale, celle mesurée pour des énergies bien supérieures au gap. Dans le cas tunnel, cette conductance différentielle tend vers zéro à l'intérieur du gap.

Ce modèle a été étendu au cas des supraconducteurs à *onde d* comme YBCO. Il faut alors prendre en compte l'orientation du paramètre d'ordre supraconducteur par rapport à l'interface avec le métal. J'ai pendant ma thèse travailler sur ce modèle pour analyser les données mesurées dans le cadre de plusieurs expériences qui ont depuis été publiées :

1) Les premiers systèmes que j'ai étudiés étaient des jonctions verticales constituées de YBCO et de MoSi, un métal amorphe, avec une barrière de tunnel ajustable [6]. J'ai utilisé le formalisme BTK pour calculer la conductance différentielle d'une interface entre un métal normal et un supraconducteur à *onde d* le long de son axe c . Après avoir extrait les principaux paramètres à partir des ajustements avec la théorie BTK, comme illustré dans les Figure 3a et b, j'ai pu simuler le comportement en température du système et expliquer l'amélioration observée de l'électrorésistance en dessous de la température critique de l'YBCO. Les conductances simulées à 0 et 100mV pour les états ON et OFF sont présentées dans la Figure 3c, ainsi que l'évolution de la température de l'électrorésistance dans l'insert. L'augmentation expérimentalement observée de l'électrorésistance peut être expliquée par le passage par l'effet tunnel des quasi-particules à l'intérieur du gap de l'YBCO.

2) L'étude suivante [7] s'est concentrée sur les mesures de transport de jonctions verticales constituées d'un empilement de $\text{La}_5\text{SrCu}_6\text{O}_{15}$ (LSCO) (électrode supérieure), BaTiO_3 (BTO) (barrière) et $\text{La}_{0.7}\text{Sr}_{0.3}\text{MnO}_3$ (LSMO) (électrode inférieure). L'application d'impulsions de tension a montré deux comportements distincts de la conductance différentielle en fonction de la polarité. Les ajustements BTK que j'ai réalisés à plusieurs températures dans ces deux états nous ont permis de caractériser leur comportement comme une éventuelle émergence d'une phase supraconductrice dans LSCO et de quantifier comment elle est affectée par son environnement électrostatique.

3) Enfin, dans le cadre de mesures de magnétorésistance ferromagnétique (FMR) avec du permalloy (un ferromagnétique) en contact avec YBCO, j'ai pu utiliser la théorie BTK pour calculer les propriétés interfaciales entre ces deux matériaux [8]. Cela nous a permis d'expliquer les expériences de FMR en calculant les densités d'états de quasi-particules dans YBCO pour deux orientations cristallographiques et comment cela peut affecter l'injection

de spin à l'interface.

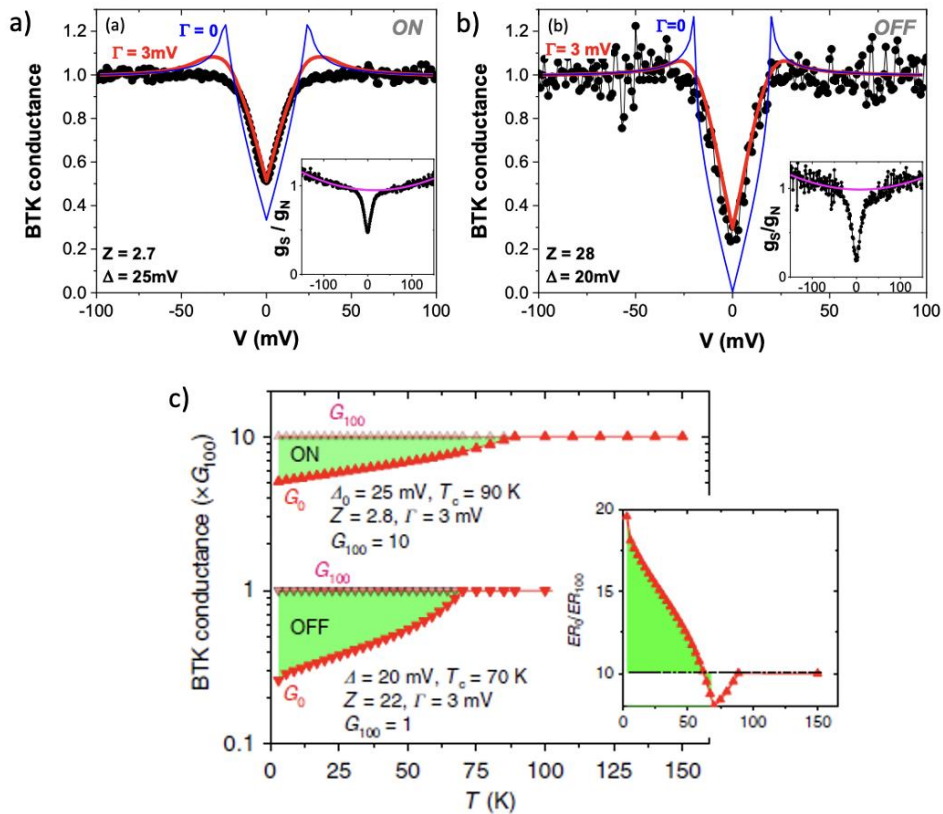


Figure 3 Ajustements numériques dans le cas a) de l'état ON, b) de l'état OFF. c) Évolutions avec la température des conductances à 0mV (G_0) et 100mV (G_{100}) à la fois pour l'état ON et l'état OFF. Dans l'insert, l'évolution en température du ratio de l'électrorésistance (ER) entre 0 et 100mV.

Ces projets m'ont permis d'acquérir l'expertise qui m'a été utile pour l'analyse de mes résultats expérimentaux que je vais désormais présenter.

1.3 EFFET DE PROXIMITE ENTRE UN SUPRA CONDUCTEUR A ONDE D ET UN FILM METALLIQUE FIN

Dans le cadre de ma thèse de doctorat, l'étude des jonctions YBCO/métal constitue une première étape pour caractériser la propagation des corrélations supraconductrices de type d dans un cas qui était, en principe, plus simple que celui du graphène et du MoS₂. De plus, étant donné qu'une fine couche de métal doit être intercalée entre le graphène (ou le MoS₂) et le YBCO pour protéger la surface de l'YBCO et améliorer la transparence de l'interface, il était important de caractériser d'abord l'effet de proximité dans l'or.

Dans une première partie, j'ai étudié des jonctions SN formées par une fine couche continue d'or reposant d'un côté (S) au-dessus du supraconducteur YBCO et de l'autre côté (N) sur le YBCO isolant (cf schéma Figure 4a). Pour expliquer les spectres expérimentaux de conductance différentielle, j'ai développé un modèle phénoménologique basé sur le formalisme BTK avec deux interfaces distinctes, l'une de type s et l'autre de type d, ainsi

qu'une résistance métallique en série. Avec l'aide de théoriciens, nous avons élaboré un modèle microscopique basé sur le formalisme d'Usadel, ce qui nous a permis de reproduire la dépendance en tension et en température de la conductance différentielle comme montrées en Figure 4b et c.

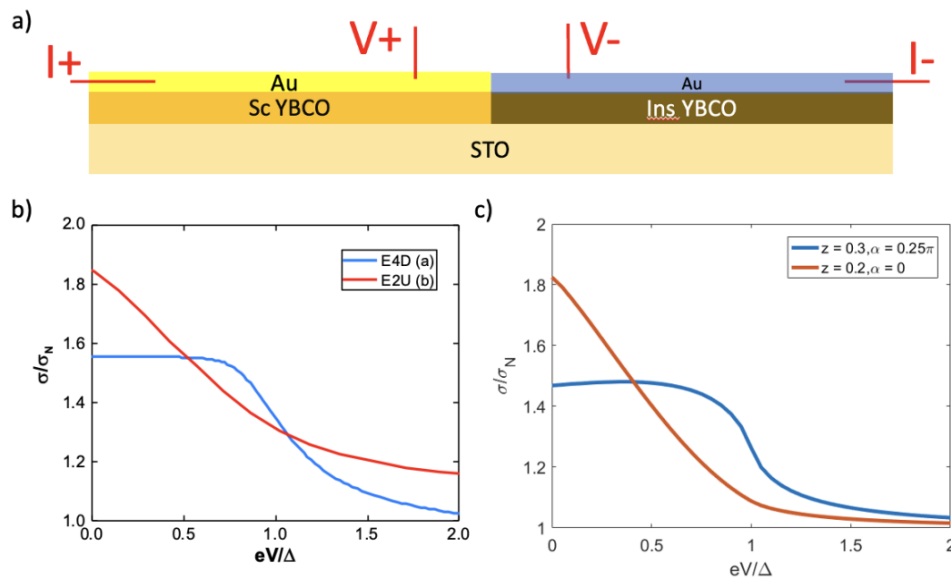


Figure 4 a) Schéma de côté avec la configuration électrique d'une jonction SN. b) Conductances différentielles expérimentales normalisées de deux jonctions SN typiques en fonction de la tension normalisée par le gap supraconducteur. c) Calculs numériques basés sur le formalisme d'Usadel.

J'ai également mesuré des jonctions SNS et pu analyser les mesures avec les connaissances acquises des jonctions SN. En effet, j'ai démontré que, en raison de la longueur de cohérence plus faible de l'or par rapport au graphène, les deux côtés de la jonction SNS peuvent être considérés comme des jonctions SN indépendantes.

À l'avenir, une étude des jonctions SNS avec une longueur plus petite entre les électrodes pourrait permettre d'observer un couplage Josephson et un courant critique. Une autre possibilité est de changer le métal de la fine couche pour influencer sur la qualité du contact ou les propriétés de transport. Enfin, il serait très intéressant d'effectuer des mesures STM à basse température comme dans la référence [10] sur l'or à la fois au-dessus de l'YBCO supraconducteur et de l'YBCO isolant pour observer l'évolution du mini-gap dans l'or. Il serait également possible de créer des contacts tunnel comme dans la référence [11], mais la géométrie serait plus contraignante.

Avant de plonger dans l'effet de proximité d'onde d dans les matériaux bidimensionnels (graphène et MoS₂), je tiens à souligner que le CHAPITRE 5 explore un régime très différent de celui des CHAPITRES 6 et 7. Dans le cas de l'or, le contact entre l'YBCO et la couche est excellent car la croissance est effectuée *in situ*. Cependant, par rapport au graphène ou au MoS₂, la longueur de cohérence de phase de l'or est beaucoup plus faible, et les effets liés à la cohérence (comme l'interférence quantique que j'ai observée dans le graphène) sont absents.

1.4 EFFET DE PROXIMITE DANS LES JONCTIONS YBCO/GRAPHENE

Comme nous l'avons vu dans l'introduction de cette thèse (au **CHAPITRE 2**), le graphène a été largement étudié avec des supraconducteurs *onde s* dans la littérature. Cependant, les études avec des supraconducteurs *onde d* sont rares, à l'exception notable d'une publication réalisée par mon prédécesseur montrant les premiers indices de l'effet de proximité entre le graphène et YBCO [12]. Ce travail expérimental a été complété par des calculs théoriques adaptés de [13], qui décrivent bien le système et les mesures expérimentales. Plus tard, nous avons démontré la propagation de paires d'Andreev de type d dans du graphène cultivé par CVD sur plusieurs centaines de nanomètres [14]. Cela signifie que la phase entre l'électron et le trou issu d'un processus d'Andreev reste constante sur la longueur de la jonction, qui varie de 50 à 800nm.

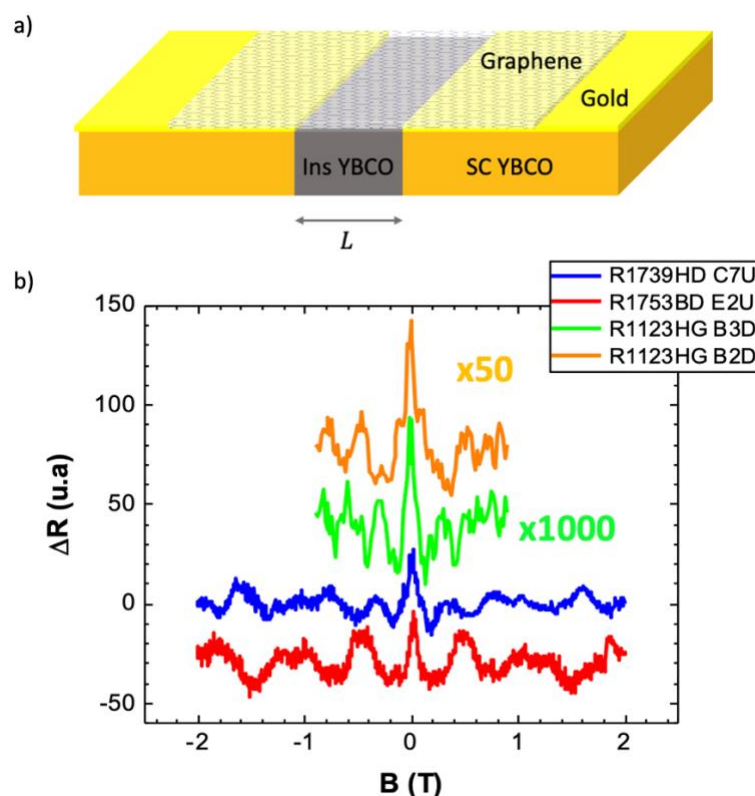


Figure 5 a) Schéma vu de côté d'une jonction YBCO/graphène/YBCO. b) Oscillations de la magnétorésistance ici mesurées dans quatre jonctions de quatre échantillons distincts.

Par la suite, j'ai étudié l'effet du champ magnétique sur la conductance différentielle des jonctions YBCO/Graphène/YBCO représentées schématiquement dans la Figure 5a. Au **CHAPITRE 6**, j'ai fourni une analyse des oscillations observées dans la magnétorésistance des jonctions de transparence intermédiaire, comme illustré dans la Figure 5b. La présence d'un pic de magnétorésistance lié à la faible localisation autour de $B = 0$, ainsi que la comparaison avec la littérature sur les oscillations de magnétorésistance dans les systèmes 2D proximisés, nous ont conduit à conclure que les oscillations de magnétorésistance observées sont liées à l'effet Altshuler-Aronov-Spivak (AAS), dont l'une des échelles caractéristiques est la longueur de cohérence de phase dépendante de la température dans le graphène.

1.5 UN NOUVEAU MATERIAU A L'ETUDE, MoS₂

Après l'étude des jonctions YBCO/Graphène/YBCO, nous avons exploré l'effet de proximité dans un autre matériau bidimensionnel, le MoS₂, pour son caractère semiconducteur et son fort couplage spin-orbite, potentiellement intéressants combinés avec un supraconducteur [15]. Il s'agissait aussi d'un candidat naturel, car ce matériau peut également être crû par dépôt chimique en phase vapeur (CVD), et la plupart des techniques de fabrication peuvent lui être appliquées. Dans une première étape, j'ai tenté de fabriquer des dispositifs analogues à ceux de YBCO/Graphène/YBCO via le transfert humide de MoS₂ CVD. Cependant, les mesures de transport ont révélé un comportement très résistif, dicté par la résistance de contact entre le MoS₂ et le YBCO. Pour résoudre ce problème, j'ai décidé d'explorer différentes approches, telles que l'exfoliation d'un composé parent (WS₂) et le développement d'une nouvelle méthode de croissance de MoS₂ directement sur le YBCO basée sur le dépôt laser pulsé (PLD) (schéma en Figure 6a). Comme expliqué dans le **CHAPITRE 7**, cette tâche est complexe car le YBCO est un oxyde fragile. J'ai dû optimiser les paramètres de croissance afin de préserver les propriétés supraconductrices du YBCO tout en déposant du MoS₂ de haute qualité.

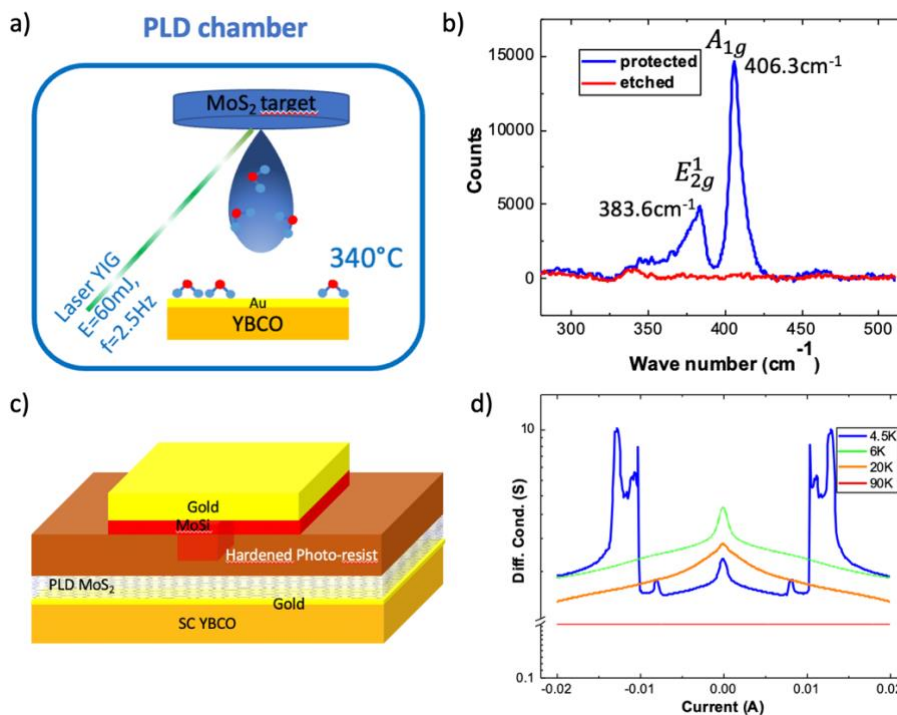


Figure 6 a) Schéma d'un bâti de PLD pour la croissance directe de MoS₂ sur des films de YBCO/or. b) Spectres Raman de MoS₂ crû par PLD (bleu) et du substrat seul (rouge). c) Schéma d'une jonction supraconductrice verticale composé de YBCO/or (électrode inférieure), MoS₂ (barrière) et MoSi (électrode supérieure). d) Conductances différentielles d'une jonction à différentes températures (échelle semi-logarithmique).

Au **CHAPITRE 7**, j'ai caractérisé à la fois l'YBCO après le processus de croissance et le MoS₂, par exemple, avec la spectroscopie Raman, comme illustré dans la Figure 6b. Cette méthode m'a permis de fabriquer des dispositifs supraconducteurs représentés dans la Figure 6c, composés du YBCO en tant qu'électrode inférieure, du MoSi (un

supraconducteur de type s amorphe) en tant qu'électrode supérieure, tandis que le MoS₂ joue le rôle d'une barrière entre les deux. Les mesures de transport électronique ont révélé un comportement SIS, quelle que soit l'épaisseur de la couche de MoS₂ (spectres de conductance différentielle présentés dans la Figure 6d). Pour l'échantillon avec la couche de MoS₂ la plus fine (~5nm), certaines jonctions ont présenté un couplage de Josephson avec un courant critique d'environ 100μA.

2 INTRODUCTION

This thesis is all about studying proximity effect in devices combining *d-wave* superconductors and two-dimensional (2D) materials, to mix their respective intrinsic electronic properties. Thus, in this introductory chapter, we first introduce the concept of superconductivity, its applications, and the superconductor used in this thesis. Then, we present the variety of 2D materials and more precisely graphene and molybdenum disulfide, the materials we chose for the experiments. Finally, we give the motivations of this whole work and what is interesting in combining superconductors with 2D materials.

2.1 SUPERCONDUCTORS

2.1.1 Basic properties of superconductors and microscopic theory

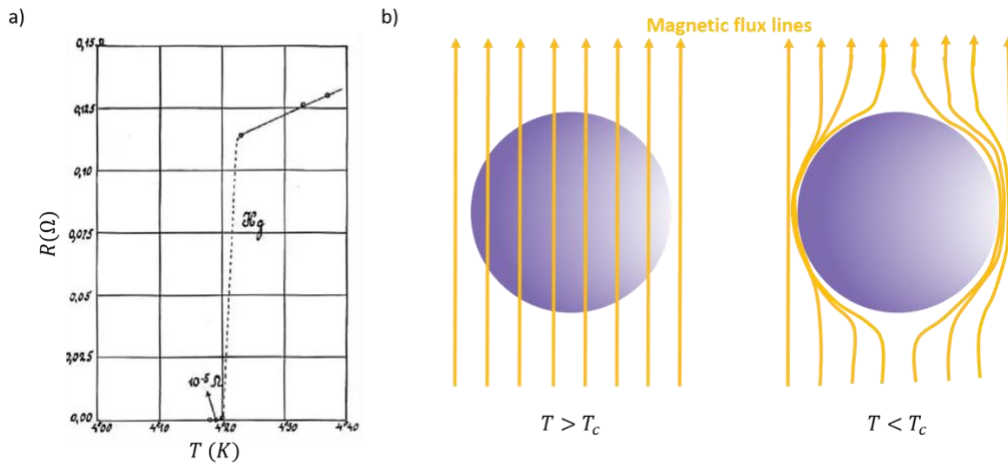


Figure 7 a) Famous picture of the Onnes labbook plotting the resistance versus temperature of mercury (Hg) b) Illustration of the Meissner effect at $T < T_c$ compared with the normal state behavior.

Superconductivity is a very old topic since it was discovered more than a century ago by Onnes [1] when he could finally go below helium liquid temperature and measure the electrical resistance of mercury as Figure 7a shows. It manifests itself by a sharp transition from a metallic state to a **zero-resistance state** at a temperature that depends on the material. It was discovered later that the magnetic field behavior of superconductors cannot be explained by simply considering superconductors as perfect metals [16]. Indeed, a perfect metal in a magnetic field would not expel magnetic field flux lines from its interior as a superconductor does with the Meissner effect as shown in Figure 7b. This effect persists up to a critical field H_c for type I superconductors at which point the superconductivity collapses. The London brothers gave a satisfactory mathematical description of the superconducting state with their two eponymous equations describing the microscopic electric field \vec{E} and magnetic field \vec{B} inside a superconductor:

$$\frac{\partial \vec{J}_S}{\partial t} = \frac{n_S e^2}{m} \vec{E} \quad 2.1$$

$$\text{curl } \vec{J}_S = -\frac{n_S e^2}{m} \vec{B} \quad 2.2$$

Here, \vec{J}_S denotes the superconducting current density and n_S is the number density of superconducting electrons in the original paper, Cooper pairs being anachronistic at that moment. This density is finite at null temperature but tends to zero as the superconductor approaches its critical temperature. e and m are respectively the electric charge and the mass of an electron. If we combine the second equation with the Maxwell equations [17], one finds back that **the electromagnetic field is screened inside the superconductor** and only penetrates on a typical lengthscale $\lambda = \sqrt{\frac{m}{\mu_0 n_S e^2}}$ called London penetration length. In superconductors, this length usually scales between tens of nanometers to microns. The two equations written above can be written differently if we fix the gauge such as $\text{div } \vec{A} = 0$:

$$\vec{J}_S = -\frac{n_S e^2}{m} \vec{A} \quad 2.3$$

This formulation has a strong physical meaning and comes directly from the canonical momentum which is $\vec{p} = (m\vec{v} + e\vec{A})$ and the fact that without applied field, the average momentum is zero.

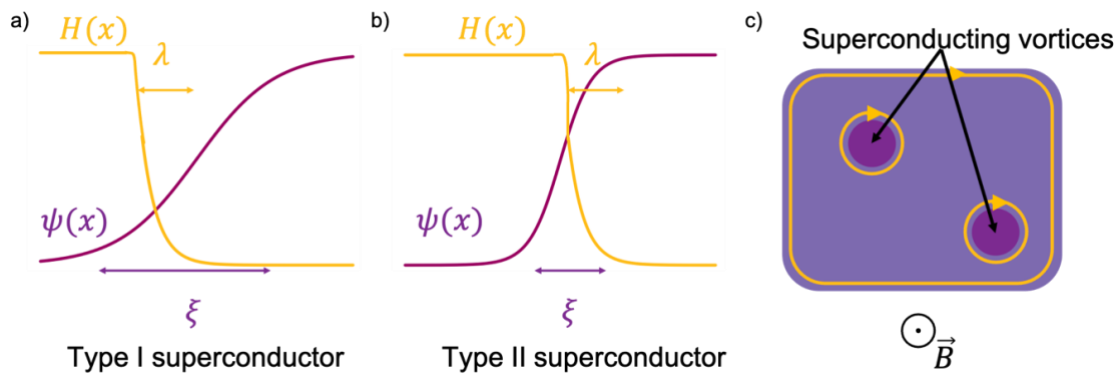


Figure 8 Magnetic field in the superconductor H and Ginzburg-Landau (GL) order parameter ψ close to a boundary as a function of the distance with their two characteristic lengths respectively λ and ξ in the case of a) a type I superconductor and b) a type II superconductor. c) A type II superconductor in an applied magnetic field \vec{B} with both screening by partial Meissner effect and superconducting vortices letting an integer number of quantum of flux enter.

This description, unfortunately, collapses for example when we consider magnetic fields that are strong enough to modify the superconducting properties throughout n_S . This problem was solved thanks to the intuition that superconductivity is described as a **phase transition theory whose order parameter is a pseudo wavefunction ψ** such as $n_S(x) = |\psi(x)|^2$ [3]. Close to the critical temperature, this order parameter gets small and the free energy of the superconductor can be expanded in powers of ψ and $\vec{\nabla}\psi$. For the sake of brevity, I will not

show these equations but they end up giving two characteristic lengthscales: an analogous London penetration length λ and a new one, the Ginzburg-Landau (GL) coherence length ξ_{GL} , both dependent on the temperature. ξ_{GL} gives the typical length for which a small disturbance in the order parameter ψ is decaying in space. It has been shown by Abrikosov [18] that if $\lambda > \frac{\xi_{GL}}{\sqrt{2}}$, it is energetically favorable for the magnetic field to penetrate inside the superconductor through **vortices** when it reaches a critical value H_{c1} up until a value H_{c2} , where superconductivity finally vanishes. In that interval, these superconductors, so-called type II superconductors, experience the Meissner effect only partially and H_{c2} can be much larger than H_{c1} . Contrary to type I superconductors, superconductivity in type II superconductors can exist at much higher magnetic field. Figure 8a and b shows how superconductors of type I and type II behave differently in the presence of an applied magnetic field and close to a boundary. Figure 8c illustrates the mixed state of a type II superconductor in an applied magnetic field \vec{B} with the presence of both screening currents and superconducting vortices letting the magnetic field penetrate through the superconductor as an integer number of the flux quantum $\phi_0 = \frac{h}{2e}$.

Although the Ginzburg-Landau theory is a convenient way to understand the magnetic and thermodynamic properties of superconductors, it does not say anything about the microscopic origin of this phenomenon. Almost 50 years were necessary to answer this question with the famous BCS theory [4], a name given in honor of its three authors, Bardeen, Cooper and Schrieffer. The argument starts with the Fermi surface of a metal being unstable against the formation of a bound pair of electrons thanks to an attractive interaction, no matter how weak it is [19]. This pair of electrons is called a **Cooper pair and is made of two electrons of opposite momenta and spins**. These pairs form a condensate and are represented in Figure 9a. This attractive interaction term does not come out if we only consider the electrons and their interaction between each other and the lattice of ions. We have to also consider the motion of the ions. The attractive interaction is mediated by the phonons of the lattice. The question is then to know if this phonon interaction can overcome the electronic repulsion. This is material dependent and that explains why some materials are not superconducting at any temperature like copper or gold for instance.

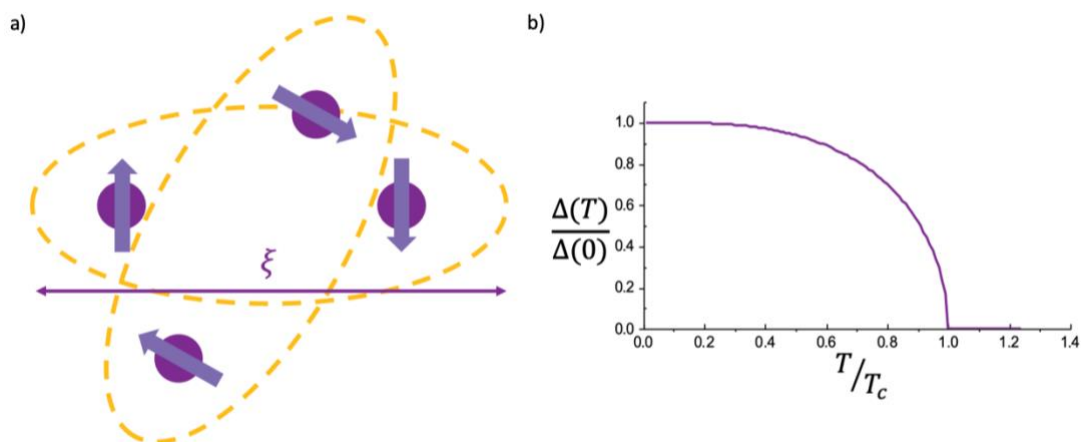


Figure 9 a) Condensate of Cooper pairs of size ξ , the coherence length of the superconductor. b) Temperature dependence of the superconducting gap Δ deduced self-consistently from

the BCS theory.

In the following paragraph, we will go quick on the mathematical resolution of the problem, only emphasizing the important results for the following chapters, especially for chapter 3. The Hamiltonian in the presence of an interaction between electrons of momentum \mathbf{k} and \mathbf{k}' , $V_{\mathbf{k}\mathbf{k}'}$ is:

$$H = \sum_{\mathbf{k}\sigma} \xi_{\mathbf{k}\sigma} c_{\mathbf{k}\sigma}^\dagger c_{\mathbf{k}\sigma} + \frac{1}{N} \sum_{\mathbf{k}\mathbf{k}'} V_{\mathbf{k}\mathbf{k}'} c_{\mathbf{k}\uparrow}^\dagger c_{-\mathbf{k}\downarrow}^\dagger c_{-\mathbf{k}'\downarrow} c_{\mathbf{k}'\uparrow} \quad 2.4$$

Here, $c_{\mathbf{k}\sigma}^\dagger$ creates an electron with momentum \mathbf{k} and spin σ . The first term is the kinetic energy one (chemical potential μ included) while the second is the interaction part. It describes the destruction of a Cooper pair followed by the creation of another one. This term is the one that needs to be approximated to find the energies of the system. We perform a **mean-field approximation** on this term:

$$\langle c_{\mathbf{k}\uparrow}^\dagger c_{-\mathbf{k}\downarrow}^\dagger c_{-\mathbf{k}'\downarrow} c_{\mathbf{k}'\uparrow} \rangle \approx \langle c_{\mathbf{k}\uparrow}^\dagger c_{-\mathbf{k}\downarrow}^\dagger \rangle c_{-\mathbf{k}'\downarrow} c_{\mathbf{k}'\uparrow} + c_{\mathbf{k}\uparrow}^\dagger c_{-\mathbf{k}\downarrow}^\dagger \langle c_{-\mathbf{k}'\downarrow} c_{\mathbf{k}'\uparrow} \rangle - \langle c_{\mathbf{k}\uparrow}^\dagger c_{-\mathbf{k}\downarrow}^\dagger \rangle \langle c_{-\mathbf{k}'\downarrow} c_{\mathbf{k}'\uparrow} \rangle \quad 2.5$$

Setting what we call energy gap for a reason that will appear later $\Delta_{\mathbf{k}} = \frac{1}{N} \sum_{\mathbf{k}'} V_{\mathbf{k}\mathbf{k}'} \langle c_{\mathbf{k}'\uparrow}^\dagger c_{-\mathbf{k}'\downarrow}^\dagger \rangle$, one gets:

$$H = \sum_{\mathbf{k}\sigma} \xi_{\mathbf{k}\sigma} c_{\mathbf{k}\sigma}^\dagger c_{\mathbf{k}\sigma} - \sum_{\mathbf{k}} (\Delta_{\mathbf{k}} c_{\mathbf{k}\uparrow}^\dagger c_{-\mathbf{k}\downarrow}^\dagger + \Delta_{\mathbf{k}}^* c_{-\mathbf{k}\downarrow} c_{\mathbf{k}\uparrow}) + \sum_{\mathbf{k}} \Delta_{\mathbf{k}} \langle c_{\mathbf{k}\uparrow}^\dagger c_{-\mathbf{k}\downarrow}^\dagger \rangle \quad 2.6$$

It is now possible to diagonalize this Hamiltonian thanks to a **Bogoliubov transformation** introducing the fermionic operators $\gamma_{\mathbf{k}\sigma}$ related to the former by:

$$c_{\mathbf{k}\uparrow} = u_{\mathbf{k}}^* \gamma_{\mathbf{k}\uparrow} + v_{\mathbf{k}} \gamma_{-\mathbf{k}\downarrow}^\dagger \quad 2.7$$

$$c_{-\mathbf{k}\downarrow}^\dagger = u_{\mathbf{k}} \gamma_{-\mathbf{k}\downarrow}^\dagger - v_{\mathbf{k}}^* \gamma_{\mathbf{k}\uparrow} \quad 2.8$$

The fermionic commutation relations impose : $|u_{\mathbf{k}}|^2 + |v_{\mathbf{k}}|^2 = 1$. Injecting this in the Hamiltonian, one gets:

$$H = \sum_{\mathbf{k}\sigma} E_{\mathbf{k}} \gamma_{\mathbf{k}\sigma}^\dagger \gamma_{\mathbf{k}\sigma} + E_0 \quad 2.9$$

With $E_{\mathbf{k}} = \sqrt{\xi_{\mathbf{k}}^2 + |\Delta_{\mathbf{k}}|^2}$ and E_0 the energy of the ground state. From this final expression for the energy of the system, one finds back the existence of the superconducting gap. Indeed, **even at the Fermi level where $\xi_{\mathbf{k}} = 0$, the energy necessary to create a quasiparticle is $2\Delta_{\mathbf{k}}$ due to the existence of a gap of size $\Delta_{\mathbf{k}}$** . There are no excited states lower in energy than this gap and it will have huge consequences on transport as we will see in chapter 3. This result is plotted in Figure 9c. It is possible to find the temperature dependence of this gap self-consistently. This result is plotted in Figure 9c. Formulae 2.7 and 2.8 tell us about the nature of these quasiparticles which are a mixture of electron and hole. They are the excitations from the ground state $|\psi_{BCS}\rangle$ made of condensed Cooper pairs that can be

written from the vacuum state $|0\rangle$ (no electron):

$$|\psi_{BCS}\rangle = \prod_{k=k_1, \dots, k_M} (u_k + v_k c_{k\uparrow}^\dagger c_{-k\downarrow}^\dagger) |0\rangle \quad 2.10$$

Therefore, they can be described by a vector $\begin{pmatrix} u \\ v \end{pmatrix}$ where u (v) is respectively the amplitude of the quasi-electron (quasi-hole) component.

BCS theory shed light on the microscopic origins of superconductivity, described its ground state that can conduct current with Cooper pairs without dissipation and its elementary excitations. This theory has known a lot of successes describing superconductors until the appearance of higher T_c superconductors whose properties did not perfectly match the BCS predictions.

2.1.2 More exotic superconductivity and YBCO

2.1.2.1 Different symmetries for the superconducting gap

Although the concept of Cooper pairs remains true for all superconductors, the electron-phonon interaction responsible for the superconductors at the time cannot explain that other materials like YBCO are superconducting since the interaction is too weak at least if there is no other interaction at stake [20]. Moreover, both non-phase-sensitive and phase-sensitive measurements have shown evidence for a more exotic superconducting order parameter [21].

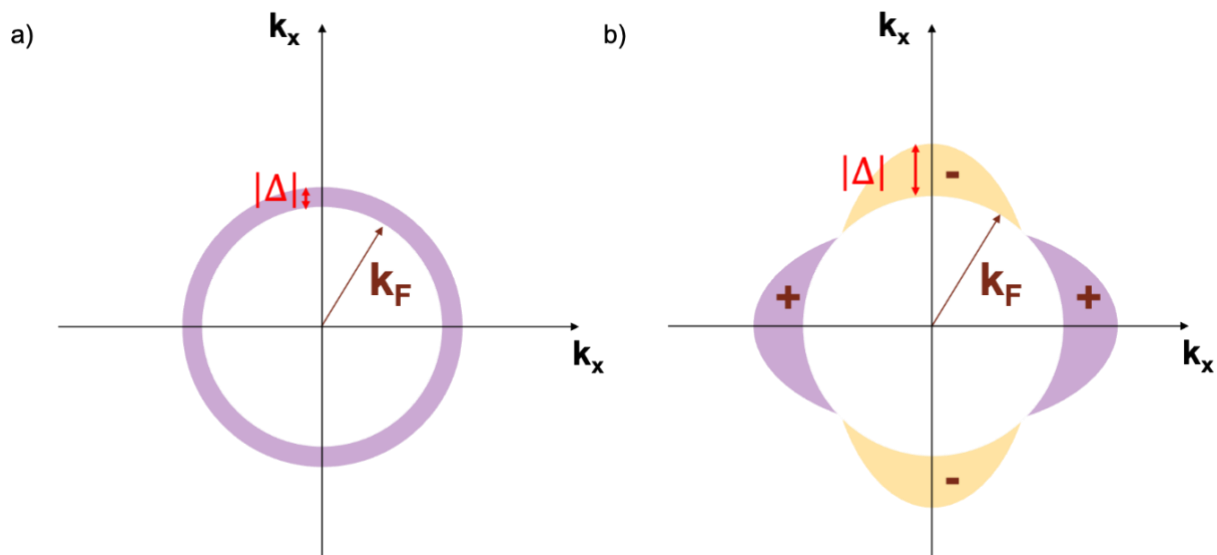


Figure 10 a) Colorplot in the 2D momentum space of the amplitude and phase of the s -wave superconducting order parameter. b) Same for a d -wave superconductor ($d_{x^2-y^2}$). The purple regions correspond to a positive phase while the yellow ones correspond to a negative phase. For $|k_x| = |k_y|$, the gap closes at what we call nodes.

For conventional s -wave superconductors, the gap Δ is an isotropic complex number whose amplitude and phase do not vary in the reciprocal space as shown on the color

plot of Figure 10a. On the contrary, **for *d*-wave superconductors, the amplitude and phase of Δ depend on \vec{k}** and some propagation directions experiments have no gap at all. Δ writes (with a the in-plane constant):

$$\Delta(\vec{k}) = \Delta_0(\cos k_x a + \cos k_y a) \quad 2.11$$

As we will see in chapter 3, this anisotropy of Δ will have huge consequences on the transport properties at the interfaces with other materials. To be noticed, *p*- and *f*-wave order parameters also exist [22,23].

2.1.2.2 YBCO, a *d*-wave high T_c superconductor

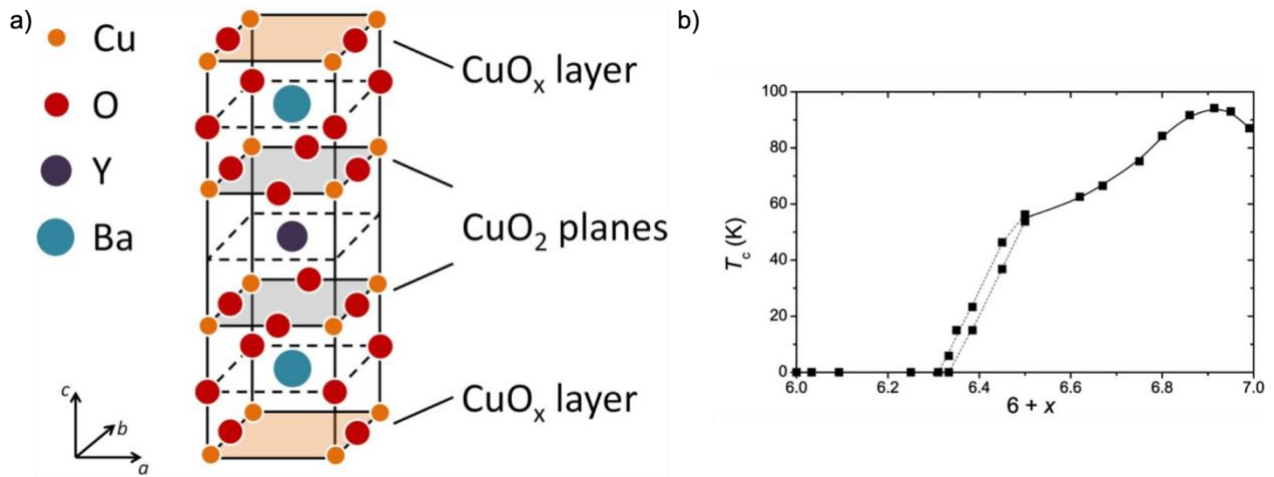


Figure 11 a) Unit cell of YBCO. Cuprates all have the CuO₂ planes, which, in the case of YBCO, is the layer where superconductivity happens. Taken from E. Stilp et al., *Sci. Rep.* **4**, 6250 (2014). b) Superconducting critical temperature as a function of the oxygen stoichiometry for YBCO. We can see the higher critical temperature occurs for an oxygen stoichiometry around 6.9. Taken from Liang et al., *Phys. Rev. B* **73** (2006).

In this thesis, I used as the main superconducting material YBa₂Cu₃O_{7- δ} (YBCO). Here, δ corresponds to the missing oxygen in the crystal structure. YBCO is an oxide that has a perovskite-like structure as shown in Figure 11a [24]. Two important features in this stack explain the properties of YBCO. The CuO₂ layer covering the a-b plane is thought to be the layer where superconductivity develops itself as it is common to all the superconducting cuprates. The other one is the CuO chain along the b-direction, where there are oxygen vacancies. This chain acts like a reservoir for extra charge carriers, more or less filled depending on the stoichiometry in oxygen. As the graph in Figure 11b exhibits, the stoichiometry of oxygen has strong implications on the superconducting properties of YBCO [25]. Here, the T_c of YBCO is plotted as a function of the stoichiometry of oxygen. While its optimum content in oxygen ($\delta = 0.08$) gives a T_c equal to 92K, for δ larger than 0.7, YBCO is no more superconducting.

Table 1 provides the main superconducting properties of optimally doped YBCO (T_c at 92K) at zero temperature. There is a clear anisotropy between the parameters in the ab-plane and those along the c-axis. As shown in this table, the superconducting coherence length ξ of

YBCO is in both cases small compared with *s-wave* superconductors like Al (1600nm) [26] and is much smaller than the quasiparticles mean free path (250nm at 15K [27]). YBCO can therefore be considered as a clean superconductor. An important point for the following is the very large values of B_{c1} and B_{c2} . In our experimental setup, the maximum magnetic field is 9T, as a consequence, the variations in the measurements due to the magnetic field will not come from a decrease in the superconducting properties of YBCO itself.

Direction	T_c	ξ	λ	B_{c1}	B_{c2}
ab-plane	92K	1.6nm	135nm	8.9mT	850T
c-axis	92K	0.24nm	894nm	50mT	130T

Table 1 Properties of optimally doped YBCO at zero temperature for the two directions of transport (in the ab-plane and along the c-axis). The magnetic fields are considered perpendicular to the direction mentioned in the table.

In addition to superconductivity, YBCO and more generally cuprates possess very rich and complex phase diagrams with for instance, depending on the doping and the temperature, an antiferromagnetic phase or a charge density wave phase [28]. These properties are not of interest to this thesis and will not be further detailed here.

2.1.3 Applications of superconductors

Now we have described both low- T_c and high- T_c superconductors, let us see some applications of superconductivity.

2.1.3.1 Superconductors as lossless current carriers

The first property of superconductors we can think of for applications is their ability to convey current without electrical resistance. This is already used for the electrical grid [29] in some places in the world. Although it is a bit harder to implement due to the cryogenic issue compared with usual high voltage transmission lines, superconducting lines have multiple advantages like the absence of losses even over long distances and smaller wires.

This absence of resistance is also necessary when one deals with high currents to generate high constant magnetic fields. Usual copper coils need to be cooled down by a refrigerated water circuit to safely reach magnetic fields around 1T Tesla and dissipate a lot of energy in Joule heating. On the contrary, superconductors can carry large currents below their critical density current without heating and loss. In the case of **superconducting coils**, type II superconductors have to be used to sustain a high magnetic field. However, vortices will form and the currents in the coil make them move. This motion dissipates energy and the superconductor has a finite resistance [17]. To avoid this, vortices have to be pinned on defects [30]. The larger is the pinning potential, the larger can be the current going through the wire without resistance. As we will see in chapter 4, I will make use of a superconducting magnet to apply magnetic fields up to 9T.

2.1.3.2 Josephson junction as a building block for superconducting electronics

A superconductor is not only a perfect conductor, it is a macroscopic quantum condensate of Cooper pairs that has a definite quantum phase. To be rigorous, the uncertainty around the value of this phase is related to the uncertainty over the number of Cooper pairs in the condensate since they are canonical conjugate quantities. However, since there is a huge number of particles in the condensate, the number of Cooper pairs and the phase can most of the time be considered as semi-classical variables.

A Josephson junction is made of two superconductors separated by a region that can be either a thin insulating barrier (S-I-S for Superconductor-Insulator-Superconductor), a normal metal or a good conductor in general (S-N-S), a ferromagnet (S-F-S) or a constriction (S-c-S),... An example of a Josephson junction is shown in Figure 12. Josephson predicted in 1962 [31] that even at zero voltage a current could emerge from a difference of phases between the two superconducting electrodes (φ_1 and φ_2) due to the **quantum tunneling of Cooper pairs from one superconductor to the other**. He established two formulae describing the so-called DC and AC Josephson effects:

$$I_s = I_c \sin \gamma \quad 2.12$$

$$\frac{d\Delta\varphi}{dt} = \frac{2eV}{\hbar} \quad 2.13$$

Here, I_s is the supercurrent, I_c is the maximum critical current and $\gamma = \Delta\varphi - \frac{2\pi}{\phi_0} \int \vec{A} \cdot \vec{ds}$ is the gauge invariant phase difference between the two superconductors with the contour taken from one electrode to the other. $\Delta\varphi$ is the phase difference, ϕ_0 is the quantum of flux and V is the voltage across the junction. In chapter 3, we will give a demonstration of the Josephson effect using the concept of Andreev bound states.

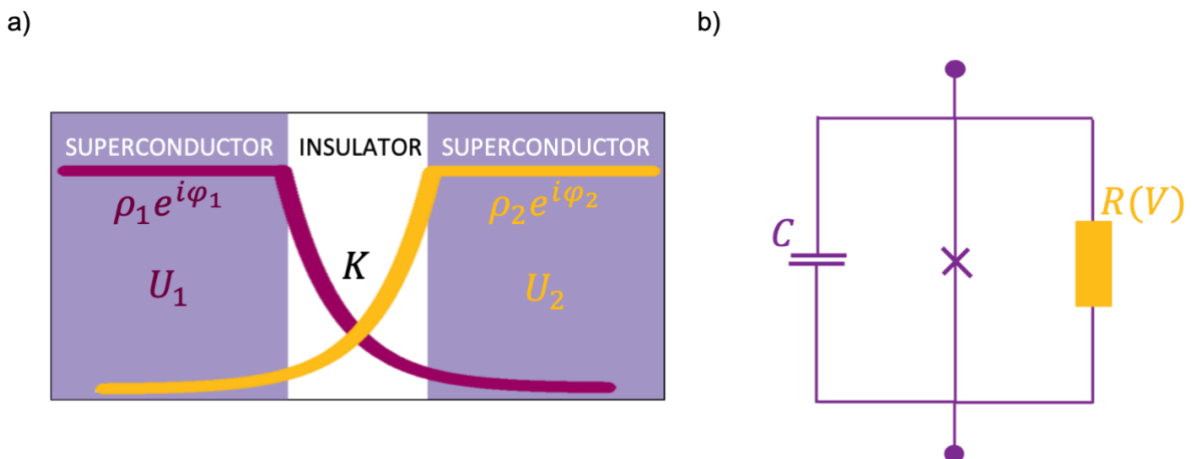


Figure 12 a) Scheme of a Josephson junction with the two macroscopic wavefunctions 1 and 2 and the energies U_1 and U_2 of each side. b) Electronic representation of a Josephson junction with the RCSJ model.

Josephson's intuition was early confirmed by experiments [32] and since his discovery, many

applications have emerged as we will see in the next sections. A Josephson junction is a non-linear electrical component and as soon as we have a non-zero voltage across the junction, the Josephson relations have to be completed to take into account the capacitive effect between the two electrodes and the dissipative part of the current due to quasiparticles. We therefore adopt a widely used model called **RCSJ model** for resistively and capacitively shunted junction [33]. These effective parameters can be tuned by changing the geometry or the materials of the Josephson junction. Two main cases of Josephson junctions are encountered: the underdamped and overdamped junctions.

Illustrations of both behaviors are shown in Figure 13 [34]. The behavior in a corresponds to an underdamped junction. This is usually the case for SIS junctions with large capacitance and resistance. The IV curve is hysteretic with different paths depending on the direction we sweep the current. When starting at zero current, the voltage will remain 0 until the current reaches I_C , and will then jump to a finite value. But when decreasing from large values of the current, the voltage will jump at a lower current I_R . The behavior in b corresponds to the opposite case of overdamped junctions, encountered with SNS junctions with lower resistance and capacitance. Here, there is no hysteresis and no jump of the voltage.

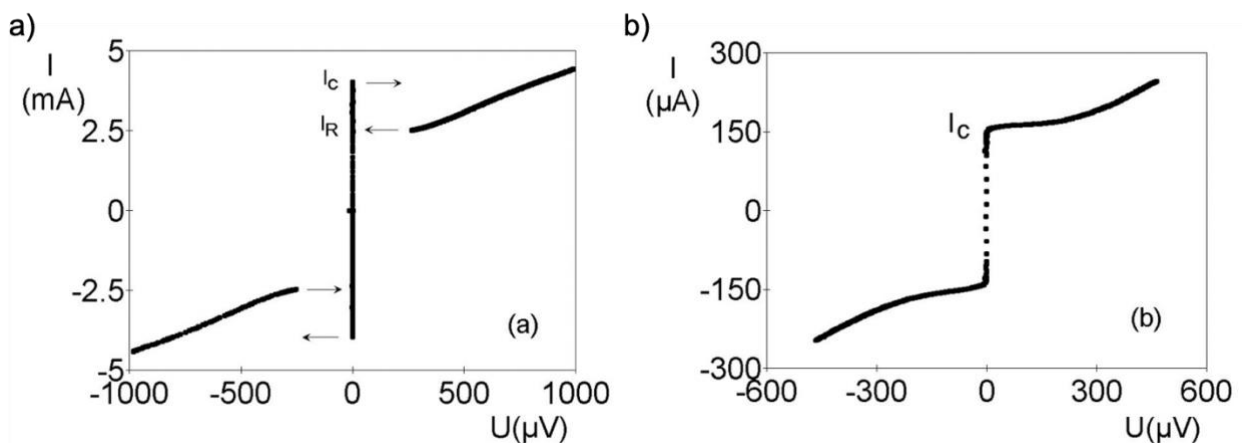


Figure 13 Experimental measurements of a) a tunnel SIS junction giving rise to an underdamped behavior (large resistance and capacitance in the RCSJ model) and b) of a weak link SNS junction giving an overdamped behavior (low resistance and low capacitance).

Figures taken from Advanced Lab course at Walther–Meißner–Institut.

Josephson junctions show a particular response in the presence of an external magnetic field similar to what happens with an electromagnetic wave on a slit, resulting in a **Fraunhofer pattern** on a screen. Likewise, the magnetic field causes a similar diffraction pattern of the critical current plotted as a function of the magnetic flux with nodes at every quantum of flux, $\Phi_0 = \frac{h}{2e}$, present in the Josephson junction area (see Figure 14). The magnetic flux penetrating the junction causes an inhomogeneity of the local value of the supercurrent (as shown in the insets of Figure 14 for two values of the flux Φ_0 and $\frac{3}{2}\Phi_0$), giving rise to oscillations of the total supercurrent.

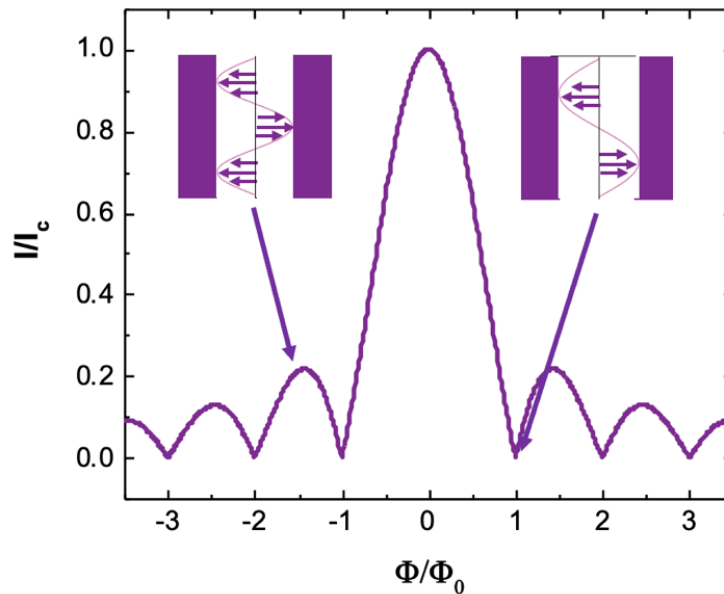


Figure 14 Fraunhofer pattern of a rectangular homogeneous Josephson junction. The normalized critical current is plotted as a function of the magnetic flux normalized by the quantum of flux. The modulation of the critical current is explained by the two schemes representing the local critical current as a function of the position along the width of the junction. Figure inspired by Tinkham, *Introduction to Superconductivity, Second Edition* (1995).

Josephson junctions are the essential components of superconducting electronics or in the fast-growing field of quantum computing [35]. We will see in the following how it is used in SQUIDs and SQIFs.

2.1.3.3 Superconducting QUantum Interference Device (SQUID)

A SQUID is a superconducting interferometric loop made of two Josephson junctions in parallel as pictured in Figure 15. The working principles of this component are the Josephson effect and the quantification of the magnetic field. At fixed current I , the presence of a magnetic field creates a phase gradient of the superconducting phases on both sides of the superconducting loop. The Josephson effect translates this into a periodic response with respect to the enclosed flux inside the loop as shown in Figure 15b [17]. SQUIDs are already used for detecting tiny magnetic fields. Usually, SQUIDs are biased with a higher current than the critical current of the junction and a magnetic field is applied to operate with the best sensitivity when the slope of voltage with respect to the flux is maximum.

SQUIDs allow the measurement of very low magnetic fields and are promising to measure tiny magnetic fields ($\sim 10^{-13}\text{T}$) produced by organs like the brain [36]. Unfortunately, maintaining the SQUID at the best operating point requires electronic feedback loops that limit the frequency of operation of the device and add some noise, detrimental for very low field measurement. Moreover, the periodicity of the signal makes it difficult to operate in case of abrupt change of magnetic field enough to jump one or several periods.

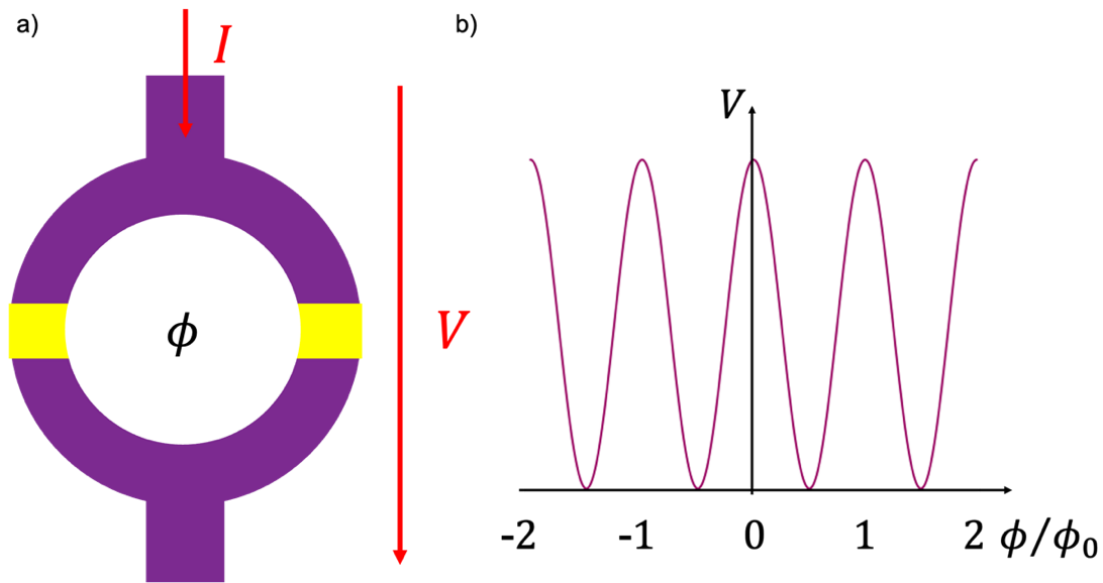


Figure 15 a) Scheme of a SQUID made of two Josephson junctions with the barriers highlighted in yellow and the superconducting tracks in purple. b) Evolution of the voltage measured at constant current bias with respect to the enclosed flux normalized by ϕ_0 .

Another promising sensor also based on superconducting Josephson junctions is the Superconducting Quantum Interference Filter (SQIF). A SQIF is a 1D or 2D array of SQUIDs with each SQUID having different loop areas. A scheme of a 1D array of SQUIDs is presented in Figure 16b [37]. The individual voltage response of each SQUID is calculated in a and the sum of the contributions of all these SQUIDs is given in c. Compared with the periodic response of individual SQUIDs, here, the response is no longer periodic but has a sharp response between zero field and the first oscillations. A DC field is applied to the SQIF in order to operate at the maximum sensitivity and where the response is linear. It allows to measure very small signals down to $\sim 10^{-15}\text{T}$ and since there is no resonance needed, it can measure a very broad range of frequencies with a single device on a chip. The reasonable size as shown on Figure 16e of the device and the possibility to use a high T_c superconductor make it easy to cool down and embark for sensing in remote applications. A small part of a SQIF is given in Figure 16d. The superconductor is YBCO, the same as I used during my PhD except here, it was grown on sapphire to be compatible with RF applications.

In this general introduction about superconductivity, I have addressed some of the main theoretical concepts that will be very useful in the following chapters, presented the superconductor I used all over my PhD, YBCO, and finally given some of the multiple applications of superconductors. Now, I will pursue with the other component of my devices that are the 2D materials.

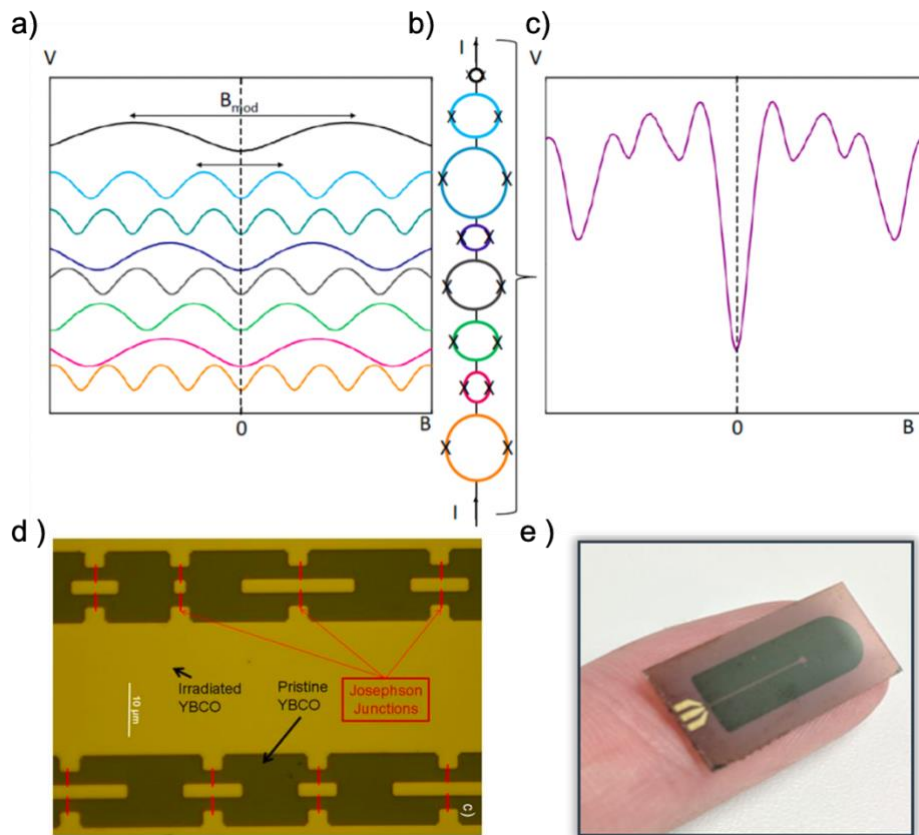


Figure 16 a) Numerical calculation of the voltage against the magnetic field for each SQUID of the SQIF shown in b). b) Scheme of the SQIF, the array of SQUIDs of different loop areas considered in a). c) Resulting voltage response of the SQIF against the magnetic field. d) A microscope image of a part of SQIF. e) Image of an antenna made with a SQIF for sensing applications. Figures taken from R. Pawlowski, PhD thesis (2019).

2.2 2D-MATERIALS

First, let us give a definition of a 2D material. It is a crystalline material made up of a single or few layers atom and in which the in-plane inter-atomic interaction are much stronger than the out-of-plane ones [38]. They are also very often called Van der Waals (VdW) materials, especially when they are made of a larger number of layers stacked (identical or not). In the following section, I will first introduce graphene. Then, I will describe the transition metal dichalcogenide family, especially molybdenum disulfide, and finally I will quickly review the methods of growth and how they allow for new applications.

2.2.1 Graphene and its properties

Graphene is the first 2D material that have been produced and characterized as a 2D material. Its discovery [39] after the successive exfoliation of graphite with the now famous scotch tape method granted its inventors a Nobel Prize since it opened an immense field of research.

2.2.1.1 Band structure, dispersion relation, and chirality

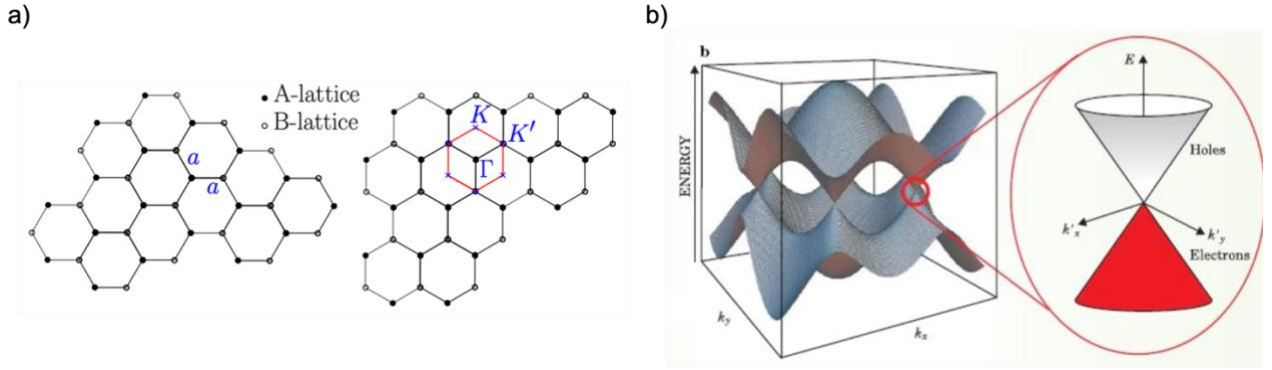


Figure 17 a) Graphene honeycomb structure in real (left) and reciprocal (right) space. b) Graphene band structure with a zoom on one of the two Dirac cones.

Graphene has a honeycomb lattice which is made of two translated triangular lattices (lattices A and B) as shown on the left side of Figure 17a. In reciprocal space, it gives the same structure with two lattices with generating vector \vec{K} and \vec{K}' (see right side of Figure 17a). The band structure of graphene has been calculated with a tight binding method by Wallace in 1947 [40] and its energy dispersion is:

$$E(\vec{k}) = \pm t \left| 1 + e^{i\frac{a\sqrt{3}}{2}(k_x + \sqrt{3}k_y)} + e^{i\frac{a\sqrt{3}}{2}(-k_x + \sqrt{3}k_y)} \right| \quad 2.14$$

Where t is the nearest neighbour hopping term, a is the inter-atomic distance which is around 142pm and \vec{k} is the electronic wavevector. This energy dispersion in the first Brillouin zone is plotted in Figure 17b and the two bands touch in six points (only two inequivalent points \vec{K} and \vec{K}' called Dirac points) where it forms cones with a linear energy dispersion. These cones are called Dirac cones, a term borrowed from high-energy physics since particles obeying the Dirac equation have a linear energy dispersion. Indeed, the linearization (valid up to 1eV) of equation 2.14 gives:

$$E(\vec{k}) = \pm \hbar v_F |\vec{k}| \quad 2.15$$

With v_F the Fermi velocity in graphene which is around 1×10^6 m/s. **This linear energy dispersion, similar to the one of photons in vacuum, provides high-energy physics properties to the quasiparticles in graphene since they obey the massless Dirac equations close enough to the Dirac points [41]:**

$$i \frac{\partial \Psi}{\partial t} = -v_F \vec{\alpha} \cdot \vec{\nabla} \Psi, \text{ with } \Psi = \begin{pmatrix} \psi_{KA} \\ \psi_{KB} \\ \psi_{K'B} \\ -\psi_{K'A} \end{pmatrix} \text{ and } \vec{\alpha} = \begin{pmatrix} 0 & \vec{\sigma} \\ \vec{\sigma} & 0 \end{pmatrix} \quad 2.16$$

Where $\vec{\sigma}$ are the Pauli matrices and K (K') corresponds to the valley index (one of the two inequivalent cones) and A (B) stands for the sublattice. The stationary solutions to this equation are chiral meaning their momentum and their sublattices A or B (called pseudospin) are locked together so that charge carriers in graphene have a definite pseudospin direction,

parallel or antiparallel to the direction of motion.

2.2.1.2 Klein tunneling

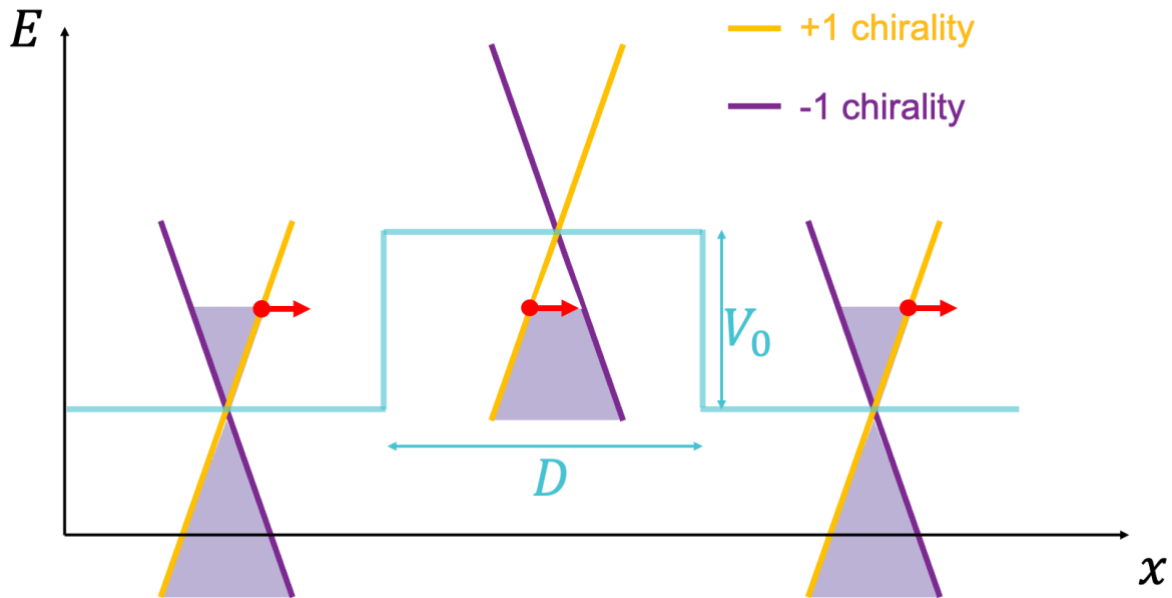


Figure 18 Illustration of the Klein tunnelling with an electron, keeping its chirality all along and as a consequence, being transmitted perfectly towards a potential barrier of width D and height V_0 . Inside the barrier, the electron is converted into a hole of same chirality. On the scheme, the initial and final Fermi level is at the Dirac points but it would be the same with a finite doping.

A direct consequence of the chirality of the charge carriers is the Klein tunnelling [42–44], this property of relativistic quantum particles to be transmitted across a potential barrier of any width and thickness. This process is pictured in Figure 18 where we see that an electron of a given chirality won't be reflected by a potential barrier but be transmitted as a hole that will then be transmitted again as an electron on the other side of the barrier. In chapter 6, we will study a similar situation except on the left-hand side, the graphene will be proximized by a d -wave superconductor.

2.2.1.3 Electronic properties

The Dirac physics of the charge carriers also provides them with remarkable transport properties. Indeed, their relative immunity to scattering grants them a **very high mobility**. This refers to the ability of a charge to move through the material as an electric field is applied. The first measured mobility was already around $10000 \text{ cm}^2/\text{V}\cdot\text{s}$ [39] for exfoliated graphene. Since then, the understanding of the sources of mobility loss has been investigated [45] and the importance of the substrate has been established [45,46] through surface phonon scattering. Nowadays, the highest mobilities are obtained either by sandwiching graphene between insulating layers of a 2D material, hexagonal boron nitride (h-BN) [47,48], or by suspending graphene [49]. This makes graphene one of the best conductors, on equal step with the best metals.

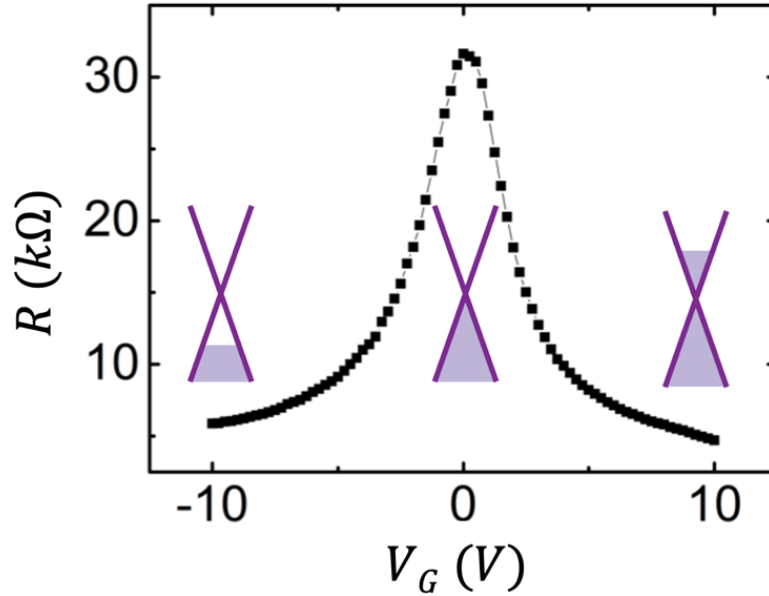


Figure 19 Typical evolution of the resistance as a function of a back gate voltage applied on graphene. For each resistance, a scheme of the filling of the Dirac cone is given. Here, the graphene has no intrinsic doping since the charge neutrality point (CNP) is exactly at 0V.

Another remarkable property of graphene is the high tunability of the number of charge carriers through the application of a gate voltage or mechanical stress. Figure 19 illustrates the tunability of the Fermi energy with a gate voltage. It does not only change the number of charge carriers but also their nature going from hole transport (p-doped graphene) at negative voltage to electron transport (n-doped graphene) at positive voltage. Here, in the absence of intrinsic doping, the charge neutrality point (CNP) where the Fermi level is exactly at the Dirac points is at zero gate voltage. It manifests by a much larger value of the resistance. Even for ideal graphene, this resistance doesn't go to infinity since the minimum conductivity of graphene is of the order of $\frac{e^2}{h}$.

Those electronic properties allow observing the quantum Hall effect [50] at room temperature, a phenomenon that arises from the quantification of the orbital of the electrons in the presence of a magnetic field. The system then becomes insulating in the bulk but conducting on the edges. Finally, the transverse resistance is quantized and is equal to: $R_{xy} = \frac{h}{e^2\nu}$, where ν is a factor that can take either integer ($\nu = 1, 2, \dots$) or fractional values ($\nu = \frac{1}{3}, \frac{2}{5}, \frac{3}{7}, \dots$) corresponding respectively to integer quantum Hall effect and fractional quantum Hall effect [51]. The peculiar properties of graphene are also at the origin of many applications we will describe in the next subsection.

2.2.1.4 Applications

The very high carrier mobility of graphene, up to $\sim 10^6 \text{ cm}^2/\text{V}\cdot\text{s}$, and its high carrier velocity makes it attractive for high-speed electronics. Moreover, graphene is a 2D material with a thickness of one single atom which is the ultimate advance in miniaturization. Finally, it is

also very **flexible and robust**. All these pros justify the use of graphene for RF transistors [41,52]. As shown in Figure 20c, graphene RF transistor [52] can reach high cut-off frequencies ($\sim 300\text{GHz}$). To obtain these results, the researchers used graphene for its very high mobility and optimized the gate coupling with a self-aligned nanowire depicted with an artist's view and a side-view scheme in Figure 20a and b. Indeed, conceiving a gate for graphene applications is tedious because the approach has to be very soft to avoid damaging graphene but at the same time to produce high-quality dielectrics.

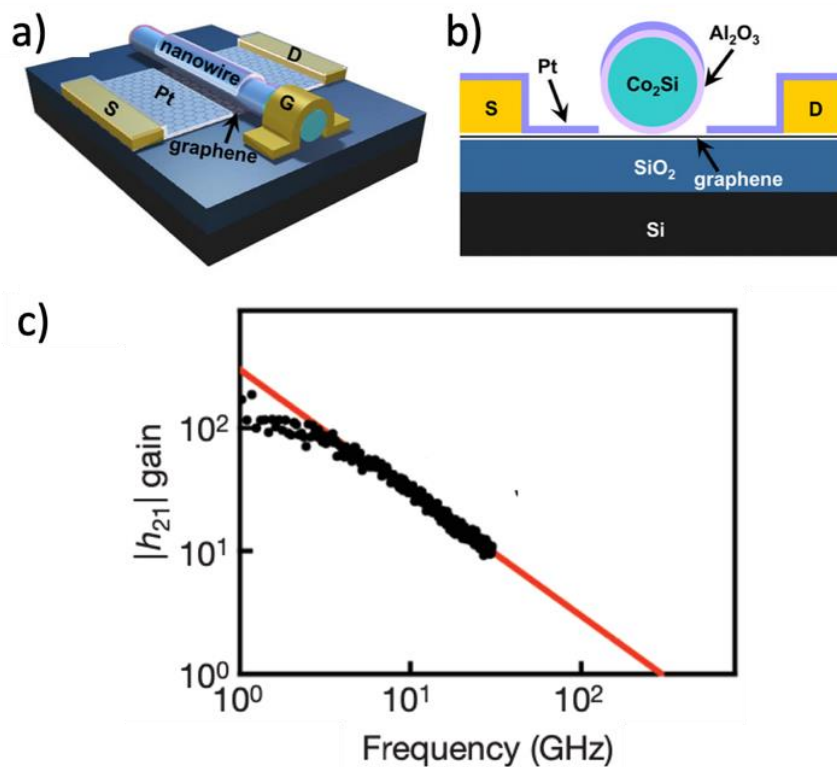


Figure 20 a) Artist view of a graphene RF transistor with a self-aligned nanowire gate made Co₂Si coated by Al₂O₃. b) Side-view of the same device. c) Gain of the device as a function of the frequency in a semi-logarithmic scale with a cut-off frequency of $\sim 300\text{GHz}$. Figures adapted from Liao et al., Nat. **467**, 305-308 (2010).

However, when it comes to transistors for logic, the semi-metallic nature of graphene, *i.e.* its lack of a band gap, limits the on/off ratio. Yet, it is possible to induce a gap in graphene by patterning nanoribbons by lateral confinement [53] or by using bilayer graphene [54] instead. In that case, a gate voltage opens a gap and allows for a larger on/off ratio. However, in both cases, the creation of the gaps goes with a decrease in mobility. We will see in the next subsection that heterostructures made with different 2D materials can help improve the performances.

Graphene not only has remarkable electronic properties but also very interesting optical properties. Since graphene is gapless, it absorbs light from the near-infrared to the visible part of the spectrum. Though one atom thick, it still absorbs around 2% of the light and its high mobility guarantees fast dynamics making it very interesting for photodetector applications [55] among others. In Figure 21, a graphene photodetector is depicted in the

inset with typical IV curves in the presence and absence of a DC light source in a quasi-short-circuit configuration. The photoelectric effect creates an electron-hole pair that separates with each going in opposite directions creating a photocurrent.

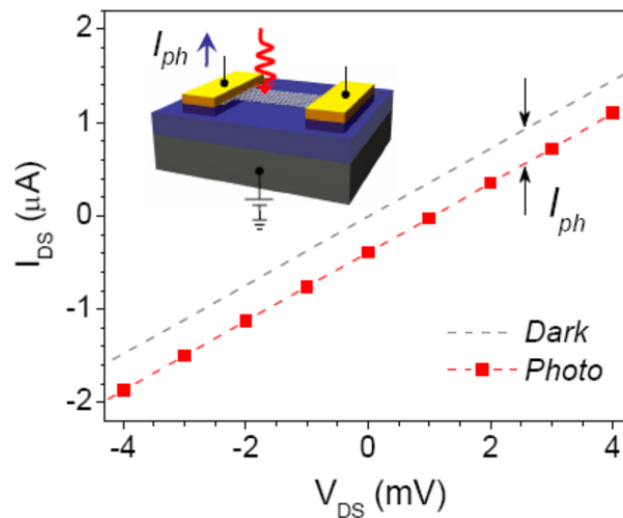


Figure 21 Example of IV curves of a photodetector in the presence (red squared line) and absence of light (black squared line). Figure taken from Xia et al., *Nature Nanotech* **4**, 839–843 (2009).

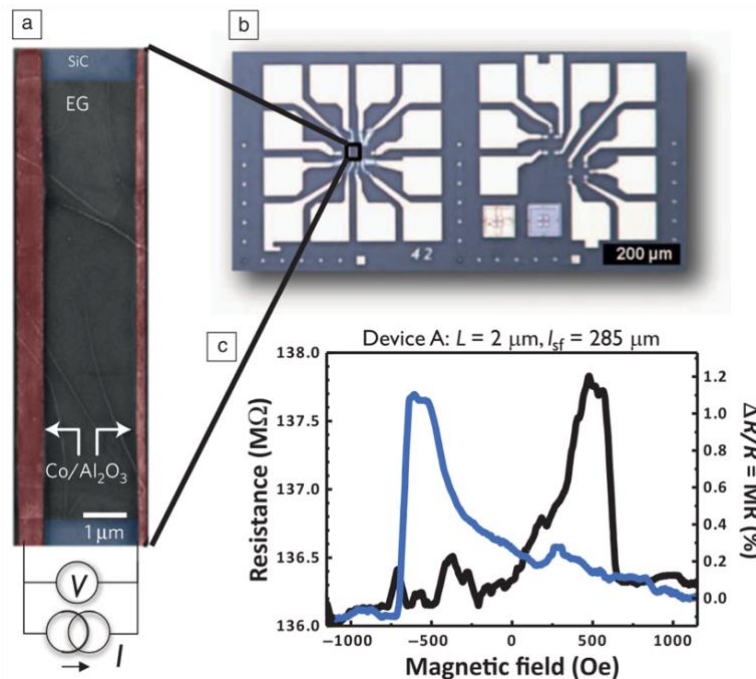


Figure 22 a) Zoomed microscopic image of a spintronic device with on the left the spin injector which is made of an electrode of cobalt (a ferromagnet) and a thin layer of alumine as a tunnel barrier with graphene. On the other side, the analyzer is built the same way. The graphene channel in the middle (2μm-long) conveys spin from one side to the other. b) Large view of the device with the gold contact pads. c) Magnetoresistance measurement with the two peaks (~1%) occurring when the injector and analyzer are in two opposite magnetic configurations. Figures taken from Dlubak et al., *Nature Phys* **8**, 557–561 (2012).

Last but not least, I would like to briefly talk about the use of graphene for spintronic applications [56]. Indeed, backscattering is strongly suppressed in graphene thanks to its band structure. Due to the quasi-absence of spin-orbit coupling (SOC) in graphene, spins can propagate over distances around $100\mu\text{m}$, much larger than in conventional metals. In Figure 22a and b [57], a lateral spintronic device is shown. It consists in two ferromagnetic electrodes linked to graphene with a thin layer of alumina (Al_2O_3) acting as a tunnel barrier. While going through the injector on the left side of Figure 22a, electrons with spin aligned with the ferromagnetic order of the cobalt electrode will be transferred preferably to the graphene layer. This polarized current flows in the graphene channel towards the other electrode called the analyzer. Depending on the ferromagnetic order in the analyzer, the transfer of the polarized electron will be more or less easy. That is the principle of tunnel magnetoresistance [58]. The two peaks in the magnetoresistance measurement at 4K presented in Figure 22c correspond to opposite polarization of the injector and analyzer and show spin information is conserved all along the lateral graphene channel.

We will now review some of the 2D materials especially Molybdenum disulfide (MoS_2) that were discovered right after graphene.

2.2.2 The wave of new 2D materials and their variety

The discovery of graphene by exfoliation in 2004 [39] unleashed the field of 2D materials (or Van der Waals) materials. Among them, a family of compounds called **transition metal dichalcogenides (TMD)** is particularly interesting. In the first part, I will shortly describe this family, then I will present molybdenum disulfide (MoS_2) I used extensively during my PhD, and finally, I will briefly give examples of early applications of this material.

2.2.2.1 The transition metal dichalcogenides (TMD) (MX_2)

Before describing the structure, TMD (MX_2) materials are defined by their compounds. The M in the formula stands for a transition metal as shown in the periodic table of elements in Figure 23a. The number of metals partly explains the diversity of behavior of TMDs from semiconductor (MoS_2 , WS_2) to superconductor (NbSe_2) or topological insulator (WTe_2). Three chalcogens (sulfur, selenium, and tellurium) make it possible for the final compound to belong to the TMD family.

Contrary to graphene which has only one crystal structure, **a TMD can have several distinct phases as shown in Figure 23b with different properties**. For instance, for MoS_2 , the 2H-phase is semiconducting while the 1T-phase is metallic [59]. These phases are not stable under the same conditions. For instance, in a work from my lab [60], researchers demonstrated that for pulsed laser deposition growth, the growth temperature of WS_2 can change its phase. Below 500°C , it is the 2H-phase that grows while for higher temperatures, the 1T-phase grows instead. Even after the growth, it is still possible to change the phase of the TMD either by chemical treatment [59], mechanical strain [61], or laser exposure [62].

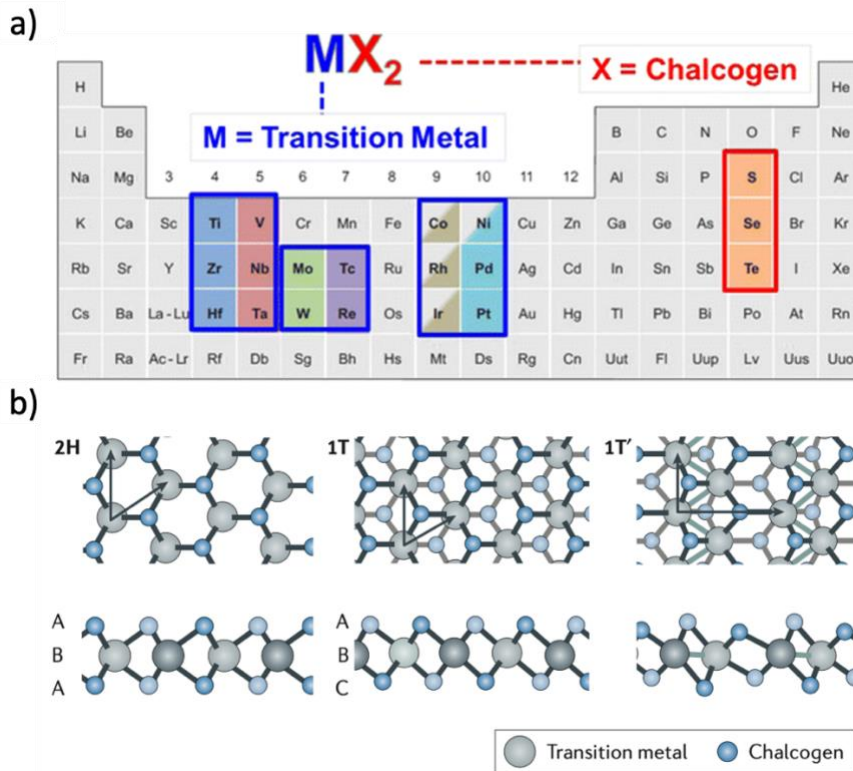


Figure 23 a) Periodic table of elements with the transition metals (M) highlighted as well as the chalcogens (X) in orange. b) The three phases TMD can be found. The 2H phase corresponds to the aligned chalcogens atoms while the 1T and 1T' phases correspond to the bottom chalcogen layer shifted with respect to the top chalcogen layer. The 1T' also breaks the alignment along the horizontal.

The properties of TMD are also very dependent on the number of layers. As presented in Figure 24 [63], density functional theory (DFT) calculations show that for bulk, four layers, and bilayers MoS_2 , the semiconducting gap is indirect while for monolayer MoS_2 , the gap is direct. This has important consequences, especially on the optical properties of MoS_2 .

Finally, I would like to stress that **TMDs have a strong spin-orbit coupling, stronger and stronger as we go down in the periodic table** represented in Figure 23a since the atoms become heavier. The splitting of the valence band of MoS_2 is around 150meV while for WS_2 it is more 400meV.

2.2.2.2 Molybdenum disulfide (MoS_2)

Now, we introduced some generalities about TMDs, I would like to stress the properties of one of them, molybdenum disulfide (MoS_2) [59,61,63]. The most stable phase of MoS_2 at ambient conditions is the 2H (trigonal prismatic polytype) pictured with 4 different points of view in Figure 25 [64]. A layer of MoS_2 is typically 0.65nm-thick. In this phase, molybdenum atoms form a triangular lattice so do the sulfur atoms on the two (bottom and top) ranks that are perfectly aligned along the z-axis. MoS_2 also exists in the 1T-phase (octahedral).

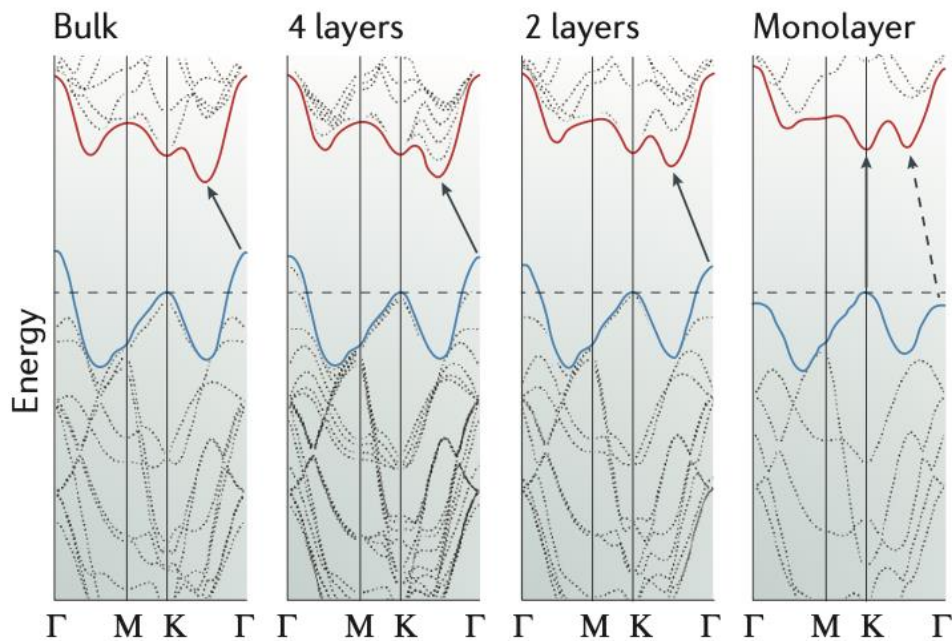


Figure 24 Density functional theory (DFT) calculations of the electronic band structure of MoS_2 for various number of layers from bulk (left) to monolayer (left). Figures taken from Manzeli et al., Nat Rev Mater **2**, 17033 (2017).

In its 2H-phase, MoS_2 is a semiconductor (metallic in the 1T-phase). As with the other TMD, its properties depend on the number of layers. For the bulk material, its bandgap is indirect with a value of 1.29eV while for monolayer MoS_2 , it is direct and experimentally measured at 2.16eV [63]. The theoretical evolution of its band structure with the number of layers is depicted in Figure 24, DFT calculations usually give satisfactory results except concerning the exact values of the gaps. Moreover, it has been shown both theoretically and experimentally that this gap can be tuned with the application of a gate voltage [65,66].

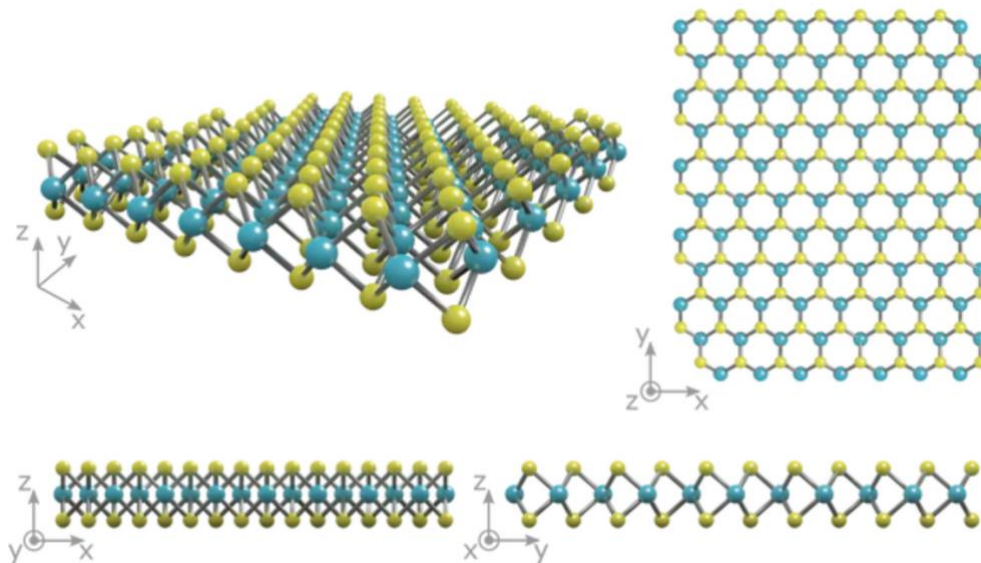


Figure 25 Monolayer MoS_2 in its 2H phase from 4 different points of view. Molybdenum atoms are colored in blue while the sulfur atoms are in yellow.

The charge carriers in MoS₂ have a good mobility that can reach $\sim 10^2 \text{cm}^2/\text{V}\cdot\text{s}$ at room temperature. DFT calculations have shown that the intrinsic limit due to phonons is $\sim 410 \text{cm}^2/\text{V}\cdot\text{s}$ [67], the extrinsic losses of mobility coming from impurities. However, at lower temperatures, the intrinsic limit increases a lot up to $\sim 2500 \text{cm}^2/\text{V}\cdot\text{s}$. Several studies [68,69] have shown **how important the substrate or capping of MoS₂ is to improve the mobility.**

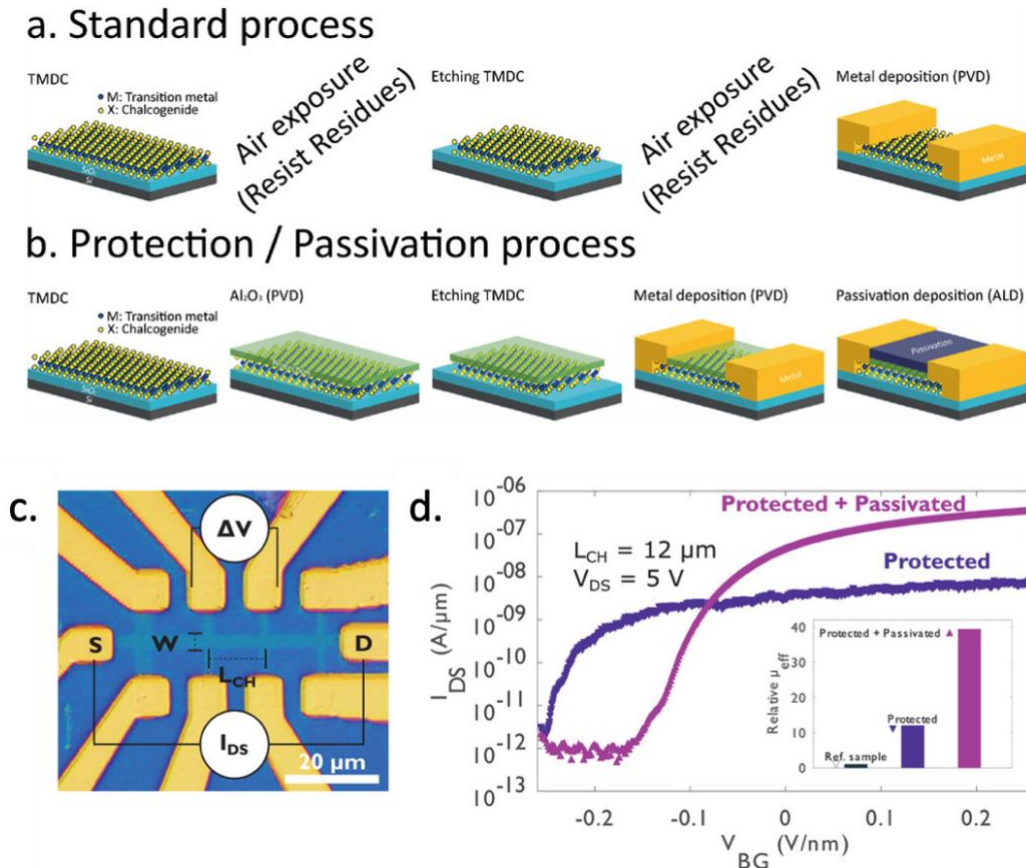


Figure 26 a) Standard process of patterning MoS₂ without particular care. b) Improved process that first protects the MoS₂ layer right after the deposition with a 1nm-thick film of alumina (Al₂O₃) before lithography and etching steps and that passivates the layer in the end with a thicker film of alumina (10nm). c) Microscope image of a long device ($L_{CH} = 12 \mu\text{m}$) made of monolayer MoS₂. d) Drain-source current (I_{DS}) against the back gate voltage (V_{BG}) at a fixed source-drain bias $V_{DS} = 5\text{V}$ for a protected device and a protected and passivated device. (inset) Relative four-probes field-effect mobility in the three processes: standard, only protection and protection+passivation of the MoS₂ layer. Taken from Brus et al., *Adv. Electron. Mater.*, **7**, 4 (2021).

Figure 26, taken from Ref. [69] carried out in my lab, illustrates a method to ensure an improvement of the mobility even after several processing steps. In a, a standard process of lithography and then etching of monolayer MoS₂ is shown in comparison with b, where the monolayer is first protected by a thin layer of alumina before being exposed to any contaminants. After the fabrication steps, MoS₂ is passivated by being covered with 10nm of alumina. Figure 26c shows the final device, a long monolayer MoS₂ channel, and the electrical configuration for the measurement presented in Figure 26d. This plot represents the drain-source current (I_{DS}) as a function of the back gate voltage (V_{BG}) for a given bias

source-drain voltage (V_{DS}). From this graph, it is possible to deduce the threshold voltage, the I_{ON}/I_{OFF} ratio allowed by the semiconductor and the field-effect carrier mobility μ_{eff} . Indeed, the conductance σ can be easily computed as $\sigma = \frac{L_{CH} I_{DS}}{W \Delta V}$ with W the width of the channel and L_{CH} its length. Then, μ_{eff} is given by: $\mu_{eff} = \frac{1}{C_{BG}} \frac{d\sigma}{dV_{BG}}$ where C_{BG} is the capacitance of the back gate. These measurements show that the device that was both protected and passivated has a much larger on/off ratio ($\sim 10^6$) compared with the one that has only been protected ($\sim 10^4$). The inset provides the comparison of the extracted mobilities, the protected and passivated devices having a mobility 40 times larger ($20 \text{ cm}^2/\text{V}\cdot\text{s}$ on average but up to 35) than a device made with standard methods (see Figure 26a) and 4 times larger than the only protected devices. This study justifies the development of protection and passivation methods. The encapsulation of MoS₂ between h-BN is also a promising road for improved electronic performances [70].

The lack of inversion symmetry of the 2H-phase results in a spin-splitting $\sim 0.15 \text{ eV}$ of the valence band of MoS₂ due to spin-orbit coupling (SOC) [41]. The hexagonal lattice of MoS₂ provides it two inequivalent points K and $-K$ related by time-reversal symmetry. In the case of monolayer MoS₂, the band gap is direct and is located at the K and $-K$ points. Therefore, the low-lying excitations can be attributed to an index whether they are from the K or $-K$ points, called valleys. This index is a quantum number called valley pseudospin which opens the field of **valleytronics**. In the same way as spintronics, valleytronics can be used to store and transfer information. **In TMDs, SOC brings a new interaction into balance since the spin and valley pseudospin are now coupled.** For instance, this can be used to manipulate spin with the valley pseudospin.

Finally, **the phase diagram of MoS₂ has revealed a superconducting dome for high doping and low temperature** as depicted in blue/green on Figure 27c [71]. The device is pictured in Figure 27a. It is a Hall bar with both a back (solid) and top (ionic liquid) gate. This strategy with two gates allows to access a wide range of carrier densities. Figure 27b shows normalized sheet resistance vs temperature for various back and top gate voltages. For a given top gate voltage ($V_{LG} = 4, 4.5, 5, 5.5, 6 \text{ V}$), the back gate voltage is varied from 2V to -4 V . The superconducting transition temperature increases as we increase V_{LG} from 4 to 5.5V but decreases for $V_{LG} = 6 \text{ V}$. We then reached a maximum critical temperature around 5.5V. This is clearer by looking at the colormap in Figure 27c since a green/blue region of very low sheet resistance can be distinguished with a critical temperature that reaches a maximum around 10K for a value of the electron density $n_{2D} \approx 1.3 \times 10^{14} \text{ cm}^{-2}$.

Though MoS₂ was first used as a lubricant, its 2D form has already found some applications as transistors [69], photodetectors and solar cells [59,64] because of its direct band gap but its still low-quality electronic properties limit its development. However, one of the applications is to couple its compatibility with band-engineering with the high-quality electronic properties of graphene. For instance, it is possible to realize transistors [72] or solar cells [73] with a combination of the two materials. In the final subsection, I will quickly review the current methods used to obtain 2D materials and how their evolution may allow for larger applications.

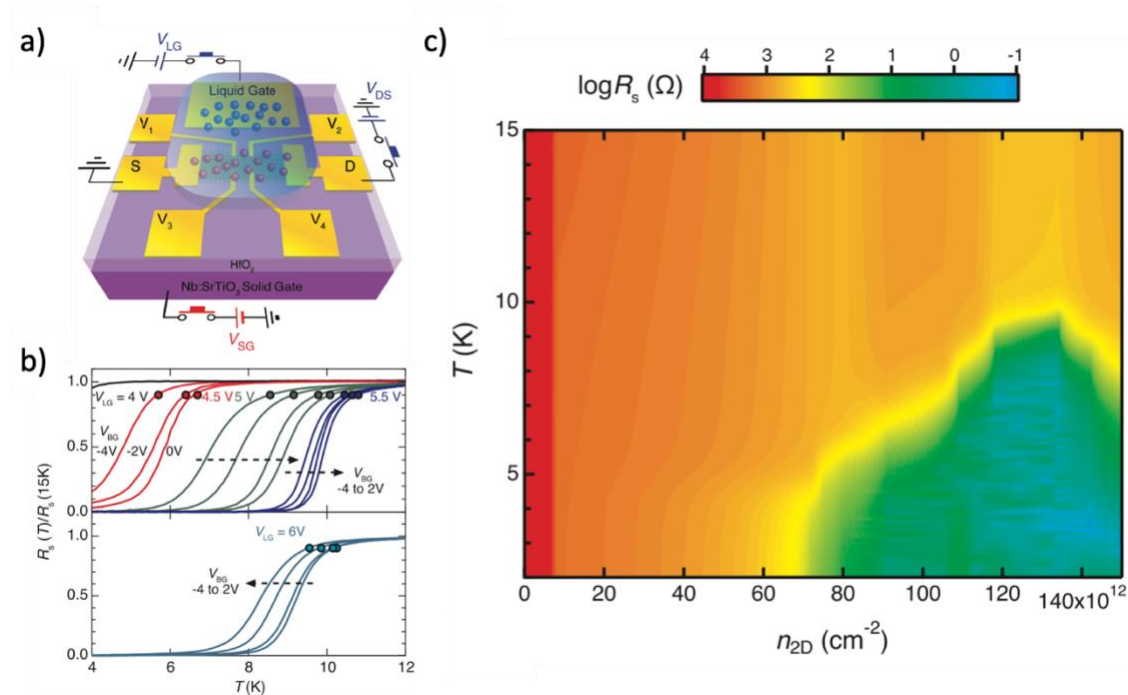


Figure 27 a) Scheme of the device with a Hall bar geometry. The current is injected between the source (S) and drain (D) contacts while the voltage is measured between V_1 and V_2 (or V_3 and V_4). There is a back gate with voltage V_{SG} and a top gate (V_{LG}). b) Normalized sheet resistance vs temperature measurements for various back and top gate voltage. c) 2D colormap of the logarithm of the resistance as a function of the 2D electron density n_{2D} (x-axis) and the temperature (y-axis). Figures taken from Ye et al., *Science* **338**, 1193 (2012).

2.2.3 New growth methods for more applications

2D materials are often materials that are present in bulk form as a stack of layers coupled between each other by Van der Waals (VdW) forces. These forces are weak compared with covalent or ionic bonds and it is then easy to exfoliate a few layers from the bulk material. I will start with the method to isolate VdW materials by the exfoliation of bulk materials and then review the growth methods that start from scratch.

2.2.3.1 Progress in exfoliation and transfer

In 2004, Geim and Novoselov opened an entire field of research with the first isolation and transport study of graphene [39] for which they were awarded the 2010 Nobel Prize. They developed a cheap and easy method to **exfoliate graphene from a bulk crystal of graphite**. It is represented in Figure 28a. This method uses scotch tape and the fact that graphene, like many 2D materials, has very strong chemical bonds inside its layers but its layers are weakly connected to each other by Van der Waals interactions. This allows to progressively make the graphite thinner and thinner as we exfoliate a random number of layers until finding monolayer graphene (or bilayer, trilayer,... as desired).

Liquid phase exfoliation [74] also starts from graphite (Figure 28, here from high-quality powder). The method relies on the interaction between graphene layers and a well-chosen

solvent. Ultrasound bath in this solvent allows the formation of flakes that can reach several microns and are almost free of defects. This method is now applied to other 2D materials.

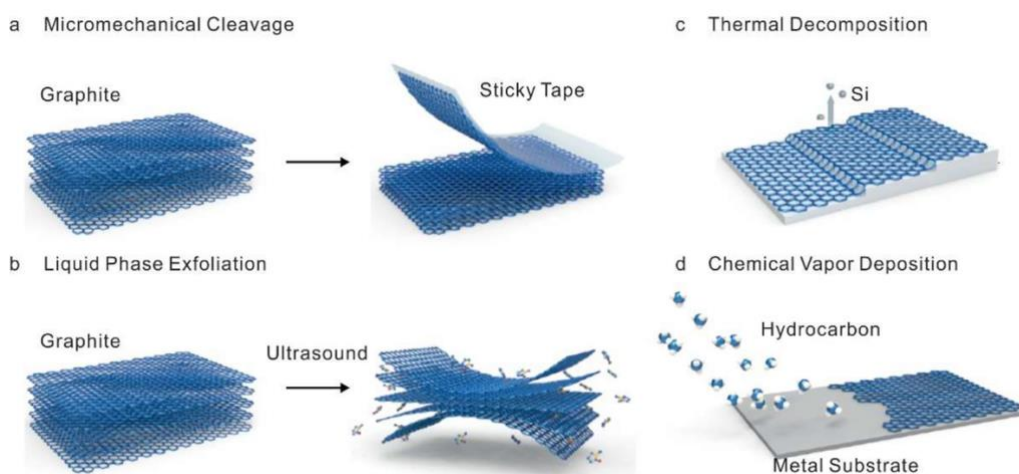


Figure 28 Schematic diagrams of: a) exfoliation, b) liquid phase exfoliation, c) thermal decomposition on silicone, and d) chemical vapor deposition (CVD). Figures taken from Lee et al., *Nanomaterials* **9**(2), 297 (2019).

The thermal decomposition of silicon carbide (SiC) is a method for growing graphene (see Figure 28c), is compatible with the silicon technology [75], making it ideal for implementing devices. The high-temperature annealing of SiC (~1600°C) in an atmosphere of argon (~1bar) creates epitaxial layers of graphene at the surface.

2.2.3.2 Chemical vapor deposition

Chemical vapor deposition is a more general method [76] for growing 2D materials even if it has been first developed with graphene [77,78]. During my PhD, I made use of both CVD graphene on copper and CVD MoS₂ on sapphire.

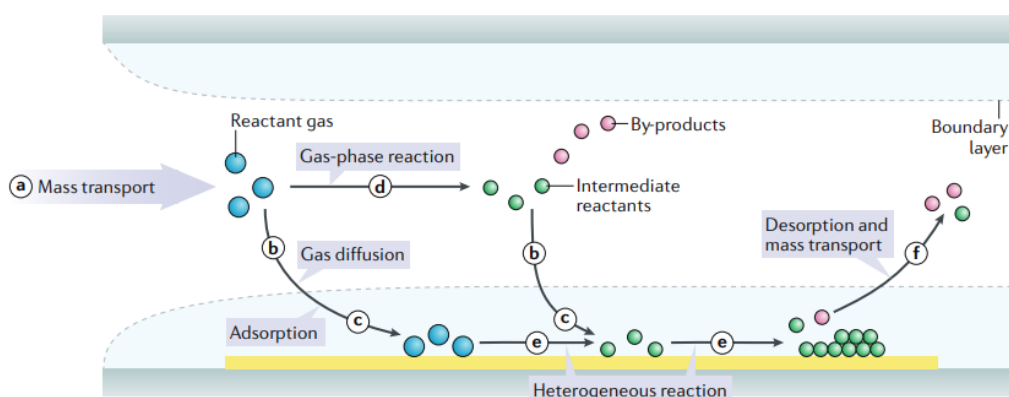


Figure 29 Scheme of a typical CVD process. Figures taken from Sun et al., *Nat Rev Methods Primers* **1**, 5 (2021).

The process takes place in a chamber in the presence of gas reactants and a substrate that

acts as a catalyst for the further reactions. In Figure 29, the CVD process is explained in detail. Step a consists of the introduction of the precursor gases (depicted as blue circles) into the reaction chamber. Then, the precursor gases can follow two potential pathways: the direct diffusion through the boundary layer (step b) and the adsorption process onto the substrate (step c). Alternatively, the precursor gases could participate in reactions within the gas phase, leading to the creation of intermediate reactants (represented by green circles) and resultant by-products (depicted as red circles) in a gas-phase reaction sequence (step d). These intermediates and by-products will then deposit onto the substrate through diffusion (step b) and adsorption (step c). Surface diffusion and heterogeneous reactions (step e) occur on the substrate's surface before the emergence of thin films or coatings. Finally, the by-products and any unreacted constituents are desorbed from the substrate's surface and are expelled from the reaction chamber as exhaust gases (step f). Typical CVD graphene processes use CH_4 or C_6H_6 as precursors with temperatures of growth reaching $\sim 900^\circ\text{C}$ and are now well mastered.

The growth of TMDs has been the subject of a lot of research [76,79–81]. The first attempts were mainly using solid targets that were heated with a continuous flow of gas inside the chamber to make the species move and deposit on the substrate (thermal vapor deposition). This often leads to the formation of triangles on the surface of the substrate. Later, the use of metal-organic species in gaseous form allowed large-scale homogeneous growth on the substrate (MOCVD). Lately, a group reported the growth by MOCVD of MoS_2 on a thin glass at $T \sim 150^\circ\text{C}$ [82] opening the way for flexible electronics with TMDs and low-temperature growth on other substrates.

2.2.3.3 Other methods

Other methods that already existed either to grow semiconductor or oxide films were pushed to their thickness limits to grow 2D materials. **Molecular beam epitaxy (MBE), used for high precision deposition of materials with sharp interfaces**, is now employed for the growth of TMDs [83,84] including topological insulators [85,86]. The principle of this method is to send beams of atoms on the substrate with a very controlled flux. The deposition is time intensive (~ 1 layer per hour for TMDs [86]) but allows for excellent interfaces and material quality, also due to the very high vacuum inside the chamber. For now, this method is the most advanced to grow heterostructures *in situ* with both TMDs and topological insulators.

Last but not least, pulsed laser deposition (PLD), which was first dedicated to the growth of oxide films, is now being used for the growth of TMDs. Its principle will be described in chapter 4 but we will here review its advantages for the growth of 2D materials. This method allows for great control of the thickness of the deposited species by tuning the different parameters like the energy of the laser or the pulse durations. This allowed early realizations of 2D films of WS_2 [87] and MoS_2 [88]. Our lab succeeded in integrating 2D materials grown by PLD to spintronic devices [60,89]. These works served as the basis for the work realized in chapter 7.

2.3 MOTIVATIONS AND STATE-OF-THE-ART

As we have seen in the last two sections, superconductors and 2D materials are two worlds in themselves. The aim of this thesis is to explore the boundary where we put into contact a high- T_c *d-wave* superconductor, YBCO, with other materials and especially 2D materials. In the following subsections, I will present the state of the art in each specific project I led during my PhD and the motivations I had. I will start with the proximity effect in normal metal thin films, especially the latest development beyond the Blonder-Tinkham-Klapwijk theory [5]. Then, I will focus on the induced *s-wave* superconductivity in graphene and letting the *d-wave* case for the beginning of the dedicated chapter. Finally, I will present works related to the proximity effect in MoS₂.

2.3.1 Proximity effect in normal metal thin films

Proximity effect in normal metal thin films has been studied for a long time both theoretically [9] and experimentally [90]. In this subsection, I will not be exhaustive but try to provide the milestones in the understanding of the superconducting proximity effect in thin films. The focus will be more on *d-wave* superconductors as my experiments deal with YBCO.

One question that has particularly interested scientists for the last four decades is whether the anisotropic *d-wave* order parameter of YBCO can be induced in a thin metallic film by proximity [91–100]. Though there was already a lot of evidence for a $d_{x^2-y^2}$ order parameter in YBCO [101], early experiments [102] with YBCO and thin films were still biased by the idea that a *s-wave* order parameter coexists with the *d-wave* one in YBCO. References [21] and [103] firmly confirmed that the only order parameter was $d_{x^2-y^2}$ giving a firm ground for further experiments with films. Multiple paths were chosen for the experiments to probe the proximity effect with *d-wave* superconductors, each accompanied by its corresponding theoretical model. Let us briefly review these paths.

2.3.1.1 STM and point contact measurements of *d-wave* superconductor/metallic films

To study the proximity effect in a thin film, it is very interesting to **probe the local density of states in the material by using a scanning tunneling microscope (STM)**. It was heavily used to directly study superconductors [104] since the single-particle density of states is obtained with a tunnel interface with a probe [5,105].

Khanin et al. [106] measured a thin film (20 – 30nm) of gold grown on top of 250nm of YBCO (001) at 77K with STM. They achieved to observe proximity effect through the appearance of a gap feature in the spectrum but not everywhere on the film. Indeed, the spectra on flat regions are flat with no features while the spectra on regions exhibit a gap feature of variable width (from 2 to 20mV) as shown in Figure 30. They explained the transparency along the (001) direction is small and then gives a too-low induced gap, unmeasurable with their set-up (figure a). When the surface is not flat, the tunneling from the CuO and CuO₂ planes increases the transparency and gives a much larger induced gap (Figure 30b). However, they did not discuss the symmetry of the induced gap.

Kohen et al. [94] measured a YBCO film along the (100) direction (in-plane) with a gold tip point. This is not a gold film but still, they succeeded in inducing a superconducting gap in gold. They explained their measurements by considering a $d+is$ order parameter. The s -wave component gets larger as the transparency between YBCO and gold increases. This order parameter would come from the inverse proximity effect with the gold tip.

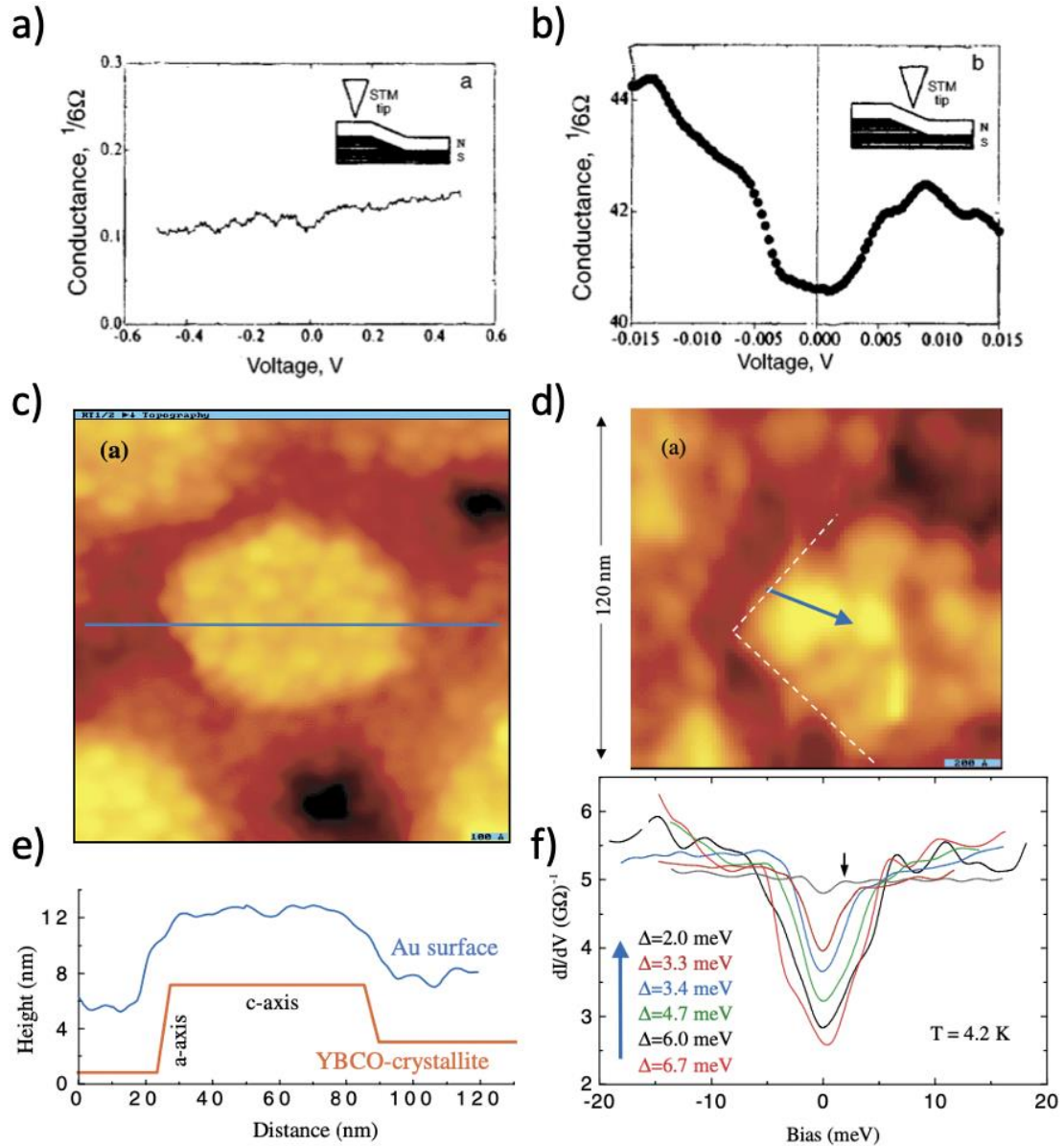


Figure 30 a) Differential conductance measured by the STM tip on a flat region of a gold layer covering a YBCO (001) film. A scheme of the tip and surface is shown in the inset. b) Differential conductance measured by the STM tip on a steep region of a gold layer covering a YBCO (001) film. The tip and surface are pictured in inset. Figures taken from Khanin et al., *Jetp Lett.* **63**, 1041–1046 (1996). c) STM topographic image (100x100nm) of a YBCO (001) film covered by 5nm of gold. d) STM topographic image (120x120nm) of a YBCO (001) film covered by 5nm of gold. The white-dashed lines correspond exposed (100) facets. e) Height profile of the crystallite shown in c. f) Differential conductance spectra at positions on the blue arrow of d.

Sharoni et al. [98] carried out STM measurement at 4.2K of a 50nm-thick film of YBCO (001) covered by 5nm of gold. They first measured the STM differential conductance of a bare YBCO sample and observed typical V-shaped conductance with a gap of width $\sim 20\text{mV}$. They observed a proximity effect in the layer of gold through the observation of a gap feature of maximum width 6.7mV as shown on Figure 30f and depends exponentially on the distance to the (100) facet. The granularity of the film allowed to measure with different orientations of YBCO namely (001) and (100). They did not measure any anisotropy in the differential conductance between the two contrary to the case of bare YBCO. **They concluded that the induced order parameter in gold shows no sign of d -wave symmetry but rather s -wave symmetry.**

On the theory side, Löfwander [99] used the Eilenberger equations to solve the problem of a d -wave superconductor in contact with a normal metal either along the (100) or (110) direction. He could tune the s -wave interaction in the normal region from interactive to repulsive (corresponding to metal like gold). He showed that indeed, the proximity effect along the (100) tends to decrease the density of states on the normal side but much less than experimentally measured. For the (100) orientation, he found a real linear combination of d - and s -wave inside the superconductor but **a s -wave order parameter on the N-side due to the destruction of the d -wave order parameter by isotropic impurity scattering.**

2.3.1.2 Transport in SN or SNS junctions

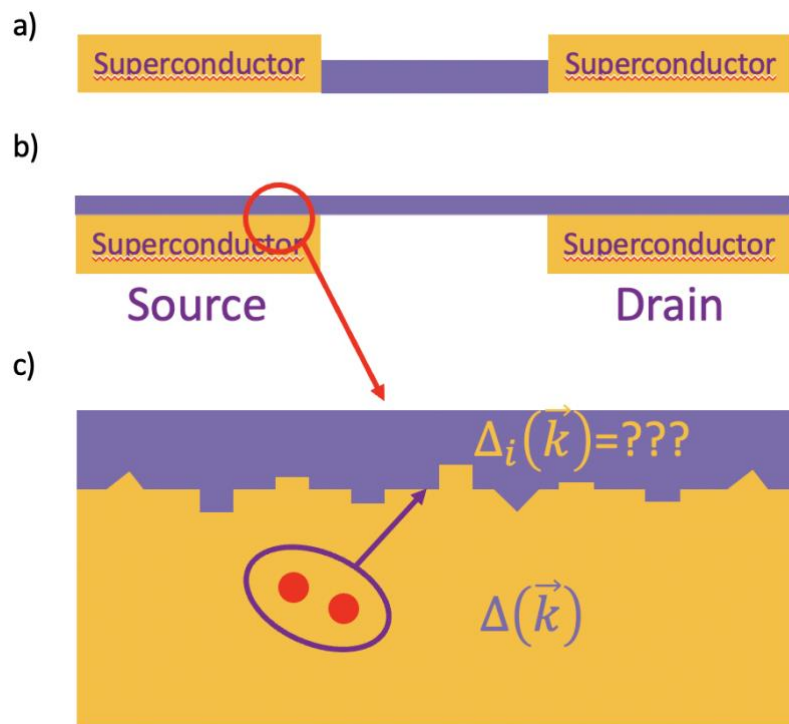


Figure 31 a) Simplified scheme of a SN-N-NS junction. On both sides, at the interface between the superconductor and the thin metallic layer acting as the bridge, there is a region similar as the one depicted in b). b) A Cooper pair at the interface between a normal metal and a superconductor. What will be the induced $\Delta_i(\vec{k})$ in the metal knowing the gap $\Delta(\vec{k})$ in the superconductor and the scattering at the interface?

Ultimately, the proximity effect in thin metallic layers is studied a lot for its applications in superconducting devices. I will focus now on this aspect since my experiments described in chapter 5 are transport measurements across YBCO/gold junctions as the one shown in Figure 31a. Studies within this geometry are quite rare for both *s*- and *d*-wave superconductors. Golubov and Kupriyanov [91] studied the superconducting proximity effect between a superconductor and a thin metallic layer (the red circle region of Figure 31a) in the dirty limit (mean free path $l \ll \xi_{GL}$ in the superconductor and $l \ll \xi_N$ in the metal). This limit allows not to consider the roughness of the interface which is smaller than the mean free paths. At that time, very early after the discovery of copper oxide superconductors, they argued that the behavior of the two kinds of superconductors should be the same in the dirty regime. Nevertheless, **they found the value of the mini-gap formed in the normal region as well as its density of states**. They found back the early result of Macmillan [107] for tunnel barrier between the superconductor and the metallic layer. It allowed them to compute the critical current of the SN-N-NS and SN-I-S junctions for all values of the transparency between the superconductor and the metal.

As pointed by Refs. [108–110], the geometry shown in Figure 31b is different from the geometry in a, which has been more studied. Indeed, in a, the charge carriers in the metal are confined to the length between the two superconducting electrodes and the density of states in this metallic layer is changed due to the reflections (normal or Andreev) at the SN interfaces. Andreev bound states will appear for energies smaller than the superconducting gap of the nearby superconductor. On the contrary, in b, the charge carriers are not confined anymore. **Volkov et al.** [108] **and Kopnin et al.** [109] **found the value of the created mini-gap in the two-dimensional electron gas (2DEG) above a *s*-wave superconductor** and showed that the critical current of Josephson with the geometry of Figure 31b can be expressed as a function of the tunnel coupling between the superconducting electrode and the 2DEG. In Figure 32, taken from Ref. [109], a scheme of a SN junction is shown in a as well as the computed mini-gap ε_g as a function of the tunneling rate between the superconductor and the 2DEG. In c is plotted the differential conductance of a SN junction as shown in a. Two features can be distinguished: first, the shape of a tunnel junction with a gap Δ coming from the superconductor itself and second, a peak at zero bias coming from the interface between the 2DEG and the proximized 2DEG of mini-gap ε_g . This geometry has known a gain of research interest recently both because of its potential use in digital superconducting circuits [111,112] and the development of new heterostructures with 2DEG [113,114] or 2D materials like graphene [115,116] and topological insulators [110,117]. However, studies with the same geometry but with *d*-wave superconductors are scarce. **Golubov et al.** [93] **first showed that in the strong disorder limit, the density of states of a metallic layer in proximity with a *d*-wave superconductor is gapless and that the induced order parameter is *s*-wave**. In a second article [118], they deduced the consequences on the transport properties of SIN junctions as well as SIS Josephson junctions. For SIN junctions, the expected zero bias peak (see chapter 3 and Ref. [105,119]) is smeared in the presence of strong disorder, and for SIS, the $I_c R_N$ products decreased a lot, much more than with *s*-wave superconductors. A study [10], not yet peer-reviewed, combines two approaches to study SNS nanoconstriction of 15nm-thick gold atop YBCO. They estimated the values of the

induced gap in gold both with STM and transport measurement. The particularity of this study is to use a vicinal substrate that allows for the growth of YBCO with its *c*-axis inclined with respect to the growth direction. **They argue that the orientation, with the CuO₂ plane facing the *in situ* grown gold film, makes the induced gap larger and more homogeneous due to a better coupling.** The aim of chapter 5 will be to explore another geometry that, up to my knowledge, has not been studied experimentally with *d*-wave superconductors.

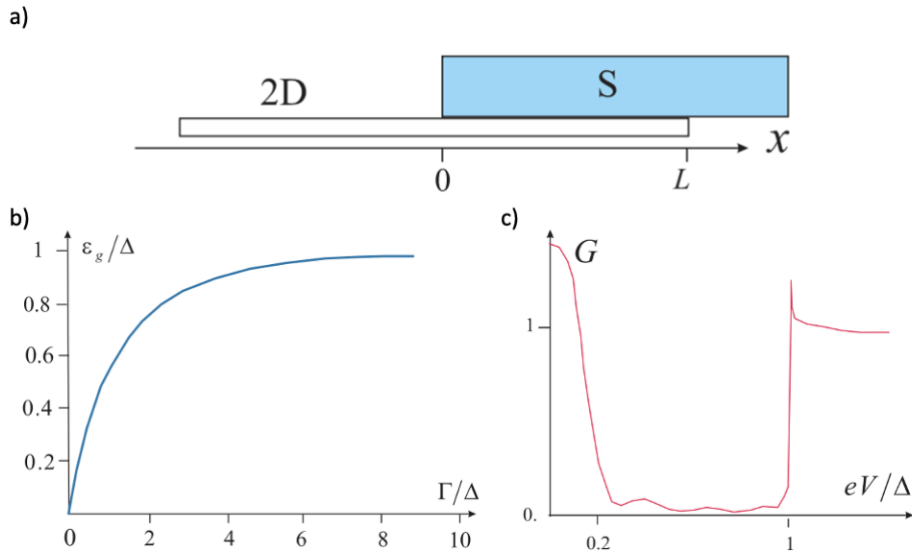


Figure 32 a) Scheme of a SN junction with the superconductor on top of a 2DEG. b) Evolution of the induced mini-gap normalized by the superconductor gap as a function of the normalized tunnel rate between the two materials. c) Normalized differential conductance of a SN junction in the geometry of a). Figures taken from Kopnin et al., *Phys. Rev. B* **84**, 064524 (2011).

2.3.2 Proximity effect in graphene

As the first isolated 2D material, graphene was also the first to be studied in proximity to superconductors.

2.3.2.1 General results

Soon after the discovery of graphene, a theoretical interest in the coupling of graphene with superconductors emerged [120–123]. The study of the Andreev reflection in graphene revealed a new phenomenon called **specular Andreev reflection** [120]. When the Fermi level of graphene E_F is larger than the induced gap Δ , the Andreev reflection is identical as for normal metals and is depicted in Figure 33b. However, for $E_F < \Delta$, the gapless band structure of graphene makes it possible for an incident electron to undergo an Andreev reflection and be reflected as a hole from the valence band, as shown on Figure 33b. This is different from the usual Andreev reflection case : the hole generated in the valence band does not trace back the trajectory of the incident electron but is specularly reflected since the group velocity of a hole in the valence band is parallel to its wave-vector. For $E_F < \Delta$, there is both specular and usual Andreev reflection occurring at the interface depending on

the energy E of the incident electron. However, the specular Andreev reflection is difficult to observe since E_F has to be smaller than Δ over the whole interface which is hard to achieve as in real, inhomogeneous samples, the local variations of E_F can be of several millielectron-Volt which is comparable with the superconducting gap of s -wave superconductors.

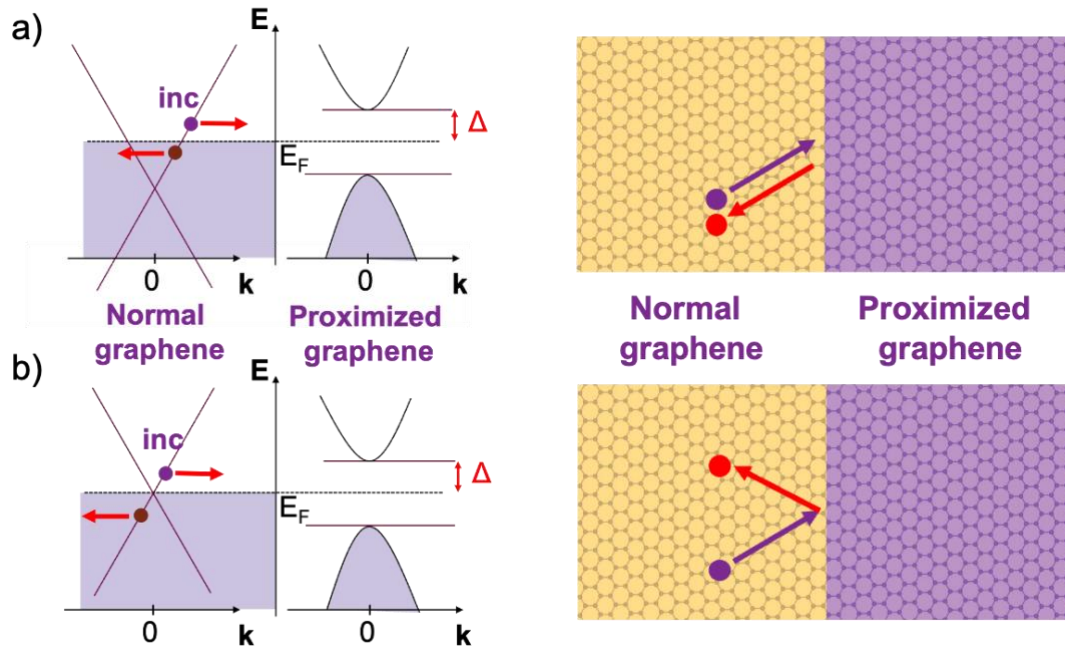


Figure 33 a) **Specular Andreev reflection** schematized both in an energy diagram and in real space. This peculiar phenomenon happens only for $E_F < \Delta$. b) Same but for the **normal Andreev reflection** in graphene when $E_F \gg \Delta$.

After the theoretical establishment of specular Andreev reflection in graphene [120], Titov and Beenaker [124] calculated the critical current of SNS graphene junctions with a s -wave superconductor. Bhattacharjee et al. [125] computed the differential conductance of SIN graphene junctions in the case of s -wave superconductivity. In a completely different context, Mazin and Johannes [126] found that the hexagonal symmetry can bare a d -wave order parameter and Linder et al. [13] then extended the model to graphene proximized by d -wave superconductors. In their article, **they provide analytical formulas to compute the differential conductance of s - and d -wave proximized graphene in contact with normal graphene.**

The first experimental results concerning s -wave superconductor/graphene heterostructures were published by Heersche et al. [127]. Some figures taken from their articles are shown on Figure 34. The device shown in Figure 34a exhibits Josephson effect as the voltage-current characteristics in b show. This is proved by the observation of a Fraunhofer-like pattern in b and Shapiro steps (not shown here). Moreover, the critical current seems to be tunable with an applied back gate voltage. This is confirmed by the color-plot in c where the differential resistance is plotted against the back gate voltage and the applied current. The critical current that separates the zero resistance region (presence of a supercurrent) in yellow and finite resistance regions in orange-red varies continuously with the back gate voltage. In

other words, **the gate electrode modulates the proximity effect in graphene.**

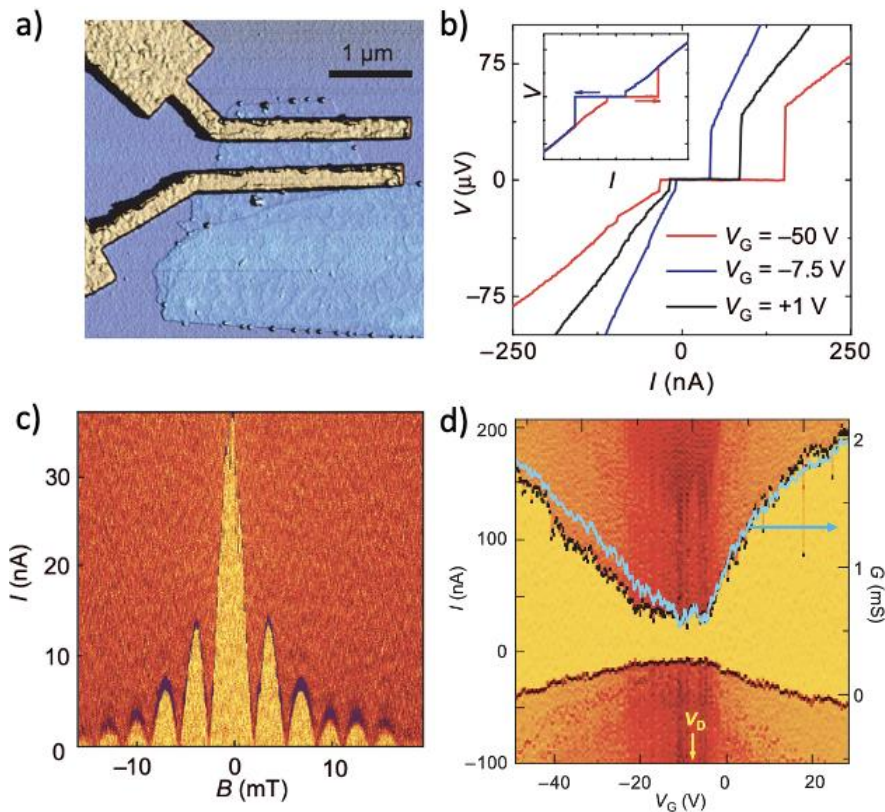


Figure 34 a) Atomic force microscopy image of a Josephson junction with a graphene monolayer as the weak link. b) Voltage-current characteristics of this device at various back gate voltages. c) Color-plot of the differential resistance as a function of the magnetic field (x-axis) and applied current (y-axis)(yellow corresponds to 0 (presence of a supercurrent) and red-orange corresponds to finite resistances). The critical current exhibits a Fraunhofer-like pattern. The current is swept from negative to positive values. d) Color-plot of the differential resistance as a function of the back gate voltage (x-axis) and the applied current (y-axis)(the color code is the same as the plot in c). The current is swept from negative to positive values. The blue line corresponds to the normal differential conductance. Figures taken from Heersche et al., Nat. 446 (2007).

This result has been confirmed by many groups [128,129] with for example CVD-grown graphene [130] or on SiC [131]. Josephson coupling has also been observed with junctions with various junction lengths [132] or with a different geometry like edge-contacted graphene [133]. Studies of single interfaces have also been carried out to study Andreev specular reflection for instance, here with a bilayer graphene [134] to have less variation of the Fermi level around the Dirac point than with monolayer graphene.

More and more works [134,115,116,135] these last years involve complex heterostructures of 2D materials stacked to create superconducting junctions. The devices are typically obtained by exfoliating each material and stacking them in a glove box. It allows to associate graphene to NbSe₂, a *s-wave* 2D superconductor and to protect the whole heterostructures by h-BN.

2.3.2.2 Graphene/superconductor junctions with magnetic field

Since chapter 6 will be mainly dedicated to the study of the magnetic field dependence of superconductor/graphene junction, I will review here the main works concerning this topic. Beyond the observation of a Fraunhofer-like pattern at magnetic fields close to zero (such as a few quanta of flux are enclosed in the junction area), experiments have been done at much higher magnetic fields thanks to the use of type II superconductors with large H_{c2} fields. In reference [136], **Amet et al. succeeded in observing a supercurrent while being in the quantum Hall (QH) regime.** Since the current in graphene can only flow on the edge in the QH regime, the supercurrent is then reduced a lot. They still could compare the differential resistance as a function of the magnetic field and gate voltage, so-called fan-diagram, between the junction in its superconducting and normal state depending on the current applied (see Figure 35a and b). When a current much larger than the supercurrent is applied (a), the fan diagram presents the typical plateaus of the QH regime, while for zero DC current applied (b), superconducting pockets are still present. They showed that even in the QH regime, a supercurrent can flow through edge Andreev bound states.

Kumaravadivel et al. [137] studied the effect of the magnetic field on a single interface between several *s-wave* superconductors and graphene in the classical regime (cyclotron radius much larger than the dimensions of the junctions). In this short review, I will only consider the case of NbN ($\Delta = 1.7\text{meV}$) as the superconductor. In Figure 35c, they studied the differential resistance spectra for different ramping procedures of the magnetic field: ZFC which means zero-field cooling (the sample is cooled down at zero field and the field is then ramped to the desired value), FC for field-cooled (the field is applied and then the sample is cooled down below the critical temperature) and finally DR for down-ramping (the sample is cooled down, then a large magnetic field is applied and finally the field is ramped down to the desired value). For a magnetic of 200mT, the normalized spectra are very different. This was confirmed by the plot of the $I_{exc}R_N$ product, I_{exc} being the extrapolation of the current with the slope at high bias and R_N , the normal resistance. This quantity is related to Andreev reflection (AR) since it accounts for the enhanced conductance due to AR. In Figure 35d and e, the influence of the ramping procedure of the magnetic field appears clearly. The researchers explained this behavior with the dynamics of vortex nucleation in the superconducting electrode. On the one hand, they argued that for the ZFC procedure, though the vortices will form in the whole superconductor, they will stay closer to the edge due to a more important pinning there. On the contrary for DR where the field decreases from a large value, the vortices will exist more easily close to the edge and then be less present at these edges. Finally, the FC procedure implies a more uniform distribution of the vortices. On the other hand, with a transmission line model (inset of Figure 35f), they argued that most of the transmission of electrons happens close to the edge of the superconducting electrode and therefore that the important value of the superconducting gap to consider is the one at this edge. However, the spatial average of the superconducting gap is decreased by the presence of vortices (normal regions inside the superconductor where the gap is 0). As a consequence, **the location of vortices influences the transport across SN junctions** depending if the vortices are closed to the edge or not. That's what they showed in Figure 35f with the correlation between the measured gap and the $I_{exc}R_N$

product.

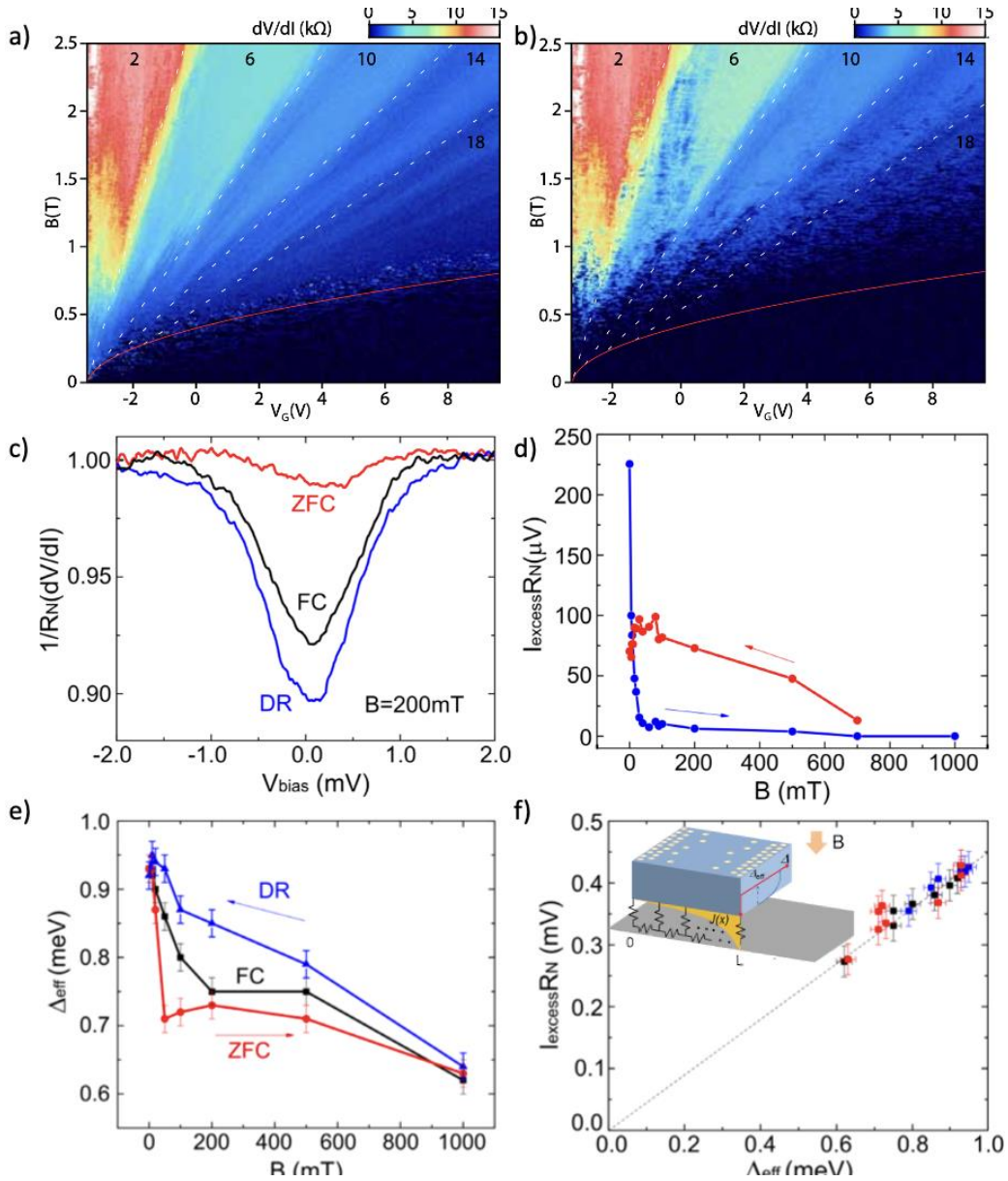


Figure 35 a) Differential resistance against the voltage back gate (x-axis) and magnetic field (y-axis) for a current applied $I_{DC} = 6$ nA $> I_c$. b) Same but with $I_{DC} = 0$ nA. The numbers on the plot are the filling factors of each plateau. The red line corresponds to the points where the cyclotron radius is half of the length of the junction. It is therefore the boundary between the semi-classical and quantum Hall regimes. Figures taken from Amet et al., *Science* **352** (2016). c) Normalized differential resistance spectra of a SN junction with an applied magnetic field of 200mT for three different ramping procedures (explained in the main text). e) Evolution of the product $I_{exc}R_N$ with the magnetic field for the ZFC and DR procedures. e) Evolution of the measured gap Δ_{eff} with the magnetic field. f) The product $I_{exc}R_N$ as a function of Δ_{eff} (inset: transmission line model to understand the magnetic field behavior of SNS junctions with the superconductor in blue and graphene in grey. The white-yellow circles are vortices in the superconducting electrode). Figures taken from Kumaravadivel et al., *2D Mater.* **4**, 045011 (2017).

2.3.2.3 Beyond *s*-wave superconductivity with graphene

In chapter 6, dedicated to YBCO/graphene junctions, I will more precisely review the literature with YBCO. A few other materials with anisotropic order parameters have been associated with graphene but studies remain rare due to the difficulty to achieve a good electrical contact between graphene and these materials. To illustrate this, an early attempt of coupling YBCO with graphene reported tunnel contacts [138]. A scanning tunneling study has been carried out with graphene on top of $\text{Pr}_{2-x}\text{Ce}_x\text{CuO}_4$ (PCCO) [139] and **its authors argued that they succeeded in inducing *p*-wave superconductivity in graphene** since they observed either V-shape tunneling conductance spectra, zero bias peak or split peaks around zero bias.

More recently, $\text{Bi}_2\text{Sr}_2\text{CaCu}_2\text{O}_{8+x}$ (BSCCO) has been used in heterostructures with graphene. Contrary to YBCO, BSCCO can be easily exfoliated and even the monolayer remains superconducting. It makes simple its association with other 2D materials like graphene. Ref. [140] reported transport measurements of graphene on top of BSCCO. They measured the flake of graphene directly on BSCCO and **claimed the opening of an induced gap in graphene by proximity with BSCCO**. Still with BSCCO, Jois et al. [141] reported Klein tunneling in BSCCO/graphene junctions, similarly as observed by Perconte et al. [12] with YBCO. This will be more thoroughly studied in chapter 6 as a preamble for my own studies of YBCO/graphene junctions.

2.3.3 Proximity effect in MoS_2

Graphene has opened the way to the study of the superconducting proximity effect in other 2D materials like TMDs. As a consequence, there are fewer works on the subject. As we will see, the lack of good electrical contacts between superconductors and MoS_2 is a drag for the development of the field though interesting theoretical prospects. In the first part, I will review these prospects. Then, I will present some early results on vertical transport while I will finish with attempts to induce and propagate superconductivity in planar devices.

2.3.3.1 Theoretical predictions

Two properties of MoS_2 are particularly interesting in a theoretical point of view. First, its hexagonal geometry provides it a Dirac Hamiltonian with a finite mass [41] and therefore exciting relativistic phenomena as we have seen for graphene with Klein tunnelling. Second, contrary to graphene, MoS_2 has an intrinsic spin-orbit coupling that for instance causes a spin-splitting of the energy bands and can have incidence on the coupling with a superconductor.

As for graphene earlier [13], **theoreticians have computed the differential conductance of a SN interface between proximized MoS_2 (*s*-wave) and normal MoS_2 [15] within the BTK formalism**. More than that, they compared it to the same calculation for gapped graphene. Indeed, the only difference in their Hamiltonians between gapped graphene and MoS_2 is the presence of spin-orbit coupling in the latter. They found spin-orbit coupling in MoS_2 enhances Andreev reflection compared with gapped graphene. Khezerlou et al. [142–

144] studied the case where superconductivity with other symmetry than s-wave was induced in MoS₂. They showed that the single-particle density of states in the proximized MoS₂ remains gapless and they could compute Andreev and normal reflection coefficients in SN junction as well as the current phase relation of a SNS junction with MoS₂ as the weak link and *p*-wave superconductors. Finally, there is a big interest in coupling superconductors and 2D TMD semiconductors since it was theoretically shown that this proximized system could give rise to unusual superconducting pairing [145]. Therefore, **superconducting heterostructures made of MoS₂ are also of great technological interest in the quest for non-trivial topological quasiparticles** [146,147] that could serve as a basis for topological quantum computing.

2.3.3.2 Vertical geometry

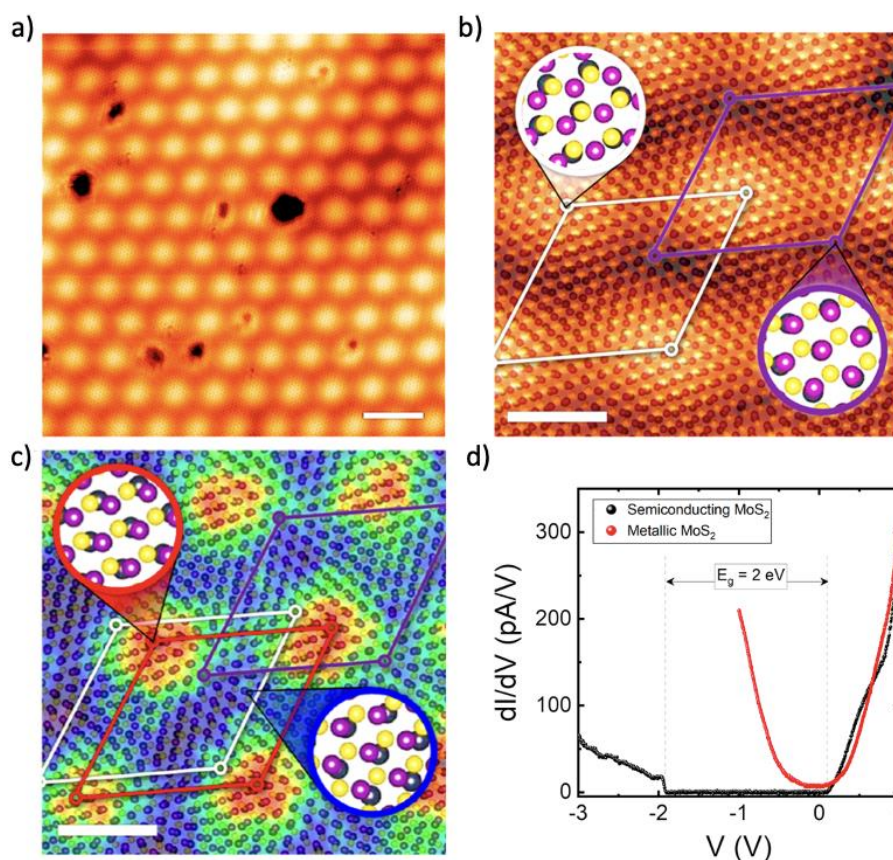


Figure 36 a) STM topographic image of MoS₂ on Pb. The scale represents 5nm. b) Another STM topographic image but this time with a model of the positions of the atoms of MoS₂. The white (violet) trapezoids respectively show the Moiré pattern unit cell formed when a sulfur (molybdenum) atom is just above a lead atom. c) Same model but this time with a colormap of the differential conductance at the energy of the coherence peak. The red trapezoid represents the Moiré pattern unit cell coming from the modulation of the conductance map. d) Comparison of the differential resistance vs bias voltage between MoS₂ on lead (red dots) and a typical semiconducting MoS₂ sample. Figures taken from Trainer et al., ACS Nano, 14 (2020).

To observe induced superconductivity in MoS₂, STM measurements at low temperatures

($T = 1.5\text{K}$) have been carried out by Trainer et al. [148]. In this study, they deposited a CVD-grown monolayer of MoS_2 on lead (Pb). They then measured the topography of the heterostructures (see Figure 36a and b) as well as the differential conductance (Figure 36c). They identified two Moiré patterns corresponding to the exact commensurability between Pb and Mo atoms (violet trapezoid) and Pb and S atoms (white trapezoid). This model was compared with the Moiré pattern formed by the modulation of the conductance at the energy of the coherence peak in Figure 36c (the induced gap is homogeneous, only the conductance changes). They observed a shift and explained this by a periodic modulation of the transparency. Indeed, the transparency is itself modulated by the orbital overlaps between MoS_2 and Pb. Finally, they observed by measuring the differential conductance as a function of the voltage bias that MoS_2 on Pb does not behave as a semiconductor as pristine MoS_2 but as a metal. ***Ab initio* and tight binding calculations have confirmed that MoS_2 first becomes metallic and then superconducting by proximity in contact with Pb.**

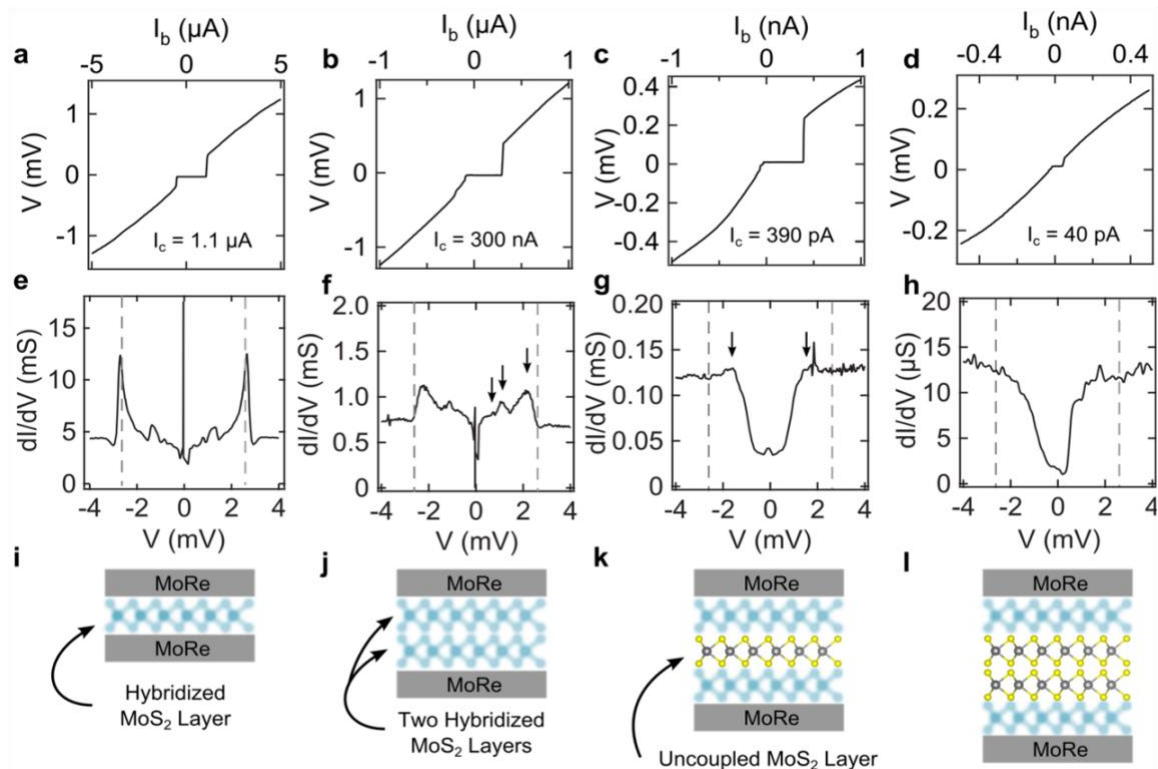


Figure 37 a-d) Voltage current characteristics of vertical junctions made of respectively 1, 2, 3 and 4 layers of exfoliated MoS_2 . e-h) Differential conductance spectra of these same junctions. i-l) Scheme of the vertical junction and the layers are either in blue (hybridized) or yellow (uncoupled). Figures taken from Island et al., *2D Mater.* **3**, 031002 (2016).

Another convenient system to study how MoS_2 behaves in close proximity to superconductors is vertical Josephson junctions as presented in Figure 37 taken from [149]. The principle is to stack a variable number of exfoliated MoS_2 layers between two superconducting made of molybdenum rhenium (MoRe), which does not oxidize in contact with 2D materials. They compared the transport properties of four devices made of a number of layers from 1 to 4. The voltage-current characteristics are given in Figure 37a-d. These

four junctions have Josephson effect but the measured critical current of these junctions decreases a lot as the thickness grows. Indeed, $I_C = 1.1\mu\text{A}$ for the monolayer while it is only 40pA for four layers, four orders of magnitude smaller. However, the differential conductance measurements in Figure 37e-h show that the resistance is also increasing a lot from the monolayer to the four-layer junction, going from $2 \times 10^2\Omega$ to $7 \times 10^4\Omega$. The $R_N I_C$ product then loses two orders of magnitude (from 0.2mV to 3 μV). The authors explained this dependence with the argument (shown in Figure 37i-l) that **the closest layer to the superconductor was hybridized with the superconductor and thus became metallic**. That would explain the low value of the resistance of the mono- and bilayer junctions. For three or more layers, there is at least one layer uncoupled which acts like a tunnel barrier. This gives higher resistances and an overall tunnel behavior to the junction. This result will be a comparison point to my experiment on superconducting vertical junctions with MoS₂ in chapter 7.

2.3.3.3 Planar geometry

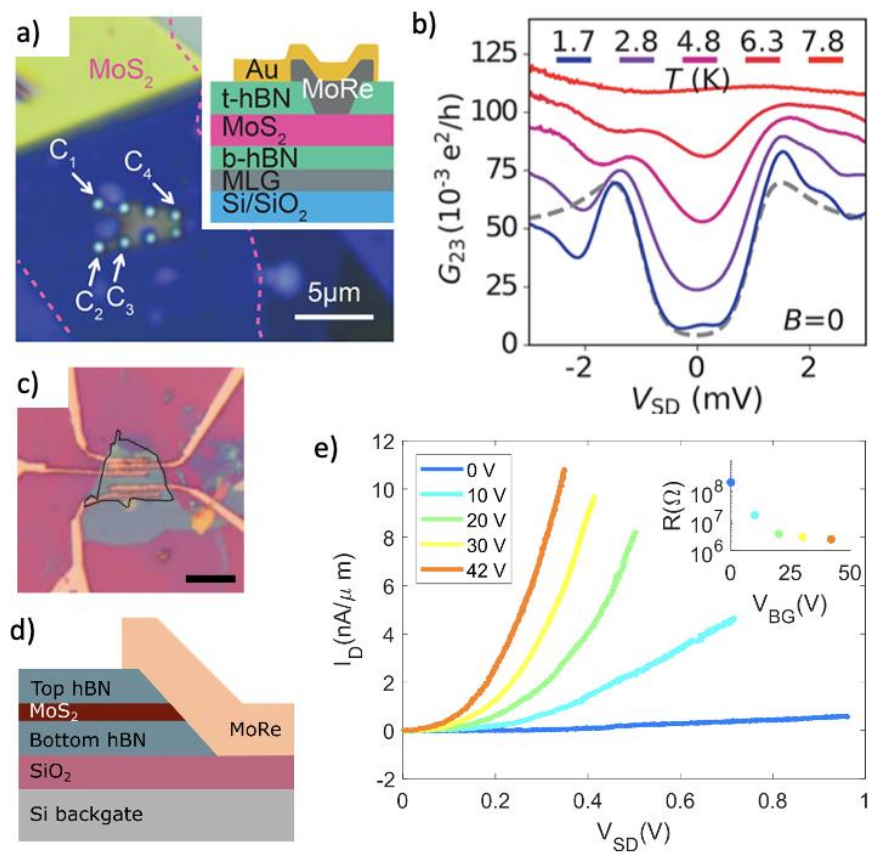


Figure 38 a) Microscope image of the device with the four contacts MoRe/MoS₂. The top inset schematically shows the various layers. b) Differential conductance spectra at several temperature between contacts 2 and 3 at zero magnetic field. Figures taken from Ramezani et al., *Nano Lett.* **21**, 5614–5619 (2021). c) Microscope image of a side-contacted encapsulated MoS₂ with MoRe. d) Scheme (side-view) of the contact between encapsulated MoS₂ and MoRe. e) Resultant current voltage characteristics of a junction between two of the contacts shown in d with a 200nm-long MoS₂ channel. Figures taken from Seredinski et al., *AIP Advances* **11**, 045312 (2021).

Now, we will review the attempt to contact MoS₂ with a superconductor in planar geometry. The goal is to inject Cooper pairs in MoS₂ and make them propagate towards the other contact through the MoS₂ layer. As for graphene, the encapsulation of MoS₂ in between a few layers of h-BN allows the protection of the 2D material and the preservation of its transport properties like its mobility by stabilizing its surface and avoiding impurities during the fabrication process. The two references I present here [150,151] try two distinct methods to realize a good electrical contact between MoS₂ and MoRe. In Figure 38a, the first approach is shown with a microscope image of the device with four contacts whose stack is pictured in the inset. A hole is opened in h-BN by e-beam lithography and then reactive ion etching. A larger contact is then defined by e-beam lithography to then deposit MoRe and gold. A measurement of the differential conductance between two MoS₂/MoRe contacts at several temperatures below and above the critical temperature of MoRe is presented in Figure 38b. The shape of these curves is tunnel meaning the transparency between the two materials is not enough to efficiently inject Cooper pairs in MoS₂. However, by applying a back gate voltage, they succeeded in observing the resonant tunneling of Andreev pairs. They argued this indicates that one of the two interfaces MoS₂/MoRe is relatively transparent. The differential conductance is therefore dictated by the less transparent (and then most resistive) MoS₂/MoRe interface.

Another method is developing to contact 2D materials like graphene [152,153]. It consists of contacting the 2D material by its edge and creating a 1D interface. Seredinski et al. [151] applied this method with encapsulated MoS₂ and MoRe. An image of the device is given in Figure 38c as well as a scheme of one of the contacts in d. They could measure the current-voltage characteristics between each of the MoRe/MoS₂ contacts (junctions of lengths 200, 500, and 500nm) and apply a voltage to the back gate electrode as seen for one junction in Figure 38e. They unfortunately reported resistances independent of the length. The resistance is therefore limited by the MoRe/MoS₂ interfaces that are very resistive as the I-V shows with a clear tunnel barrier they attributed to a Schottky barrier. They proposed to change the superconductor for one that would reduce this barrier. This method could nevertheless help the development of planar devices and build Josephson junctions with high-quality encapsulated 2D materials.

To my knowledge, there is no successful attempt to couple a high-T_c *d-wave* superconductor with MoS₂, motivating the research presented in chapter 7 of my thesis.

2.4 STRUCTURE OF THE THESIS

After this general introduction to both superconductors and 2D materials with a review of the proximity effect in thin metallic layers, graphene, and MoS₂, the next chapter is about the theory of proximity effect and Andreev reflection. More precisely, I first introduce the basic concepts necessary to understand Andreev reflection, the so-called BTK theory, in the case of *s*- and *d-wave* superconductors. This theoretical part is illustrated by experimental results in which I have been involved in the understanding and fitting of the data.

The following chapter is about experimental techniques I have used to fabricate,

characterize, and measure my superconducting devices. Since during my PhD, I studied several geometries of superconducting devices, the first part is dedicated to the fabrication of superconducting planar junctions while the second one to vertical junctions. The third part discusses the tools in the lab to characterize and check the properties of the materials during and at the end of the process. Finally, I describe the apparatus used to measure the samples at cryogenic temperature with a magnetic field.

The first results I want to show concern superconducting planar junctions with a metallic layer. The aim is to study how superconductivity is induced in a thin layer of gold on top of superconducting YBCO. To this aim, I conducted transport measurements on two kinds of systems: SN junctions between proximized gold and gold atop insulating YBCO and SNS junctions with the thin layer of gold acting as the bridge between two superconducting YBCO electrodes. The study of the SN junctions is analyzed with two different theoretical approaches: one based on the BTK formalism and the other one on Usadel equations. This chapter about a thin metallic layer is helpful to understand the two next chapters since a metallic layer is intercalated between YBCO and the 2D materials to protect YBCO and improve the electrical contact.

The next chapter is dedicated to YBCO/graphene junctions. The first part consists of a review of the state-of-the-art of YBCO/graphene junctions, especially the work done in the lab by David Perconte. He measured the effect of a back gate voltage on the differential conductance of a single interface between proximized graphene and normal graphene and identified it as Klein-like tunneling of Andreev electron-hole pairs. Then, I show published results on which I helped for the understanding of the experimental data. The article is about the coherent propagation of *d-wave* Andreev electron-hole pairs in a graphene channel over several hundreds of nanometers. Finally, the last part deals with a study of many samples of the influence of the magnetic field on the transport properties of YBCO/graphene/YBCO junctions. It is focused on oscillations in the magnetoresistance of junctions of intermediate transparency for magnetic fields between 0 and 2T.

The last project presented in this thesis is devoted to another 2D material, MoS₂. The first part shows preliminary results on transport measurements of CVD-grown MoS₂ deposited on top of YBCO planar junctions (as done with graphene). Contrary to graphene, the wet transfer of MoS₂ I developed does not guarantee good electrical contact between the 2D material and YBCO. As a consequence, all the measured junctions presented featureless tunnel-like differential conductance spectra. The second part is dedicated to the development of a new growth method of MoS₂ on YBCO in order to improve the electrical contact. This task was challenging and required a lot of time because YBCO is a complex and fragile oxide, very sensitive to the atmosphere composition and heat. After the characterization of both the superconductor and MoS₂, I present in the third part the integration of this method into the study of superconducting vertical junctions. Among all the measured junctions, two behaviors emerged. The first one analyzed is a tunnel-like behavior between the two superconducting electrodes while the second one is the presence of a critical current and therefore Josephson coupling at low temperature.

I conclude this manuscript with short to middle-term prospects like the optimization of the transfer process of CVD-grown MoS₂, the use of the transfer platform to allow the study of more exotic exfoliated 2D materials, and finally, the development of the PLD method to grow other TMDs like NbSe₂, allowing for full *in situ* processes.

3 SUPERCONDUCTING PROXIMITY EFFECT AND TRANSPORT AT THE INTERFACE WITH A SUPERCONDUCTOR

In the introductory chapter, I have shown that some materials have superconducting properties below a critical temperature. While intrinsic to some materials, early measurements [90,154] also demonstrated that metals, initially lacking superconductivity, can acquire superconducting properties when in proximity to superconductors. In this chapter, I will first show how this so-called “superconducting proximity effect” allows for an initially non-superconducting material (later referred to as “metal” or “normal metal” for simplicity) to show some superconducting properties. I will then present an effective model to treat the transport properties of the interface between a superconductor and a metal. After these two theoretical parts, I will present some published examples on which I worked during my PhD that illustrate these theoretical developments.

3.1 ANDREEV REFLECTION AND SUPERCONDUCTING PROXIMITY EFFECT

3.1.1 Superconducting proximity effect

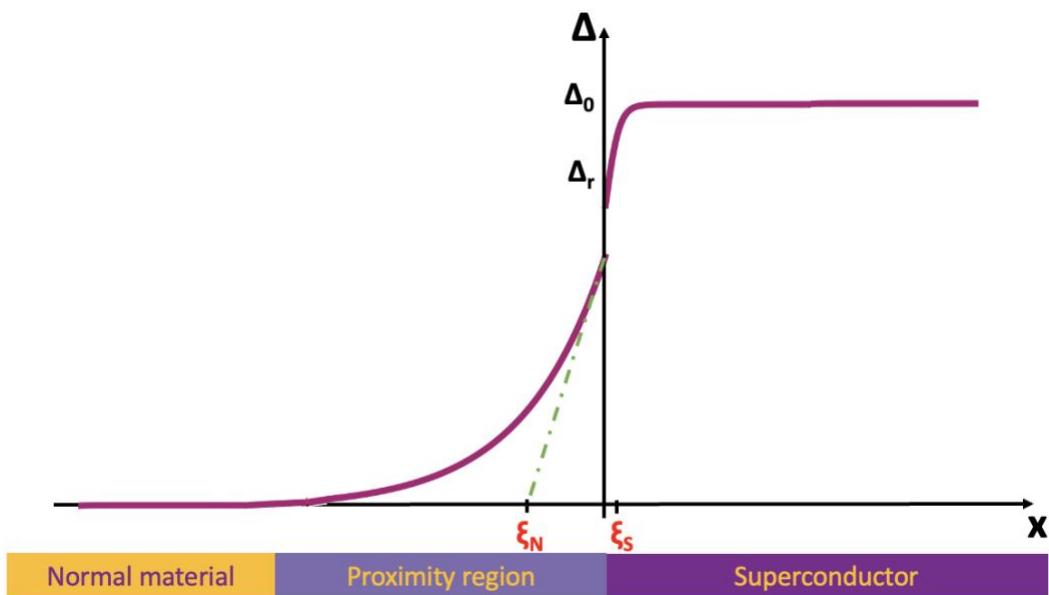


Figure 39 Different length scales at stake in a normal material/superconductor interface (inspired by Ref. 6). ξ_N is the coherence length of the normal metal over which the proximity effect fades. Δ_0 is the amplitude of the order parameter in the superconductor far from the interface. Indeed, the presence of the interface weakens the superconductivity with a reduced order parameter Δ_r at the interface. The superconducting order parameter returns to its bulk value over ξ_S which is called healing length.

When a normal metal is in contact with a superconductor, Cooper pairs from the superconductor can leak into the normal metal [155]. As we will see more precisely in the following, this creates a finite pair potential Δ (usually called “gap” on the superconducting side and sometimes “mini-gap” on the normal side) in the density of states in a thin region

close to the interface as shown in Figure 39. An intuitive explanation is given by the non-locality of the electrons at the interface between the two materials. **The electrons in the metal close to the interface with the superconductor are sensitive to the order parameter of the superconductor.**

More rigorously, this **boundary conditions problem** has been treated early on by de Gennes [9] in the simpler case of dirty superconductors, that is to say with an electronic mean free path of electrons l much smaller than the superconducting coherence length ξ_S . This approximation makes the things easier since the exact atomic structure of the interface is averaged out and the large scale motion of electrons is described by a diffusion equation. As we will see in chapter 5, it is possible to compute continuously physical quantities close to the interface between a superconductor and a normal metal with proper boundary conditions. It allows to describe the creation of a gap in the density of states of the normal metal by proximity. To be more precise, the proximity with a superconductor induces electronic correlation in the normal metal following the relation given in chapter 2 [155]:

$$\Delta(\vec{r}) = V_N \langle \psi(\vec{r} \uparrow) \psi(\vec{r} \downarrow) \rangle \quad 3.1$$

with V_N the electron-electron interaction constant in the normal metal.

In the next section, I will focus on the microscopic mechanism occurring at the interface.

3.1.2 Single-particle density of states and Andreev reflection mechanism

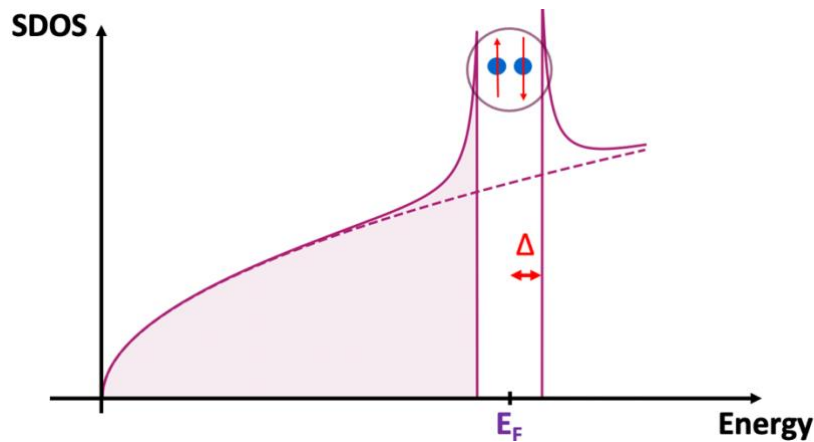


Figure 40 Single particle density of states (SDOS) of a 3D superconductor with a superconducting gap Δ as a function of the energy level. The colored region has to be understood as the filling of the electronic states below the Fermi level E_F . Inside the superconducting gap of amplitude 2Δ , there is no single electronic state.

Let us now focus on the interface between the two materials at the microscopic scale. As shown in Figure 40, and contrary to the case of a normal metal where electrons fill the available states up to the Fermi level, the electrons in a superconductor form pairs of electrons close to the Fermi level in an energy range Δ , the superconducting gap, into which electrons -forming Cooper pairs- condense into a macroscopic quantum state [4,17]. This peculiar property has very important consequences on the transport properties at the

interface with other materials.

Indeed, let us consider the simple case of a superconductor/metal junction and of an electron inside the metal moving toward the interface with a superconductor. At zero temperature, it could only penetrate into the superconductor if its energy E is above the superconducting gap. Otherwise, it cannot be transmitted and will be reflected. In fact, this situation holds only if we restrict ourselves to first-order processes. However, in the case of superconductors, there is a finite probability for a **second-order process** corresponding to the electrons being transmitted in the superconductor by Andreev reflection.

This later process is depicted in Figure 41. To describe it, let us first consider an electron moving toward the interface with an energy E greater than the Fermi level E_F but inside the superconducting gap of the superconductor. At the interface, the electron cannot be transmitted since there is **no available single particle state in the superconductor at this energy**. However, it is possible for another carrier to simultaneously be transmitted to form a Cooper pair in the superconductor. To conserve charge and momentum, a hole of energy $E_F - E$ and wavevector norm $\sqrt{k_e^2 - \frac{2mE}{\hbar^2}}$ is created along with the incident electron, where k_e is the incident electron wavevector and m its mass and \hbar the reduced Planck constant. This hole travels backward compared with the incident electron. Spin conservation with the Cooper pair on the other side of the interface then imposes that the retro-reflected hole has the opposite spin compared with the incident electron. **This process of the retroreflection of an electron as a hole in the metal along with the creation of a Cooper pair in the superconductor is the so-called Andreev reflection.**

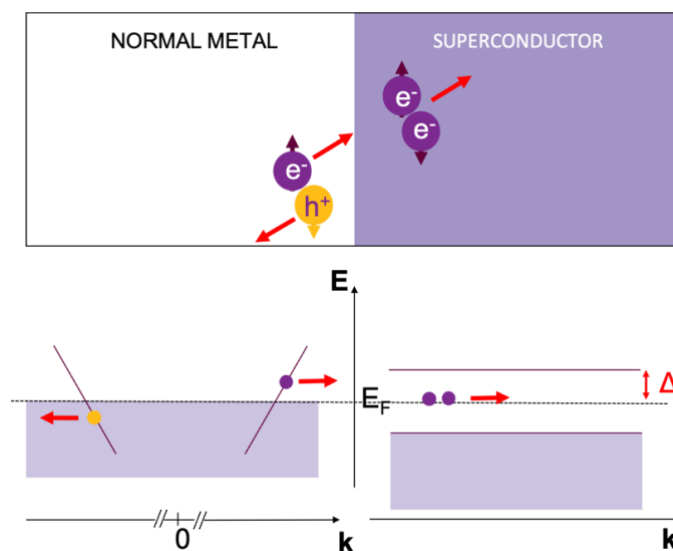


Figure 41 Schematic of the Andreev reflection at an interface between a normal metal and a superconductor. (Top) Spatial representation of the process. (Bottom) Energy diagram representation. On the metal side, the solid line corresponds to the electron state and the dashed line to the hole state. The red arrows account for the direction of motion of the particles.

This process describes what is happening for perfect interfaces, that is, in the absence of scattering close to the interface and for matching Fermi levels on both sides. However, as

we will see in section 3.2, the probability of Andreev reflection, electron reflection (backscattering), and electron tunneling depends on the transparency of the interface. In the case of finite transparency, there is a combination of Andreev reflection and backscattering.

Andreev reflection is the microscopic origin of the superconducting proximity effect, transferring the intrinsic electronic correlations from the superconductor to the metal. It is a **coherent process**, which means electrons and holes on the metallic side have a well-defined phase at the interface, set by the phase of the superconducting side. This phase difference between the two quasiparticles is subjected to scattering in the metal and correlations finally vanish further away from the interface. This is why the superconducting proximity effect disappears over the coherence effect of the normal metal (Figure 39), the phase difference being lost over that distance. In a ballistic material, this coherence length is given by:

$$\xi_N = \frac{\hbar v_F}{k_B T} \quad 3.2$$

Where v_F is the Fermi velocity, T the temperature and k_B the Boltzmann constant. In the case of a diffusive material, it becomes [156]:

$$\xi_N = \sqrt{\frac{\hbar D}{k_B T}} \quad 3.3$$

with D the diffusion constant of the metal.

3.1.3 Bogoliubov-de Gennes formalism

To quantify Andreev reflection with respect to usual reflection, Bogoliubov-de Gennes (BdG) formalism [157] – derived from the Bogoliubov transformation we saw in chapter 2 – is a useful formulation, allowing to deal with the interface between a superconductor and another material. This material can for instance be a normal metal [5], a ferromagnet [158], a Weyl semi-metal [159], or any material with a known band structure.

The proximity effect is an interfacial problem. We need a formulation to match wavefunctions on both sides to solve it. Bogoliubons in the superconductor introduced in chapter 2 is a useful formalism to solve the boundary condition problem. They are described by a vector $\begin{pmatrix} u \\ v \end{pmatrix}$ where u (v) is the amplitude of the quasi-electron (resp. quasi-hole) and by $\begin{pmatrix} f \\ g \end{pmatrix}$ on the metallic side as both sides should be described with similar quantities. For simplicity, we will restrict ourselves to a one-dimensional problem with a potential $V(x)$, chemical potential $\mu(x)$, and an energy gap $\Delta(x)$. An electron with amplitude f will therefore follow the Schrödinger equation, as the associated hole with amplitude g will follow the complex conjugate of the latter:

$$i\hbar \frac{\partial f}{\partial t} = \left[-\frac{\hbar^2 \nabla^2}{2m} - \mu(x) + V(x) \right] f(x,t) + \Delta(x)g(x,t) \quad 3.4$$

$$i\hbar \frac{\partial g}{\partial t} = \left[\frac{\hbar^2 \nabla^2}{2m} + \mu(x) - V(x) \right] g(x,t) + \Delta^*(x)f(x,t) \quad 3.5$$

Here, the superconducting gap couples the quasi-electron and quasi-hole wavefunctions. This formalism, allows for for exact calculation or numerical simulations of the spatial evolution of the quasi-electrons and quasi-holes excitation in the metal, close to the interface. However, scattering at the interface is not taken into account. In the next section, I will show how to use it to compute the differential conductance between a superconductor and a normal metal and how the interface transparency is included.

3.2 BLONDER-TINKHAM-KLAPWIJK THEORY

The last paragraph introduced a practical formalism to study the interface between superconductors and other materials. The Blonder-Tinkham-Klapwijk (BTK) theory [5,155], uses the BdG method in a 1D system, and provides a simple model to **compute the differential conductance of an interface between a superconductor and a normal metal of any transparency.**

3.2.1 BTK Model and generic resolution method

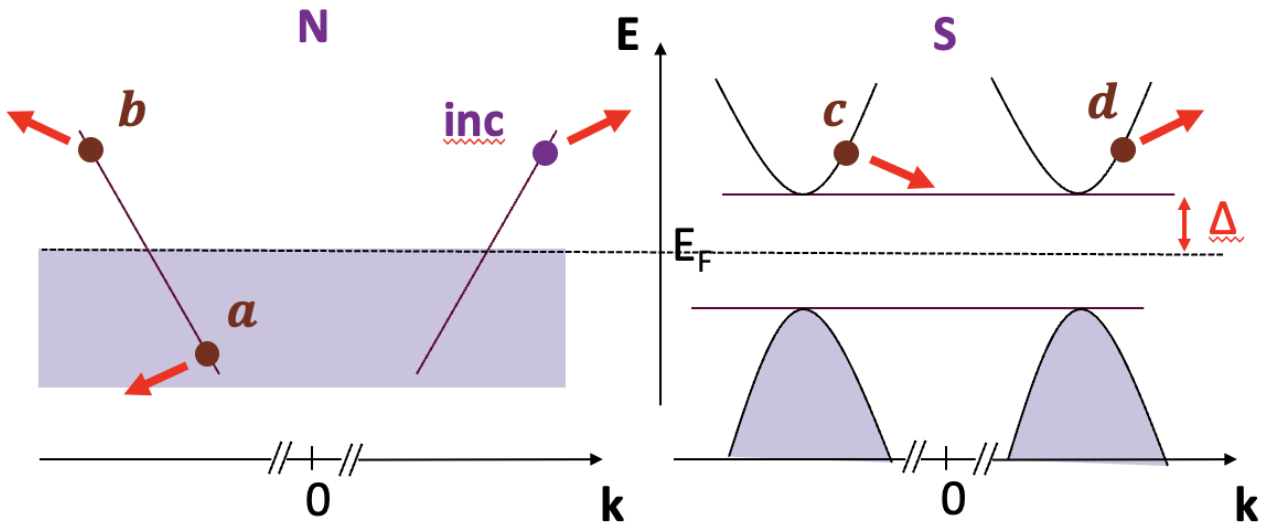


Figure 42 Schematic of all the possible events at the interface with their respective amplitude of probability and the direction of propagation of the created quasiparticle in real space represented by the red arrows. The superconducting gap Δ is represented on the superconducting (S) side and the filling of the bands is represented in purple.

This model has been developed to describe point contacts between a superconductor and a normal metal, with ballistic carriers arriving at an interface of variable transparency. This allows to consider the same equilibrium Fermi distribution for all the incoming particles, shifted by the applied potential as it is usual in mesoscopic transport theories [160]. It

assumes an electron moving along the x direction with energy E described by a harmonic wave of wavevector q^+ : $\begin{pmatrix} 1 \\ 0 \end{pmatrix} e^{iq^+x}$. To take into account the elastic scattering in the vicinity of the interface, a Dirac-potential of strength H is chosen: $V(x) = H\delta(x)$.

Before solving the boundary condition equations, we have to identify the potential events at the interface to define the wavefunctions describing reflected and transmitted carriers as shown in Figure 42. For an incoming electron, taken to have an amplitude 1, there is an Andreev reflected hole with amplitude $a(E)$ and an ordinary reflected electron with amplitude $b(E)$. Concerning the transmission, both the creation of a quasiparticle on the same side of the Fermi surface $c(E)$ and on the opposite side $d(E)$ are present. Therefore the transmitted (ψ_t) and reflected wavefunctions (ψ_r) can be described by:

$$\begin{aligned}\psi_r &= a \begin{pmatrix} 0 \\ 1 \end{pmatrix} e^{iq^-x} + b \begin{pmatrix} 1 \\ 0 \end{pmatrix} e^{-iq^+x} \\ \psi_t &= c \begin{pmatrix} u \\ v \end{pmatrix} e^{ik^+x} + d \begin{pmatrix} v \\ u \end{pmatrix} e^{-ik^-x}\end{aligned}\tag{3.6}$$

With : $\hbar k^\pm = \sqrt{2m(\mu \pm (E^2 - \Delta^2))}$ and $\hbar q^\pm = \sqrt{2m(\mu \pm E)}$.

To find the coefficient a , b , c , and d as a function of the energy E of the incident electron, one uses the continuity of the wavefunction at the interface ($x = 0$) giving: $\psi_{inc}(0) + \psi_r(0) = \psi_t(0)$. Then, by integrating the Bogoliubov-de Gennes equation between $-\varepsilon$ and ε and taking the limit $\varepsilon \rightarrow 0$ gives: $\frac{\hbar}{2m}\{\psi'_{inc}(0) + \psi'_r(0) - \psi'_t(0)\} = H\psi_t(0)$. The matching of the wavefunctions with these boundary conditions gives the amplitudes of the different events and the probabilities are the square of their modulus, which we will not describe in this manuscript. We will only give the formula for the Andreev reflection coefficient a in the case of a perfect interface ($Z = 0$):

$$a(E) = \left(\frac{E}{\Delta} \pm i \sqrt{1 - \left(\frac{E}{\Delta}\right)^2} \right) e^{i\varphi}\tag{3.7}$$

Here, φ is the superconducting phase. In the absence of another superconductor, this phase can be chosen to be zero. This coefficient $a(E)$ has a modulus of 1 and its phase is:

$$\chi = \varphi - \arccos\left(\frac{E}{\Delta}\right)\tag{3.8}$$

Experimentally, there are in the BTK model several quantities of interest such as the **scattering parameter Z** , as well as the expression of the electronic current I for a given excitation. Z is dimensionless and given by $Z = \frac{mH}{\hbar^2 k_F} = \frac{H}{\hbar v_F}$. The limits of Z correspond to physical cases, such that a perfect transparency interface is given by $Z = 0$ and a non-transparent interface (across which conduction is only possible by tunneling) by $Z \gg 1$. The other important quantity, the current I for a section of surface S , is given by:

$$I = 2N(0)ev_F S \int_{-\infty}^{\infty} [f_{\rightarrow}(E) - f_{\leftarrow}(E)]dE \quad 3.9$$

Here, $f_{\rightarrow}(E)$ and $f_{\leftarrow}(E)$ are the distribution function where we compute the current for carriers going on each direction.

$$f_{\rightarrow}(E) = f_{FD}(E - eV) \text{ with } f_{FD}(E) = \frac{1}{1+e^{E/k_B T}} \quad 3.10$$

$$f_{\leftarrow}(E) = A(E)[1 - f_{\rightarrow}(-E + eV)] + B(E)f_{FD}(E - eV) + [C(E) + D(E)]f_{FD}(E) \quad 3.11$$

We then use that $A(-E) = A(E)$ (by symmetry of the problem around the Fermi energy) and the sum of the probability is equal to 1 ($A(E) + B(E) + C(E) + D(E) = 1$) and $f_{FD}(-E) = 1 - f_{FD}(E)$ to derive the final equation:

$$I = 2 N(0) ev_F S \int_{-\infty}^{\infty} [f_{FD}(E - eV) - f_{FD}(E)][1 + A(E) - B(E)]dE \quad 3.12$$

Once the coefficients A and B found, it is possible to compute the differential conductance $\frac{dI}{dV}$, which allows for physical insight, onto which we can add the temperature dependence as we will see section 3.3.2. For now, let us consider $T = 0$. The normalized differential conductance reduces to:

$$G = \frac{dI}{dV} = 1 + A(E) - B(E) \quad 3.13$$

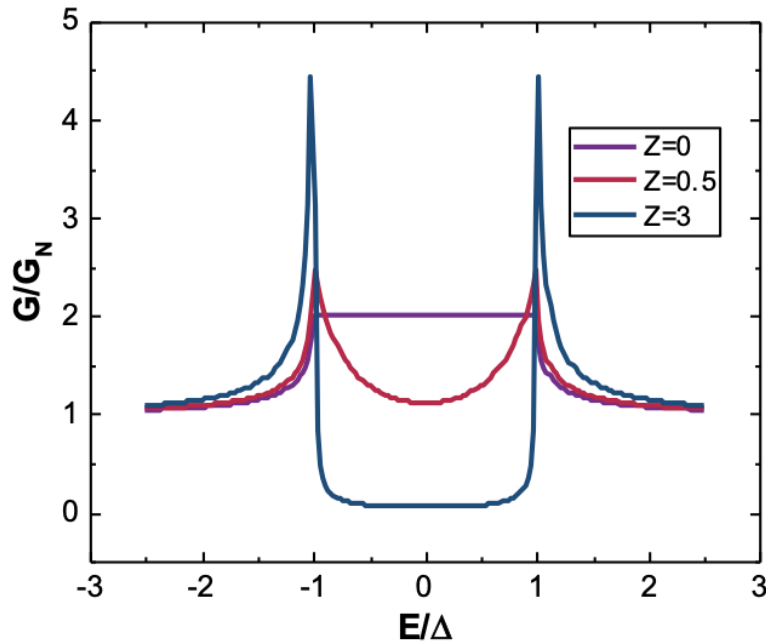


Figure 43 Numerical simulations of the differential conductance with the BTK model for $Z=0$, 0.5 and 3.

Some simulations of the differential conductance, for different interface transparencies, are plotted Figure 43. In the case of a perfect interface ($Z = 0$), the differential conductance at

energies below the superconducting gap is entirely due to Andreev reflection. Since Andreev reflection corresponds to the reflection of an incoming electron into a hole with the creation of a Cooper pair, we expect a doubling of conductance with respect to the normal state conductance. The differential conductance outside the gap is due to the creation of quasiparticles in the superconductors (process C in Figure 42) and the exponentially vanishing Andreev reflection (process A). For $Z \gg 1$, the differential conductance describes a tunnel junction, as the ones encountered when measuring tunnel barriers and performing STM measurements. It shows signatures of the density of states of the probed superconductors [104]. In this regime, Andreev reflection is absent but we can notice on the orange plot of Figure 43 the peaks at the superconducting gap edges. These so-called coherence peaks are linked to the emergence of superconducting coherence and of the local superconducting order parameter. Finally, for intermediate values of the parameter Z , there is a mixture between Andreev reflection and normal reflection inside the gap of the superconductor.

3.2.2 Josephson effect

In chapter 2, I introduced the concept of Josephson junction. Here, we will see we can derive the Josephson relation. According to Figure 44a, we consider now two superconductors separated by a normal metal of length L . We assume the two interfaces are perfect ($Z = 0$) so that the Andreev reflection coefficient is given by 3.7. In this specific case, and before doing any calculation, we notice that particles inside the junction (electrons or holes) can be trapped inside its metallic weak link by the Andreev reflection. We therefore expect quantized energy levels so-called Andreev bound states (ABS). The energy of these states can be found by a Bohr-Sommerfeld quantization argument since the phase accumulated along a closed loop must be an integer of 2π , giving:

$$\varphi \pm \arccos\left(\frac{E}{\Delta}\right) + k_e L + k_h L = 2n\pi, n \in \mathbb{Z} \quad 3.14$$

With $k_e = k_F \pm \frac{E}{v_F}$ and $k_h = -k_F \mp \frac{E}{v_F}$ respectively the wavevector of the electron and hole and φ the phase difference between the two superconducting condensates on both sides. In the short junction limit i.e. $\frac{|\Delta|L}{v_F} \ll 1$, we can neglect the propagation term and:

$$E = \pm |\Delta| \cos \frac{\varphi}{2} \quad 3.15$$

In the case of a finite barrier, the scattering inside the junction is assumed to be energy-independent and we are adopting the convenient scattering matrix method [160]. The reasoning, while similar, now considers scattering matrices with coefficients that represent the transmission or reflection of each transport channel. Without entering too many details, the energy of the Andreev bound state with a barrier of transmission $T = |t|^2$ is:

$$E = \pm |\Delta| \sqrt{1 - T \left(\sin \frac{\varphi}{2} \right)^2} \quad 3.16$$

The evolution of the energy as a function of the relative phase between the superconductors is plotted in Figure 44b.

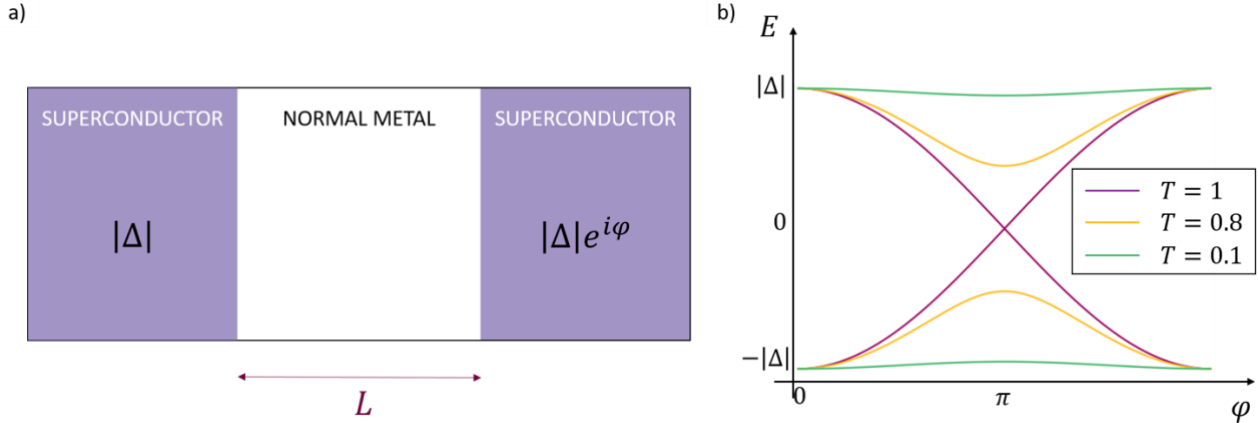


Figure 44 a) Scheme of a Josephson junction of size L . The phase of the superconductor is taken equal to zero for the left side and φ on the right one. b) Andreev bound states energy as a function of the relative phase between the two superconductors for three transmission probabilities. Except in the case of a perfect transmission ($T = 1$), the two other cases are gapped.

We now want to compute the contribution of these Andreev bound states to the current, the supercurrent. By noticing that $\frac{dE}{dt} = VI = \frac{dE(\varphi)}{d\varphi} \frac{d\varphi}{dt}$ and $\frac{d\varphi}{dt} = \frac{2eV}{\hbar}$, we deduce that:

$$I(\varphi) = -\frac{e\Delta}{2\hbar} \sum_j \frac{T_j \sin \varphi}{\sqrt{1 - T_j \left(\sin \frac{\varphi}{2} \right)^2}} \quad 3.17$$

Where we summed over all the channels of transmission T_j in the junction. For a tunnel junction (all $T_j \ll 1$), we find back the relation derived by Josephson [31]: $I(\varphi) = I_c \sin \varphi$.

3.2.3 Limitations and improvements of the BTK model

The BTK theory is widely used for its simplicity and its reliable qualitative explanation of many interfacial problems between superconductors and metals. However, this theory deals with a one-dimensional system without magnetic field using very specific assumptions on scattering and describing the interface as perfectly punctual (1D quantum point contact). We will come back to these assumptions in the following.

3.2.3.1 Dimensionality of the interface

The BTK theory was extended in the 3D case in Ref. [161]. The author derived the expressions for the normal and Andreev reflection probabilities in the case of a 3D interface and not as BTK in an ideal point contact geometry. He found that the differential conductance

computed in this case may be very different from the BTK formula if the barrier at the interface sufficiently depends on the energy of the incoming particles. Otherwise, BTK appears to be an excellent approximation to the complex 3D calculation.

Mortensen et al. [162] have studied the impact of the angle dependence of the Andreev reflection and consequently of the differential conductance. The presence of a Fermi velocity mismatch between the normal metal and the superconductor implies the existence of a relation on the angles of reflection analogous to Snell's law:

$$k_F^S \sin \theta_t = k_F^N \sin \theta \quad 3.18$$

Where k_F^S (k_F^N) is respectively the Fermi wave vector in the superconductor (normal metal), θ the angle of the incident electron and θ_t the angle of the transmitted quasiparticle. As a consequence, for $\frac{k_F^N}{k_F^S} > 1$, a critical angle exists for the transmission to happen ($\theta_c = \sin^{-1}\left(\frac{k_F^S}{k_F^N}\right)$) and therefore **the transmission probability and the overall differential conductance depend on the incident angle.**

3.2.3.2 Scattering close to the interface

The description of the scattering can be improved as done by [21] using a finite potential U over a length L . The results obtained can differ significantly from the BTK theory especially in the case of a potential barrier U close to the Fermi energy where resonances can appear and significantly change the differential conductance. In particular, different dispersion relations on both sides of the N/S interface can significantly change the differential conductance for low values of the scattering parameter Z as shown by the same authors [23].

3.2.3.3 Magnetic field

The one-dimensional assumption has also consequences on electronic transport properties when using a magnetic field. **At high magnetic fields** (cyclotron radius R_c smaller than the characteristic lengths of the junction), the carriers' trajectories are strongly affected and describe **cyclotron orbits** giving rise to rich physical phenomena [164,165]. In particular, it allows the formation of edge states, with both electrons and holes bouncing at the interface due to Andreev reflections, as shown in Figure 45a. **At low magnetic fields, the presence of disorder has an effect similar to weak localization** in metals with a twist: scattering can induce multiple attempts of Andreev reflections for a single incident electron [166]. For finite scattering factor Z , at low bias and low magnetic field, Andreev reflection is therefore enhanced. This effect disappears both with the magnetic field B and with the energy E of the incident electron since a random phase (through the random path length l and enclosed area A between two reflections) will add up and reduce the effect. For instance, for a two-reflection process as pictured in Figure 45b, the phase difference between the reflected electron and the returning electron is:

$$\Delta\phi = \frac{2El}{\hbar v_F} + 4\pi \frac{BA}{\phi_0} \quad 3.19$$

Where L is the path length, A the area enclosed between this path and the superconductor interface, and $\phi_0 = \frac{h}{2e}$ is the quantum of flux.

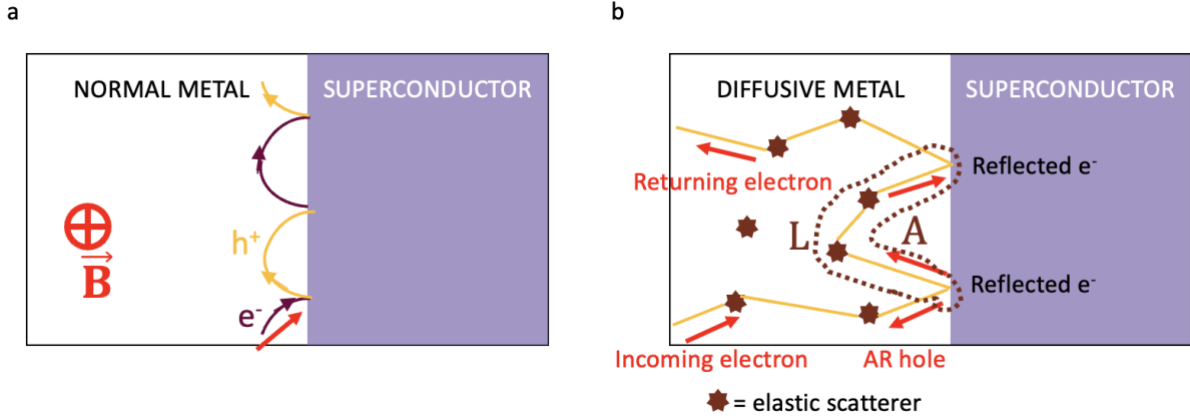


Figure 45 a) Andreev reflection in the presence of a high perpendicular magnetic field. b) Andreev reflection in the presence of disorder made of random scatterers. L and A stands for the length of a path of an electron and A the area enclosed by this path and the superconductor.

Although BTK theory relies on simple assumptions, it showed impressive reliability in the understanding of interfacial transport. It even recently got a renewed interest thanks to the recent quest for exotic quasiparticles at the interface between superconductors and topological insulators, while many theories developed to understand these phenomena start with similar ideas. In the specific case of 2D materials, that we are interested in for this thesis, Linder et al. [13] (chapter 6) generalized the Bogoliubov-de Gennes equations in the case of a Dirac spinor, dedicated to the study of superconductor/graphene junctions, while developments done by Kashiwaya et al. [105] also generalized it to anisotropic superconductors like d -wave ones as described in the following paragraph 3.3.1.

3.3 APPLICATIONS TO D-WAVE SUPERCONDUCTORS

As we have seen in chapter 2, YBCO is a d -wave superconductor. It has an anisotropic gap which impacts the transport properties. An extension of the BTK theory has been developed to **take into account the orientation of the interface with respect to the crystallographic orientation of the superconductor**. This theory presented in section 3.3.1 will be very useful to understand the data acquired with three different systems in sections 3.3.2, 3.3.3 and 3.3.4.

3.3.1 d -wave superconductors

In this section, I will point out the differences between d -wave and s -wave superconductors. First, we depict a scheme of Andreev reflection in the case where the d -wave order parameter orbitals are tilted by an angle α from the interface superconductor/normal metal interface

(Figure 46). This general case has been treated in Ref. [105] and experimentally by scanning tunnelling microscopy in Ref. [167]. A first difference is directly linked to the anisotropy of the superconducting gap close to the interface which, instead of being constant whatever the crystallographic orientation of the material (*s-wave* case), now depends on the crystal direction and is taken as:

$$\Delta(\vec{k}) = \Delta_0 \cos[2(\theta_N - \alpha)] \quad 3.20$$

Where θ_N and α are respectively the incident electron angle with the interface and the angle of the superconducting order parameter with the interface.

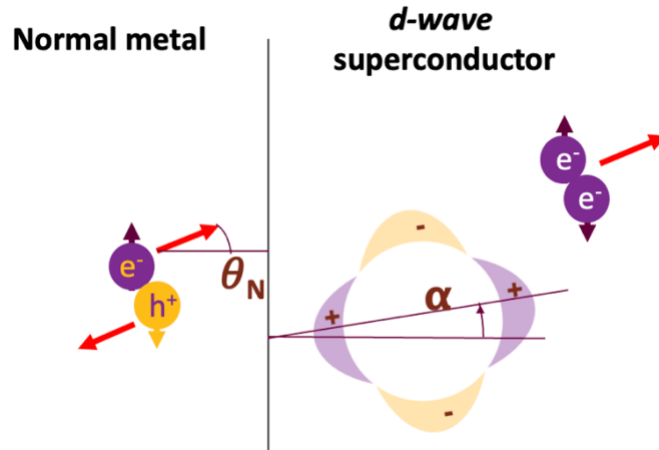


Figure 46 Andreev reflection at a normal metal/*d-wave* superconductor interface, with its order parameter tilted by α from the interface and θ_N is the angle of the incident electron with the interface.

One can then compute the differential conductance at zero temperature with the BTK formula 3.13. Two extreme cases are shown in Figure 47, corresponding to $\alpha = 0$ (left) and $\alpha = \pm\pi/4$ (right).

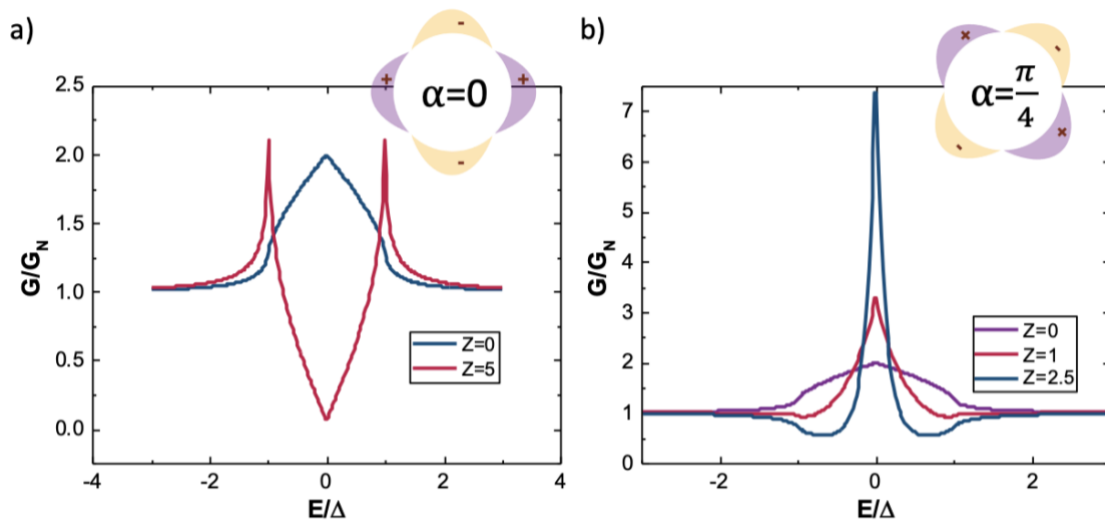


Figure 47 Calculated differential conductance of an interface between a normal metal and a *d-wave* superconductor in the case of $\alpha=0$ (left) and $\alpha=\pi/4$ (right).

For $\alpha = 0$, the differential conductance presents similarities with the simple *s-wave* case. For perfect transparency ($Z = 0$), we get an Andreev peak (twice the normal-state conductance) instead of a plateau observed in the *s-wave* case, while for low transparency ($Z \gg 1$), the conductance describes a tunnel-like behavior with a notable difference being a non-zero conductance at zero bias contrary to the *s-wave* case. These two discrepancies are due to the closing of the gap in the *d-wave* case that allows for the propagation of quasiparticles in the superconducting material.

For $\alpha = \pi/4$, the situation is similar at perfect transparency but, while increasing the scattering parameter Z , a zero bias peak appears. **This peak is due to the formation of Andreev bound states at the interface.** Indeed, the hole-like and electron-like quasiparticles transmitted through the interface have opposite phases in this case. This is equivalent to a Josephson junction with a phase difference of π between electrodes being infinitely close to each other. The energies of the bound states are then all degenerated at 0 and that creates the divergence.

These two examples aim to emphasize the higher complexity and variety of the conductance spectra of *d-wave* superconductors. The next sections are dedicated to original applications [8,168] I studied and modeled during my PhD for which the BTK approach allows to understand their transport properties.

3.3.2 Simulation of the temperature dependence

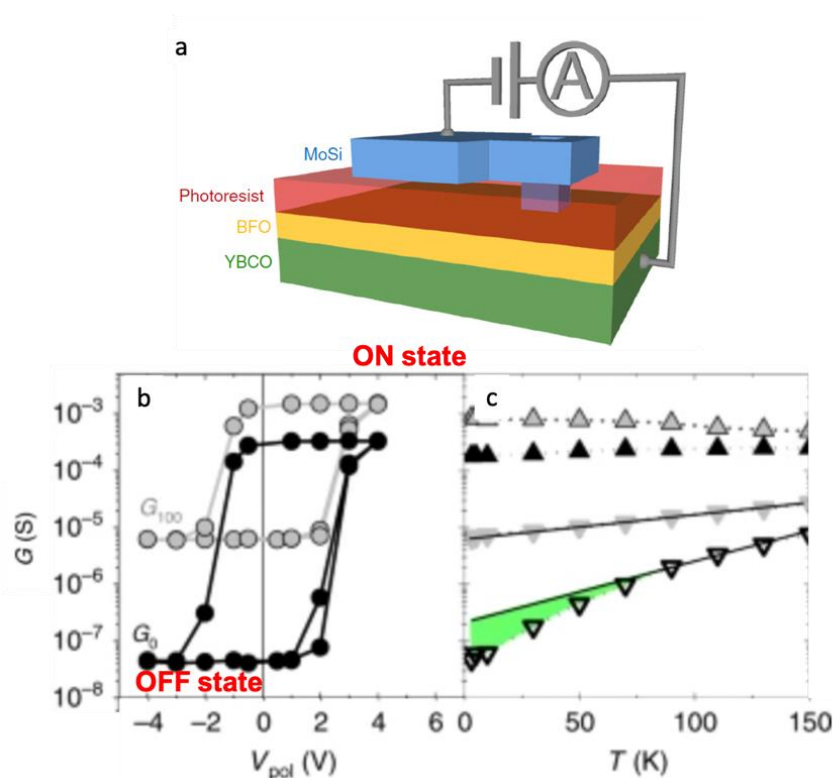


Figure 48 Figures taken from Ref. [168]. a) Scheme of the vertical junctions made of 30nm-thick YBCO, a given thickness of BFO, and 100nm of MoSi. b) Differential conductance as a function of the poling voltage pulse applied to the junction measured at 0mV (black dotted

line) and 100mV (grey dotted line) at 5K. c) Differential conductance with respect to the temperature measured at 0 (in black) and 100mV (in grey) for the ON (upper plots) and OFF (lower plots) states. The green filling shows the strengthening of the effect compared with the expected temperature dependence.

I performed the modelization of transport experiments based on samples fabricated and measured in my lab by Victor Rouco. They consist of vertical junctions patterned by a two-step optical lithography as represented schematically in Figure 48. The fabrication process of these junctions, which I also used to realize the superconducting devices I present in chapter 7, can be found in chapter 4 and in Ref. [168]. As shown in Figure 48, the bottom electrode is made of YBCO while the top electrode is made of a low- T_c superconductor molybdenum silicon (MoSi). In between, a variable thickness (from 0 to 15nm) of BiFeO₃ (BFO) is grown. The fabrication allows measuring in a 2-probe configuration of micrometric vertical junctions.

We distinguish two operating modes of these devices depending on the value of the voltage bias we apply. For low voltage (typically $< 200\text{mV}$), we probe the conductance of the junction by measuring the current passing through the junction (reading mode). For higher voltage bias (V_{pol} in Figure 48b), we enter the writing mode where the voltage bias we apply is enough to change durably the properties of the junctions. In Figure 48b, for each data point, we applied a polling (or writing) voltage V_{pol} to the junction before measuring the conductance of the junction using a voltage bias either 0 or 100mV (respectively in grey and black data points). The evolution of the conductance is hysteretic and shows two states of conductance that can be reached reversibly (here, reproduced twice): the junction acts as a memory, also called a memristor, that can be written electrically and read with a non-destructive small bias voltage. We therefore define the "ON" state as the highest conductance state while the "OFF" state is the lowest conductance state.

Figure 48f displays the evolution of the conductance with the temperature in the two states and at the two reading voltages (0 and 100mV). For the ON state, the behavior of the conductance remains metallic at all temperatures (the conductance slightly increases as the temperature decreases) while the OFF state shows an insulating behavior between 90 and 150K. We noticed however that, below 90K (the superconducting transition temperature of YBCO), the measured conductance gets much lower than the expected temperature evolution. The green area highlights this loss in conductance below the critical temperature of YBCO.

To understand this effect, I considered the differential conductance with respect to the bias voltage applied to the junction. At low temperatures, Figure 49a and b show a strong temperature dependence at low voltages both in the ON and OFF states. This is reminiscent of a junction between a metal and a superconductor for a large scattering parameter Z . To treat these data, it is first necessary to remove the background. For this, I used the Brinkman-Dynes-Rowell (BDR) [169] theory which allows modelizing tunnel junctions between oxides by taking into account asymmetries of the tunnel barrier. After subtracting this background, I normalized the obtained conductance by its high bias values. This allows for fitting the data with the d -wave BTK model I developed as shown in Figure 49c,d (black dot). I carried out

two fits (blue and red plain lines). The first one (in blue) is the original BTK model and presents large coherence peaks that are not present in the experimental data. This absence can be related to the disorder close to the interface that reduces the quasiparticles' lifetime. This finite lifetime τ is taken into account in the BTK model by adding an imaginary part to the energy [170,171] :

$$E \rightarrow E + i\Gamma \text{ where } \Gamma = \hbar/\tau \quad 3.21$$

We can see that this description is closer to the experimental data reducing both the height of the coherence peak and the depth of the tunnel dip at zero bias.

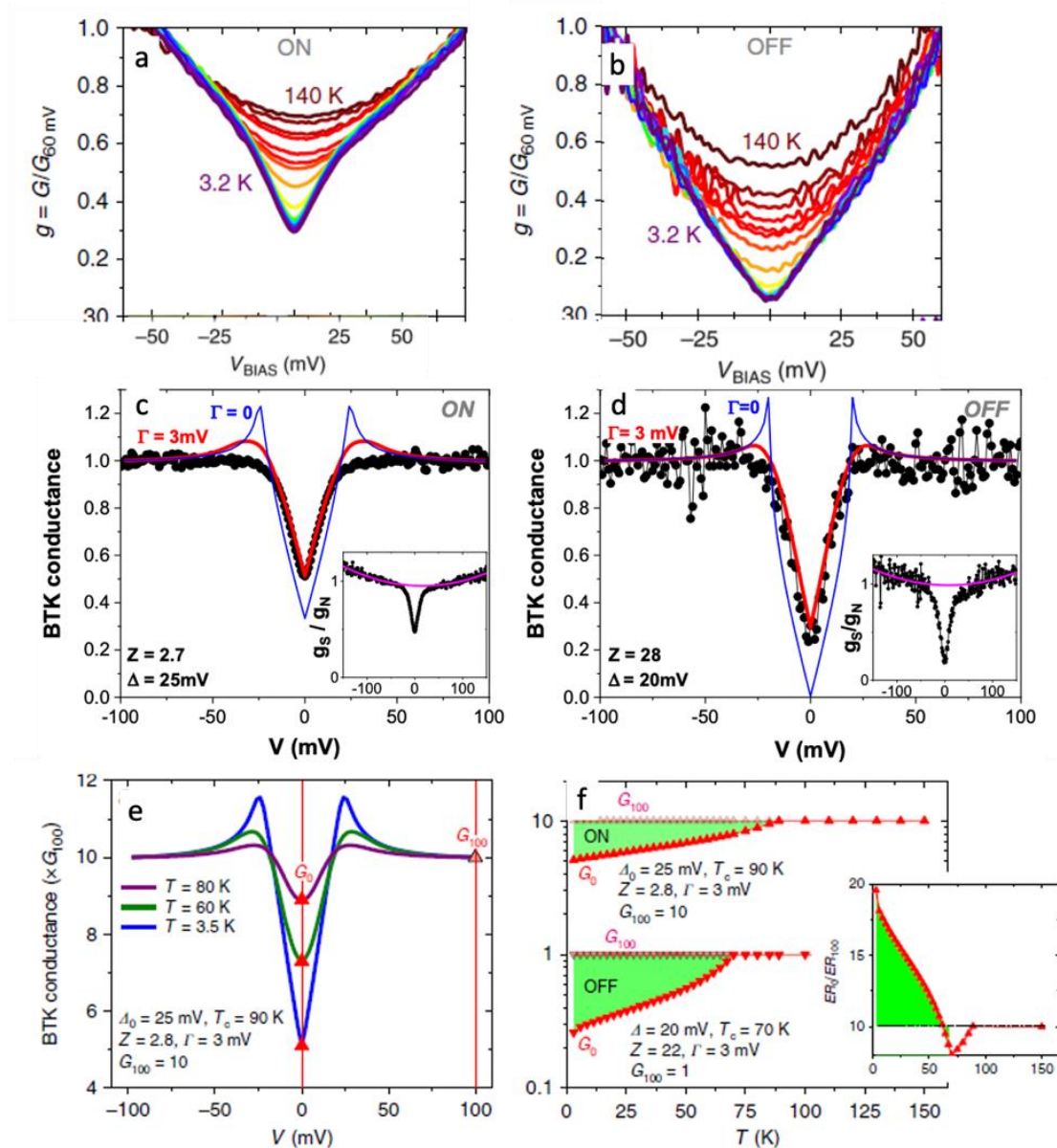


Figure 49 a,b) Differential conductance spectra for the ON and OFF states at different temperatures. c,d) Differential conductance after removal of the background (see text) and normalization for the ON and OFF states (black dots). A fit with d-wave BTK is shown with the red plain line. e) Numerical simulation of the temperature behavior of a junction

described by the *d*-wave BTK theory. *f*) Temperature evolution of the conductance simulated for the junction in the ON and OFF state with the filled green region accounting for the superconducting strengthening compared with normal evolution. The inset shows the simulated electroresistance ratio ER_0/ER_{100} as a function of the temperature.

Once I found the parameters to correctly fit the conductance spectra, I simulated the behavior of the vertical junction for higher temperatures. To do so, I took into account both the smearing of the Fermi-Dirac distribution in the expression 3.12 and the temperature dependence of the superconducting gap. For the temperature dependence of the gap, I fitted the value of the gap with the experimental data using the ansatz [172]:

$$\Delta(T, T_c) = \Delta_0 \tanh\left(b \sqrt{\frac{T_c}{T} - 1}\right) \quad 3.22$$

Finally, it is possible to simulate the differential conductance from zero temperature to the critical temperature. Figure 49e shows 3 examples of the differential conductance spectra with the parameter in the legend while Figure 49f shows the complete simulation as a function of the temperature both for the ON and OFF states and for 0 and 100mV. We can see that the enhancement present in Figure 48c can be explained by the superconductivity inside the gap of YBCO as shown on Figure 49f.

The system we studied is made of a tunable tunnelling barrier between a high- T_c superconducting oxide and an amorphous metal. A strong electroresistance is measurable at all temperatures, with a strong enhancement observed below the T_c . The BTK modelization I performed proved that the enhancement is due to the opening of the superconducting gap, in a regime in which transport is dominated by quasiparticle tunnelling. This superconducting effect allows to strongly enhance the electroresistance effect at low ($< 90K$) temperatures.

3.3.3 Demonstration of superconductivity in $La_5SrCu_6O_{15}$

The model I developed also allowed us to study different systems. I therefore also participated in the modelization of an experiment performed at Complutense University (Madrid) [7]. Here, the geometry is similar to the one in the previous section, except the bottom material is not YBCO but $La_5SrCu_6O_{15}$ (LSCO). This material is not superconducting in its pristine form even down to a few milliKelvin [173]. The vertical junctions are made of 10nm LSCO cuprate layers (top electrode) grown on 4nm ferroelectric $BaTiO_3$ (BTO) on 30nm Sr doped La manganite $La_{0.7}Sr_{0.3}MnO_3$ (LSMO) (bottom electrode) epitaxially deposited onto (001) $SrTiO_3$ (STO) substrates. The measurements done on these junctions are similar to the ones explained in the previous section. We poll the junction with large voltage pulses and then read the resistance with smaller voltage biases. Figure 50a shows a hysteresis loop with two distinct states, a high resistance state (HR) and a low resistance (LR) state corresponding to the two different polarization states of BTO. Indeed, BTO is a ferroelectric material, which means voltage pulses imply a piezoelectric response and an accumulation or depletion of charges at the interface depending on the sign of the pulses. This accumulation/depletion creates doped/depleted regions that are modulating the tunnel behavior of the whole

junction. At 100K, the resistance as a function of the writing voltage shows an analogous hysteretic behavior as in the last section, typical of the ferroelectric material tunnel barrier. The differential conductance spectra of the junction in both states are shown in Figure 50b for temperatures going from 5 to 200K. At low energies ($< 25\text{mV}$), there is a diminution of the conductance at low temperatures ($< 60\text{K}$). This means there is a gap in the single-particle density of states that can arise from various origins (electronic correlations). In the following, I will show that this system fits very well with the existence of a *d-wave* superconducting phase in LSCO.

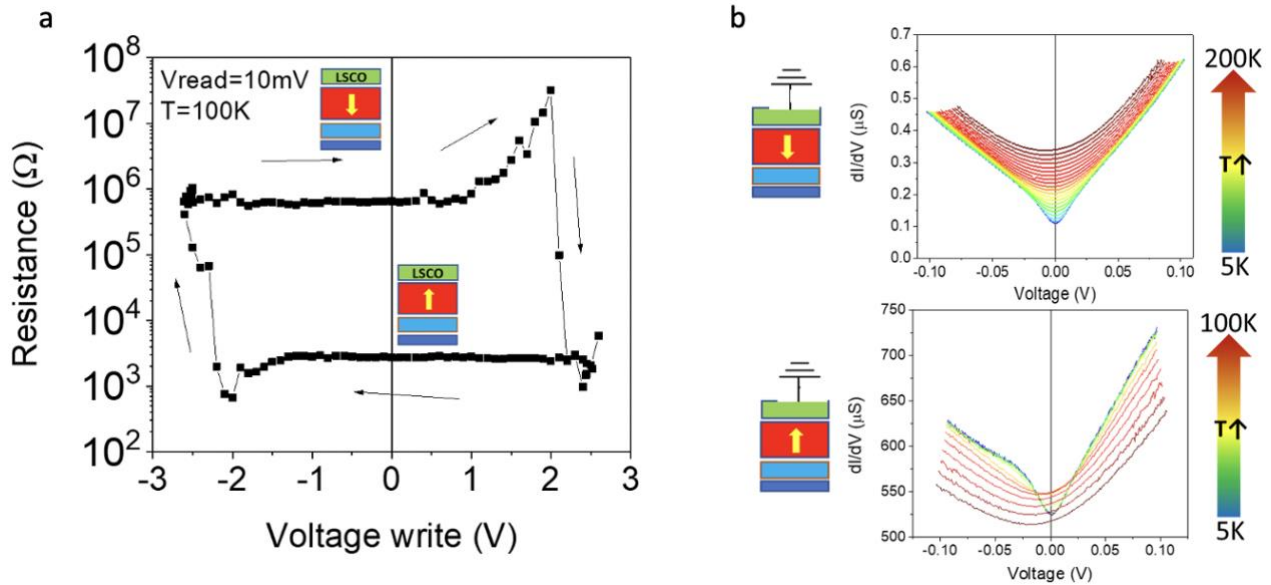


Figure 50 Figures taken from a paper in preparation. a) Resistance versus the applied voltage writing measured with a voltage of 10mV. b) (upper panel) Differential conductance spectrum of the high resistance state (polarization of BTO pointing down) and (lower panel) Differential conductance spectrum of the low resistance state (polarization pointing up).

We apply the same removal of the background and its characterization thanks to the BDR theory [169] and normalization (with respect to the high bias conductance) as in the previous section and we get the plots in Figure 51a and b. Under this form, I found it to be possible to fit the experimental data with the *d-wave* BTK model presented in the last two sections. There is a good agreement between the fits as shown in Figure 51a,b with the black lines corresponding to the BTK fits of the experimental points for the high resistance (HR) state in a and low resistance (LR) state in b. The quality of the fits allowed to extract the gap value of the model and plot it as a function of the temperature in Figure 51c. This dependence can be well fitted by the formula 3.22 [172]. This allows to find the predicted superconducting transition temperature in both states: $\sim 70\text{K}$ for the HR state and 50K for the LR state. The polarization state of the junction and therefore the doping profile has a strong influence on the extracted superconducting gap and the critical temperature of the LSCO layer.

In summary, the BTK analysis I performed suggests the appearance of a superconducting phase in LSCO, and has allowed us to quantify how it would be affected by the polarization state of BTO.

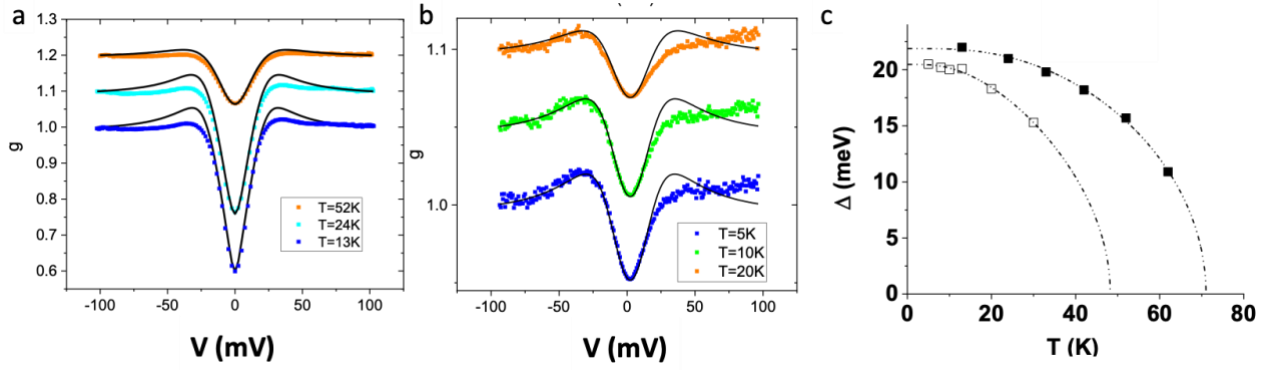


Figure 51 a) Normalized differential conductance spectra (scatter) in the high resistance state for $T = 13, 24,$ and 52K and their BTK fits. b) Normalized differential conductance spectra (scatter) in the low resistance state for $T = 5, 10,$ and 20K and their BTK fits. c) Extracted values for the superconducting gap for HR state (black scatter) and LR state (white scatter) and their fits (according to equation 3.22).

3.3.4 Quasiparticle density of states and spin-injection in YBCO

In this section, we deviate a bit from the previous part in the sense we consider here the interface between YBCO and a ferromagnet, $\text{Ni}_{80}\text{Fe}_{20}$ (Py), studied in my lab by Santiago Carreira. In the presence of a ferromagnet, the two spin populations at the Fermi level are no longer equivalent and the proximity effect is different from the normal metallic case. However, our study can give some qualitative interpretation of experimental facts observed in ferromagnetic resonance (FMR) experiments.

The geometry of the experiment is depicted in Figure 52a. The sample consists of a stack of a substrate, either SrTiO_3 (001) (STO) or NdGaO_3 (001) (NGO), 30nm-thick YBCO (001) *i.e.* c -axis and 15nm of the ferromagnet Py. An interlayer of Au was added for the samples grown STO to prevent the oxidation of Py at the interface. To measure a FMR signal, we apply an in-plane magnetic field to saturate the magnetization of the ferromagnet while we apply a weak oscillating magnetic field perpendicular to the DC field with a coplanar waveguide to make the magnetization precess. We then measure the derivative of the absorbed power of this signal dP/dH by modulating the DC magnetic field at low frequency ($\sim 80\text{Hz}$). On the left of Figure 52b, a typical FMR absorption spectrum is presented for a given frequency f of the AC field with a resonance that can be fitted by the derivative of a Lorentzian function. This fit gives two parameters: the resonance field H_{res} and the linewidth of the resonance ΔH_{pp} . The frequency of the AC field is plotted against the resonance magnetic field for a stack STO//YBCO//Au//Py in Figure 52b (middle plot). All the samples measured were well described (fit in red) by the Kittel formula [174] as shown in the middle plot in Figure 52b:

$$f = \gamma \mu_0 \sqrt{H_{res}(H_{res} + M_{eff})} \quad 3.23$$

With γ the gyromagnetic factor, μ_0 the vacuum magnetic permeability and M_{eff} the effective magnetization of the ferromagnet. The linewidth ΔH_{pp} plotted with respect to f in Figure

52b (right plot) is well described by a linear expression [175]:

$$\mu_0 \Delta H_{pp} = \frac{2\alpha f}{\sqrt{3}\gamma} + \mu_0 \Delta H_0 \quad 3.24$$

In this expression, there are two terms, the frequency-independent contribution ΔH_0 and α which is the Gilbert damping factor.

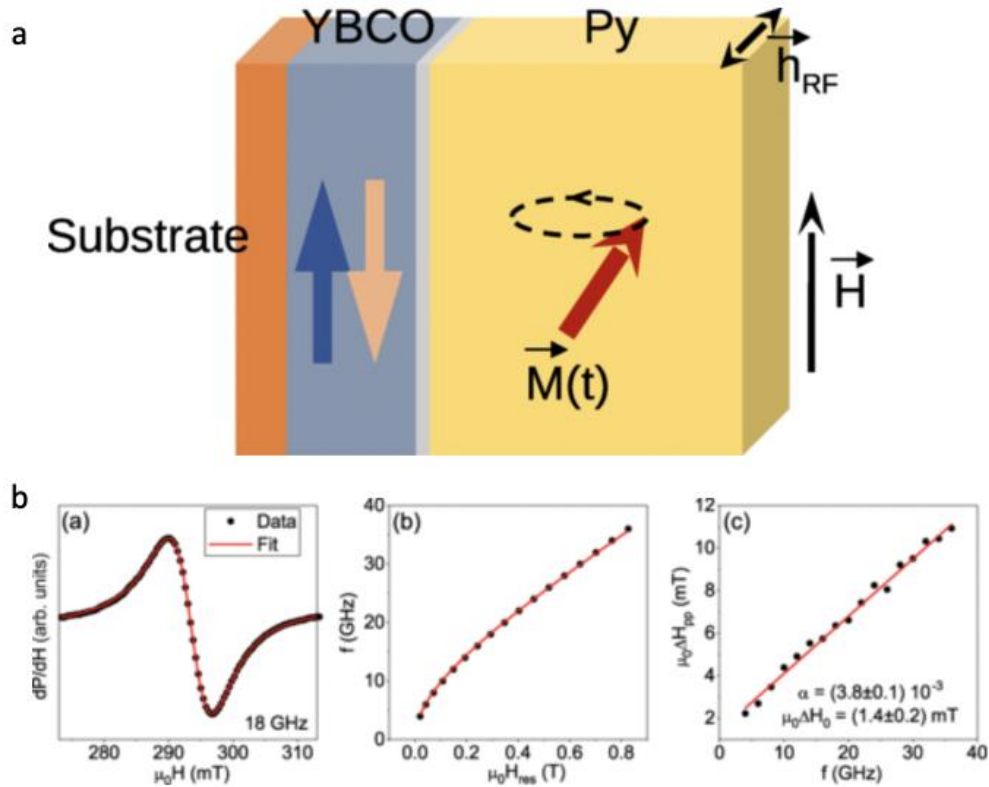


Figure 52 a) Sketch of the experimental geometry for the ferromagnetic resonance (FMR) experiments. b) (from left to right) FMR absorption spectrum and fit, frequency vs $\mu_0 H_{res}$ and $\mu_0 \Delta H_{pp}$ vs frequency obtained for the sample made of STO//YBCO//Au//Py. Figures taken from Carreira, *Phys. Rev. B* **104**, 144428 (2021).

Physically, we want to quantify the influence of YBCO on the magnetization of Py through their interface. Indeed, spins can be injected into YBCO, and depending on whether YBCO is or is not in its superconducting state, the spin injection may be radically different as it is for charge transport in the BTK model. The increment or lowering reflects this spin injection in a material.

In Figure 53, if we focus on (a) and (b), the behavior of the Gilbert damping factor is the same for the two samples for temperatures from roughly 150 to 70K with a small drop at the superconducting transition temperature but differs radically below 70K. While the sample with STO substrate has a constant Gilbert damping below 70K, the one of the sample with NGO increases and is even larger at low temperature than above the transition temperature. However, the substrate does not influence the behavior of the control samples without YBCO. Therefore, the difference between the two YBCO samples comes from the growth on the substrate as shown by atomic force microscopy in Figure 53(c) and (d).

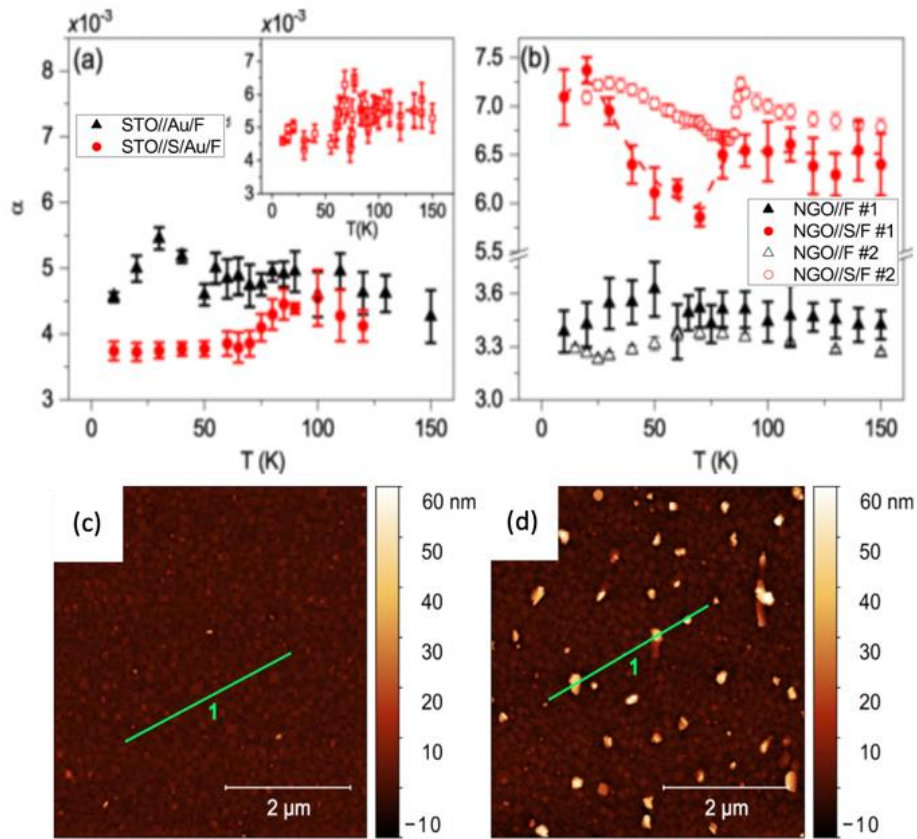


Figure 53 Temperature dependence of the Gilbert damping factor for the samples with the STO substrate (a) and for the NGO substrates (b). On each graph, the control samples data points appear with triangles while the samples with YBCO have dots. Atomic force microscopy (AFM) image of a YBCO thin film grown on (c) STO and (d) on NGO.

This difference in the growth manifests itself as a punctual different crystallographic axis for the YBCO film. After the growth of Py, the interface will then be of a different nature depending on the position as schematized in the inset of Figure 54(a). But the crystallographic orientation makes that the direction of transport is different and the quasiparticle density of states can be drastically different as shown in Figure 54(a) for transport along the $\alpha_g = 0$ and Figure 54(c) along $\alpha_g = \pi/4$. Indeed, along the $\alpha_g = \pi/4$ direction, the surface density of states has the zero bias peak due to Andreev bound states at the interface. The spin injection is then larger in this direction [176]. The temperature evolutions for the two directions are represented in Figure 54(b) and follow completely different trends below the superconducting transition temperature.

The study of the AFM images allows us to estimate the area of the $\alpha_g = \pi/4$ facets between 1% and 1.7% depending on the estimate. However, these regions have a conductivity around 10 times larger than the $\alpha_g = 0$ direction. Therefore, the ratio 10%/90% chosen in the numerical calculation in Figure 54(d) sounds reasonable for a qualitative explanation. On this plot, the surface density of states of quasiparticles presents a small upturn below the transition temperature but starts increasing when the temperature decreases due to the Andreev bound states. As stated in Ref. [176], the larger the density of states, the larger will be the spin injection, and as a consequence, the Gilbert

damping factor will follow a similar trend in temperature.

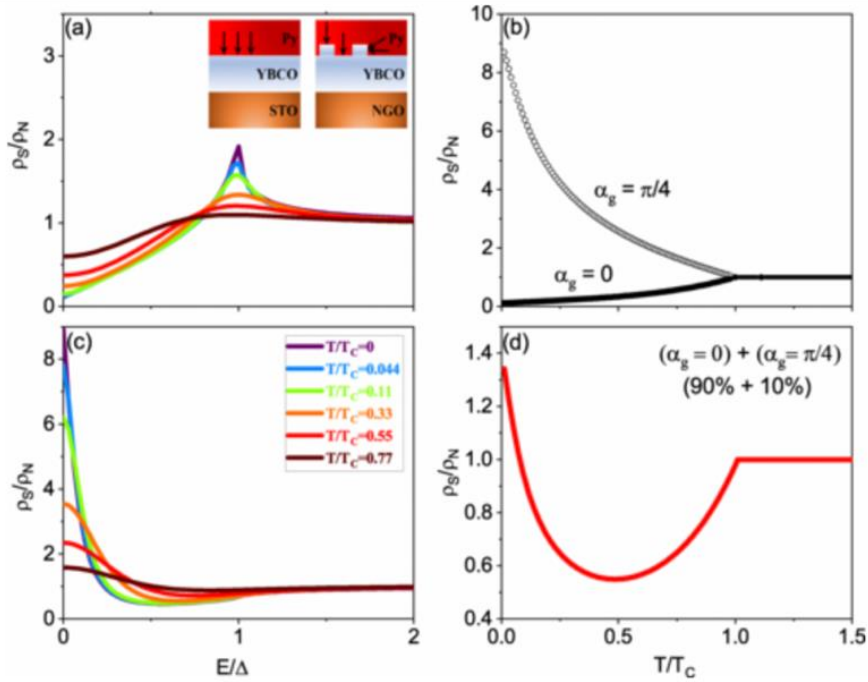


Figure 54 Calculated surface density of states for an interface with (a) YBCO (001) ie $\alpha_g = 0$, (c) YBCO (110) ie and $\alpha_g = \pi/4$ for different temperatures. The inset in (a) shows the possible direction for spin injections depending on the surface orientation on the two substrates STQ (left) or NGO (right). (b) Temperature dependence of the zero energy density of states for quasiparticles injected along the $\alpha_g = 0$ and $\alpha_g = \pi/4$ directions. (d) Surface density of states for quasiparticles for a ratio 10%/90% contributions of respectively the $\alpha_g = \pi/4$ and $\alpha_g = 0$ orientations.

This final example presented the study of a *d*-wave superconductor/ferromagnet interface and how a BTK-related analysis allowed me to compute the densities of states at the surface of the *d*-wave superconductor for two distinct crystallographic orientations. These calculations made it possible to understand FMR experiments.

3.4 CONCLUSIVE REMARKS

In this chapter, I have discussed the superconducting proximity effect from the Andreev-reflection perspective. I have used the general case of an interface between a metal and a *s*-wave superconductor to illustrate how the BTK model allows describing the transport across it as a function of the interface transparency. I have also shown how this model was extended to the case of *d*-wave superconductors by Tanaka et al. This model will be used to analyze some of the experiments I will describe in the next chapters. I have detailed how I applied the model to different experiments carried out in my group, in which the analysis I performed contributed to understanding different physical effects. These span from the superconductivity-related enhancement of tunnel electroresistance and memristive effect in cuprate/metal junctions (YBCO/MoSi) [168], the emergence of interfacial superconductivity in cuprate (LSCO) /ferroelectric junctions [7], to spin pumping effects in cuprate/ferromagnet

interface [8]. These three cases illustrate how the generalized BTK theory could help in understanding complex physical phenomena with a simple but efficient model.

4 GENERAL FABRICATION, CHARACTERIZATION, AND MEASUREMENT METHODS

In this chapter, I will introduce the main experimental tools I used to fabricate, characterize, and measure my samples. These samples, as we will see, follow mainly two geometries that I will detail here. In the first section, I will detail the fabrication steps used for planar junctions while the second will be dedicated to vertical junctions. These correspond to different approaches to study superconducting heterostructures made with 2D materials and d -wave superconductors. I will then present the main characterization methods I used to check the materials' quality. Finally, I will introduce the transport measurement setups I used to measure my samples' electrical properties at low temperatures and under an applied magnetic field.

4.1 FABRICATION OF PLANAR SUPERCONDUCTING DEVICES

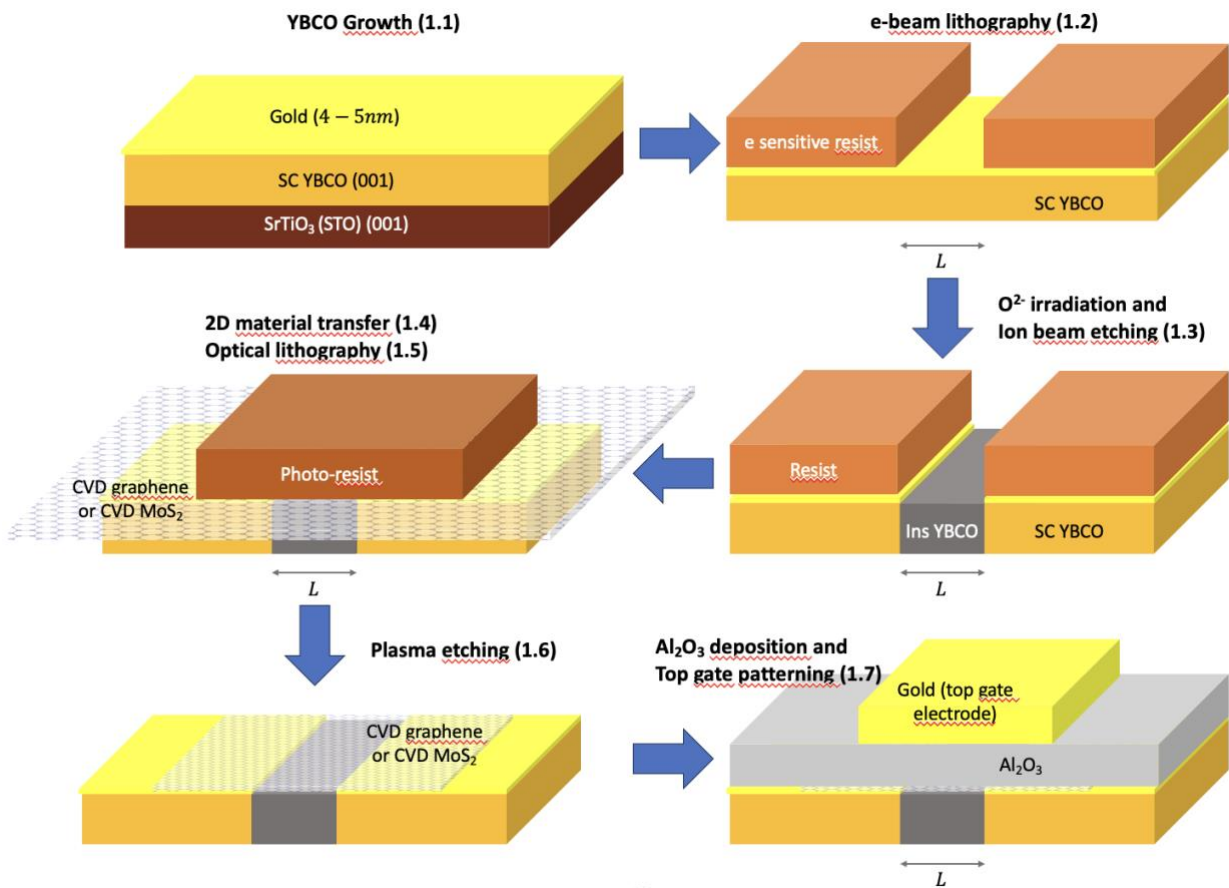


Figure 55 Simplified fabrication process of a superconducting planar junction with the main steps mentioned in their corresponding section. The STO substrate is not represented except in the first scheme.

The goal of my PhD is to study the coupling between d -wave high- T_c superconductor and

2D materials. I used a superconducting oxide, $\text{YBa}_2\text{Cu}_3\text{O}_7$ (YBCO), whose electrical properties dramatically depend on the way it has been grown, especially its doping level in oxygen and its crystallographic axis as we have seen in chapter 2, as well as 2D materials which require specific conditions to handle. Contrary to the coupling between 2D materials and low- T_c superconductors [127,129,177], **it is not possible to grow the oxide superconductor on top of the 2D material**. Instead, we had to develop a method to **deposit the 2D material on YBCO with the best electrical contact possible**. This difficulty implies a complex and long fabrication process.

Following the schematic plan given in Figure 55, I will describe the fabrication process generically called “**masked ion irradiation**”. The main idea is that the superconducting circuit is not etched out of a thin film, but instead, is written using ion irradiation to pattern insulating regions to allow the deposition of 2D materials. This approach is composed of the growth of the YBCO film, the electron-beam lithography followed by the ion irradiation, then, the etching and cleaning of the surface before the transfer of the 2D material and its patterning and finally the fabrication of the top gate electrode.

4.1.1 Step 1: Growth of the superconducting thin films

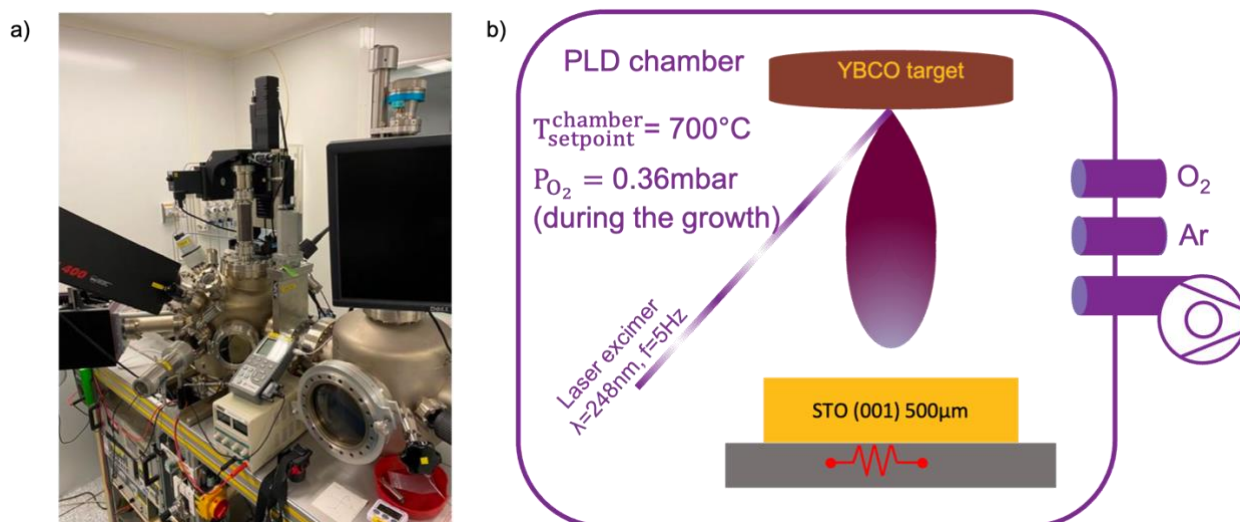


Figure 56 a) Photograph of the PLD setup used for the growth of YBCO thin films. b) Simplified scheme of the PLD chamber and some of the main parameters for the growth of YBCO.

To grow YBCO, we use pulsed laser deposition (PLD) as shown in Figure 56a. A simplified scheme of this deposition technique is sketched in Figure 56b. This method relies on the evaporation of a target locally heated by intense laser pulses. Atoms are ejected in a plasma that forms a “plume” (of the shape of a feather), which results from the high-energy atoms interacting with the reacting gas inside the chamber. Atoms deposit on the surface of the heated substrate in front of the target. Many parameters are at stake to grow high-quality thin films: the laser wavelength, the repetition rate of the pulses, the oxygen pressure (in the case of an oxide), the substrate temperature,... [178]. This method allows us to grow high-quality YBCO films, having an epitaxial structure, and which T_c dramatically depends on both

the growing and cooldown condition, with particular attention to the O₂ partial pressure during and after deposition as well as the cooling down speed, as we will see below. To fabricate our planar geometry samples, we grew c-axis YBCO (written also YBCO (001)). We use SrTiO₃ (STO) (001) substrates. This material allows for the epitaxial growth of YBCO due to their small lattice mismatch. The films are grown with an excimer laser ($\lambda=248\text{nm}$). After pre-ablating the target, the growth occurs under an oxygen pressure of 0.36mbar and by setting the holder temperature at 700°C [8,179]. During the cooldown, an oxygen pressure of 700mbar is maintained to obtain optimally doped crystals. To maximize homogeneity, the substrate rotates during the growth to allow the pulses to reach different areas. The target is pre-ablated just before the growth, using the same growth parameters as those set for the sample. All these precautions guarantee the reproducibility of the quality of the films.

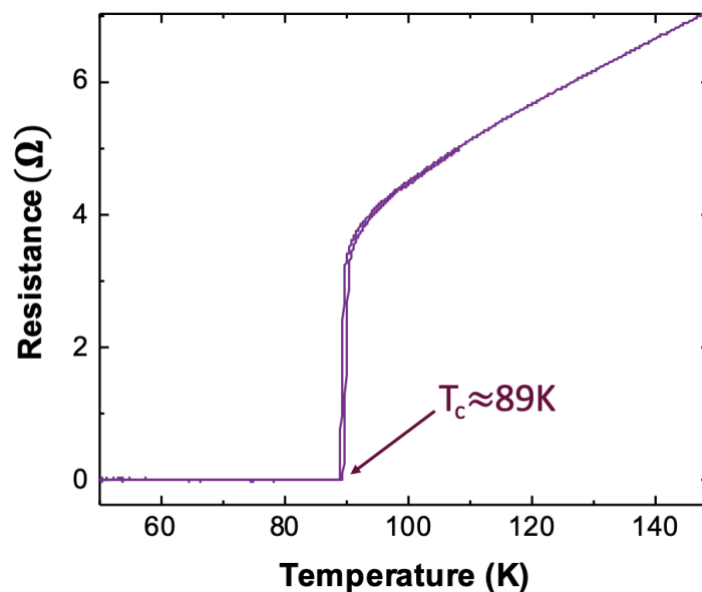


Figure 57 Resistance versus temperature of a typical YBCO thin film (50nm) with an applied current of 10 μ A.

In this manuscript, except when mentioned otherwise, the films are 50nm-thick YBCO (001). They have been grown either by Anke Sander, Santiago Carreira, or Javier Briatico. A thin layer of gold or platinum (from 5 to 50nm) may be deposited in situ by PLD directly onto YBCO after cooling down at room temperature. **This layer serves both to protect the first top unit cells of YBCO and also to improve the electrical contacts with other materials [180].** This layer cannot be too thick (compared with the mean free path in the metal) to get a proximity effect between YBCO and the 2D material. Therefore, either we grow a thin layer (between 4 and 10nm) or we grow a thicker layer that is subsequently etched via ion beam etching (see 4.1.3) to ultimately obtain a thin one. The former will give a continuous but more granular film than the latter. During my PhD, I mainly chose the first path since the presence of grain on the gold film has been shown to reduce the contact resistance [181,182]. A typical plot of the resistance versus the temperature of one of our films is given in Figure 57. The superconducting transition temperature is generally around 89K at the beginning of the fabrication process. Let's notice at this point that the multiple steps and chemical treatments can alter the superconducting properties. However, we

checked that, in the case of planar junctions, the fabrication procedure does not depress the superconducting T_c of the contacts below 80K.

4.1.2 Step 2: Electronic lithography patterning of irradiation mask

To allow superconducting coupling between the electrodes of the planar devices, the length L of the junctions has to be submicrometric. Indeed, as we will see in chapter 6, to have a coupling between the electrodes, the Andreev electron-hole pairs have to keep their phase coherence so the length L between the electrodes has to be at most a few ξ_N , the coherence length of the normal material. For CVD graphene, for example, ξ_N is a few hundreds of nm [14,183,184]. This resolution is not achievable by optical lithography but it is easily achieved by electron-beam lithography (EBL). The latter technique consists of exposing an electron-sensitive resist with a focused beam of electrons that scans the sample according to a predefined pattern. Using EBL, it is theoretically possible to achieve sub 10nm resolution while using a 100keV e-beam apparatus coupled with suitable substrates and resist. This limitation is not set by the beam radius, but rather by the diffusion of electrons in the resist or the production of secondary electrons by the substrates [185]. However, in our process, another difficulty arises from the use of very thick ($\sim 600\text{nm}$) resist necessary for patterning YBCO by oxygen ions irradiation (see section 4.1.3). Let us note that, when dealing with non-conductive substrates or with really thick resists, the charges of the incident electron beam build up atop the resist and cannot be expelled on the timescale of the lithography and this strongly reduces the resolution.

The first step consists in designing the titanium/gold pads, for contacting the sample, and alignment marks by EBL. These marks allow for multiple-level alignments with the EBL, necessary for our process. For this step, we use PMMA (polymethyl methacrylate) A7 with a thickness of the order of 600nm , allowing us to achieve $\sim 100\text{nm}$ resolution. To improve the resolution and allow for evacuation of the charges atop the resist, a thin layer of aluminum ($\sim 20\text{nm}$ -thick) is sputtered atop the resist.

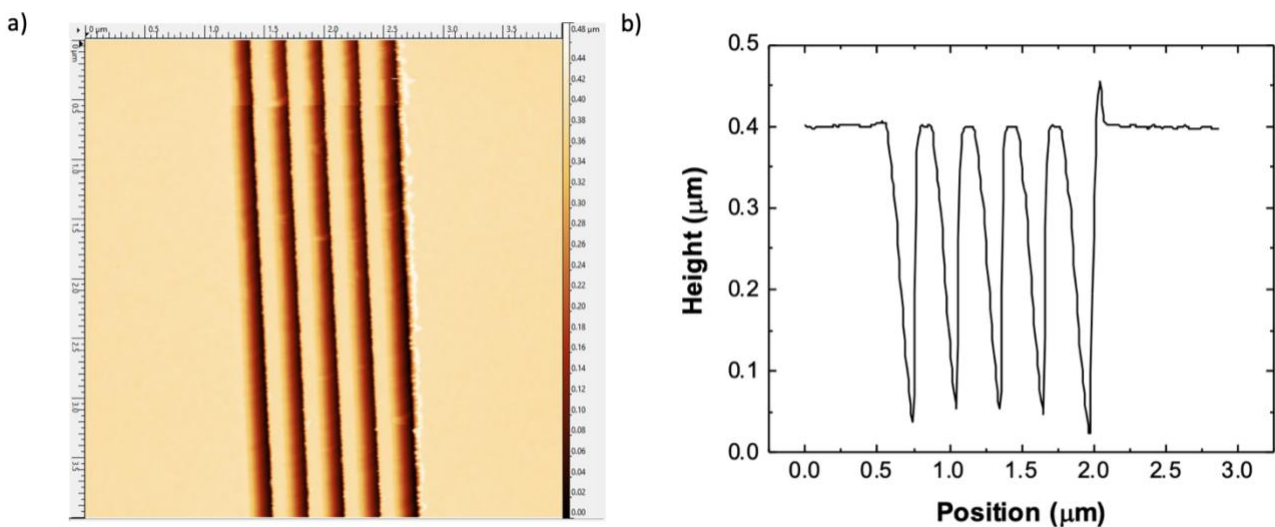


Figure 58 a) Atomic force microscopy picture ($4 \times 4\mu\text{m}$) of five designed-to-be 200nm -wide junctions spaced over 100nm . b) Cut of the picture in a) allowing the measurement of the

effective dimensions after the development of the resist.

After deposition and lift-off, we pattern the superconducting tracks and the junctions (see Appendix). This patterning is then carried out using two beam settings, first with a high current for low-resolution patterning ($>1\mu\text{m}$), using high aperture opening and fast beam scanning speed to increase the patterning speed (typically for the superconducting tracks), and then using a lower current and a thinner beam, with low scanning velocity to achieve higher precision and define the YBCO/2D/YBCO junctions. The details of the process, performed by Christian Ulysse at C2N are presented in Appendix.

After developing the resist, it is possible to check the achieved lithography resolution by Atomic Force Microscopy (AFM). Figure 58a and b show one of the most challenging patterns we realized which nominally consists of five 200nm-wide junctions separated by 100nm. Even if the AFM tip does not reach the bottom of the hole made by resist, we can infer from this measurement that the size of the junctions corresponds to the drawn pattern, having a size of $(200 \pm 14)\text{nm}$ over the five junctions.

4.1.3 Step 3: Oxygen ion irradiation

Oxygen ions irradiation across the resist masks (defined by EBL), allows to locally make YBCO insulating. It's a crucial step for allowing to deposit of a 2D material on top of YBCO/insulator/YBCO junctions to study the proximity effect at the 2D/YBCO interfaces. **The progressive decrease of the YBCO critical temperature and its increase of resistance, until becoming insulating, depends on the dose of O^+ ions** we use [186–188]. This is due to the disorder created by the ions going through the film. These ions, which are relatively light compared to Y, Ba, and Cu, mainly displace the atoms of oxygen. These new defects are created across the entire thickness of our samples, as the penetration length of oxygen ions at 70keV being around 150nm in YBCO, well beyond the 50nm thickness of the YBCO films, but less than 600nm in the resist. This can be verified by computing the propagation of these ions by Monte Carlo calculations [189] both in the YBCO film and the resist. We voluntarily overdose the irradiation to ensure that the exposed YBCO becomes insulating, using a dose of 5×10^{14} ions per cm^2 accelerated at 70keV. This step is carried out with Yann Legall at iCube, at the University of Strasbourg.

Once the irradiation is done, the superconducting tracks are defined. However, there is still around 5 to 10nm-thick gold or platinum covering the whole sample, electrically shorting the insulating YBCO. Before removing the PMMA mask, I etched this layer with Ion Beam Etching (IBE). This method consists of mechanically etching the surface of the sample with accelerated (300V), non-reactive, argon ions (50mA for a density current on the target around $0.3\text{mA}/\text{cm}^2$). The operation is monitored with a mass spectrometer to check when to stop but it usually lasts less than a minute for 5 to 10nm of metal. For this step, the ion beam is set perfectly perpendicular to the surface in order to reach the bottom of the thin junctions. Indeed, even with the rotation of the sample holder, the junctions are sometimes so thin (100nm) compared with the thickness of the resist ($> 600\text{nm}$) that some metal could stay due to the shadow effect. This metal would short the 2D material deposited during the next step.

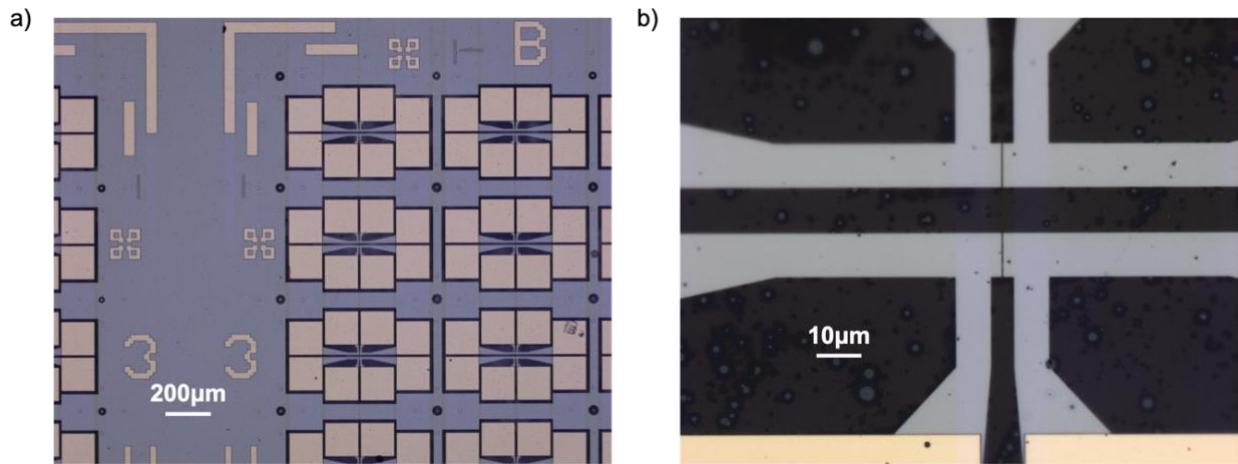


Figure 59 Optical images of a sample after ion beam etching with magnification $\times 5$ for a) and $\times 100$ for b).

We then proceed to the removal of the resist in acetone after having done an oxygen plasma to soften the resist that has become harder after the O^+ irradiation and IBE. Optical images are given in Figure 59 at that stage. In chapter 5, we will keep this metallic layer to probe the proximity effect in the metal instead of the 2D material. An additional optical lithography step will be necessary to protect the metal above the junctions but not the metal that shortens all the rest. For the comprehension of the reader in the whole manuscript, when I refer to a junction a device as "R1739BD C7U", "R" stands for "Real" the name of the PLD chamber, "1739" means it is the 1739th sample grown in this chamber. "BD" is for "Bas Droite" which is translated bottom right. There is also "BG" "Bas Gauche" (bottom left), "HG" "Haut Gauche" top left and "HD" "Haut Droit" top right. And finally, "C7" is the name of the device and since each device has two junctions, we name the upper one U and the lower one D.

4.1.4 Step 4: 2D material transfer

Now the superconducting tracks and the junctions are well patterned, we have to deposit the 2D materials on YBCO. We propose here two distinct methodologies: the wet transfer of chemical vapor deposition (CVD)-grown 2D materials and the dry transfer of exfoliated crystals. These techniques allow the deposition of 2D materials onto patterned gaps, facilitating the investigation of the proximity effect with YBCO. This growth method consists of flowing reacting gas species on a catalytic surface at high temperatures. It starts from the nucleation point and extends, allowing for an almost perfect monolayer when using the right growth conditions [190]. Growth is optimized on specific substrates to increase quality, meaning that we have to transfer the 2D material onto our samples. In this thesis are studied CVD-grown graphene on copper and molybdenum disulfide (MoS_2) grown on sapphire. The chart Table 2 sums up the transfer process in both cases. The transfer method of graphene is relatively standard [191] and has already been used [12,14] but I developed the MoS_2 transfer during my PhD.

Step	Graphene transfer	MoS ₂ transfer
1	Cut with scissors the copper film	Cleave the sapphire with a diamond tip
2	Spin-coat a thick layer of PMMA	Spin-coat a thick layer of PMMA
3	Dissolve copper in diluted ammonium persulfate remove the graphene on the wrong side of copper with clean room cloth wait 1 day in solution	Dissolve sapphire layer with a 4mol/L NaOH solution wait 2 weeks in solution
4	Transfer to water solution using a silicon wafer wait 1 day	Blow the solution with a pipette on the surface to make it separate transfer to water using a silicon wafer wait 1 day
5	Transfer on the sample dry at 70°C for 10 minutes acetone and IPA baths.	Transfer on the sample dry at 70°C for 10 minutes acetone and IPA baths.

Table 2 Comparison between graphene and MoS₂ transfer.

Although the conditions for the MoS₂ transfer seem vigorous, we will see in section 4.3.2 that the Raman spectra is not affected after the transfer.

4.1.4.1 2D material pick-up technique

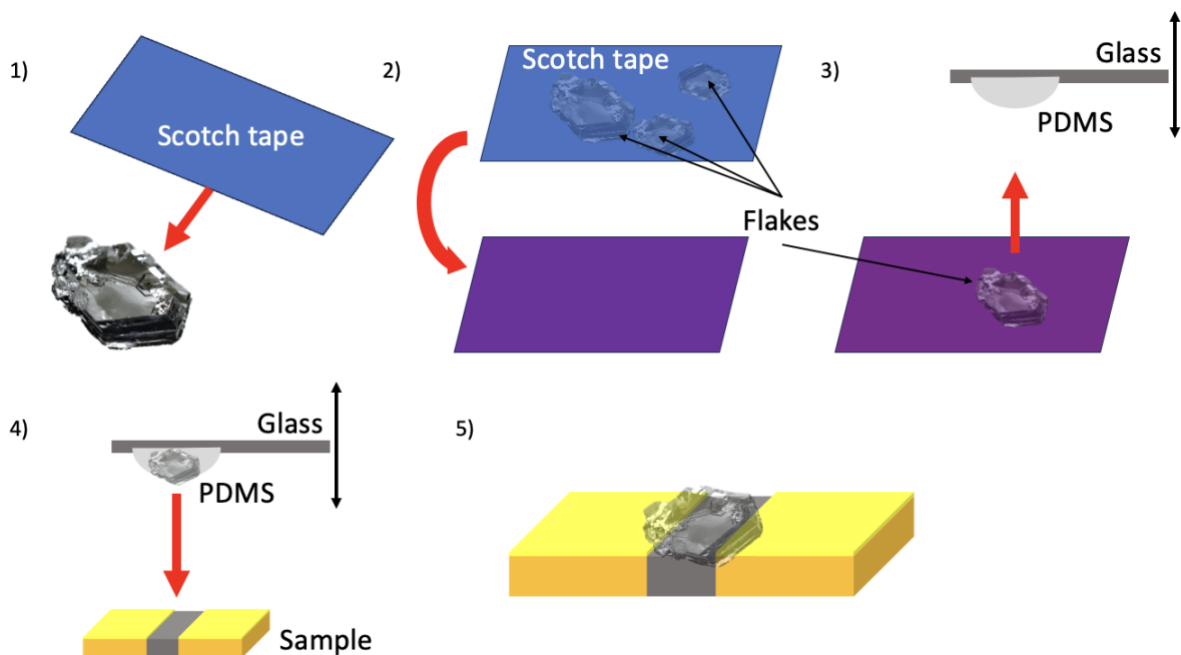


Figure 60 Schematic views of the successive steps of the stamping method for the dry transfer of exfoliated 2D materials.

Numerous VdW materials are available in high-quality crystals that can be exfoliated, allowing tens of micrometer-wide 2D flakes. This allowed us to test to realize our devices by exfoliating directly crystals with the now famous scotch tape technique [39]. Usually, 2D flakes are exfoliated and the superconductor is grown atop after testing the thickness of the flakes. But in our case, as underlined before, it is not possible to grow YBCO atop. Therefore, while using flakes, it is necessary to align them with the existing structures. To allow the superposition of several flakes or to place a flake on a sample, we used a newly implemented pick-up tool to transfer exfoliated flakes from an initial substrate (after the exfoliation) to a final one.

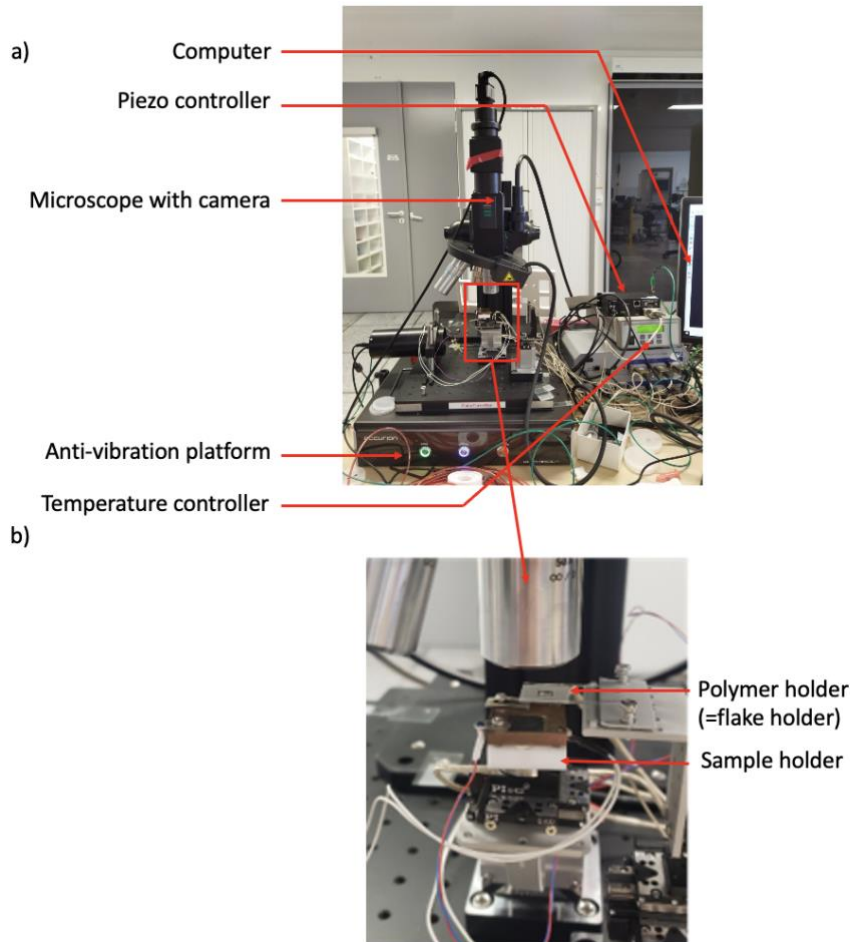


Figure 61 Transfer platform for 2D materials present in the lab. a) Overview and b) zoom on the sample holder and polymer holder that holds the flake to transfer onto the sample.

First, following Figure 60, we exfoliate flakes (1) and transfer them randomly on a Si/SiO₂ substrate (2). Then, we localize the flakes and possibly carry out AFM measurements (see section 4.3.1) to measure the thickness. Then, we use the transfer platform (3) detailed in Figure 61. We set the silicon substrate on the sample holder and stamp the flake with a polymer (PDMS for Polydimethylsiloxane) that we can heat on the polymer holder (see Figure 61b). Then, we replace the silicon substrate with the sample of interest on the sample holder and stamp the flake onto the sample (4). To do that, we approach the two holders, move the sample holder with the piezo controller, and make contact. We heat to expand the polymer and adhere to the surface of the sample and finally, we cool it and drive the polymer

away very gently to keep the flake on the sample. In chapter 7, we will examine some results of this procedure on tungsten disulfide (WS_2) carried out with the help of Julian Peiro.

4.1.5 Step 5: Optical lithography of the 2D material

Once the 2D material is deposited, either in the form of a flake or on a large scale, we have to shape it to follow the existing tracks and avoid short circuits. I did so by optical lithography and plasma etching. The principle is to use a photoreactive resist I exposed with a predefined design. I did it in three different ways: using a physical mask or scanning the sample with a focused laser beam. These two methods are present in the lab but a more versatile, fast, and very easy-to-use method is available: maskless lithography also called optical projection lithography. In each case, the design is made by 2D CAD (computer-aided design) to realize a design that is either reproduced on a mask or directly written onto the sample. It is possible to do several layers of lithography by realigning each step to the ones previously realized. In the specific case of projection lithography, this alignment is done by using the same lens used for the lithography, by adding a filter blocking UV light. Once alignment is done, the chosen system exposes the pattern, either once (optical lithography), by scanning the sample linearly (laser lithography), or by exposing the sample by separating it into writing fields (maskless lithography). Then, the resist is developed and the sample is cleaned in water. The optical lithography recipes can be found in the Appendix.

4.1.6 Step 6: Plasma etching of the 2D material

The patterning of 2D materials, once all the above steps are completed, is delicate. They are indeed sensitive to handle and they can be easily damaged on the scale of the sample, even when protected, when using mechanical etch as IBE, that we described before. Several techniques, specially dedicated to these materials, allowing for precise etching of 2D materials and control over their thickness, have been developed (see Ref. [192] for a review). In our case, I used plasma etching with a Nextral plasma etcher. This etching process relies on creating an oxygen plasma that oscillates thanks to an RF electric field. The energy of the moving ions allows for breaking Van der Waals chemical bounds states and therefore selectively etch most 2D materials. For instance, we etch monolayer graphene with a power of 30W for 30 seconds in an atmosphere of 100sccm of O_2 .

4.1.7 Step 7: Top gate fabrication

At that point, it is already possible to carry out transport measurements. However, in order to protect the samples, and to realize a top gate to change the doping level, we can deposit a layer of alumina (Al_2O_3). Indeed, we saw in chapter 2 that the properties of 2D materials can be easily tuned while applying a back or top gate voltage, by modulating the Fermi level. The top gate in particular usually allows for a bigger change of the Fermi level while using a lower voltage as the electric field E is $E = \frac{V}{d}\sqrt{\epsilon}$ with V the voltage applied, d the thickness of the dielectric and ϵ its dielectric constant and that the thickness of the bottom dielectric is dictated by the substrate used. On the other hand, the top gate requires the growth of a dielectric atop the 2D materials with a thickness typically of the order of 50nm in our case. We chose alumina (Al_2O_3), which has a dielectric constant close to 9 at all

temperatures [193,194], both for realizing the top gate and protecting the used 2D materials during the fabrication process [69].

The alumina is deposited by a combination of e-beam evaporation and ALD. We first grow 0.8nm of aluminum with a homemade e-beam evaporator, using an electron gun to locally warm the target, allowing us to realize a high-quality sticking layer. We then take out the sample, allowing for the Al to naturally oxidize.

The growth by e-beam evaporation of Al, while allowing good quality oxide, is not adapted for thick dielectrics. We therefore use this first layer as a seed layer for atomic layer deposition (ALD) grown Al_2O_3 . The ALD growth of Al_2O_3 is composed of multiple cycles, illustrated in Figure 62, and which can be described as follow [195]: (a) trimethylaluminum is injected and reacts with the surface. The reaction is driven by the strength of the Al-O bond. (b) H_2O is injected into the chamber. It will replace the methyl group bonded to aluminum atoms and we get the exact same configuration as in the beginning at the end of the cycle. (c) This cycle is repeated to progressively add materials and obtain multiple layers.

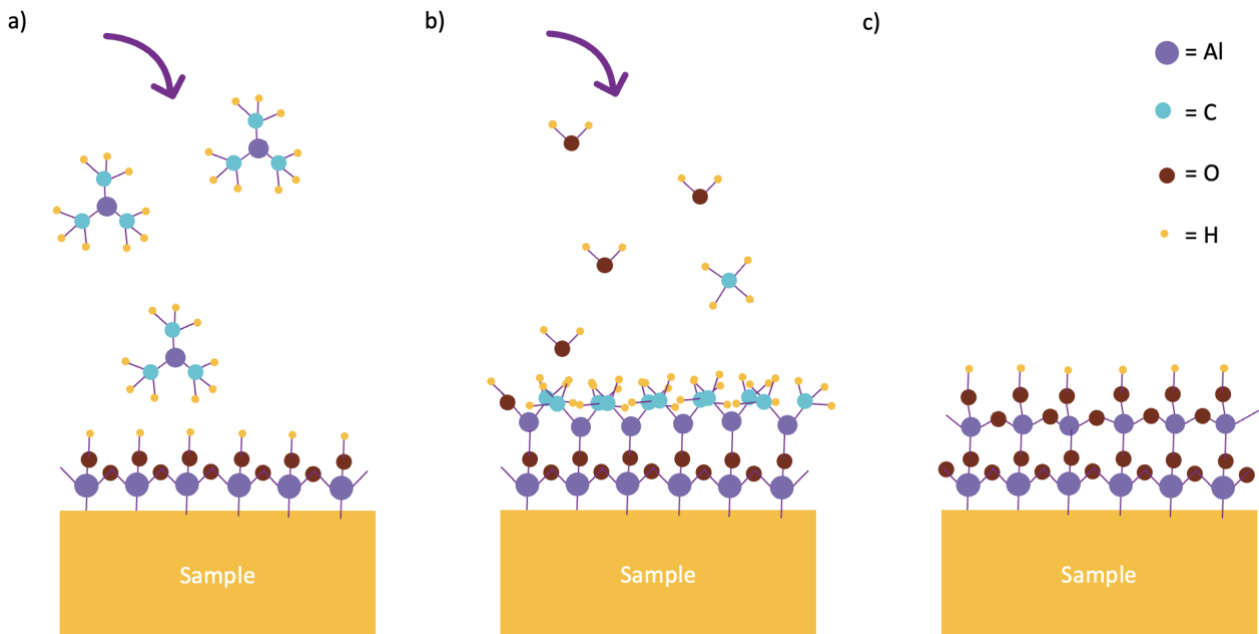


Figure 62 a) First step of the cycle, one injects a pulse of trimethylaluminum (TMA) inside the chamber heated at 200°C . TMA reacts with the surface by replacing the O-H bond with the very solid Al-O bond. b) After injection of H_2O , the methyl groups are replaced by hydroxyl groups on aluminum. c) We are back to the initial state and we can start another cycle.

Once the 2D material is fully covered by amorphous alumina, we pattern the electrodes. Because alumina is sensitive to alkaline solutions that are used for development, we did not use optical lithography for this step as the development will thin this barrier. Instead, we opt for an electronic lithography followed by evaporation of Ti(10nm)/Au(100nm) and lift-off. Figure 63 shows two optical images of a sample after all the fabrication steps. Optimally, there will be 35 devices to measure on such a sample. However, all are not covered with 2D materials. This can be checked by AFM and/or using Raman spectroscopy (see section 4.3.2), allowing us to focus on devices where we are sure of the quality of the transferred 2D

material (see 4.3).

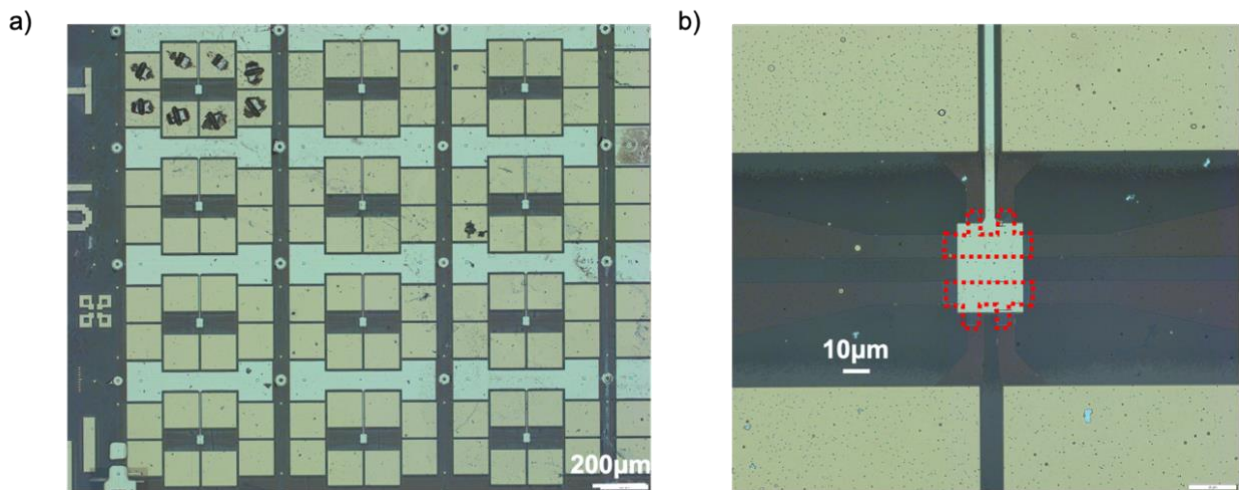


Figure 63 A sample after the whole fabrication process. a) Optical image of several devices (x5) b) zoom (x50) on one single device. The graphene layer is emphasized by the red-dotted contour.

4.2 FABRICATION OF VERTICAL SUPERCONDUCTING DEVICES

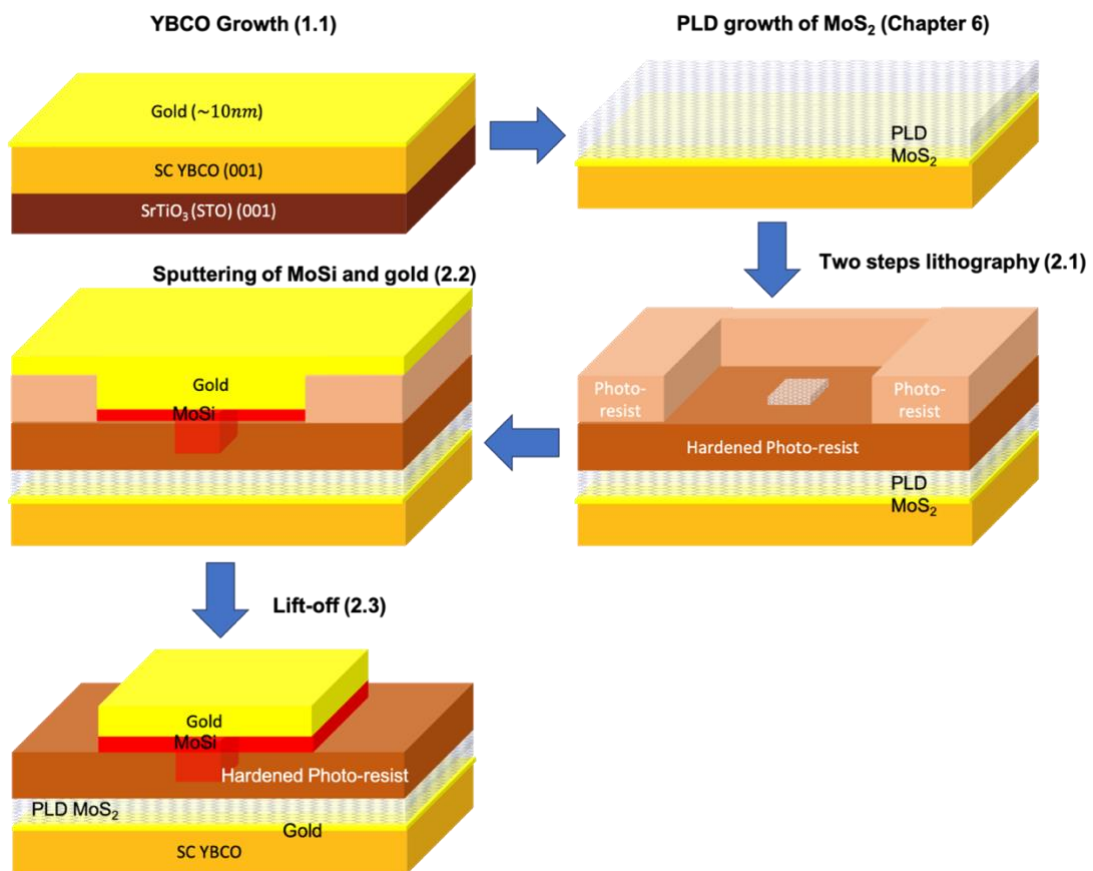


Figure 64 Simplified fabrication process of superconducting vertical junctions with MoS_2 grown by PLD. Each main step is represented with the corresponding part in the manuscript.

During my PhD, I had the occasion to work with another geometry than planar junctions

explained above. I built vertical superconducting junctions to probe the proximity effect between YBCO and MoS₂ grown by PLD as explained in chapter 7. The aim of this structure is to measure the resistance of micrometric devices made of a bottom electrode of YBCO, a top electrode made of molybdenum silicon (MoSi), an amorphous *s-wave* superconductor and MoS₂ in between. In this section, I will detail the fabrication process of these vertical junctions following Figure 64. I start with a bare substrate of STO and the growth of YBCO and the layer of gold (~10nm) is the same as done in 4.1.1. Then, the growth of MoS₂ by PLD and its optimization will be treated in detail in chapter 7. In this section, I will concentrate on the two-step lithography (4.2.1) of the resist apertures, and on the sputtering of the top electrode (4.2.2). Finally, I will comment on the way I wired my sample since there are some specificities (4.2.3).

4.2.1 Two-steps lithography of resist apertures

The bottom electrode and barrier of the junctions are fabricated in **two steps of large-scale PLD deposition**, the first consists of growing YBCO and gold and the second of growing MoS₂. The aim is to measure vertical junctions with a micrometric section (from 1 to 20μm) in order to get sizable resistances, in the range of the instrumental resolution. To do so, the strategy is to deposit micrometric “pillars” of the top electrode, electrically separated from the bottom electrode (except at the junction itself) by an insulating spacer. The used technique consists of using a hardened layer of resist with patterned holes. The resist mechanically stabilizes the pillars and avoids any shortcuts between the different junctions.

To pattern the micrometric square holes, the protocol starts with depositing a 50%-diluted photoresist SU8 onto the sample, followed by a 4000rpm, 60-second spin-coating. Subsequent steps involve a 90°C, 60-second soft bake, UV illumination for square hole patterning using an energy of 60mJ, a 20-second development in MF319 developer, rinsing in deionized water, and N₂-assisted drying. The resist's permanence and durability are achieved through a 180°C, 60-second hard bake, rendering it resistant to illumination, development, and lift-off processes.

Defining the contacts involves a sequential approach: once the sample has cooled, another layer of resist (SPR 700 1.2) is directly deposited and spin-coated at 6000rpm for 60 seconds. This layer is then soft-baked at 90°C for 60 seconds. To facilitate the lift-off process, the sample is immersed in chlorobenzene for 10 minutes, followed by rinsing with deionized water and subsequent drying using N₂.

4.2.2 Sputtering of the top electrode

Sputtering is a physical vapor deposition method employed for the purpose of depositing thin layers of designated target material onto a substrate. By generating a discharge plasma through the application of high DC voltage or an RF source, energetic ions are produced and directed toward the target material, resulting in the expulsion of surface atoms. These atoms subsequently aggregate and eventually settle onto a substrate positioned in close proximity.

I used magnetron sputtering to deposit 50nm of $\text{Mo}_{80}\text{Si}_{20}$ (MoSi) and then 50nm of gold. Here, the vacuum chamber is filled with low-pressure Argon (Ar) gas, followed by the application of high DC voltage between the target material (functioning as the negative pole) and the chamber wall (acting as the positive pole). This electrical configuration generates an electric field around the target, leading to the ionization of Ar gas and the consequent formation of Ar^+ ions. These ions will then collide with the target surface. If the energy carried by these ions exceeds the binding energy of the target atoms, the atoms are expelled from the target, creating a plasma in the chamber. This plasma then condenses onto the sample surface, resulting in the deposition of a fine layer of the target material. To localize the plasma in the vicinity of the target, a strong magnetic field is positioned behind the target material. This arrangement amplifies the plasma density close to the target, which enhances the deposition rates. It also serves to shield the substrate and the remaining chamber components from undesired interaction with the plasma. Figure 65 shows a depiction of the deposition chamber and a schematic representation of the process.

Once the deposition is finished, the sample is bathed for 20 minutes in acetone. We then submit it to a flow of acetone until the metal has lifted off. Finally, we clean the sample in ethanol and dry it with nitrogen.

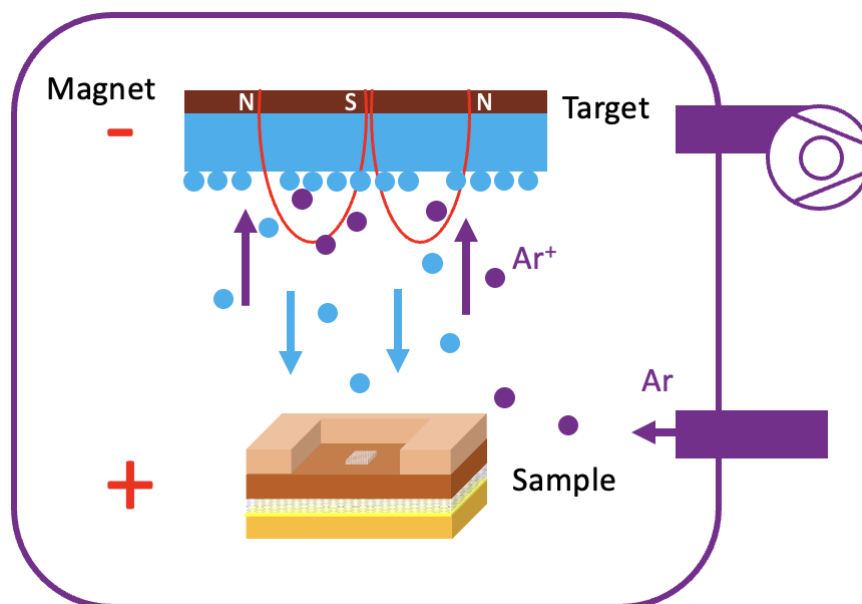


Figure 65 Scheme of the magnetron sputtering setup.

4.2.3 Specificities of the wire bonding in the case of the vertical junctions

Wire bonding is used both for planar and vertical junctions. In the lab, our bonding machine allows for the use of gold or aluminum wires. For planar junctions, I used exclusively gold wires to avoid the deoxygenation of YBCO by the aluminum wires. To measure the resistance of the vertical junction, I have to connect wires at the top electrode on the patterned contacts but also at the bottom electrode. This is made difficult since I deposited a layer of hardened resist. Therefore, I have to scratch the surface to access the layer of YBCO and connect it with a wire. I have done this on the four corners of the sample and I then bonded and added

some silver paste to improve the electrical contact and its durability. These bonds are made with gold wires since they are in direct contact with YBCO. The contacts of the top electrodes (gold/MoSi) can be done either with gold or aluminum wires. A picture of a sample glued on a chip and bonded is given in Figure 66.

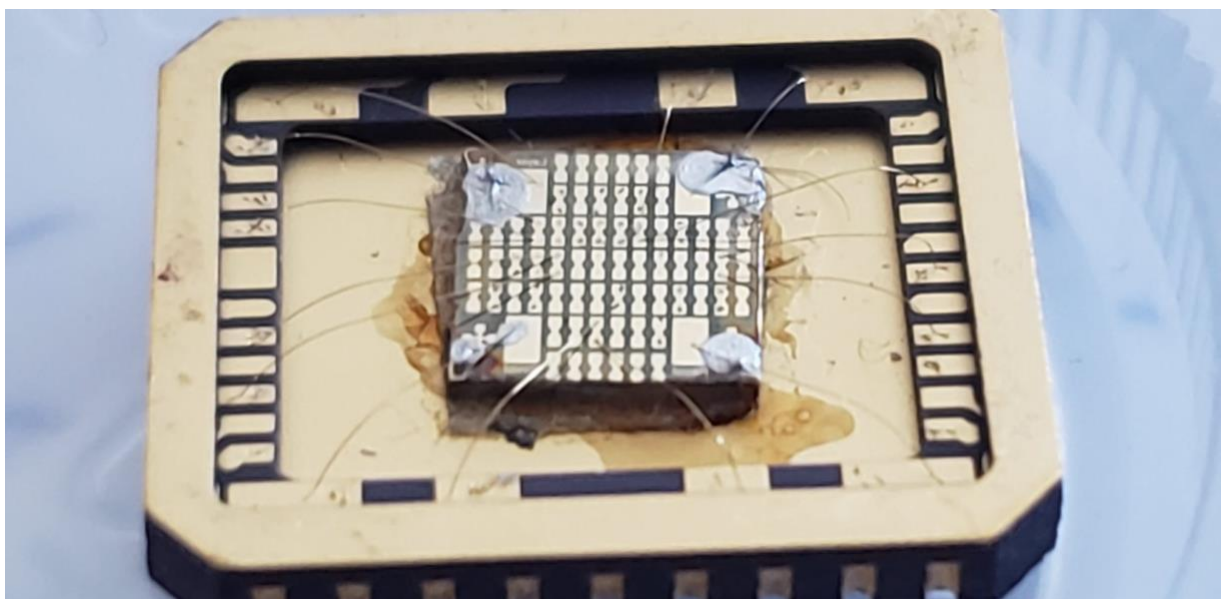


Figure 66 Sample glued on a chip. At the four corners, a wire is bonded with silver paste to contact the YBCO layer above.

4.3 MATERIALS CHARACTERIZATION

I studied 2D materials from different origins: exfoliated, CVD- or PLD-grown. These materials have to be properly characterized. Moreover, all over the fabrication process, it is necessary to check whether the previous steps were successful or not and whether the quality of each material has been conserved. We will first describe atomic force microscopy and then Raman spectroscopy, which is a precious tool to study 2D materials.

4.3.1 Atomic force microscopy (AFM)

Atomic Force microscopy (AFM) is very useful in many aspects during the fabrication process. **It allows to characterize the surface topography of a sample, its roughness, and its thickness, or to check some lithography steps.** AFM uses a tip, whose end is chemically etched to be as thin as a single atom, placed at the extremity of a cantilever as pictured in Figure 67a. We used AFM in the tapping mode, for which the tip is placed atop the sample and the cantilever is set to oscillate close to its resonance frequency. The motion of the cantilever is monitored through the reflection of a laser on a photodetector. The interaction between the extremity of the tip and the surface perturbs the motion of the cantilever, changing the amplitude and phase. Finally, a feedback loop maintains the amplitude of oscillations constant by modifying the height of the tip above the sample. This mode is particularly adapted to determine the topography of the sample because it is non-invasive. We can have access to the topographic profile of the surface line by line (Figure 67c) as the tip scans the surface allowing us to draw a 2D map (Figure 67b). We used this technique to

measure the thickness of 2D materials down to the monolayer and to check the correct development of the resist after our lithography steps.

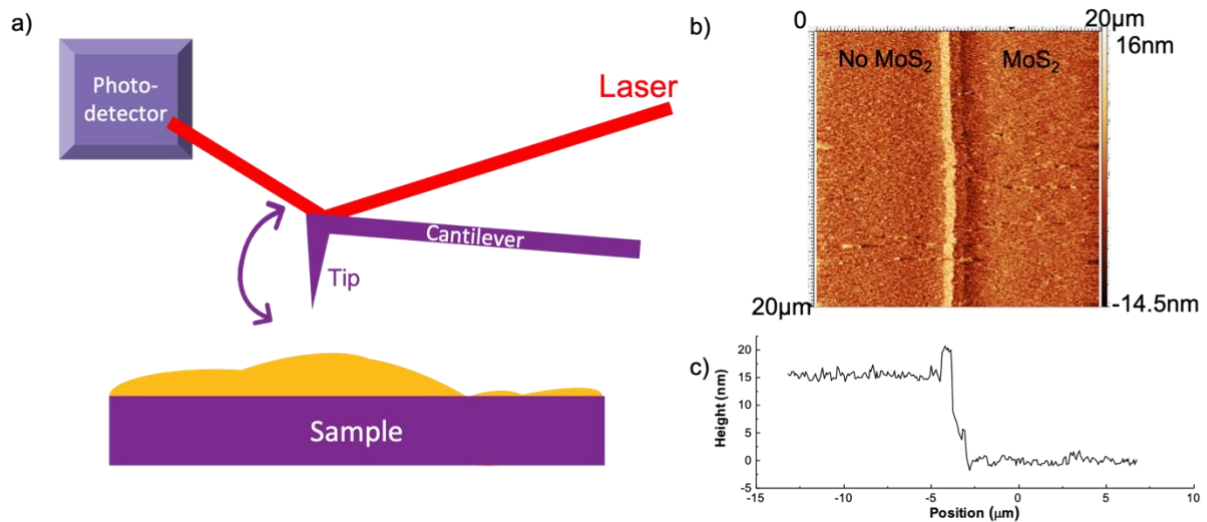


Figure 67 a) AFM principle scheme. b) 2D topographic AFM image ($20 \times 20\mu\text{m}$) of a step. c) Horizontal cut of the 2D map. The step between two distinct regions is clearly visible.

4.3.2 Raman spectroscopy

Contrary to bulk materials, 2D materials are sometimes hard to observe both by optical microscope and AFM as they can be as thin as a single layer. I therefore used Raman spectroscopy to **determine the presence or not of 2D material between the gaps of my junctions and get information on their quality**. This technique is based on the interaction between the coherent light of a laser, focused through a microscope, and the lattice vibrations of the material as the photons interact with the lattice and are reflected, absorbed, or scattered. During the measurement, the laser shines the surface and the scattered photons exiting the sample are diffracted with a grating. The inelastically scattered photons are detected in a detector, giving the Raman spectrum, while the elastically scattered ones are mostly stopped by a chromatic filter. The measured variations of the light wavelength are due to the exchange with phonons of the lattice, with the photons having lost energy constituting the Stokes part of the spectrum (the most studied and the one presented in Figure 68) while the ones that gained energy constitute the Anti-Stokes part.

As different materials have different lattice parameters and phonon structure (due to different symmetries, atoms...), Raman spectroscopy is a very convenient tool to recognize 2D materials as each material has a particular spectral signature [196–198]. In addition, it allows for **inferring the thickness, up to a few layers, of 2D materials** as early shown for graphene [199] and for WS₂ [22].

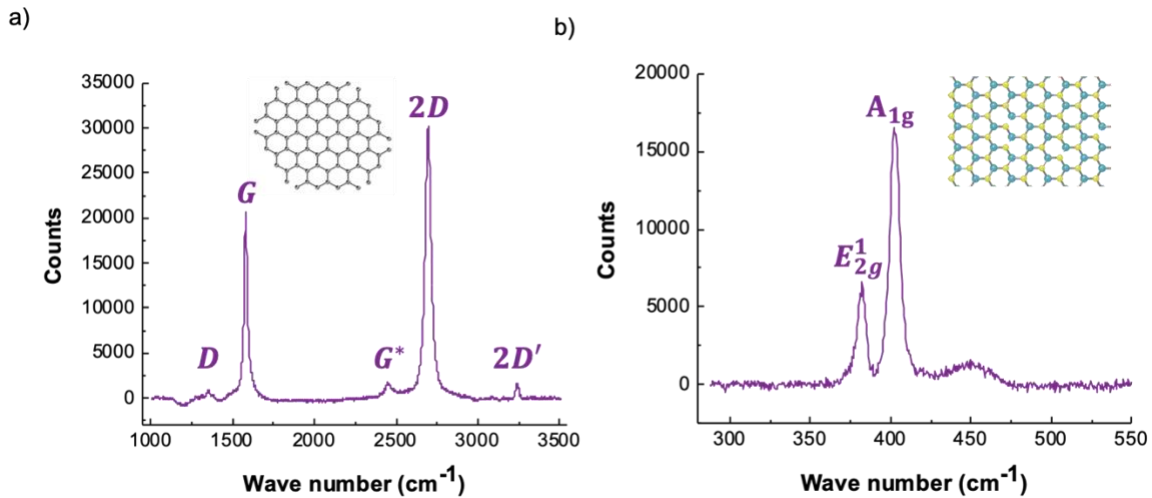


Figure 68 Raman spectra of a) CVD monolayer graphene on silicon oxide and b) CVD monolayer MoS₂ on sapphire.

Figure 68 shows the Raman spectrum I measured for both graphene and MoS₂. We can see for graphene (a) the characteristic peak *G* (around 1500cm⁻¹) common to all graphitic structures while the *2D* peak (around 2700cm⁻¹) is characteristic of graphene. The ratio between the two allows to determine the thickness of graphene [199]. The peaks *G** and *2D'* are present even in perfect graphene monolayer while the peak *D* (~1300cm⁻¹) comes from the present of defects. In our case, this peak is particularly small testifying to the high crystallinity of our CVD graphene. In the case of MoS₂ (b), there are two characteristic peaks *E*_{2g}¹ (~380cm⁻¹) and *A*_{1g} (~405cm⁻¹). Their distance and the ratio between their amplitudes allow to deduce the number of layers as we will see in chapter 7.

4.4 TRANSPORT MEASUREMENTS

To study the proximity effect, I have to measure transport properties from the critical temperature to the lowest temperature we can reach with our cryostats. Indeed, most of the effects I studied, such as proximity and coherence effects, while starting at nitrogen temperature, are easier to characterize when the temperature is decreased. As we will see in 4.4.1, the cryostat from Cryogenics[®] we used is well suited for our measurements at low temperatures and with a magnetic field. We will first present the general working principle of this cryostat and we will discuss the electrical measurements in a second section.

4.4.1 Cryogenic system and magnetic field control

Though we have a few cryostats at our disposal, the results of this thesis were mainly measured on a Cryogenics[®] cryostat. This cryostat is a helium closed-cycle cryostat using a cryocooler, connected to a Helium compressor whose temperature is regulated by exchange with a chilled closed loop circuit.

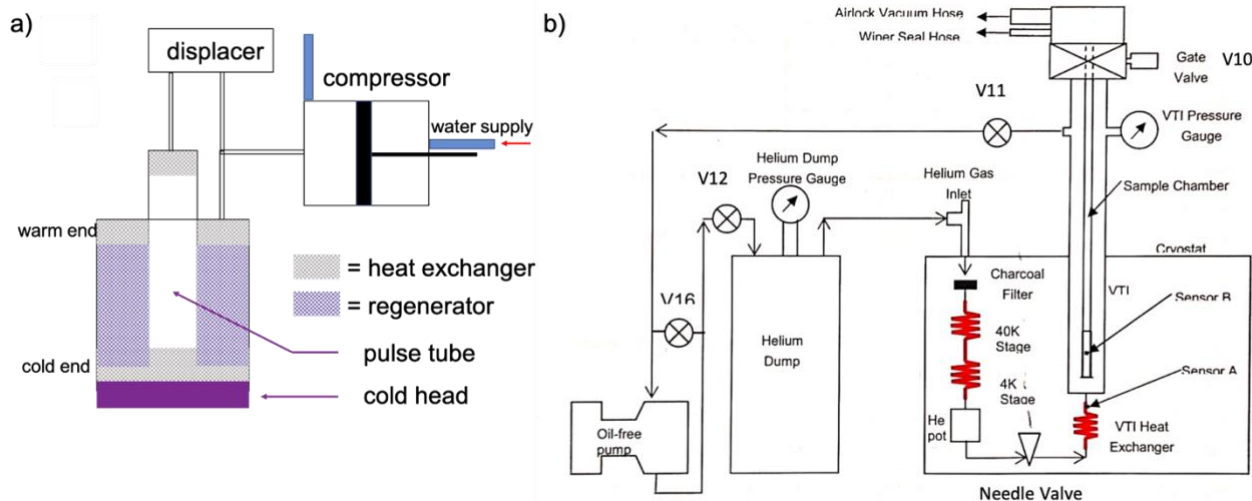


Figure 69 a) Schematic view of a pulse tube cryocooler. b) Schematic diagram from the manufacturer to describe the circulation of gas for cooling the samples.

This system is cooled by a cryocooler represented in Figure 69a. It is a Helium-based thermodynamic machine made to reach low temperatures (below 4K) and composed of a deformed compressor that brings the mechanical work, a displacer whose only aim is to increase the Carnot efficiency and the pulse tube. The operation of a pulse tube is a cyclic process: the compressor pressurizes helium and sends it into the pulse tube. Helium enters the hot heat exchanger, where it releases heat, causing it to cool down and expand. The expanded helium then moves into the regenerator, where it absorbs heat from the regenerator material and cools even further. This cooled helium enters the cold heat exchanger, where it is further cooled down, and it creates a low-temperature environment at the cold end. The gas returns to the pulse tube's warm end, where the process repeats. The cold head, in contact with the cold end through the cold heat exchanger, maintains cold the inside of the cryostat, isolated from the outside by a vacuum shield, containing two stages and the superconducting magnet.

Figure 69b helps to understand how the sample gets cold inside the variable temperature insert (VTI) and how its temperature is regulated. Another closed cycle of helium is circulating thanks to an oil-free pump. It gets through the two stages maintained cold by the cold head and arrives at the helium pot. The helium pot and the VTI are connected through a tunable needle valve adjusting the pressure inside the VTI. The VTI temperature is primarily controlled by the pressure of helium via the $P(T)$ curve of helium and it can also be adjusted by a resistor that will warm helium.

The cryostat has a superconducting magnet (able to reach going from $\pm 9T$ at 1T/min). Superconducting coils are not limited by Joule heating and can therefore achieve fields limited only by the critical current and field of the superconductor. Following the scheme in Figure 70, the circuit is made of a part outside the cryostat with copper wires connected to the power supply. This external part is connected to superconducting wires inside the cryostat. It is possible to keep the stored energy LI^2 (where L is the inductance of the wires and I the current) in the superconducting magnet without sustaining a current by using a

superconducting switch which can be thermally switched ON and OFF.

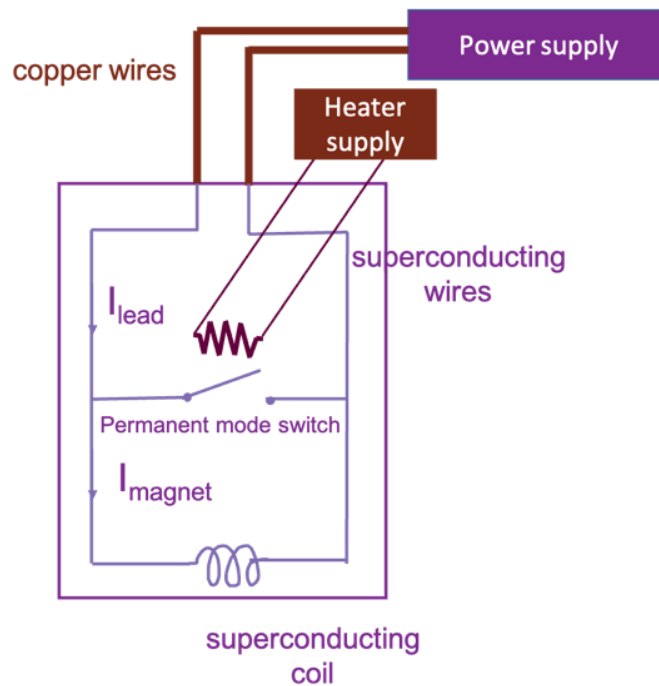


Figure 70 Simplified scheme of the superconducting magnet in the Cryogenics© system.

To illustrate the way it works, let us consider that the magnet is at a given field in the permanent mode. This permanent mode means the switch is on (the switchable region is superconducting) and the current I_{magnet} makes loops with almost no dissipation and the field is particularly stable. In that case, the current I_{lead} and I_{magnet} are completely independent and the lead current can be set to zero. When we want to change the magnetic field, we have to ramp the lead current to the same value as the one in the superconducting loop. When this is the case, we turn the switchable region into the resistive state. Now, we can ramp again the current but this time with a rate below the maximum rate to avoid quenching the magnet that is to say breaking the superconductivity in the wires. When the desired value is reached, we cut the heater and the switchable region will be back to its superconducting state. We can then ramp the current in the leads back to zero.

4.4.2 Electrical measurements

As shown in the following chapters, the resistances of the devices measured in this thesis span several orders of magnitudes, from $\text{m}\Omega$ to $\text{G}\Omega$. For resistance less than $100\text{k}\Omega$, I use a stable current source (Keithley 6221) to inject current while measuring the voltage with a nanovoltmeter (Keithley 2182) as shown in Figure 71a. The impedance of the nanovoltmeter is limiting the upper range of measurable resistances. For resistances higher than $100\text{k}\Omega$, I voltage bias the device and measure the currents with an electrometer (Keithley 2635) while applying a gate if necessary with the Keithley 2450 as shown in Figure 71b.

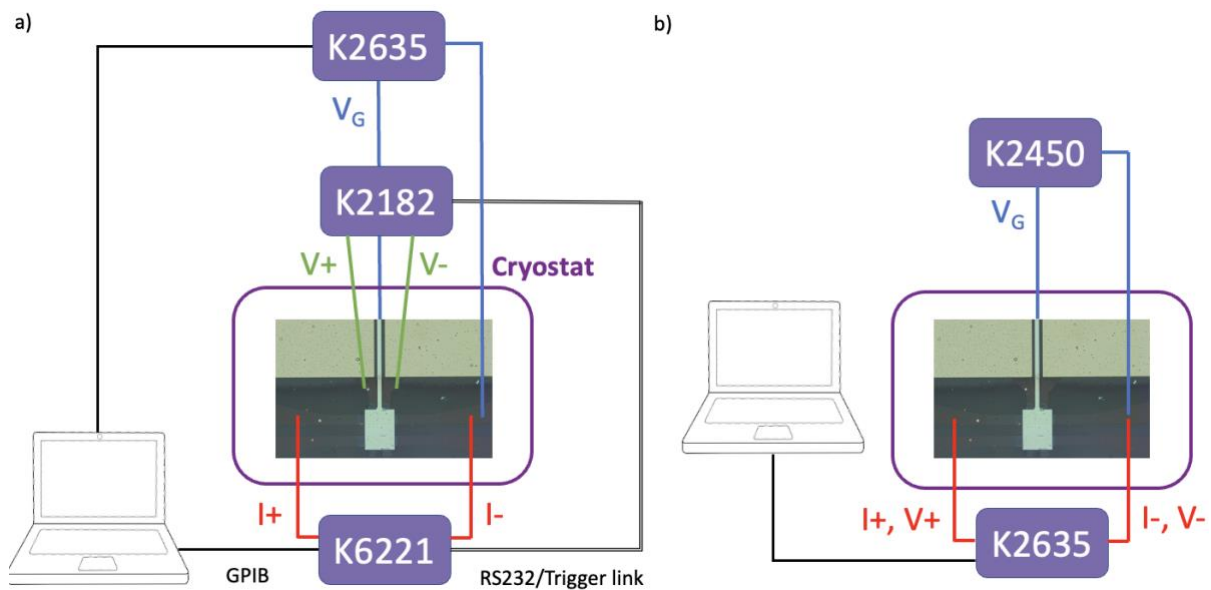


Figure 71 Electrical configurations a) in the delta mode for current biasing with the Keithley 6221 and 2182 (the K2635 is used to apply a gate voltage) and b) in voltage biasing with the Keithley 2635 (the K2450 is used to apply a gate voltage).

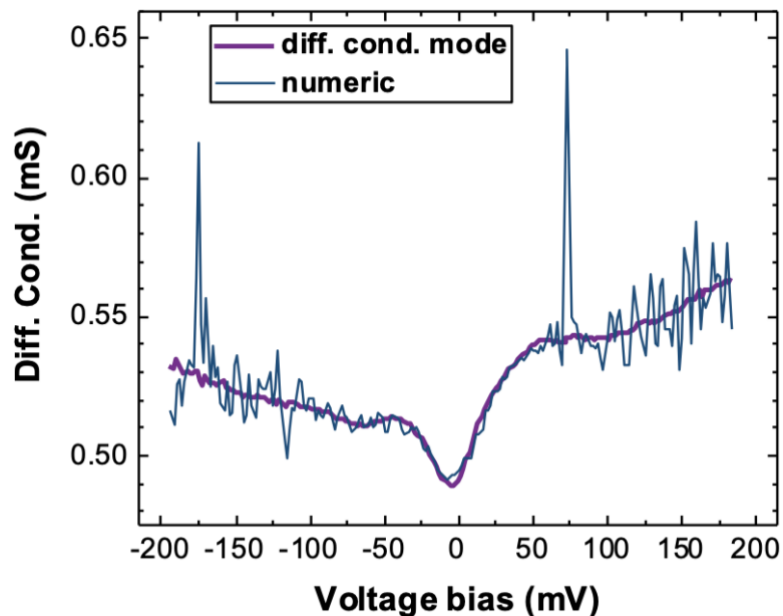


Figure 72 Comparison between the numerical derivation of the differential conductance (dark blue line) against the differential conductance mode from Keithley (purple line).

Coupling the K6221 and K2182 allows for measuring resistances below $100\text{k}\Omega$ by applying the current and measuring the voltage when ramping an external parameter (temperature, magnetic field, gate voltage...). It also allows to use of an optimized mode by the manufacturer as illustrated in Figure 72. In the first case (dark blue plot), the current is ramped and the voltage is measured at each point. The differential conductance is then computed numerically. In the second case (purple plot), the current is ramped in a slot way and the measure is averaged over several points. This is set by choosing a step dI from I_{start} to I_{stop} , allowing to access the "Differential Conductance" of the sample without

communicating with the computer to gain speed [200]. It uses an extra parameter called δI that we can fix to a few times the step dI for best results. The instruments will compute the differential resistances for the values of the current: $I_0 = I_{start} + n \times dI$ with the formula:

$$\frac{dV}{dI}(I_0) = \frac{V(I_0 + \delta I) - 2V(I_0) + V(I_0 - \delta I)}{4\delta I} \quad 4.1$$

For very resistive junctions (100k Ω), I used another setup to measure the differential conductance in a 2-probe configuration as shown in Figure 71b. The signal is generally noisier both because it is a numerical derivation and because for large resistances, the currents circulating can be very small (< 100nA) and then the noise will be more visible.

4.5 CONCLUSIVE REMARKS

We have seen in this chapter the most important steps in the fabrication process of the samples of this thesis in 4.1 and 4.2. We examined the main tools we have to characterize the different materials we deal with in part 4.3. Finally, in 4.4, we focused on the low-temperature transport measurement setup and how the electrical measurements were done.

5 PROXIMITY EFFECT IN YBCO/METAL PLANAR DEVICES

While this thesis ultimately focuses on the superconducting proximity effects between YBCO and 2D materials, studying analogous YBCO/metal junctions seems an elementary first step to characterize the propagation of *d-wave* superconducting correlations in a simpler case, and to establish a comparison point for the ulterior experiments with the more complex 2D materials. Moreover, this study is helpful to understand experiments with 2D materials because a thin layer of metal has to be intercalated between them and YBCO to protect the YBCO surface and improve the interface transparency [12,180].

In the first part of this chapter, I will present results on single interface junctions made of YBCO and gold and show the effects of the induced *d-wave* order parameter at the interface as well as how it affects the pairing symmetry in the proximized material. Finally, I will present results on two interfaces (YBCO/Au/YBCO) superconducting junctions with a bridge of gold.

5.1 STUDY OF SN JUNCTIONS

5.1.1 Geometry of the samples

One of the simplest systems to study the induced superconductivity in gold by YBCO is in a vertical or side SN junction as done extensively in the literature [91,92,106,201,202]. In our case, we made a planar SN junction to study how this geometry may affect the properties of the interface and how superconductivity is propagating in our channel. The geometry presented in Figure 73c corresponds to a continuous thin layer of gold (10nm thick) lying on one side above superconducting YBCO and on the other side on insulating YBCO. My hypothesis is that gold on top of the superconducting YBCO is proximized with a *d-wave* symmetry due to YBCO's order parameter. I want to study the "junction" between this proximized gold and the gold above the insulating YBCO. This system is interesting in the sense there is no material change between the two sides of the junction, the only difference being that **the gold layer on the left of Figure 73c is proximized by YBCO. Thus, there should be no Fermi level mismatch neither strong scattering nor the S (proximitized Au) / N (not proximized Au) interface, since it is the very same material on the two sides of the junction. That is, we expect a very transparent interface. All of the above justifies the designation of "SN junction" even if the proximized gold is not an intrinsic superconductor.**

The geometry of the electrodes is shown in Figure 73a and b. The highlighted blue part (false color image) corresponds to the gold on top of the insulating YBCO. All the junctions presented in this chapter have been measured in a 4-probe configuration with the injected current bias (between I+ and I-) and voltage measurement (between V+ and V-) set as displayed in Figure 73a. The measurements were carried out in the so-called "delta mode" using the K6221 and K2182 as explained in chapter 4.

As shown in the zoomed picture in Figure 73b, the voltage probes are placed a few microns from the proximized Au (S) / not proximized Au (N) interface (yellow/blue in Figure 73c), on

both sides of it. The placement of the electrodes is illustrated on the sketched side-view in Figure 73c.

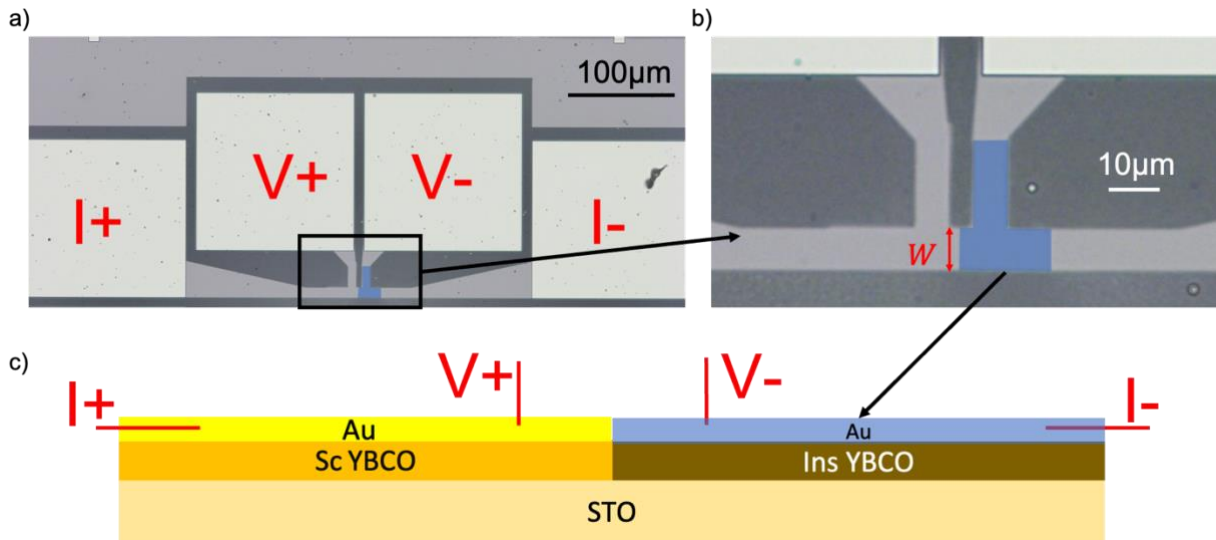


Figure 73 a) Geometry of a whole device with the electrical configuration. b) Zoom on the SN junction under study. The gold layer with insulating YBCO is colored in blue to be more visible. W is the width of the SN interface. For the device with a U in their name, $W = 10\mu\text{m}$ while for D devices, $5\mu\text{m} \leq W \leq 6\mu\text{m}$ since the interface has been etched after an optical lithography whose alignment precision is around $1\mu\text{m}$. c) Side-view of the SN junction with the points where the electrical measures are taken.

5.1.2 Differential conductance and symmetry of the gap

As seen in chapter 3, the BTK theory and its extensions allow for computing the differential conductance as a function of the energy. To compare with this model, it is therefore useful to plot the conductance of the studied junctions as a function of the bias voltage as shown in Figure 74, where I measured the conductance of different junctions. These figures present three SN junctions I will use as an example to illustrate the studies presented in this chapter. The geometry of these three junctions is similar except for the first one (E4D in Figure 74a) which has a reduced width as shown in the right of Figure 74a compared with the ones in b and c.

5.1.2.1 Measurements performed at 2K

Let us first look at the resistances of these junctions at high voltage bias. The junction E4D (a) has a resistance of 12.5Ω for a width of around $6\mu\text{m}$. E2U (b) has a resistance of 8.7Ω for a width of $10\mu\text{m}$. Finally, the junction E7U (c) has a resistance of around 25Ω for a width of $10\mu\text{m}$.

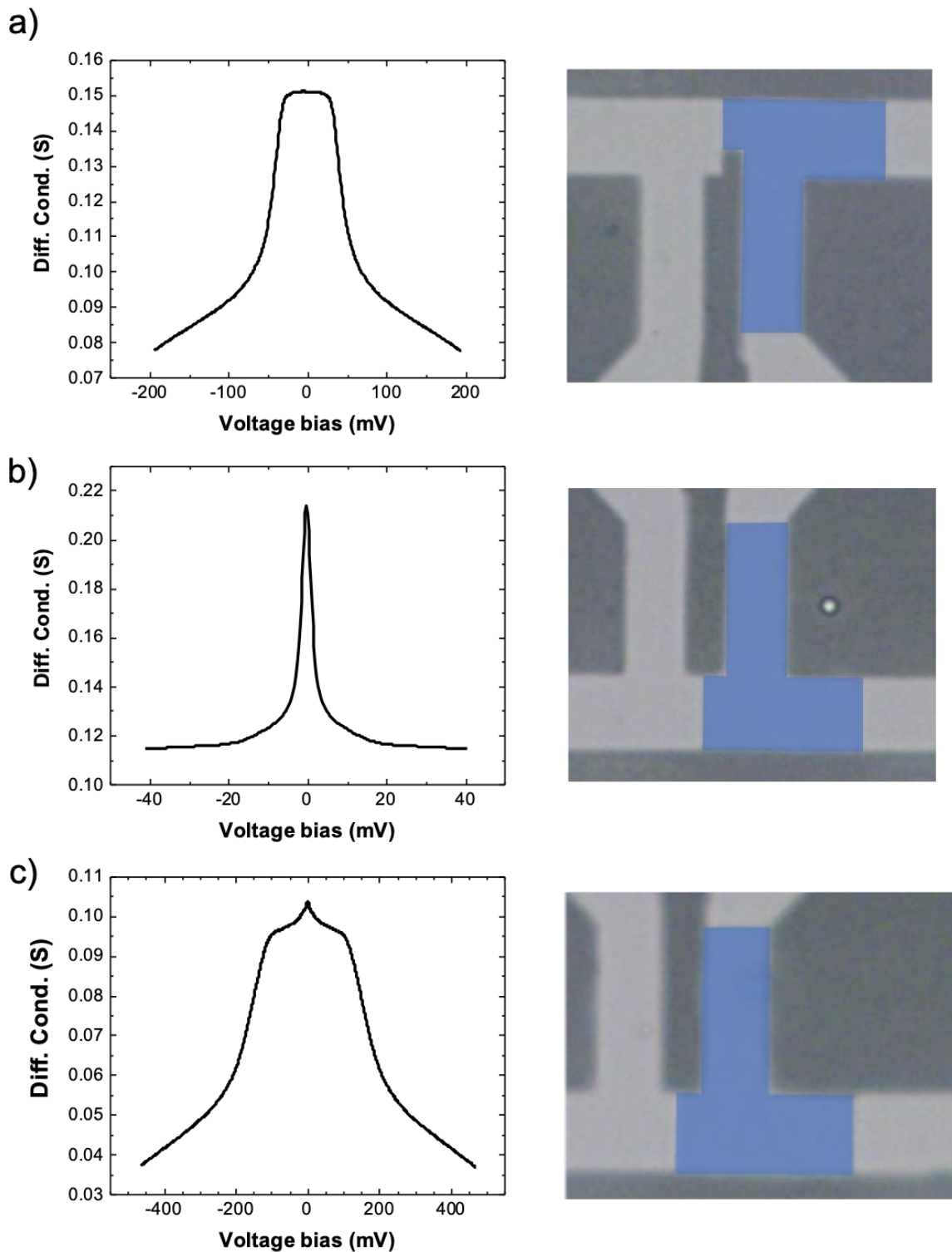


Figure 74 (Left) Differential conductance measurements of 3 different junctions at 2K and without magnetic field: a) E4D, b) E2U, and c) E7U. Their respective microscope image is shown on the right.

Overall the SN junctions I measured on different chips (around 10 different junctions), the product of the geometrical width with the resistance is constant except for the junction E7U (c) which is particularly resistive. Though the junctions chosen as examples are on the same chip, there are variations between their measured characteristics. The differential

conductance of the junction E4D (a) has a shape reminiscent of the one of a transparent SN interface with a *s-wave* superconductor with an apparent superconducting gap around 50mV. A reminder of chapter 3 is given in Figure 75a and b that exhibit simulations of the differential conductance of SN interfaces in the *s-* and *d-wave* cases. This observed gap is much larger than the one of YBCO, $\Delta \sim 25\text{mV}$. Therefore, to avoid confusion, we will call this an apparent gap δ . For E4D (a), $\delta \sim 50\text{mV}$. The differential conductance of E2U (b) has a different shape, resembling the differential conductance of a SN interface with a *d-wave* superconductor with $\delta \sim 2 - 3\text{mV}$.

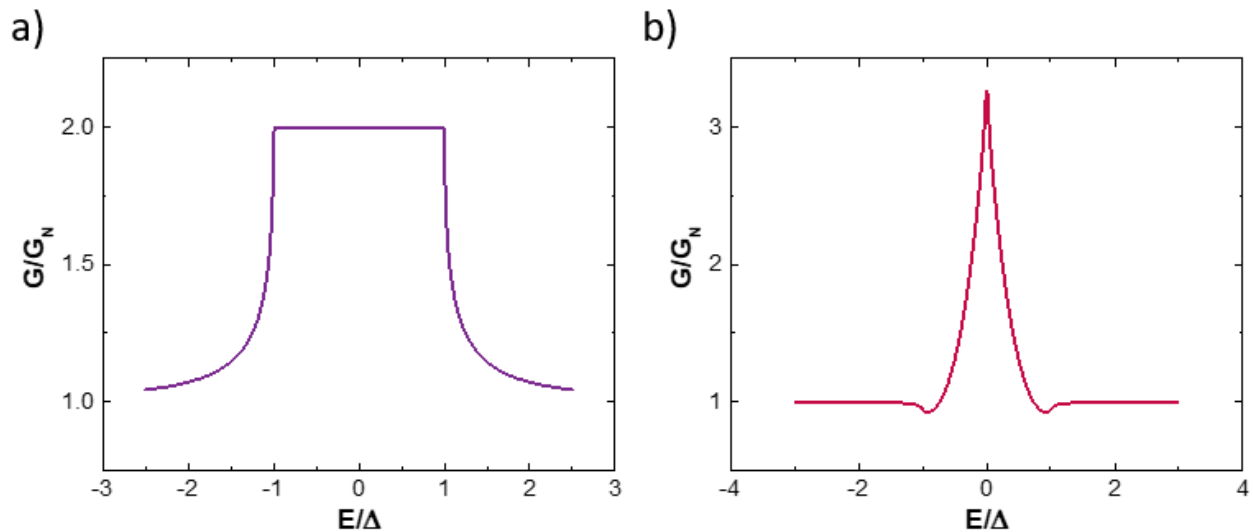


Figure 75 Simulation of the normalized differential conductance spectrum of: a) a perfectly transparent ($Z=0$) SN interface in the *s-wave* case. b) a SN interface in the *d-wave* case ($Z = 1$) with an angle $\alpha = \pi/4$.

Finally, the differential conductance of the junction E7U (c) seems to be a combination of the two symmetries with a larger square shape feature with an inner peak at zero bias. The apparent gap here is $\delta \sim 180\text{mV}$.

Despite all these differences in resistance, the observed gap δ , and the shape of the low bias peak, we can notice that the differential conductance at zero bias is between 1.5 to 1.9 times larger than the differential conductance at high bias. Let's recall that for a perfectly transparent SN junction, this ratio is equal to 2. Now, let us focus on the temperature and field variations of the measured conductance spectra.

5.1.2.2 Temperature dependence of the conductance

I carried out transport measurements at different temperatures (2 – 300K) and magnetic fields (from 0 to 9T). Figure 77 displays the same junctions as in Figure 74, and stresses the evolution of their conductance spectra, measured as a function of the voltage bias. It is plotted for different temperatures ranging from 2K to 90K (the temperature at which YBCO is not superconducting).

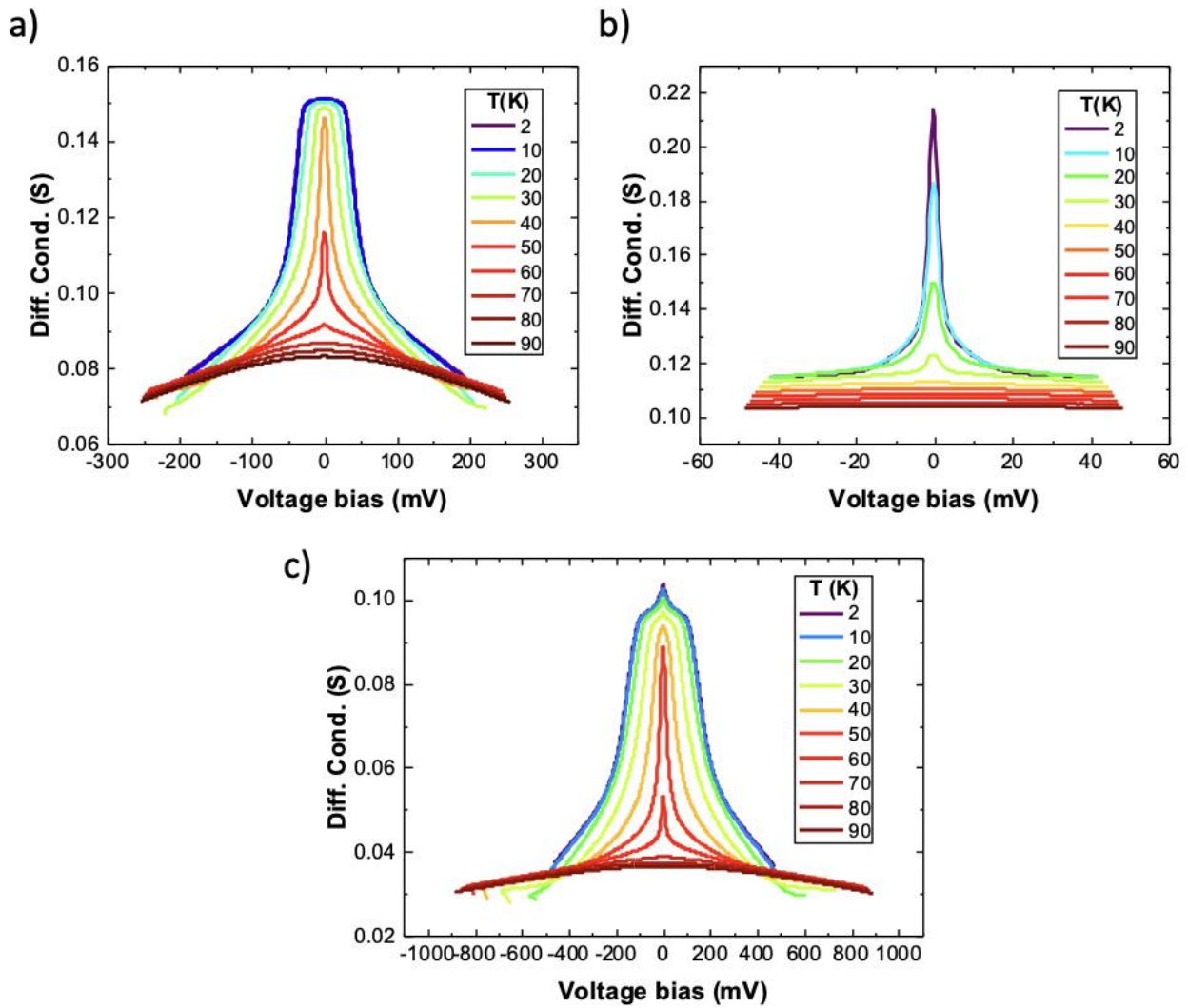


Figure 76 Differential conductance measurements at several temperatures: a) E4D, b) E2U and c) E7U.

For all junctions, the central features we discussed based on the measurements at 2K evolve with temperature. However, this happens differently depending on the junctions. To illustrate this statement, I plotted the evolution of the zero bias conductance as a function of the temperature in Figure 77a. For junction E2U (b), the central peak loses more than one-half of its amplitude at 20K and finally disappears for $T \sim 40$ K. Above this temperature, the differential conductance does not exhibit any feature and is flat. On the other hand, for E4D (a) and E7U (c), their central conductance peaks are still visible up to 70K and the variation of the height of the peak is slightly above 40K and starts accelerating above. In Figure 77b, the normalized width is plotted as a function of the temperature. Here, the width δ is computed as the maximum of the derivative. The width of the differential conductance of E4D (a) first decreases slowly until 10K and then the decrease accelerates until the gap reaches zero. E7U(c) follows a similar trend with even a plateau until 10K before a sharp decrease towards zero. On the contrary, the width of E2U (b) (not shown) increases as the temperature increases whatever the method used (width at half maximum, maximum of the derivative,...). This is due to the low value of the width $\delta \sim 2 - 3$ mV. Thermal effects are visible and cause an enlargement of the peak as $k_B T/e \approx 1$ mV at $T = 10$ K comparable with the

width of the central feature. I chose not to represent it to avoid confusion. Nevertheless, both Figure 76b and Figure 77a show a decline of the central feature of E2U (b) with increasing temperature.

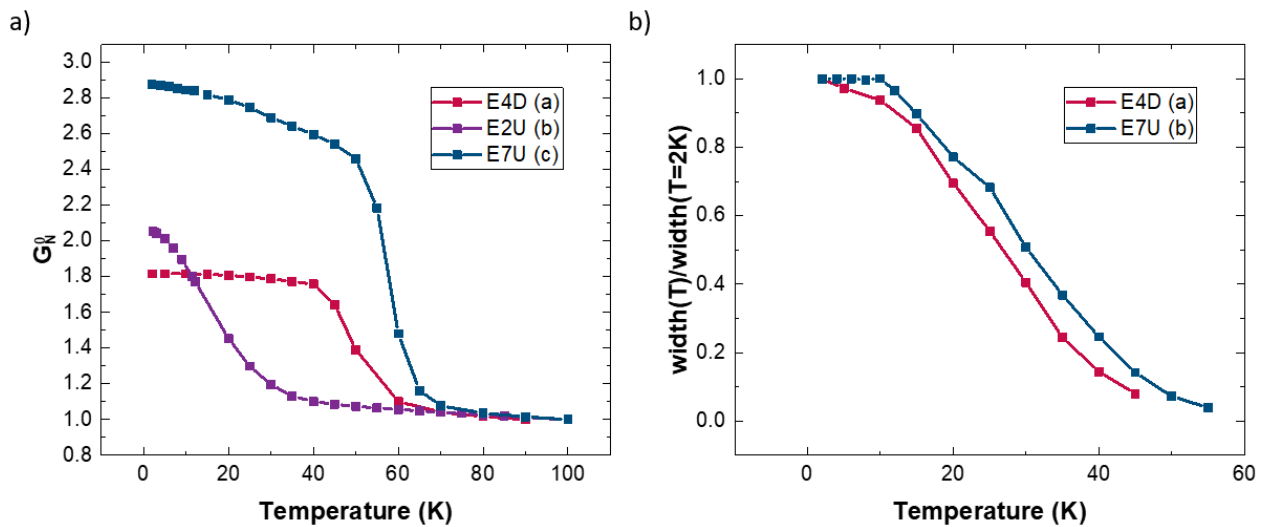


Figure 77 a) Evolution of the zero bias conductance with the temperature of E4D (a), E2U (b), and E7U (c). b) Evolution of the normalized width (computed as the maximum of the derivative of the differential conductance) with temperature of E4D (a) and E7U (c). The one of E2U (b) is not shown because its very small width, comparable with the thermal smearing is not relevant (see main text for details).

5.1.2.3 Magnetic field dependence of the conductance

Figure 78 presents the variation of the differential conductance spectra while applying an out-of-plane magnetic field. The upper critical field H_{c2}^{YBCO} of YBCO is 150T [203] The out-of-plane magnetic field has a strong effect on the three junctions while, as for the temperature, having slightly different effects. Concerning the height of the central feature, the differential conductances of E4D (a) and E7U (c) do not evolve much (< 2% variation) and even slightly increase in the case of E4D (a) at 9T compared with the absence of field as shown on Figure 79a. On the contrary, the differential conductance of E2U (c) evolves a lot with a magnetic field and the amplitude of the central peak at 9T loses two-thirds of its value at zero field. This plot is shown in Figure 79a with the right axis. For E4D (a) and E7U (c), the magnetic field reduces the width of the central features as shown in Figure 79b. The dependence is exactly the same for these two differential conductances that have similar shapes except at zero bias. In terms of voltage bias, E4D (a) goes from $\delta \sim 50mV$ at zero field to $\delta \sim 20mV$ at 9T. E7U (c) goes from $\delta \sim 180mV$ to $\delta \sim 70mV$. For E2U (b), δ is slightly increasing up to 9T whatever the method used to compute it (width at half maximum or maximum of the derivative). I decided not to show its evolution in Figure 79b to avoid confusion but the plot in Figure 78b shows that the magnetic field has a strong effect on the differential conductance.

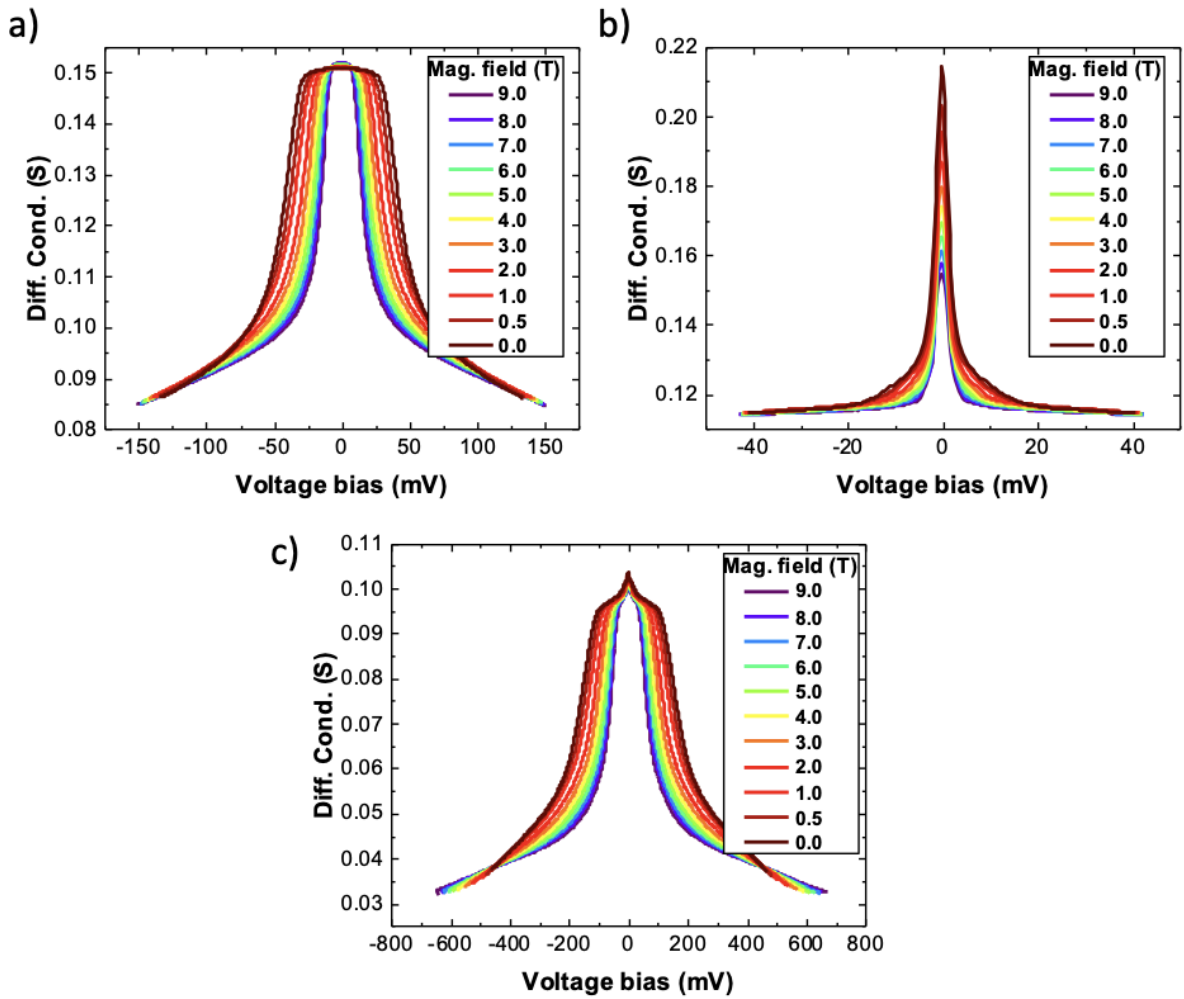


Figure 78 Differential conductance measurements at several out-of-plane magnetic fields : a) E4D, b) E2U, and c) E7U.

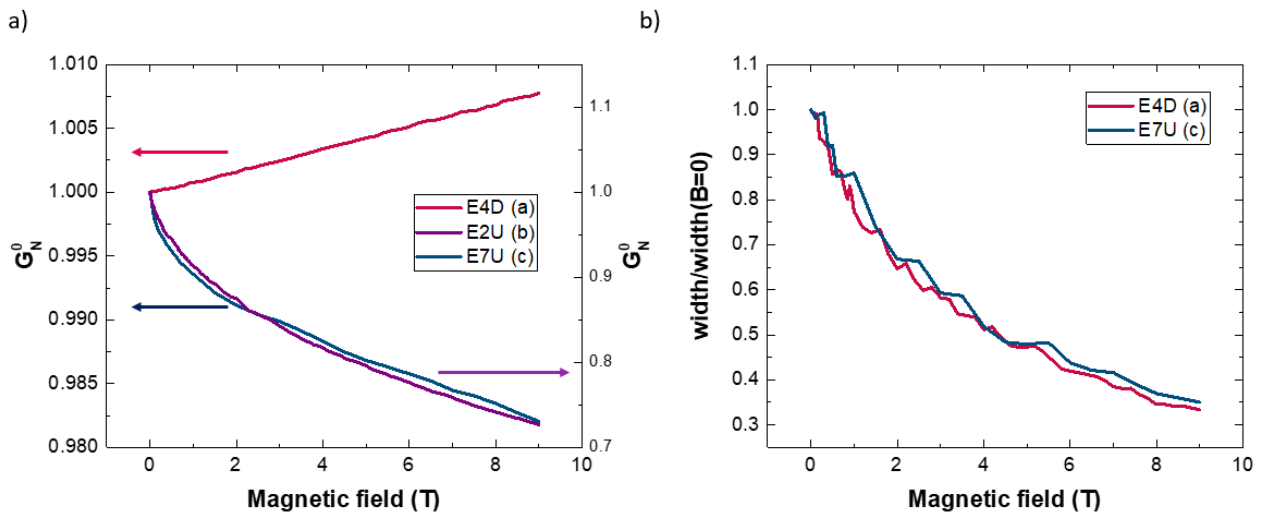


Figure 79 a) Evolution of the normalized zero bias conductance with the magnetic field for E4D (a), E2U (b), and E7U (c). b) Evolution of the normalized width (computed as the maximum of the derivative of the differential conductance) with the magnetic field.

The upcoming sections have the following objectives: initially, to normalize the data in order

to facilitate a theoretical comprehension and fitting of the experiments, enabling the extraction of characteristic parameters related to the proximity effect. Following that, I will present an initial approximation of the system to explain the measurements of differential conductance. Lastly, a more elaborate model will be introduced, which effectively captures the physics at the interface by solving the Usadel equation with appropriate boundary conditions.

5.1.2.4 Procedure of normalization

We have seen that the three differential conductances taken as examples have low-temperature features I attribute to Andreev reflection as explained in the following. The three curves have a background that corresponds to the normal state of the junctions. In order to isolate the features at low temperatures from the background, I will normalize the differential conductances. This allows us to compare the experimental data to theoretical models and then extract the physical parameters of the junctions by fitting. I will present two different methods and give their advantages and drawbacks. The first method, used for example in Ref. [6], consists in dividing the differential conductance at low temperature by the one at 90K, just above the superconducting transition of YBCO. More precisely, I first choose a voltage bias V_c above all superconducting gaps present. Then, I add the difference between the low-temperature and high-temperature differential conductance at this bias. This makes the two curves coincide at the chosen voltage bias. Then, I divide the low-temperature conductance by the corrected high-temperature one. Here is a mathematical formulation of the normalized conductance g at voltage bias V and temperature T :

$$g(V, T) = \frac{G(V, T)}{G(V, 90K) + G(V_c, T) - G(V_c, 90K)} \quad 5.1$$

Where $G(V, T)$ is the differential conductance at voltage V and temperature T . This normalization method has been applied for the three junctions under study in Figure 80.

This method has the advantage to only rely on the measured data at a low temperature and a high temperature. However, it has two main drawbacks. First, in this set of data, the normalized curves do not remain constant at 1 after a given voltage bias. In our case, this is due to the significant variation of the normal resistance between 2K, the lowest temperature, and 90K, just above the superconducting transition of YBCO. This non-flat behavior makes it more difficult to compare with simulations where the differential conductance reaches 1 above a given bias (for a comparison, see the simulations given in Figure 75). Second, the normalization slightly depends on the chosen bias V_c , which also complicates the analysis.

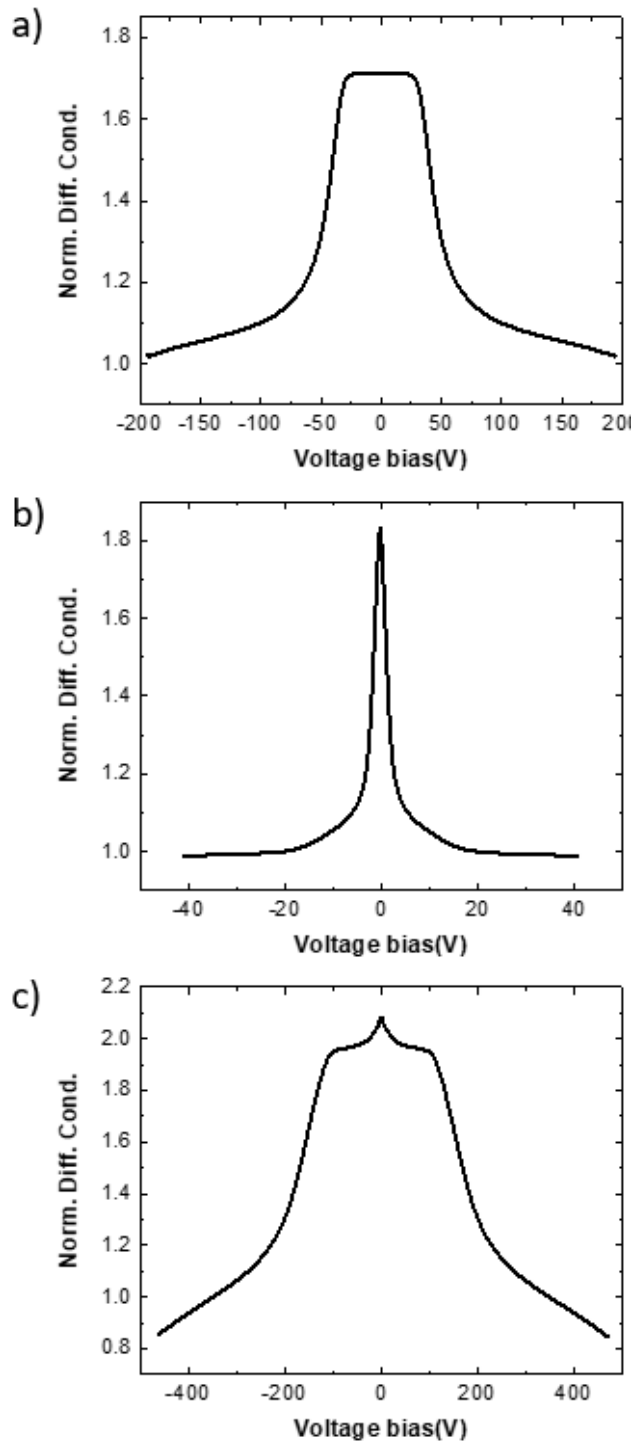


Figure 80 Normalized differential conductance by the high temperature (90K) measurements for the three junctions : a) E4D, b) E2U and c) E7U.

Therefore, I decided to try another method to normalize the data. I removed the parabolic background of the differential conductance to get differential conductances at a high bias (above any superconducting gap) equal to 1. First, I fit the edges of each differential conductance plot by a second-order polynomial function. Once the parameters are found, I divide point by point the experimental data (black lines on the left side of Figure 81) by the polynomial (red lines on the left side). It gives the normalized differential conductance presented on the right-hand side of Figure 81 for the three junctions presented in Figure 74.

The main advantage of this method is that it provides normalized conductances that are equal to 1 for large biases. It allows for a direct comparison with the theoretical models. The drawback is that this normalization is arbitrary in the sense that I chose the degree of the polynomial function, I could have chosen any other function to fit the edges of the differential conductance.

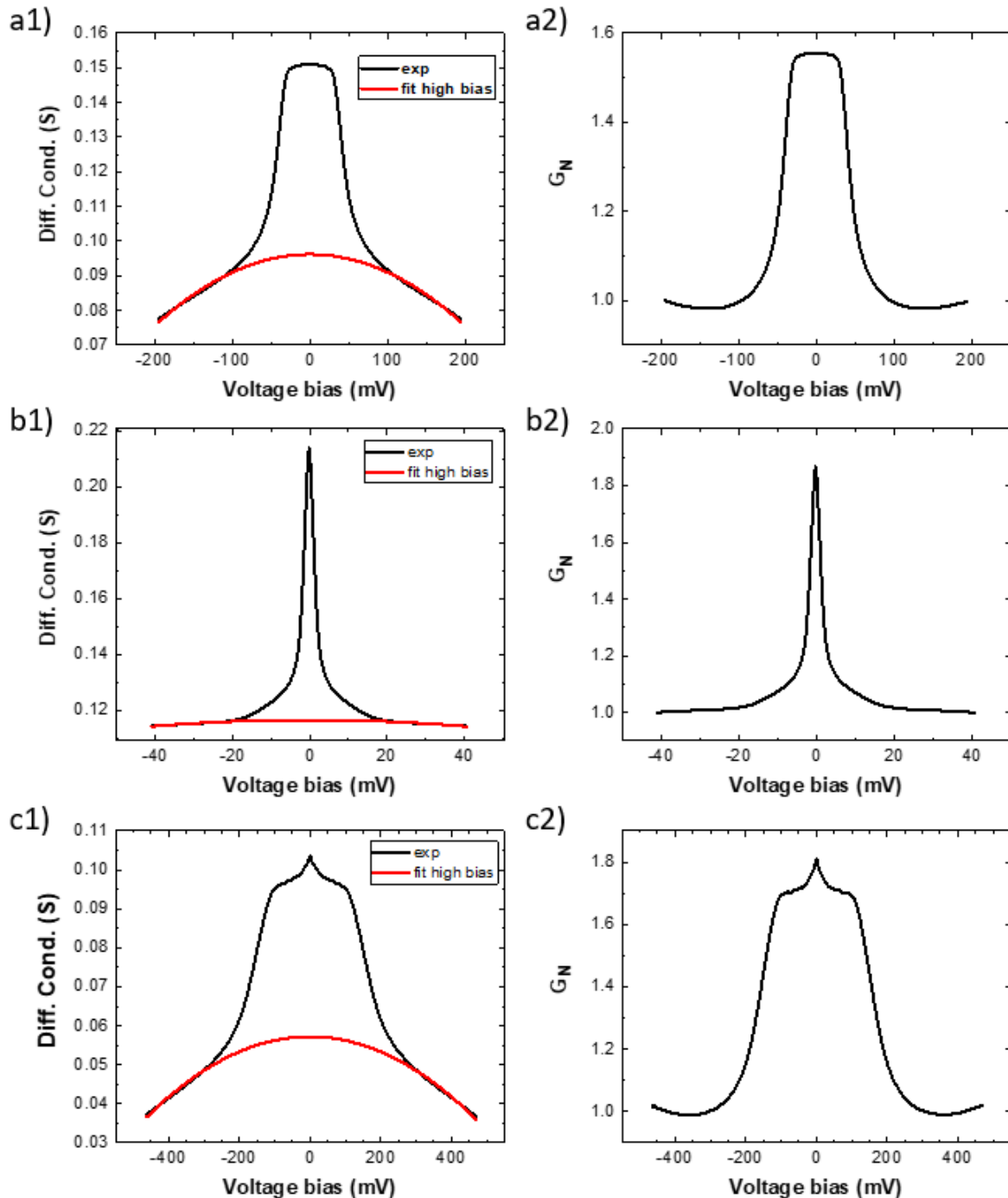


Figure 81 Illustration of the normalization procedure for the three junctions presented above (with the same letter as before: a for E4D, b for E2U, and c for E7U). On the right, the experimental differential conductance (black line) is plotted with a polynomial fit (order 2) only on high bias values. On the left is plotted the resulting normalized differential

conductance.

As we can see in Figure 81, once renormalized, the central peak observed in the conductance has an amplitude of ~ 1.55 for E4D (a2), ~ 1.9 for E2U (b2), and ~ 1.8 for E7U (c2). In the following, I will use these normalized data for the analysis. The plots at various temperatures (Figure 76) reveal that, for all three junctions, the differential conductance curves converge towards the curve for 2K, and exhibit minimal changes within the temperature range of 2 to 5K. This is also evident in Figure 77a. Consequently, in what follows, I will assume that the measurement at 2K does not differ from the expected zero-temperature behavior. Consequently, I will neglect temperature effects in that temperature range for fitting purposes, which simplifies the related calculations.

5.1.3 BTK-inspired model

From now on, I will base my analysis on the normalized data obtained in Figure 81, with the normalization based on the polynomial background removal. In chapter 3, I presented the BTK theory in the case of a point contact that can also reliably be applied to vertical junctions and with *d-wave* superconductors as we have seen. Here, I will present an adaptation of the BTK formalism which will allow us to have a first description of the system. This model, presented in 5.1.3.1, takes into account the presence of different contributions, approximated under the form of resistances in series respectively corresponding to *s-* and *d-wave* contributions to the resistance as well as a metallic contribution. I will then explain the tunable parameters in 5.1.3.2 and how I used them to fit the experimental data. I will show that, while relatively simple, this model represents a good first approach to our system. I will finally give an interpretation of my model in 5.1.3.2.

5.1.3.1 Adaptation to the BTK model taking into account *s-* and *d-wave* contributions

Using the sole BTK theory with a *s-wave* order parameter, it is not possible to fully reproduce the behavior of the conductance of our junctions as a function of the probed energy (in particular E2U (b) and E7U (c)). I therefore started to use a model with a *d-wave* order parameter, which is consistent with the pairing symmetry of the order parameter of YBCO. However, it still failed to encompass the physics of the measured junctions (E4D (a) and E7U (c) as shown with the simulations in Figure 75) since the conductance spectrum has a square shape which is unusual with *d-wave* superconductors. Typical differential conductance spectra for both symmetries are presented earlier in Figure 75. I also noticed that the shape of the differential conductance spectrum of E7U (c) looked similar to a sum of both *s-* and *d-wave* contributions.

From this observation, I developed a phenomenological model, presented in Figure 82. It assumes the presence of two interfaces: one corresponding to a *d-wave* BTK interface and the second one a *s-wave* BTK interface. It also assumes there is in series a voltage drop across gold, which has a finite resistance R_{met} .

This phenomenological model, as I will present in the following section, allows me to reproduce the shapes of the conductance spectra of my junctions while using reasonable

values of the parameters (gaps, Z factor, angle α ...). The code for the whole SN junction, combining BTK s - and d -wave theories as well as R_{met} (see Figure 82), is provided in the Appendix.

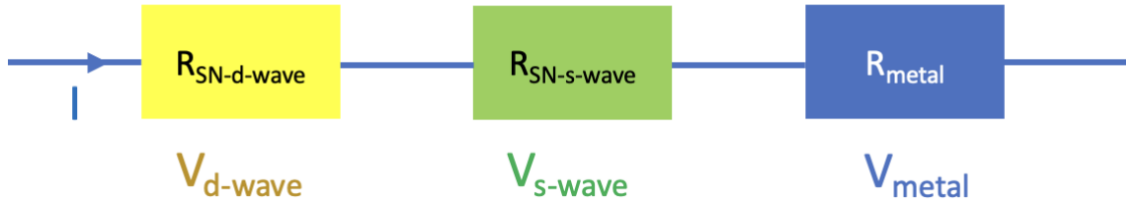


Figure 82 Equivalent electrical of a phenomenological model with two interfaces, one d -wave and the other s -wave, and a metallic resistance R_{met} in series.

5.1.3.2 Illustration of the model

In this section, we will review the parameters of the model used to fit the differential conductances of the junctions. This will allow us to extract some insights into the nature of the measured SN junctions. The main extracted parameters, corresponding to the plots in Figure 85, are summarized in Table 3.

Enlargement of the energy scale (x-axis) due to R_{met}

First, I would like to discuss the role of the metallic resistance in series, R_{met} . If R_{met} increases, on the one hand, the width will increase because it adds an extra voltage drop to the total voltage bias. On the other hand, the height of the central feature will decrease. Figure 83 illustrates this affirmation with a simple numerical calculation. In this simulation, I only consider one SN interface (s -wave) for simplicity. The way it would be measured includes a metallic part. It is then equivalent to a BTK calculation with a finite resistance in series. For $R_{met} = 0.001R_{SN}$, the BTK plot is almost undisturbed with a doubling of the conductance inside the superconducting gap (the overall gap is the superconducting gap). However, as I increase R_{met} , the central features widen and its height decreases. For $R_{met} = 2R_{SN}$, the height only goes to 1.2 but the apparent gap is more than four times larger than the initial superconducting gap Δ_0 . This example shows that even if the presence of a resistance in series may explain the enlargement of the central feature, it also implies the diminution of its height.

d -wave and s -wave interfaces

This phenomenological model is based on the presence of two distinct SN interfaces. One is formed with a d -wave superconductor and a normal metal while the other one is made of a s -wave superconductor and a normal metal. The first interface has a d -wave superconductor and a normal metal on the other side. For both interfaces, the parameters are the superconducting gap, respectively Δ_{d-wave} and Δ_{s-wave} , the scattering parameter, Z_{d-wave} and Z_{s-wave} , that tells whether the interface is transparent or tunnel and a broadening term,

Γ_{d-wave} and Γ_{s-wave} . I only used Γ_{s-wave} to slightly smoothen the very sharp angles of the *s-wave* differential conductance. The weight of both contributions in the final differential conductance is given by the values of the high bias resistance (further any superconducting gap), R_{d-wave} and R_{s-wave} . Last but not least, and only for the *d-wave* interface, the angle α between the gap node and the interface. This angle, depending on its value, gives rise to many different shapes of the differential conductance of the *d-wave* part. The definition of this angle with respect to the interface is given in Figure 84.

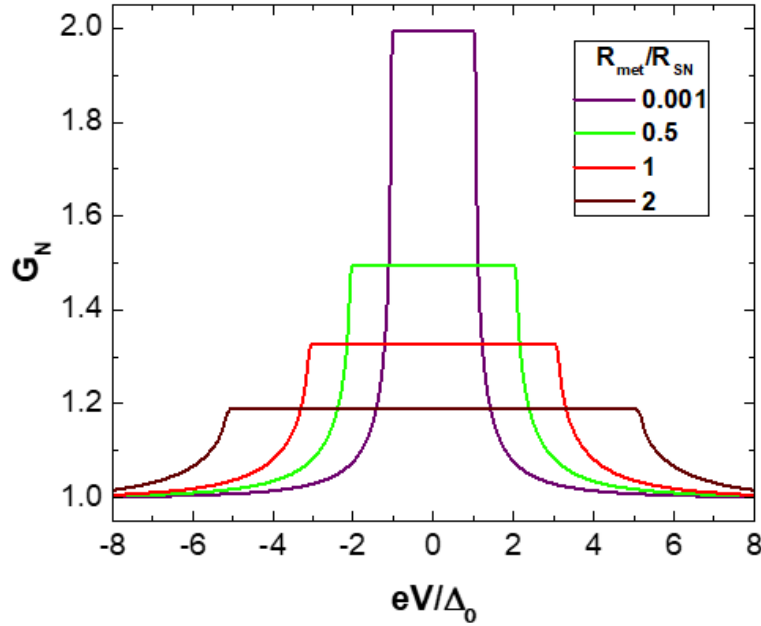


Figure 83 Numerical calculation of the differential conductance of a perfectly transparent SN interface (normal resistance R_{SN}) with the BTK theory (*s-wave*) in series with a finite resistance R_{met} .

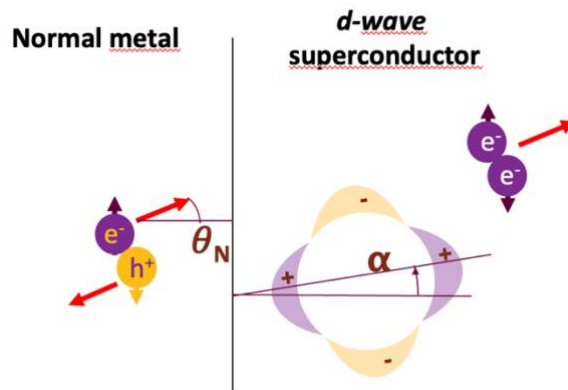


Figure 84 Definition of the angle α of the *d-wave* order parameter with respect to the interface between a normal metal and a *d-wave* superconductor.

Application of the model

Now, we will review the parameters of the fits shown in Figure 85 for each junction (see Table 3) and extract some physical insights from their values.

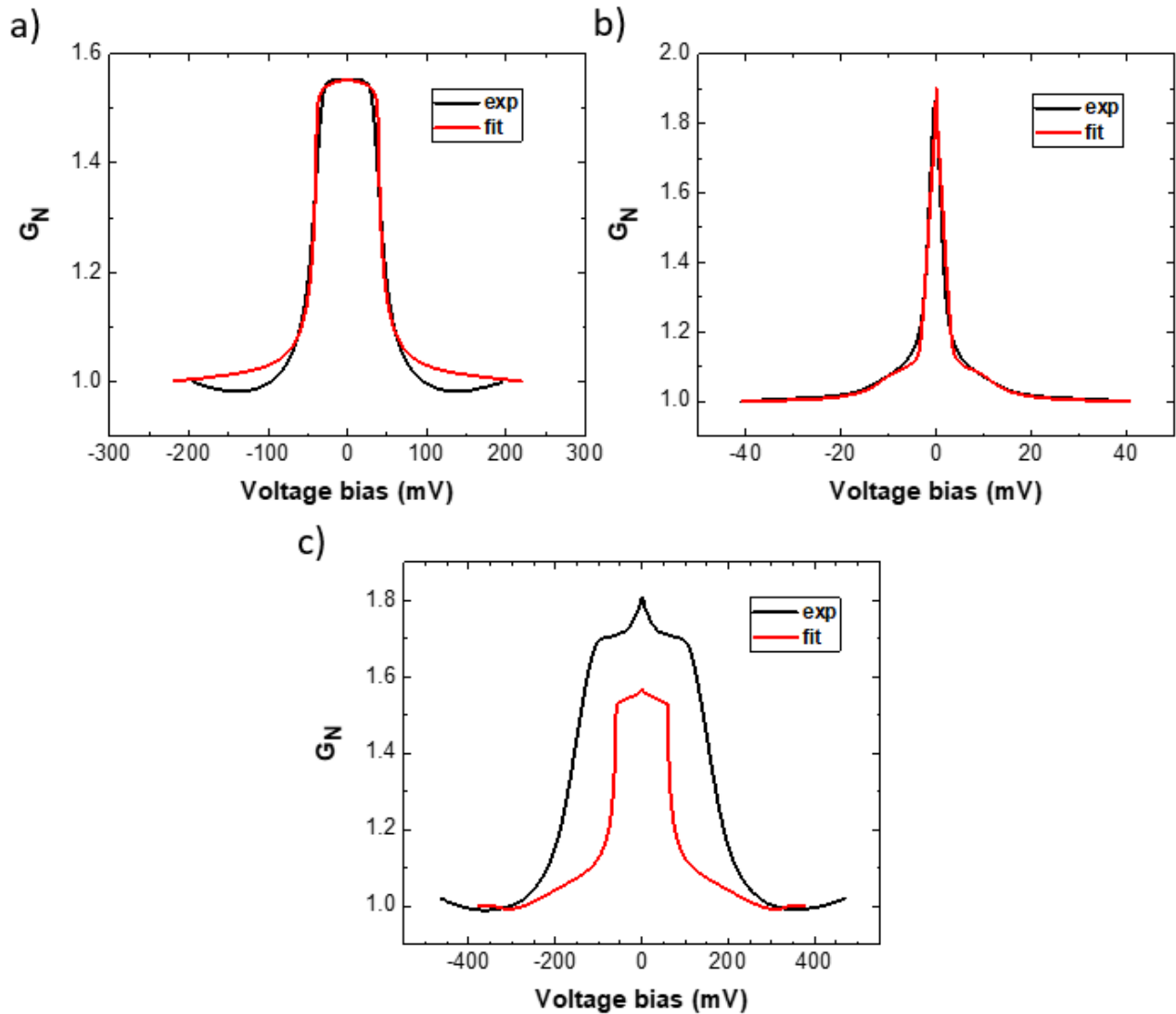


Figure 85 Fits of the normalized differential conductance of the three junctions with the hand-waving model: a) E4D, b) E2U, and c) E7U.

Name	$\Delta_{d\text{-wave}}$	$Z_{d\text{-wave}}$	$\Gamma_{d\text{-wave}}$	α	$\Delta_{s\text{-wave}}$	$Z_{s\text{-wave}}$	$\Gamma_{d\text{-wave}}$	$R_{s\text{-wave}}/R_{d\text{-wave}}$	$R_{\text{met}}/R_{d\text{-wave}}$
E4D	25mV	0.001	0	0	22mV	0	0.5mV	8	2.5
E2U	2mV	0.7	0	$\pi/4$	2mV	0	0.5mV	0.4	0.3
E7U	32mV	1	0	$\pi/4$	25mV	0	0	4	2.5

Table 3 Recap of the parameters for the fits of the three junctions E4D, E2U, and E7U.

E4D (a): The differential conductance of the junction has a square shape and therefore, we expect a large *s-wave* component. Indeed, in the fit presented in Figure 85a, the *d-wave* BTK gap is 25mV while the *s-wave* one is 22mV. The transparency of both junctions is perfect

($Z_{d-wave} = 0$ and $Z_{s-wave} = 0$). The best fit corresponds to $\alpha = 0$ and the ratio of the resistance between the d -wave and s -wave interface $R_{s-wave}/R_{d-wave} = 8$ is large and accounts for the square shape, majoritarily coming from the s -wave interface. The metallic resistance $R_{met}/R_{d-wave} = 2.5$ allows for a slight enlargement of the width of the central feature as explained above.

E2U (b): The differential conductance of this junction shows a sharp zero-bias peak reminiscent of the behavior found in the case of a d -wave superconductor in contact with a normal metal with $\alpha = \pi/4$. The fitting parameters corresponding to Figure 85b, show that the total differential conductance is a combination of both s - and d -wave contributions: $\Delta_{d-wave} = 2\text{mV}$ and $\Delta_{s-wave} = 2\text{mV}$, though the dominant contribution comes from the d -wave interface with $\alpha = \pi/4$. Here, we have $R_{s-wave}/R_{d-wave} = 0.4$ and $R_{met}/R_{d-wave} = 0.3$.

E7U (c): The differential conductance spectrum of this junction combines a square-shaped low-bias peak with an inner feature at zero bias. Moreover, the width of the central feature is $\sim 200\text{mV}$. This last element makes it difficult to fit because it is complex to enlarge the central feature without decreasing too much the height of the central peak. Indeed, as explained above, increasing the width of the feature with a larger R_{met} leads to a decrease in the height of the peak. The found fit parameters render the general shape of the peak. The gaps are much larger here: $\Delta_{d-wave} = 32\text{mV}$ and $\Delta_{s-wave} = 25\text{mV}$ with the angle $\alpha = \pi/4$. Here, I found $R_{s-wave}/R_{d-wave} = 4$ and: $R_{met}/R_{d-wave} = 2.5$.

Comments on the parameters

While this model is the first approach to the treatment of this system, the extracted fitting parameters can give some insights into the behavior of the junctions that may help for the theoretical explanation as we will see in the following. In all these calculations, the scattering parameter of the s -wave interface is 0 corresponding to a perfect interface. This makes sense since the interface proximized gold/gold is expected to be perfect. Moreover, this s -wave interface between a proximized layer of gold and a normal layer of gold, a few coherence lengths away from the interface should not exhibit scattering or an abrupt change of Fermi level, justifying the quality of the interface. Concerning the d -wave interface, two different angles have been used $\alpha = 0$ and $\alpha = \pi/4$ to reproduce the shapes of the differential conductance given as examples. One thing we learned from the fits is that the s - and d -wave gaps seem correlated. Indeed, the d -wave gap is always a bit larger than the s -wave gap. This is consistent with the fact that s -wave correlations originate from the scattering of the d -wave order parameter and are therefore smaller. Finally, I will discuss the values of the different resistances incorporated in the model. Except for the E2U (b) junction, the resistance of the s -wave contribution is larger than the d -wave one. A recap of the different resistances is given in Table 4. This behavior of E2U (b) may be related to the orientation of the order parameter ($\alpha = \pi/4$) that may be less favorable for the current to flow. For the other two, the d -wave resistance is smaller than the s -wave one. Finally, the metallic resistance in series is in these three examples between one-fourth and one-third of the

global resistance. It is possible to get an order of magnitude of the expected resistance of the metallic section using Thomson's formula [204] for the conductance of thin films. Knowing the conductivity of bulk gold at 2K is roughly $\sigma_0 \approx 2\text{S.m}^{-1}$ [205] and its mean-free path is $l \approx 38\text{nm}$ [206], the conductivity of the gold film of thickness $t \approx 10\text{nm}$ is:

$$\sigma = \sigma_0 \times \frac{t}{2l} \times \left[\ln\left(\frac{l}{t}\right) + \frac{3}{2} \right] \approx 7.5 \times 10^6 \text{S.m}^{-1} \quad 5.2$$

And then, the expected resistance of the $10\mu\text{m}$ -wide and $2\mu\text{m}$ -long metallic section is: $R_{met}^{exp} = \frac{L}{tW\sigma} \approx \frac{2 \times 10^{-6}}{10 \times 10^{-9} \times 10 \times 10^{-6} \times 7.5 \times 10^6} \approx 2.7\Omega$. This is consistent with the estimated R_{met} from the simulations given in Table 4.

Ω	R_{met}	R_{s-wave}	R_{d-wave}
E4D (a) : $R_N = 12.5$	2.7	8.7	1.1
E2U (b) : $R_N = 8.7$	1.5	2.0	5.1
E7U (c) : $R_N = 28.5$	9.5	15.2	3.8

Table 4 Recap of the normal resistance, R_{met} , R_{s-wave} and R_{d-wave} for each junction.

5.1.3.3 Interpretation of the model

The model I developed assumes there are two interfaces that can be described by the BTK formalism, one with a *s-wave* order parameter and the other one with a *d-wave* order parameter as well as a metallic resistance in series. A descriptive scheme is given in Figure 86 and it will help the discussion about both the justification of the presence of two effective interfaces and their positions. Let us start from the left side of the figure. A thin (smaller than the scattering length) layer of gold is covering YBCO, a *d-wave* superconductor. The electrical contact between the two has been shown to be excellent [12,207] and is made over several tens of microns. The first consequence is that this interface YBCO/Au will not be measured by the set of electrodes because of the four probe measurement and the very low interface resistance. A second consequence is that we can assume that a *d-wave* order parameter is induced in the thin gold layer and that it won't change much over the thickness of gold since this layer is thinner than the scattering length [93]. Indeed, here the interface between superconducting YBCO and gold being along the (001) direction, the in-plane momentum of the particles will be conserved during the processes occurring at the interface. Therefore, incident, reflected, and transmitted particles see the same order parameter. As a consequence, there will be no *s-wave* correlations nor surface states created and **the induced order parameter in gold above YBCO will be only *d-wave*.**

Going toward the right side of Figure 86, the superconducting YBCO below gold is replaced by insulating YBCO. The current, that can circulate both in YBCO or gold on the left, can no longer circulate in YBCO on the right and is restrained to the gold layer. It creates a constriction of the current, analogous to the one created by a constriction in a superconductor. This is the position I qualify as SN junction. **At this position, the presence**

of the constriction gives rise to a *s-wave* contribution coming from a loss of the *d-wave* order parameter [93]. At that point, there are two order parameters coexisting with two different symmetries *s* and *d*. These two order parameters create electronic correlations in the layer of gold placed above the insulating YBCO. However, these correlations decrease as the distance with the interface increases but not with the same characteristic lengths. *s-wave* correlations persist up to the coherence length in the layer of gold while *d-wave* ones fade over the mean free path in the layer [93]. This is the starting point of the two interfaces model I described earlier. In Figure 86, I placed the speculated position of each “SN” interface between proximized gold and normal gold with the different symmetries *s* or *d*. Close to the boundary between superconducting and insulating YBCO, the first interface being encountered may be the “*d-wave* interface” because this is where *d-wave* correlations disappear. Further of the boundary, there may be the “*s-wave* interface” where *s-wave* correlations vanish. The “” aims at stressing that these “interfaces” are not sharp and well-defined interfaces but more continuous changes of the electronic density of states in the gold layer. Finally, the electrodes being deported with respect to the YBCO boundary, they also measure on one side some proximized and normal layer of gold. This will account for R_{met} . This modelization with two “interfaces” is an approximation since they are in fact not localized but spread. This approach nevertheless allows the application of the BTK theory. This simple model and the related calculation, while submitted to approximations, make it possible to extract physical parameters that are relevant to the physics at play in our systems and is a good starting point for its study. The approach developed in the following allows us to treat this continuous interface problem.

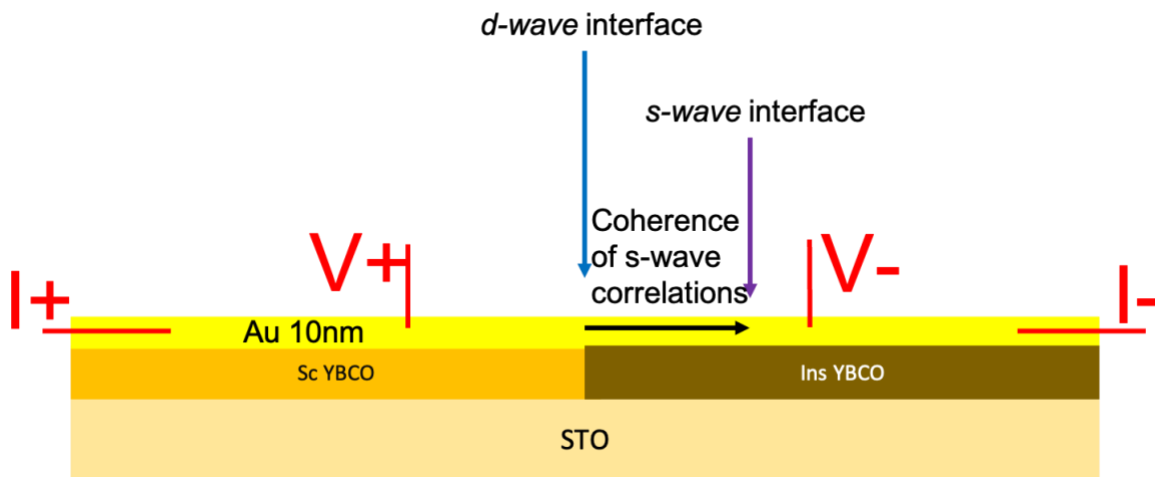


Figure 86 Scheme of a SN junction and the placement of the various interfaces related to the equivalent electrical model. The current and voltage probes are also depicted.

5.1.4 Numerical resolution using Usadels equation

The theoretical work that follows has been realized with the help of our collaborators, Tim Kokkeler and Sebastian Bergeret from Centro de Física de Materiales, San Sebastian, Spain. It relies on the use of Usadel formalism to describe the proximity effect at the interface described in Figure 87 by adding the formalism of circuit theory of superconductivity [208] extended to the case of *d-wave* superconductors [95,97]. Contrary to the previous model

which does not take into account the scattering in the normal metal, this model treats the scattering in a continuous way and the physical quantities are computed self-consistently. Therefore, the phenomenological term R_{met} which we introduced in the BTK modelling is naturally taken into account. This treatment is necessary since the resistance of the normal metallic layer on the blue side may be of the same order as the effective SN interface.

5.1.4.1 Model

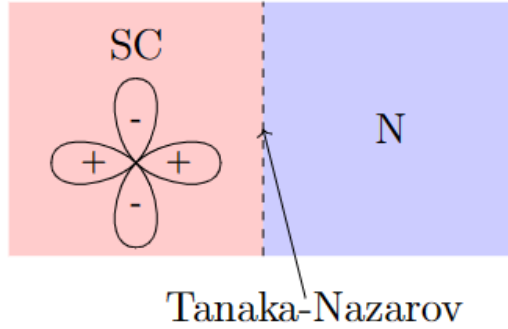


Figure 87 Scheme of the system used for the calculation. The lateral junction between proximized gold and normal gold is approximated to a SN junction.

In this model, the system is depicted in Figure 87. It is made of a bilayer of superconducting YBCO covered by Au (red) and a layer of standing Au (blue). We assumed scattering can occur in the Au film (either above the superconducting or insulating YBCO) but that its thickness is small compared with the mean free path. The electrical contact with YBCO being good (low contact resistance due to optimized *in situ* growth of Au), the layer of Au above YBCO (in red) is assumed to be fully proximized with a *d-wave* order parameter [93]. In the red part of the scheme, the current can flow either in Au or YBCO but once in the blue part, it can only flow in Au. This constriction acts like an effective interface of finite transparency between proximized Au (red) and normal Au (blue). In this model, the inverse proximity effect that would decrease the value of the order parameter in YBCO is neglected because YBCO's thickness is much larger than gold's one.

5.1.4.2 Usadel formalism in a nutshell

Without entering too much into details, the resolution method is based on the numerical resolution of Usadel's equation. For this paragraph, I will mainly refer to [209,210]. The starting point of the quasiclassical formulation is the description in terms of Green's functions of both the electrons and holes due to the electron-hole coupling in superconductors (see chapter 3 about Bogoliubov-de Gennes equation). It allows the treatment of non-uniform superconductors. For example, the retarded Green function for the electron is:

$$G^R(\vec{r}, t | \vec{r}', t') = -i\theta(t - t') \langle \psi_H | \{ \psi_\sigma(\vec{r}, t), \psi_\sigma^\dagger(\vec{r}', t') \} | \psi_H \rangle \quad 5.3$$

Where θ is the Heaviside function, $|\psi_H\rangle$ the ground-state stationary wave-function, ψ_σ the annihilation operator of an electron of spin σ and $\{, \}$ is the anti-commutation operator. The

electron-hole coupling implies the use of a larger dimension Green's function, solution of the Gorkov equation [211] which describes non-uniform superconductors:

$$G^R(\vec{r}, t | \vec{r}', t') = -i\theta(t - t') \widehat{M}(\vec{r}, t | \vec{r}', t') \quad 5.4$$

With:

$$\widehat{M}(\vec{r}, t | \vec{r}', t') = \left\langle \begin{pmatrix} \{\psi_{\uparrow}(\vec{r}, t), \psi_{\uparrow}^{\dagger}(\vec{r}', t')\} & \{\psi_{\uparrow}(\vec{r}, t), \psi_{\downarrow}(\vec{r}', t')\} \\ -\{\psi_{\downarrow}^{\dagger}(\vec{r}, t), \psi_{\uparrow}^{\dagger}(\vec{r}', t')\} & -\{\psi_{\downarrow}^{\dagger}(\vec{r}, t), \psi_{\downarrow}(\vec{r}', t')\} \end{pmatrix} \right\rangle_0 \quad 5.5$$

Where $\langle \rangle_0$ stands for the statistical average over the whole system state. Usadel showed [212] that for diffusive conductors, the Green's function becomes isotropic when averaged over the disorder:

$$\widehat{G}_{dis}^R(\vec{r}, t - t') = -i\theta(t - t') \langle \widehat{M}(\vec{r}, t | \vec{r}', t') \rangle_{dis} \quad 5.6$$

To find the Green's function with respect to the energy E , one has to consider the Fourier transform of \widehat{G}_{dis}^R that can be written:

$$\widehat{R}(\vec{r}, E) = \begin{pmatrix} G & F \\ F^{\dagger} & -G \end{pmatrix} \quad 5.7$$

This matrix is solution of the Usadel equation:

$$\hbar D \widehat{V}_r(\widehat{R} \widehat{V}_r \widehat{R}) = [-iH_0 + i\hbar \Gamma_{sf} \widehat{\sigma}_z \widehat{R} \widehat{\sigma}_z, \widehat{R}] \quad 5.8$$

With $H_0 = \begin{pmatrix} E & i\Delta(\vec{r}) \\ i\Delta^*(\vec{r}) & -E \end{pmatrix}$ and Γ_{sf} the spin-flip scattering rate (not considered in the following). The physical properties are expressed in terms of G and F . For instance, the local single-particle density of states at energy E is given by:

$$\rho(\vec{r}, E) = \rho_n \text{Re } G(\vec{r}, E) \quad 5.9$$

5.1.4.3 Tanaka-Nazarov effective interface

We solve the Usadel equation on the normal Au side (blue part in Figure 87). Since the superconducting order parameter is zero in this region, it is reduced to:

$$\partial_x(G \partial_x G) = [iE \sigma_z, G] \quad 5.10$$

Where G is the angle averaged retarded Green's function.

The so-called circuit theory for *s-wave* superconductors [208] treats diffusive conductors and was extended to cover *d-wave* superconductivity as well [95,97]. In our case, the boundary condition at the effective interface ($x = 0$ at the boundary between the red and blue part) is:

$$G \partial_x G(x=0) = \int_{-\frac{\pi}{2}}^{\frac{\pi}{2}} d\phi (1 + T_1^2 + T_1 \{C, G(x=0)\}) \quad 5.11$$

Where T_1 the transparency of the effective Au/Au interface and $C = H_+^{-1}(1 - H_-)$, with $H_{\pm}(\phi) = \frac{1}{2}(G_S(\phi) \pm G_S(\pi - \phi))$ and G_S being the bulk Green's function of a d -wave superconductor with $\Delta(\phi) = \Delta \cos 2(\phi - \alpha)$. In this approach based on Usadel's equation, there is only one effective interface contrary to the BTK-inspired method.

5.1.4.4 Results of the simulation and parameters

This formalism can be used to treat the differential conductance of the junctions E4D (a) and E2U (b) as examples. Their behavior can be reproduced using this theoretical description. As in the BTK-inspired model, the angle α is 0 for the E4D (a) junction while $\pi/4$ for the E2U (b) junction. The differences between the two differential conductances come from the difference in the transparency of the effective interface, the junction E4D having a higher transparency ($z = 0.05$) than E2U ($z = 0.2$). These interfaces have very high transparencies and are nearly perfect as the differential conductance data suggested. The numerical calculation of the normalized differential conductance at zero temperature is presented in Figure 88a. It is plotted as a function of the energy normalized by the superconducting gap of YBCO. The computed calculation for the differential conductance of E4D presents a broad peak in the same way as the experimental differential conductance (see Figure 88b). The one of E2U has a sharper shape likewise the experimental differential conductance.

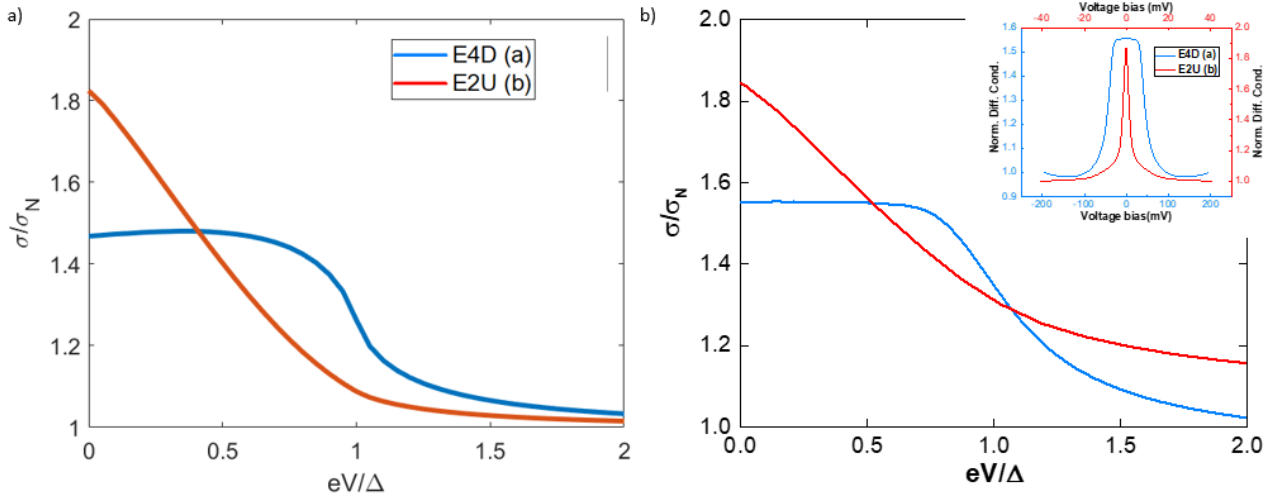


Figure 88 a) Results of the calculation done by Tim Kokkeler for the junction E4D and E2U described earlier. The normalized differential conductance is plotted with respect to the normalized voltage bias. Here, $\alpha = 0$ with $z = 0.05$ for E4D and $\alpha = \pi/4$ with $z = 0.2$ for E2U. b) experimental normalized differential conductance at 2K as a function of the normalized energy. The gap Δ cannot be found with the BTK-inspired method since there is a s - and d -wave gap but I chose a gap close to the sum of the gaps (40mV for E4D and 2mV for E2U). The data as a function of the voltage bias are given in the inset for comparison.

5.1.4.5 Evolution with temperature

It is possible to carry out this numerical calculation at non-zero temperature and therefore check if it fits with the experimental observations. The temperature manifests itself in the calculation by two effects. First, the finite temperature smears the differential conductance since more quasiparticle modes are implicated in the transport (Fermi-Dirac distribution). Moreover, temperature also reduces the order parameter. This effect is slight for $T < T_c/2$ but the shrink is more important for $T > T_c/2$. In Figure 89a, the differential conductances at zero bias of the junctions E4D (a) and E2U (b) were computed as a function of the temperature with the same parameters as before. As a reminder, I provide the experimental measurements of the zero bias conductance in Figure 89b. First, we can notice that the shapes of the theoretical and experimental plots are very similar. The plateau at temperatures below 40K experimentally observed for E4D is well reproduced by the simulations. The decrease above in the simulation is less pronounced than in the experiment. In terms of numbers now, first, the experimental normalized differential conductances at 2K do not have the same values as in Figure 88b. This comes from the normalization which is not the same in the two cases. In Figure 89b, the data are normalized by the high-temperature ones while in Figure 88b, they are normalized with the polynomial method explained in Figure 81.

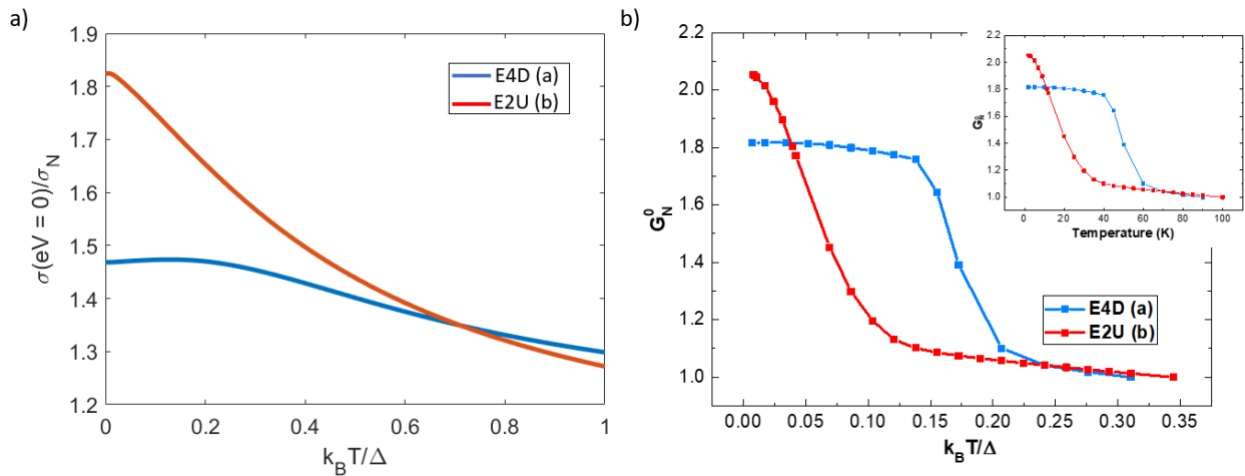


Figure 89 Numerical calculation of the normalized differential conductance at zero bias as a function of the normalized thermal energy using the Usadel theory with Tanaka-Nazarov boundary conditions for the E4D and E2U junctions. b) Experimental normalized zero bias conductance vs normalized temperature by the YBCO gap ($\Delta \sim 25$ mV) for E4D and E2U. The inset is the same as in the main figure but with the temperature.

Concerning the temperature, I represented the experimental measurement with the normalized temperature by the gap Δ of YBCO. Since $\Delta = \kappa k_B T_c$ with $\kappa \approx 2.5 - 3.5$ for YBCO depending on the orientation [167], it is equivalent to plot it as a function of $\frac{T}{\kappa T_c}$. The plateau in the simulation of E4D (blue) goes until a value that is close to the experimental measurement (0.2 for the simulation and 0.15 for the experiment). There is less agreement in the case of the E2U junction but that may be due to the extremely small observed gap in the differential conductance spectra of E2U (see Figure 88b and the values of the gaps

deduced from the BTK-inspired method in Table 3). With a smaller gap, we would find an experimental plot closer to the simulation. **The model developed in this subsection allows the reproduction of two of the experimental differential conductances (a and b) and extracts the parameter of the scattering at the interface. Finally, it also reproduces well the temperature behavior of both measured junctions.**

5.1.4.6 Discussion on the junction E7U

Before switching to SNS junctions in the next section, I would like to explain why the model developed with the Usadel formalism struggles to “fit” the data. As we have seen, the junction E7U (c) is particularly resistive compared with the two others, and the BTK-inspired model gave an estimate for the metallic resistance $R_{met} \sim 9.5\Omega$ larger than the two others. That may be due to the quality of gold at that place of the sample. It implies that the metallic resistance becomes more important compared with the resistance of the interface (in the Usadel formalism). It results in two visible transitions with two different voltage scales. The smaller voltage scale is associated with the change of conductance of the SN interface for the junctions E4D (a) and E2U (b). The second one is not related to energy but more to a current. When the current becomes large ($I \sim I_c^{Au}$), the proximized gold on top of YBCO will turn normal. The ratio between the proximized and normal conductance is not limited by a factor of 2 contrary to the SN resistance. This is what explains the larger factor between the conductance at zero and at large bias. In the next section, we will see again this explanation to explain the differential conductances of SNS junctions.

5.2 STUDY OF SNS JUNCTIONS

On the same chips as in the previous section, SNS junctions were patterned to study more similar systems as the 2D/superconductor planar junctions described in chapter 3 and whose results are given in chapters 6 and 7. Here, the normal bridge separating the two superconducting electrodes is made of a thin layer of gold.

5.2.1 Comments on the chosen geometries

In this study of SNS junctions, I decided to present only junctions with voltage electrodes connected to the central track through gold and not the superconductor. Indeed, as shown in Figure 90, all the devices have their voltage electrodes made of gold on top of insulating YBCO. The length L of the junction between the superconducting electrodes is equal to 200nm for the devices R1859BD B2U (a), R1859HD B5U(b), and R1859BG A2D (c). The two first junctions have electrodes made of gold with a 25 μm -long track of gold while the voltage electrodes of the (c) junction are themselves 200nm-long junctions. We have to note that the (c) junctions were patterned with a 3 μm -wide constriction.

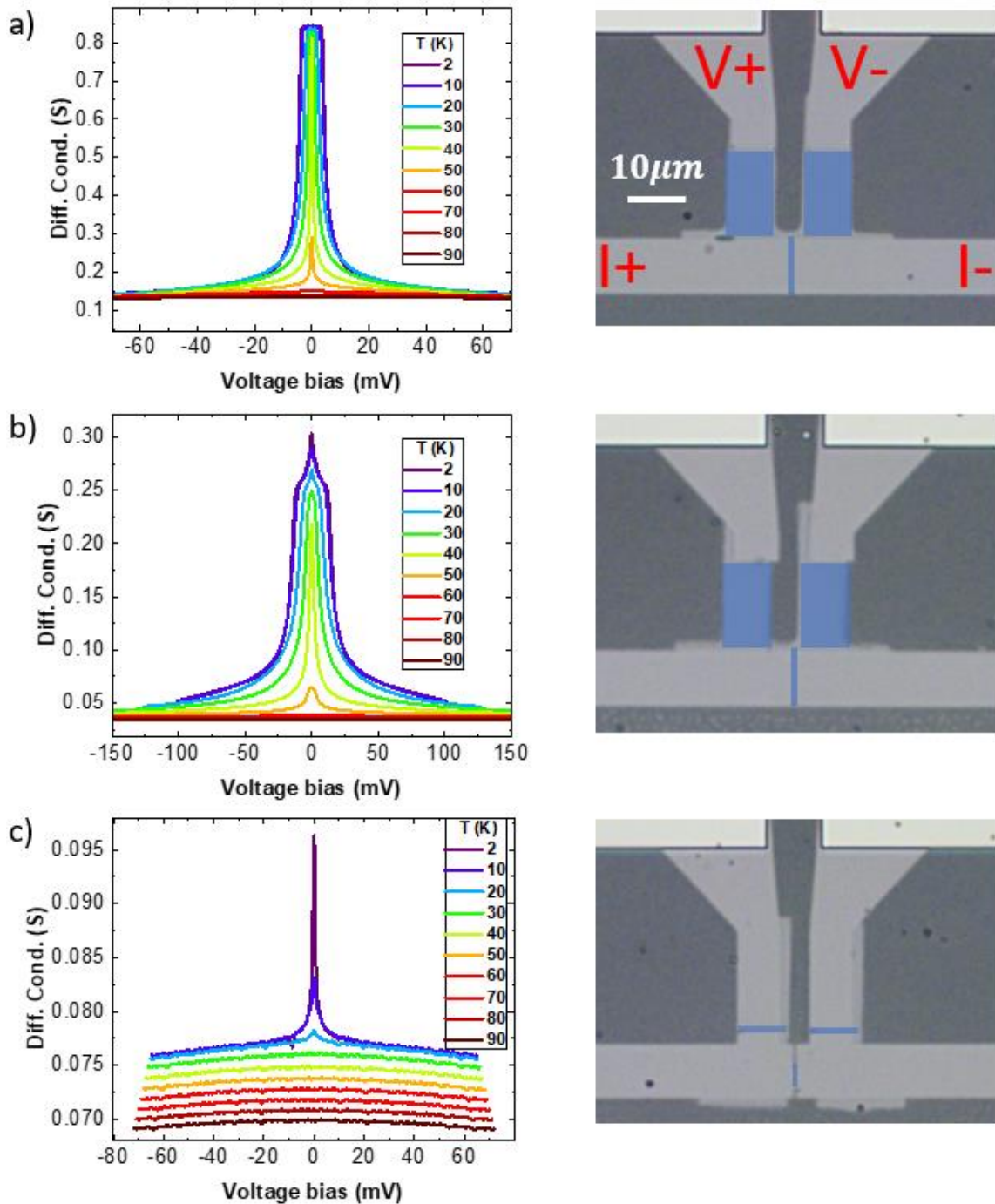


Figure 90 (Left) Differential conductance measurements of 3 different junctions at several temperatures from 2 to 90K: a) R1859BD B2U, b) R1859HD B5U, and c) R1859BG A2D. (Right) Their respective microscope. The colored part in blue corresponds to regions where YBCO was irradiated and is then insulating.

5.2.2 Results

In Figure 90 on the left, I report the differential conductance spectra at several temperatures of the junctions shown on the right and presented in the previous subsection. We can notice here the same diversity in shapes, levels of resistance at high bias ($eV > \Delta_{YBCO}$), and widths δ of the central feature as for the SN junctions presented in the previous section. The device

in a) has a square shape with relatively similar conductance at high bias $\sim 0.15S$ with an observed width $\delta \sim 4mV$. Junction c) shows a sharp peak ($\delta \sim 1mV$) in its conductance spectra. The relatively low conductance at high bias comes from the constriction as observed with other junctions (not shown). The junction in b) has a shape combining a relatively large square feature ($\delta \sim 14mV$) and a peak at zero bias. Its conductance at high bias is around $0.05S$ which is low for a junction without constriction. We can note that was also the case for the SN junction with a similar shape in the previous section (SN junction E7U (c)).

Another point that has to be highlighted is the ratio between the zero-bias conductance and high-bias conductance. For SN junctions, this ratio was between 1.5 and 2 while in the case of SNS junctions, except for A2D (c), the ratio goes from 6 to 9. The evolution of the normalized conductance at zero bias with the temperature is given in Figure 91a. We can see three distinct behaviors. The zero bias conductance of the junction (a) which has a square shape, almost does not evolve until a temperature ($\sim 40K$) where they sharply decrease. G_N^0 of the junction (b) linearly decreases until the same temperature and starts decreasing very fast above that temperature. Finally, the one of junction (c) sharply decreases already at low temperature.

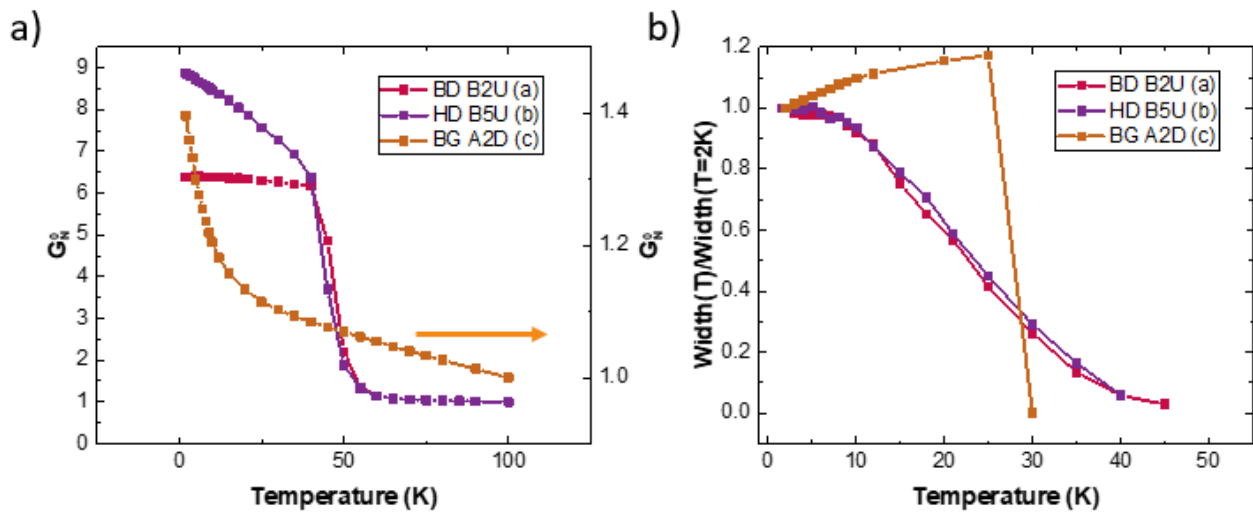


Figure 91 a) Evolution with the temperature of the normalized differential conductance at zero bias for the junctions previously presented. B) Evolution of their normalized visible gap (defined as the maximum of the derivative of the differential conductance) with temperature.

In Figure 91b, I present the evolution of the width of the central feature with the temperature. The normalized width of junctions (a) and (b) behave more or less the same with temperature with a plateau below $10K$ and above a sharper decrease. The width of the (c) junction on the contrary increases with the temperature before falling to zero. As mentioned in the previous section for the junction E2U (b) (see 5.1.2.2), this comes from the fact that the width of this junction is very small ($\delta \sim 1mV$) to be compared with the thermal voltage $k_B T / e \sim 1mV$ at $10K$. As a consequence, until a peak exists (below $30K$), the thermal broadening makes it appear larger than it is in reality. At $30K$ and above, the peak has completely disappeared.

5.2.3 Discussion

I will now discuss these experimental data with the help of the knowledge acquired with SN junctions in the previous section.

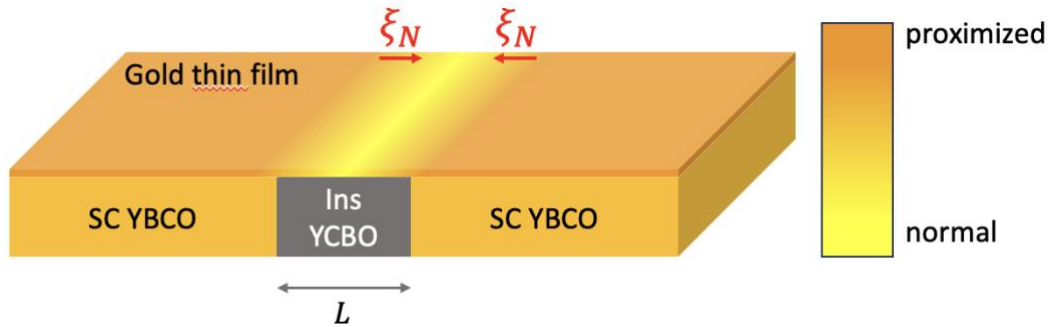


Figure 92 Scheme of a SNS junction. The superconducting YBCO is shown in orange while proximized gold above YBCO is shown in darker orange while proximized gold above the insulating YBCO is represented by a gradient of orange and yellow (normal gold).

5.2.3.1 Absence of Josephson coupling

First, though we are dealing with SNS junctions (for a,b and c), none of them exhibited Josephson coupling. This can be explained by comparing the phase-coherence length ξ_N in the gold deposited by PLD and L as represented in Figure 92. With a mean-free path l around 3nm and a Fermi velocity ($v_F \sim 10^6 \text{m/s}$), we deduce the diffusion constant $D = lv_F/2 \approx 1.5 \times 10^{-3} \text{m}^2/\text{s}$. Then, the phase-coherence length of gold is : $\xi_N = \sqrt{\frac{\hbar D}{k_B T}} \approx 76 \text{nm}$ with $T = 2\text{K}$. As a consequence, **the phase between the electron and hole of the Andreev pair is lost too quickly and it is impossible for a supercurrent to be sustained over 200nm-long junction.**

5.2.3.2 SNS junction as two uncoupled SN junctions

This estimate of the phase-coherence length in the gold thin film also allows to neglect interference effects between quasiparticles going back and forth in the cavity formed by the gold channel contrary to what we observed with graphene [14]. Therefore, **the two SN interfaces of the SNS junction can be considered independently and their contributions just add up.** That explains why the shapes of the SNS junctions are very reminiscent of the ones of the SN junctions. We can compare the plots of the SN junctions in Figure 76 and the ones of the SNS junctions in Figure 90. Since $L = 200 \text{nm}$ is much lower than the typical grain size of YBCO ($> 1 \mu\text{m}$), the orientation of the order parameter is the same for the two SN interfaces. The two contributions have the same shape and simply add up. Especially, their gaps add up.

5.2.3.3 Role of the metallic channel

However, contrary to the SN case where the metallic section between the SN interface and the voltage probe was very large ($> 2 \mu\text{m}$) compared with $\xi_N \approx 76 \text{nm}$, for SNS junctions, it is

no more the case since $L = 200\text{nm}$ and there is proximized gold on both sides of the SNS junctions. This has two consequences.

First, In the case of SNS junctions, the central feature width ($\delta < 20\text{mV}$ for all the SNS junctions) does not reach large values as was the case for the SN junction E4D (a) ($\delta \sim 50\text{mV}$) and E7U (c) ($\delta \sim 180\text{mV}$). The enlargement effect of the central feature I explained in the last section is less important in the SNS case since we expect a lower fraction of the resistance of the metallic channel over the total resistance of the SNS junction ($R_{met} \ll R_{SNS}^{tot}$) compared with the SN case ($R_{met} \sim R_{SN}^{tot}$). Second, the phase-coherence lengths on both SN interfaces represent a larger fraction of the total metallic section. **The resistance of the proximized part being inferior to the normal metallic section, at low temperature and low current, the total resistance of the gold channel decreases.** Though this may allow for a larger conductance at zero bias than in the SN case, this does not explain the factors 6 to 9 between the conductance at zero bias and the conductance at large bias (shown in Figure 91a). This large increase in the conductance in the case of the SNS junctions could also come from an onset of Josephson current. Even if $\xi_N < L$, since the transparency of the SN interface is excellent (see previous section), there may be still some coupling between the macroscopic wave functions of the two electrodes giving rise to a small supercurrent [213]. Though we did not measure any supercurrent, this may be enough to increase significantly the differential conductance at low bias.

5.3 CONCLUSIVE REMARKS

This chapter was dedicated to the measurement of YBCO planar junctions with metals. In the first section, I studied SN junctions formed by a continuous thin layer of gold lying on one side (S) above the *d-wave* superconductor YBCO and on the other side (N) on insulating YBCO. It has been possible to understand the experimental data with one model directly inspired by the BTK theory and another one derived from the circuit theory of superconductivity. The second section focused on SNS junctions and exploited the knowledge acquired with SN junctions since I have shown that these SNS junctions can be treated as a sum of two SN junctions.

There are still challenges and questions to elucidate with these systems. I already started to fabricate new samples with a reduced length of the metallic channel to try reaching Josephson coupling. We would also like to better understand the effect of the angle α of the superconducting order parameter on the differential conductance. Alongside this work with gold, I initiated a new set of samples made with platinum as the thin metallic layer on top of YBCO to see if another metal would change the transport properties of the junctions. Finally, low-temperature STM measurements as done in Ref. [10] could be a very interesting experiment to carry out on my devices since it would allow to see the spatial variation of the induced gap in the metal.

Beyond its intrinsic interest, this chapter can be seen as a preliminary to the study of 2D materials junctions because it allows for easier theoretical analysis. However, junctions with metals probe a regime where the electrical contact with YBCO is excellent as the metal is

grown *in situ* but where the coherence length is very short which is the exact opposite of what we probe with 2D materials where the deposition often makes the electrical contact with YBCO tunnel but where the coherence in the 2D material channel is much larger and can reach a few hundred nanometers as we will see in the next chapter.

6 PLANAR YBCO/GRAPHENE JUNCTIONS

Graphene's discovery opened the 2D materials' research area. From the beginning, superconducting proximity effects in these novel materials attracted much attention due to their really peculiar electronic properties. In chapter 2, we have seen that there have been a lot of studies concerning graphene and *s-wave* superconductors. This chapter will be dedicated to the *d-wave* superconducting proximity effect in graphene. The reason why the *d-wave* symmetry has been much less investigated is the difficulty of having good electrical contact between graphene and the *d-wave* superconducting cuprates, which are both complex and fragile materials, unlike *s-wave* ones. In our laboratory, Perconte et al. [12,14,180] developed a method to transfer CVD-grown graphene onto YBCO and obtained interfaces with good quality. My work in this area has focused on the superconducting proximity effect in graphene/*d-wave* superconductor junctions, particularly focusing on the propagation of superconducting correlation in graphene and on magnetic field effects. For this, I measured planar YBCO/Graphene/YBCO junctions as shown in Figure 93. They are made of two superconducting electrodes in YBCO, covered by a thin layer of gold and separated by YBCO rendered insulating by ion irradiation (see chapter 4). The monolayer graphene acts like a bridge between these two electrodes and forms a kind of Josephson junction.

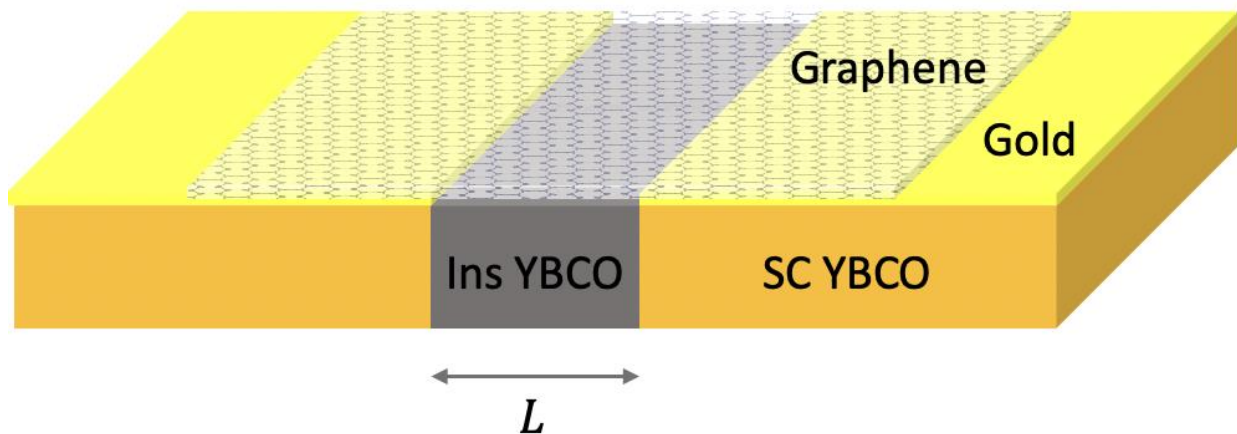


Figure 93 Schematic view of a YBCO/Graphene/YBCO junction as studied in this chapter.

I start this chapter by reviewing the previous studies about *d-wave* superconductors and graphene, mainly the one from my lab with YBCO [12]. In the second part, I describe the results of the coherent propagation of Andreev *d-wave* pairs in a graphene channel on hundreds of nanometers. The measurements were carried out by my predecessor David Perconte before I started my PhD, and I only took part in the analysis of the results. Finally, I present the results I obtained on the influence of a magnetic field on the differential conductance of YBCO/Graphene/YBCO junctions.

6.1 PREVIOUS WORKS ON D-WAVE SUPERCONDUCTORS/GRAPHENE JUNCTIONS

Attempts to couple *d-wave* superconductors with graphene are relatively scarce. Sun et

al. [138] reported in 2014 the fabrication of Hall bars with graphene on top of YBCO and found highly resistive electrical contacts between the two materials. This study is the only one reporting transport measurements between *d-wave* superconductors and graphene before the article of Perconte et al. [12], prior to my PhD, that I will review in the following. More recent work, besides the work in our lab, includes that from Wu et al. [214], who coupled exfoliated $\text{Bi}_2\text{Sr}_2\text{CaCu}_2\text{O}_{8+x}$ (BSCCO) and graphene. Their measurements of the differential conductance spectrum of the device, though tunnel, show strong evidence for an induced gap in graphene. Another study [141], published recently, exhibited transparent BSCCO/Graphene junction with evidence for Klein tunnelling of Andreev quasiparticles as shown in [12] with YBCO and graphene.

I will summarize the state of the art in my laboratory previous to the PhD, which essentially corresponds to the article of Perconte et al. [12], This work focuses on the study of large junctions, patterned by optical lithography techniques presented in chapter 4. Here, large means that the length $L = 5\mu\text{m}$ of the junction, pictured in Figure 93, is much larger than the phase-coherence length in graphene, $l_\phi \sim 100 - 300\text{nm}$ (typical for CVD-grown graphene). Since any induced Andreev pair correlations will decay on a length shorter than the length of the graphene canal the graphene/YBCO interfaces can be considered as independent. I will first present the particularities of working with high- T_c superconductors for proximity devices and contact quality. Then, I will describe a model that helped to describe the experimental data. Finally, I will review the experimental results obtained by measuring the differential conductance of the junctions at low temperatures and by applying a gate voltage. All the developments described here will allow for the other studies performed in this chapter, and in particular for the study of shorter junctions in 6.2.

6.1.1 Fabricating high-quality interfaces and measurement configuration

Fabricating transparent interfaces between YBCO and graphene is complicated for several reasons. As we have seen in chapter 2, YBCO is a complex oxide, fragile against heating and a low oxygen pressure atmosphere. Moreover, the YBCO top layer tends to deteriorate if not carefully protected. Because of all these limitations, it is difficult to grow graphene directly on top of YBCO, for instance by CVD [190]. Reversely, we cannot grow YBCO on top of graphene, contrary to what is done with low- T_c superconductors [127,177,134,215], like Aluminium or Niobium, since it will destroy the graphene monolayer below and will not grow anyway because of the lattice mismatch with graphene. **These two limitations required the development of a dedicated method to deposit graphene on the superconductor.** This method has been explained in detail in chapter 4 and is based on the wet transfer of CVD-grown graphene. The patterning of the graphene monolayer is also described in chapter 4.

The resulting device is represented in Figure 94a. The yellow areas correspond to the superconducting tracks with the thin gold layer above. The brown regions are areas where YBCO was irradiated by O^+ ions and is now insulating and where gold was etched to avoid short circuits. The patterned graphene monolayer is highlighted by a red outline. To measure the differential conductance shown in Figure 94 taken from Ref. [12], the measurement configuration is such that the current goes from electrode 1 to 4 while the voltage is

measured between 3 and 4. This 3-probes configuration allows to measure the conductance of a single Au/Graphene interface located on the side of the electrode 4 (see Supplementary of Ref. [12]). Indeed, between 3 and 4, where the voltage drop is probed, the YBCO leads are in the superconducting state since the applied current is low ($I < 20\mu\text{A}$) giving a low current density ($j < 4 \times 10^3 \text{A} \cdot \text{cm}^{-2}$) which is much below the critical current density $j_c \sim 10^6 \text{A} \cdot \text{cm}^{-2}$ for YBCO at 77K. Moreover, the YBCO/Au interface has a negligible resistance contribution. This comes from the study of metallic SNS junctions presented in the previous chapter, from which we deduced that the resistance due to the YBCO/Au interface, only part of the overall resistance ($< 30\Omega$), is small compared with the overall resistance of YBCO/Graphene junctions ($\sim 1\text{k}\Omega$).

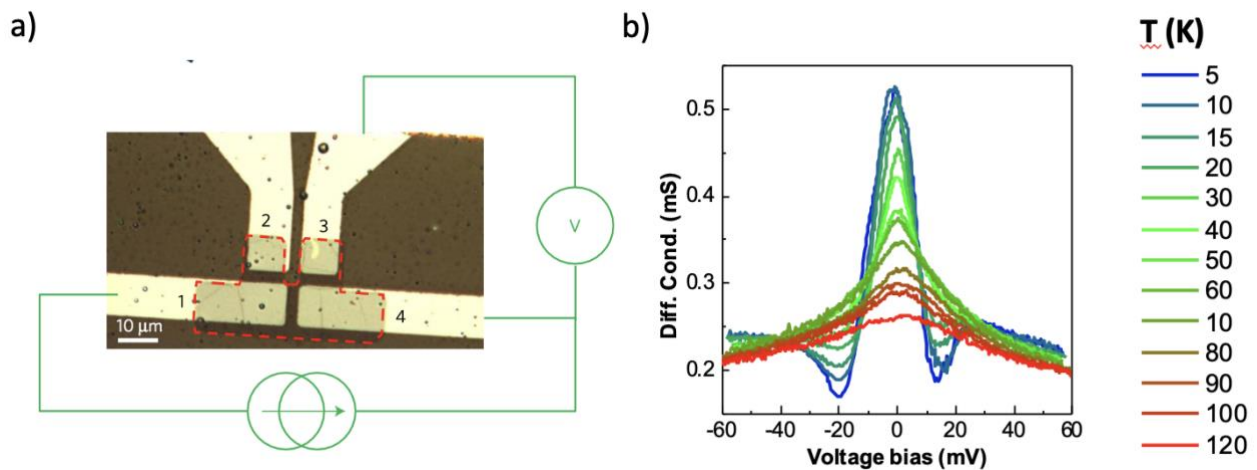


Figure 94 a) Microscopic image of a large junction. The graphene sheet is emphasized by a red contour. The 3-probe configuration used in b) is shown. b) 3-probe measurement of the differential conductance of a large junction as a function of the voltage bias and for different temperatures. Figures taken from Perconte et al., Nat. Phys. **14** (2017).

6.1.2 Differential conductance at low temperature

The differential conductance spectra presented in Figure 94b were taken at different temperatures going from 120K, where YBCO is in its normal state so there are no effects linked to its superconducting properties, to 5K, a temperature at which superconducting and proximity effects should be the strongest due to a fully opened gap in YBCO and enhanced electronic coherence. At 120K, this conductance is slightly enhanced ($\sim 20\%$) close to zero bias while, as the temperature decreases, a zero bias peak emerges as well as two conductance dips at around 20mV. At 5K, the peak reaches a value around twice the one measured at 60mV outside the superconducting gap (typically $\sim 20 - 30\text{meV}$ in YBCO). This is typical of a transparent SN junction as I presented in chapter 3, but also has some signatures due to the presence of graphene. Using a high- T_c superconductor with larger gaps like YBCO should expectedly allow for observation of specular Andreev reflection. However, in our samples, the doping level of the graphene monolayer is too high to observe specular Andreev reflection and in the following [12], we will assume $E_F \gg \Delta$.

6.1.3 Model

To model the interface, Perconte et al. [12] used the model of Linder and Sudbø [13], in the *d-wave* case, by assuming that (Figure 95a and b):

- 1) The graphene atop the superconductor is proximized and has a gap Δ with exactly the same symmetry as the superconductor below (*s-wave, d-wave,...*).
- 2) Graphene far from the superconductor is in the normal phase.
- 3) There is a region (N') in between which is not superconducting but has a different doping with energy U_0 than the other two regions as shown in Figure 95b. In this model, corresponding to a SN'N junction, we will consider only the interface between the proximized graphene (S) and the normal graphene (N) far from the superconductor, as schematized in Figure 95a.

Once all the parameters are fixed, the resolution method is similar to the one explained in chapter 3. Except that, in the case of graphene, the quasiparticles are described by a spinor, as already seen in chapter 2. The consequence is that the BdG wavefunction is described by a 4-vector (only 2-vector for a normal metal) and the BdG Hamiltonian by a 4x4 matrix. We match the wavefunctions at the two interfaces and we get the reflection (and transmission) coefficients. The BTK conductance is then given according to the formula 3.13 (chapter 3).

6.1.4 Tunability with a back gate voltage

Experimentally, we can modify the Fermi level E_F of the normal region by applying a voltage to the back gate made of STO (see Figure 95a) but not the one of graphene above the superconductor since this latter screens the electric field. On the colormap shown in Figure 95c, we can get Figure 94b if we follow the "C" horizontal dashed line. The doubling of the conductance at zero bias is a strong argument in favor of the presence of Andreev reflection at the interface between proximized graphene and normal graphene. But if we fix the voltage bias and go along the back gate voltage, there are oscillations at all energies due to the variation of the Fermi level of the normal graphene E_F with the back gate voltage.

We will now use the SN'N model to understand these oscillations and extract relevant parameters through a fitting. In the measurement shown Figure 95c, there is a periodic modulation of the differential conductance with the applied back gate voltage. The model of a SN'N junction takes into account the Fermi energy E_F of the normal region and assumes a doping U_0 of the N' region. Charge carriers experience Andreev reflection at the SN' interface. Following the scheme of Figure 95b and the explanation of Klein tunneling [43,216] given in chapter 2, the resulting charge carriers will go through this potential barrier simply acquiring a phase $\chi = \frac{w(E_F - U_0)}{\hbar v_F}$ where w is the width of the N' region and v_F is the Fermi velocity of graphene. This phase factor changes if we vary E_F through the back gate voltage and it modulates the differential conductance due to destructive and constructive interference in the "quantum well" (quasiparticles are not trapped here).

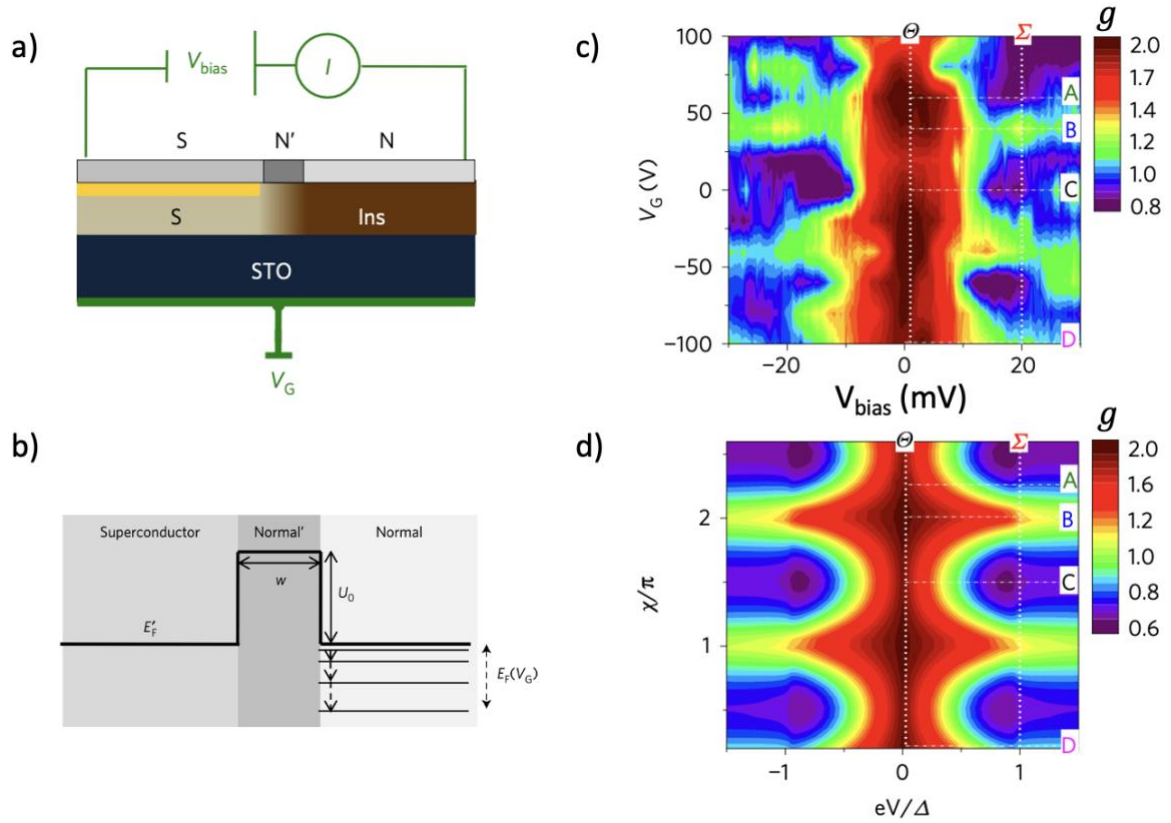


Figure 95 a) Scheme of the gating and measurement wiring with the three distinct regions of graphene (S, N' and N) in agreement with the model explained in the main text. b) Energy level diagram of these three regions with the tunable Fermi level of the normal zone with a gate voltage. c) Experimental 2D maps of the normalized differential conductance as a function of the voltage bias (x-axis) and back gate voltage (y-axis) at 5K. d) Numerical simulations reproducing the experimental observation with $\chi = \frac{w(E_F - U_0)}{\hbar v_F}$. Figures taken from Perconte et al., *Nat. Phys.* **14** (2017).

The calculation in Figure 95d shows the normalized differential conductance as a function of the energy eV normalized by the proximized gap Δ (x-axis) and the phase factor $\chi = \frac{w(E_F - U_0)}{\hbar v_F}$ (y-axis). This phase is the phase gained by electrons or holes in the N' region. **As we change the back gate voltage, we change the value of E_F , and as a consequence χ resulting in constructive or destructive interferences in this quantum well of width w . The excellent match between the experiment and the numerical calculation allows to confirm the SN'N model and explain the origin of the conductance oscillations. Indeed, the periodic modulation measured with the back gate voltage is Klein tunnelling of *d-wave* Andreev pairs. A similar observation has recently been made with exfoliated graphene and another *d-wave* high T_c superconductor $\text{Bi}_2\text{Sr}_2\text{Ca}_1\text{Cu}_2\text{O}_{8+\delta}$ (BSCCO) and explained with the same 3 regions model [141].**

6.2 COHERENT TRANSPORT OF ANDREEV D-WAVE PAIRS

Motivated by the observation of Andreev reflection at a single interface and its modulation with a gate voltage, we decided to study shorter junctions made of two YBCO/Au/Graphene

interfaces [14] seeking for Josephson coupling between the two electrodes. In these devices, the length L of the junctions (see Figure 93) is *a priori* close to the phase-coherence length of graphene, l_ϕ . While we have not obtained Josephson coupling so far in our experiments due to the lack of two transparent interfaces on the same junctions, I will show you in this section that it is possible to show that the induced *d-wave* Andreev pairs in graphene propagate coherently in the graphene channel acting as a tunable cavity. This section shows results [14] that were measured by David Perconte before my PhD. I contributed to the understanding of the observed behavior. In the first part, I briefly go through the fabrication, measurement configuration, and experimental results. Then, I describe the model and finally, I will show how this model accounts for the behavior of these junctions.

6.2.1 Geometry of the junctions and measurements

The patterning of short junctions (of length $L < l_\phi$), required electronic lithography, allowing to fabricate junctions of a few 100nm to 1 μ m, as explained in chapter 4. A typical junction is shown in Figure 96a. As previously presented, the graphene layer is patterned to fit the superconducting tracks. Figure 96b and c are the corresponding unzoomed optical images of the device before and after the metallic gate fabrication, described in chapter 4. The electrodes numbered from 1 to 4 allow the measurement of the differential conductance of the junction in 2-, 3- or 4-probes measurements while the top gate makes it possible to change the Fermi level of graphene below it in complement of back gating.

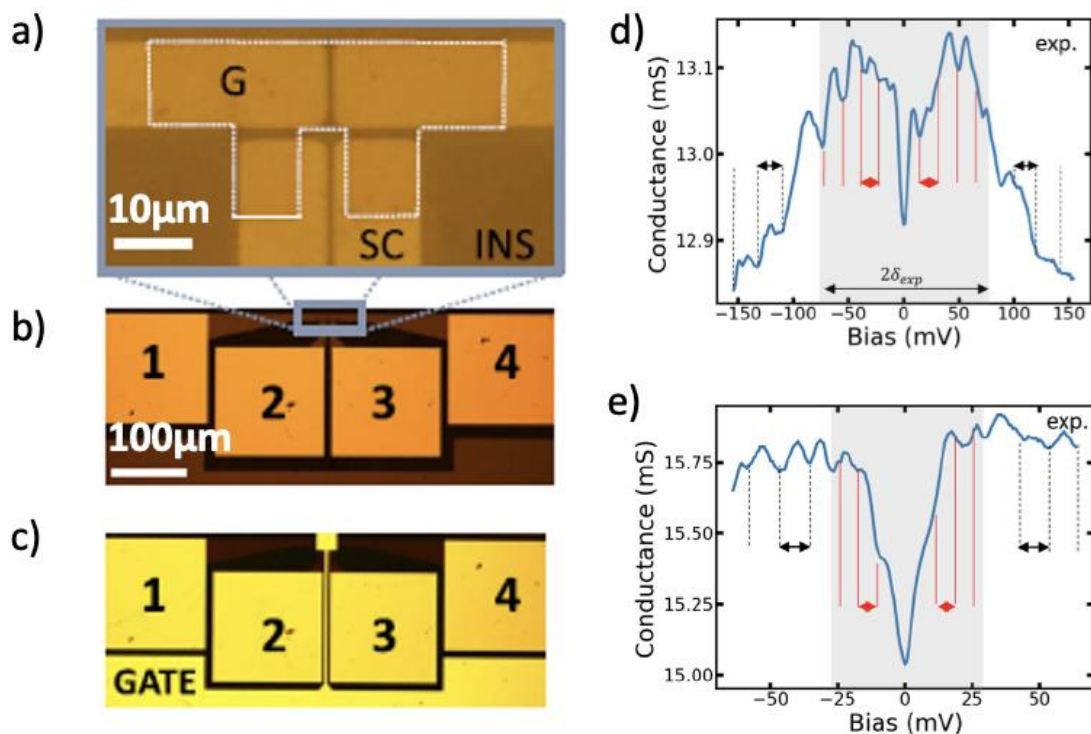


Figure 96 a) Microscope image of a typical junction with the graphene layer highlighted by the white dotted line. The superconducting tracks are lighter than the insulating (irradiated) regions. b) A larger view of the device with the four gold contacts. c) Device at the same scale but this time after the last fabrication step: the metallic gate deposition. d) Experimental differential conductance versus the voltage bias at 3.2K of the junction B3U. e) Same for the

junction B4U. The vertical lines point towards the oscillations. The grey area stems from the regions inside the proximized gap. d) A scheme to explicit the interference effects occurring both with *d*-wave Andreev pairs (left) and usual charge carriers (right) in the graphene cavity. Figures taken from Perconte, Seurre et al., *Phys. Rev. Lett.* **125**, 087002 (2020).

The plots in Figure 96d are measured in a 3-probes measurement, the currents being injected between electrodes 1 and 4 and the voltage measured between 1 and 3. This allows measuring the interface YBCO/Au/Gr (on the side of electrode 1) and the graphene channel. It then avoids the voltage drop at the second interface close to the electrode 4. Thus one measures the YBCO/Au/Graphene interface, the proximized graphene/normal graphene interface, and the graphene channel in series. The two differential conductance spectra presented in Figure 96d and e exhibit a decrease inside the grey area corresponding to a voltage bias $|\delta_{exp}| < 75\text{mV}$ for B3U and 25mV for B4U. This is reminiscent of a tunnel behavior of SN junction as seen in chapter 3. There are also oscillations highlighted by the red and black vertical dashed lines. The red and black oscillations have two distinct periods.

6.2.2 Modelization of the system

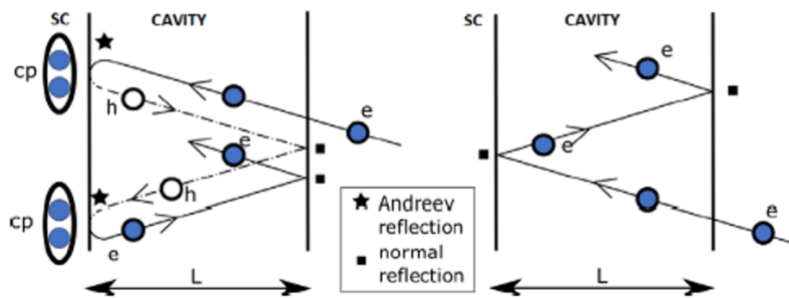


Figure 97 A scheme to explicit the interference effects occurring both with *d*-wave Andreev pairs (left) and usual charge carriers (right) in the graphene cavity. Figure taken from Perconte, Seurre et al., *Phys. Rev. Lett.* **125**, 087002 (2020).

In comparison with the single interface case, the presence of a second interface confines the charge carriers inside a cavity made of graphene. Indeed, these junctions correspond to cases where one interface is transparent (Andreev reflection probability is close to 1) while the other one is tunnel with the usual reflection dominating. This situation is in fact **a Fabry-Pérot cavity**. As pictured in Figure 97, both the usual charge carriers on the right or the *d*-wave Andreev pairs can experience interference effects like in a Fabry-Pérot interferometer. Indeed, for the former (on the right-hand side), this is a graphene cavity of length L and they are reflected or transmitted at each end of the cavity leading to the constructive interference condition: $2kL = 2n\pi$ where k is the wavevector of the charge carrier since it travels twice the cavity for one cycle. In the case of the Andreev particles (Figure 97 on the left-hand side), an electron enters the cavity and is Andreev reflected into a hole. If the other end of the cavity is not as transparent, there is no Andreev reflection but only normal reflection, so the hole is reflected back. At the transparent interface, this hole is Andreev reflected into an electron that follows the same path and is reflected into an electron. Altogether, one complete cycle is $4L$ giving the condition: $4kL = 2n\pi$. Since in both

cases, $k = \frac{V}{\hbar v_F}$ where V is the voltage bias applied to the cavity and v_F is the Fermi velocity in graphene, we expect two characteristic frequencies for the modulation: $V_{long} = \frac{\hbar v_F}{2L}$ corresponding to the interference of usual charge carriers and $V_{long} = \frac{\hbar v_F}{4L}$ for the interference of Andreev pairs.

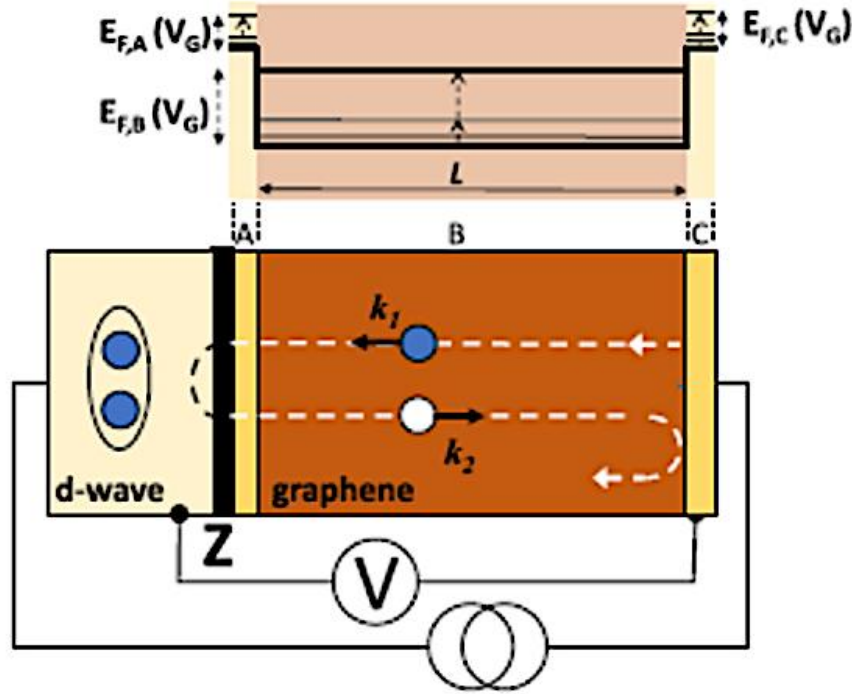


Figure 98 Scheme summarizing the main ideas of the developed model. The top part represents the energy levels at stake while the bottom scheme represents the different regions and the measurement configuration. Figure taken from Perconte, Seurre et al., *Phys. Rev. Lett.* **125**, 087002 (2020).

I contributed to the elaboration of a numerical model that considers the above interference phenomena as well as the association in series of different interfaces to explain more quantitatively the experimental data. This model is schematized in Figure 98. As previously said and shown on the scheme, the measurement is carried out in a 3-probes configuration. Experimentally, we found it difficult to get a symmetric junction with two transparent interfaces. The model takes it into account by considering only Andreev reflection on the left side while on the other side, there are only normal reflections. Then, there are two contributions to the final conductance, the YBCO/Au/Graphene interface conductance, G_1 (using the extended BTK model for d -wave superconductor normal metal junction), and the proximized graphene cavity, G_2 . The latter incorporates the Linder and Sudbø model I presented in the previous section and the propagation/reflection of the Andreev electrons and holes as well as the usual charge carriers. These two contributions are:

$$G_1(V_1) = \int_{-\frac{\pi}{2}}^{\frac{\pi}{2}} d\theta (16(1 + |\Gamma_+|^2) \cos(\theta)^4 + 4Z^2(1 - |\Gamma_+ \Gamma_-|^2) \cos(\theta)^2) / (|4 \cos(\theta)^2 + Z^2(1 - \Gamma_+ \Gamma_-)|^2) \quad 6.1$$

With: $\Gamma_{+/-} = eV_1/|\Delta(\theta_{+/-})| - \sqrt{(eV_1/|\Delta(\theta_{+/-})|)^2 - 1}$ and $\theta_+ = \theta$, $\theta_- = \pi - \theta$. Z is the scattering parameter of the YBCO/Au/Graphene interface, $\Delta(\theta) = \Delta \cos [2(\theta - \alpha)]$ with θ the angle of the incident electron and α the angle between the superconducting order parameter and the interface. V_1 is the voltage drop across this interface. As we have seen in the previous chapters, the extended BTK model does not present oscillations and therefore only the homojunction contribution G_2 will produce the oscillations:

$$G_2(V_2) = \int_{-\pi/2}^{\pi/2} d\theta (1 - r^2) \cos(\theta) + r_A^2 \cos(\theta_A) \quad 6.2$$

$\theta_A = \arcsin \left((eV_2 + E_f)/(eV_2 - E_f) \sin(\theta) \right)$ and θ the electron angle of incidence with respect to the interfaces. r and r_A depend on many parameters I will detail in the following. This contribution will give rise to the oscillations in the conductance spectrum. With the same method used in chapter 5, we compute the current $I = \int G(V)dV$, obtain $G_1(I)$ and $G_2(I)$. This allows us to compute the conductance when the two building blocks are connected in series:

$$G(I) = \frac{1}{1/G_1(I) + 1/G_2(I)} \quad 6.3$$

Using $V = \int \frac{1}{G(I)} dI$, we finally obtain $G(V)$.

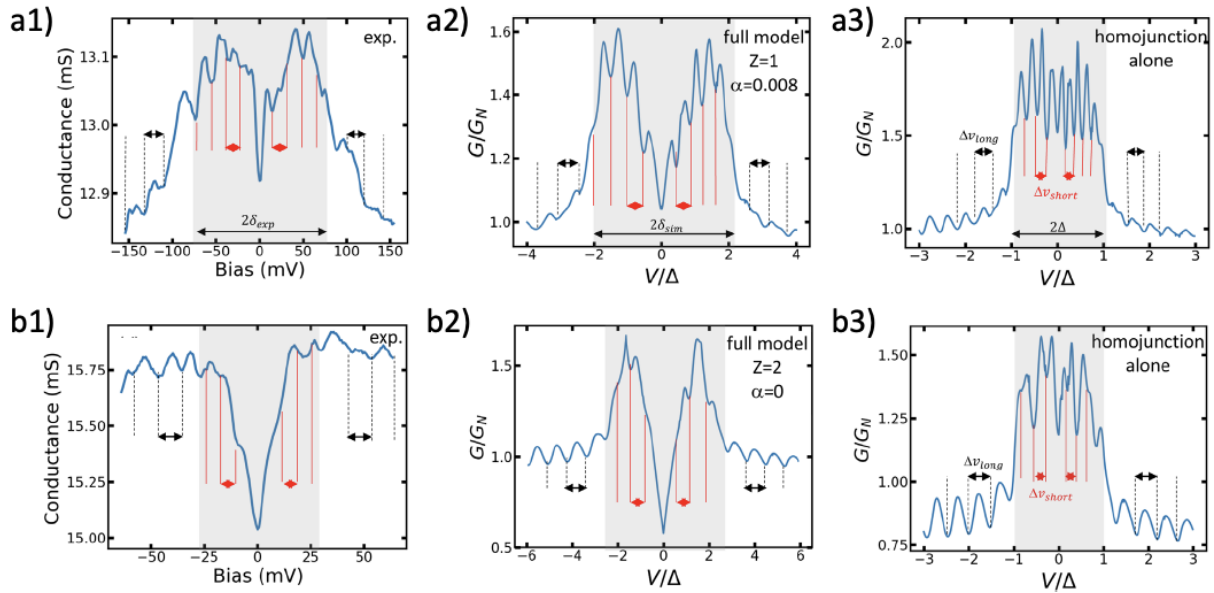


Figure 99 The plots in a and b come respectively from the junction B3U and B4U whose experimental differential conductances have already been shown earlier but are repeated for clarity. For each, 1) is the experimental differential conductance versus the voltage bias at 3.2K, 2) is the full model simulation of the normalized conductance against the normalized energy and 3) is the simulation of the differential conductance of the proximized graphene cavity only. For all plots, the grey-shaded area stems from the superconducting gap-related feature. Figures taken from Perconte, Seurre et al., Phys. Rev. Lett. **125**, 087002 (2020).

There are two regimes of oscillations with different periods. Inside the superconducting gap feature (grey shaded in Figure 99a1 and b1), the period is ΔV_{short} due to the *d-wave* Andreev pairs. On the contrary, outside this region, the period is ΔV_{long} only due to the interferences of the usual charge carriers. For the two junctions B3U and B4U, these oscillations are present on the differential conductance due to the homojunction only which are plotted respectively in Figure 99a3 and b3. The full model including the homojunction and the YBCO/Au/Graphene interface is given in Figure 99a2 and b2. Here, we review the role of each parameter in the simulation by taking the two examples of Figure 99b and c. To determine the period of oscillations ΔV_{short} and ΔV_{long} , the important parameters are $\Lambda = \frac{L}{\lambda_{F,A}}$, the reduced cavity's length where $\lambda_{F,A}$ is the Fermi wavelength in the region A, and the reduced Fermi energy in the region A $\varepsilon_{F,A} = \frac{E_{F,A}}{\Delta}$ with Δ the superconducting energy gap induced in A since they determine the periods of oscillations inside the cavity. $\varepsilon_{F,B} = \frac{E_{F,B}}{\Delta}$ and $\varepsilon_{F,C} = \frac{E_{F,C}}{\Delta}$ only changes the amplitude and the phase of the oscillations but not their periods. The scattering parameter Z and the angle α between the YBCO *d-wave* antinode and the interface of the homojunction determine the shape of the background, especially the presence of a dip or a peak as we have seen in chapter 3. The angle α , the signature of *d-wave* superconductivity, is particularly important since the behavior of some junctions cannot be interpreted in the absence of this parameter that is to say in the framework of the (*s-wave*) BTK theory [5].

Another example of junctions, for which this time the conductance increases at low bias is shown in Figure 100a. To reproduce the experimental data in that case, it is necessary to use $\alpha = \pi/8 \approx 0.39$ as represented in Figure 100b. This junction presents the same oscillatory behavior with two distinct periods inside and outside the superconducting gap, highlighted by the red and black dashed lines. The 2D colormap in Figure 100c shows the evolution of the oscillations when we apply a voltage on the top gate electrode. We can see oblique patterns coming from the modulation by the gate V_G . The theoretical model used for single differential conductance spectrum reproduces very well these obliques lines which suggest that E_F and therefore k_F varies proportionally with V_G as in the previous section. This modulation then comes once again from the condition: $2Lk_F = 2n\pi$.

As represented in Figure 100b and d, the numerical calculation allows to well describe the shape and oscillations of the conductance measured during these experiments. From these fits, it is possible to extract the period of oscillations of both *d-wave* Andreev pairs and normal charge carriers in the graphene cavity. The y-axis of Figure 100e displays the corrected period measured for both types of carriers (red dots for Andreev pairs and black dots for usual carriers) in five different samples with different L . Indeed, due to the presence of the background resistance in series with the homojunction, the measured period is distorted (larger) compared with the one expected by the cavity characteristics since there is a voltage drop outside the graphene cavity. Fortunately, we can extract this value from the simulation because we can "subtract" the background due to the YBCO/Au/Graphene interface and only consider the homojunction as plotted in Figure 99a3 and b3. In Figure 100e, the two dotted lines correspond to the Fabry-Pérot expected periods with respect to

L . These interferences testify that there is coherent propagation of both *d-wave Andreev pairs and usual charge carriers*. However, we noticed that the amplitude, though large for $L \in [100,300]$ nm becomes much smaller for larger junctions suggesting the coherence length may be smaller than $1\mu\text{m}$ but more of the order of 300nm at $\sim 4\text{K}$ which is in agreement with mean-free path in CVD graphene between 100nm and 260nm obtained by charge carrier mobility experiments [217].

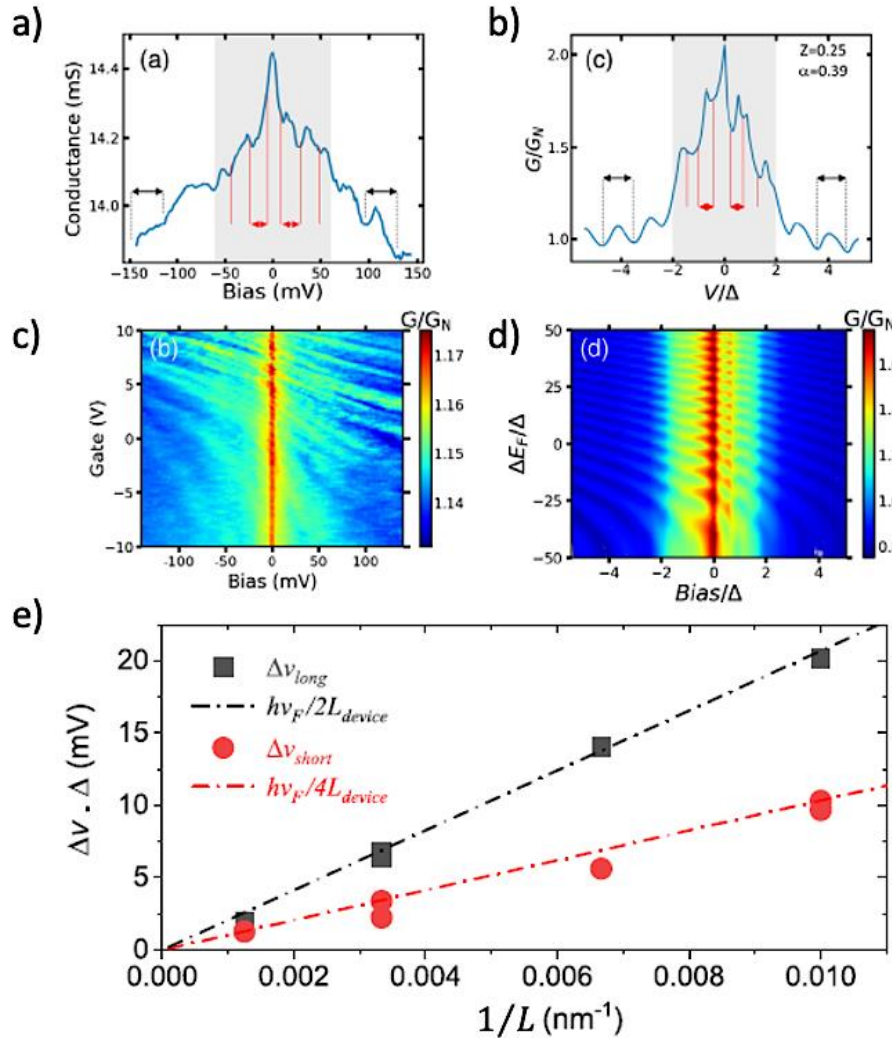


Figure 100 a) Experimental differential conductance against the voltage bias. The two distinct periods of oscillations are highlighted by red arrows (from Andreev pairs interferences) and black arrows (usual charge carriers interferences). The shaded area corresponds to the superconducting gap feature. b) Numerical simulation of the differential conductance against the normalized voltage V/Δ with the same notations as a). c) Experimental 2D map of the differential conductance with respect to the voltage bias (x-axis) and the voltage applied to the top gate electrode (y-axis). d) Numerical 2D map simulation of the differential conductance as a function of V/Δ and the reduced Fermi energy in region B, $\varepsilon_{F,B} = \frac{E_{F,B}}{\Delta}$. e) Corrected period of oscillations $\Delta v \cdot \Delta$ both for short and long oscillations as a function of L^{-1} for different devices. The red (respectively black) dotted line is the expected interference period for the Andreev pairs (the usual charge carriers) for a Fabry-Pérot interferometer. Figures taken from Perconte, Seurre et al., Phys. Rev. Lett. **125**, 087002 (2020).

These two sections have proven that not only *d-wave* superconducting correlations can be induced by YBCO into graphene but that the superconducting correlations survive in graphene up to several hundreds of nanometers motivating further works in my thesis. Most of my efforts have consisted of measuring magnetic field effects. These are summarized below.

6.3 MAGNETIC FIELD EFFECT ON SHORT JUNCTIONS

All over my PhD, I studied oscillations in the magnetoconductance, which I measured in many junctions as shown for example in Figure 101b. They correspond to junctions with intermediate transparency, that is to say with barrier transparency lower than the junctions studied in the first section. In this paragraph, I will describe in the first part the transport properties of these junctions, and in the second part, I will discuss possible explanations for the oscillations in the magnetoresistance.

6.3.1 Physical description of the oscillations in the magnetoresistance

6.3.1.1 Geometry and first measurements

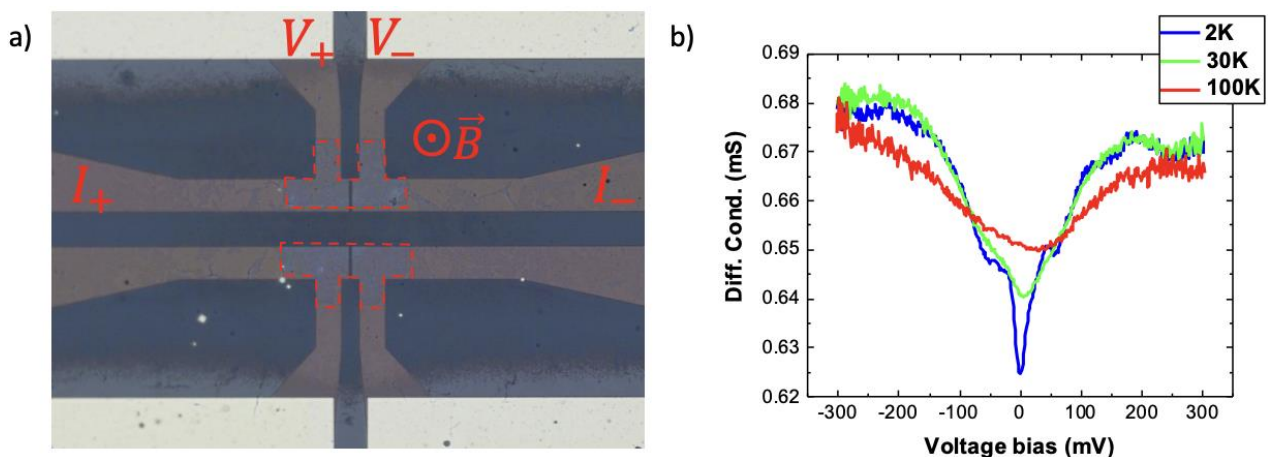


Figure 101 a) Microscope image of two devices (U and D) with the graphene layer highlighted by the red dotted line and the magnetic field orientation considered in the following unless otherwise stated. The typical electrical configuration is given for the upper device. b) Differential conductance vs voltage bias of the junction R1739BD C3U at several temperatures measured in the delta mode configuration of the instruments.

In the previous section, I showed the behavior of YBCO/Graphene/YBCO junctions having a sub-micron graphene channel between the two superconductors. The junctions described in this section have the same geometry as the ones studied in section 6.2 and an example is given in Figure 101a, with L going from 50nm to several hundreds nm. Some devices, so-called double junctions, are made of two junctions spaced by 200 or 300nm of superconducting YBCO below as shown in Figure 102. This last geometry with two junctions in a row is an attempt to increase the superconducting coupling between the two electrodes. Indeed, the in-between superconducting island aims at strengthening the superconducting proximity effect in the whole junction.

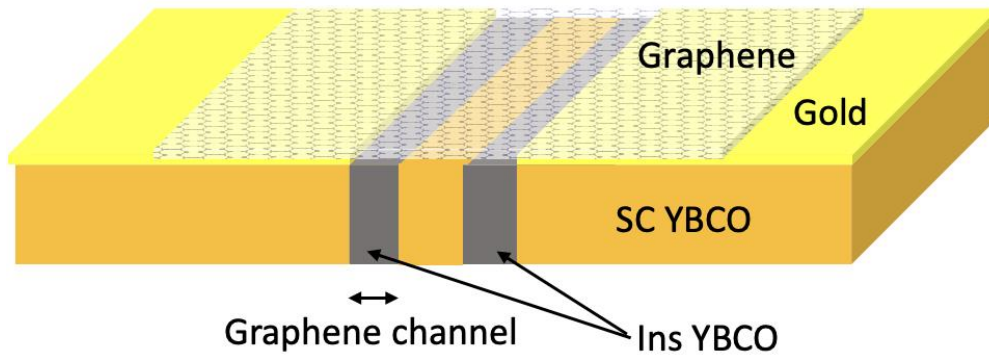


Figure 102 Scheme of a so-called double junction in the manuscript. L is the distance between the superconducting electrodes.

Unless otherwise stated, the magnetic field will be out-of-plane as pictured in Figure 101a. We noticed the junctions with intermediate transparency have a peculiar perpendicular magnetic field dependence compared with either the more transparent and more tunnel junctions. The differential conductance of the junctions is measured with the “delta mode” described in chapter 4 and in a 4-probes configuration, the current being injected along the horizontal superconducting track (in Figure 101a) and the voltage drop measured between the two vertical tracks.

The differential conductance of the examples in Figure 101b (junction C7U) is typical of the studied junctions. It has a dip in its differential conductance spectrum at zero bias over a range $\pm 25\text{mV}$ compared with its value at $\pm 200\text{mV}$. It is going deeper and deeper as we are lowering the temperature. This feature is reminiscent of conductance of a SN junction upon the opening of a superconducting gap below T_c . The typical width of this gap is $\delta \sim 25\text{mV}$ which is consistent with the superconducting gap of YBCO. This central feature is superimposed on a background present at all temperatures. For all junctions showing magnetoresistance oscillations in this chapter, the conductance is of the order of $\sim 1\text{mS}$.

6.3.1.2 Magnetoresistance oscillations

In Figure 103, I present the measurements and data treatment of one of the junctions for which I measured magnetoresistance oscillations. These data correspond to the sample R1739BD C7U. In particular, Figure 103a presents differential conductance spectra for different magnetic fields ranging from 0 to 1T. In addition to a decrease in the background conductance, as the magnetic field increases, a first raw observation of the conductance allows seeing an oscillation of the conductance close to zero bias. Indeed, the conductance decreases when increasing the magnetic field from 0 to 0.2T and increases again when increasing the field to 0.4T. This oscillation can be characterized by plotting the differential conductance at a fixed voltage bias as a function of the magnetic field, or by measuring directly the magnetoresistance as done in Figure 103b. This measurement was taken by sweeping the magnetic field (at 0.1T/min) while measuring the resistance for a given value of current. This plot exhibits oscillations up to 2T as well as a peak of resistance at zero magnetic field. To highlight these oscillations, I removed the background. I chose to do so by smoothening the experimental data with an average of over 200 points which washes out

the oscillations but keeps the background as shown in the red plot in Figure 103b. We then plot the difference between the experimental data and the smoothed curve in Figure 103c. This procedure has been applied in reference [218] to extract oscillations from a slow-varying background. This treatment effectively reveals that the oscillations' period is $\sim 0.4\text{T}$.

The strategy used above to subtract the background allows to compute the Fast Fourier transform (FFT) of the signal, which is shown in Figure 103d. On this FFT plot, two frequencies (in T^{-1}) appear and give periods around 0.4T and 0.8T which are in agreement with the value previously found. In the following, the graph showing the magnetic field oscillations' periods will be obtained from this spectral analysis.

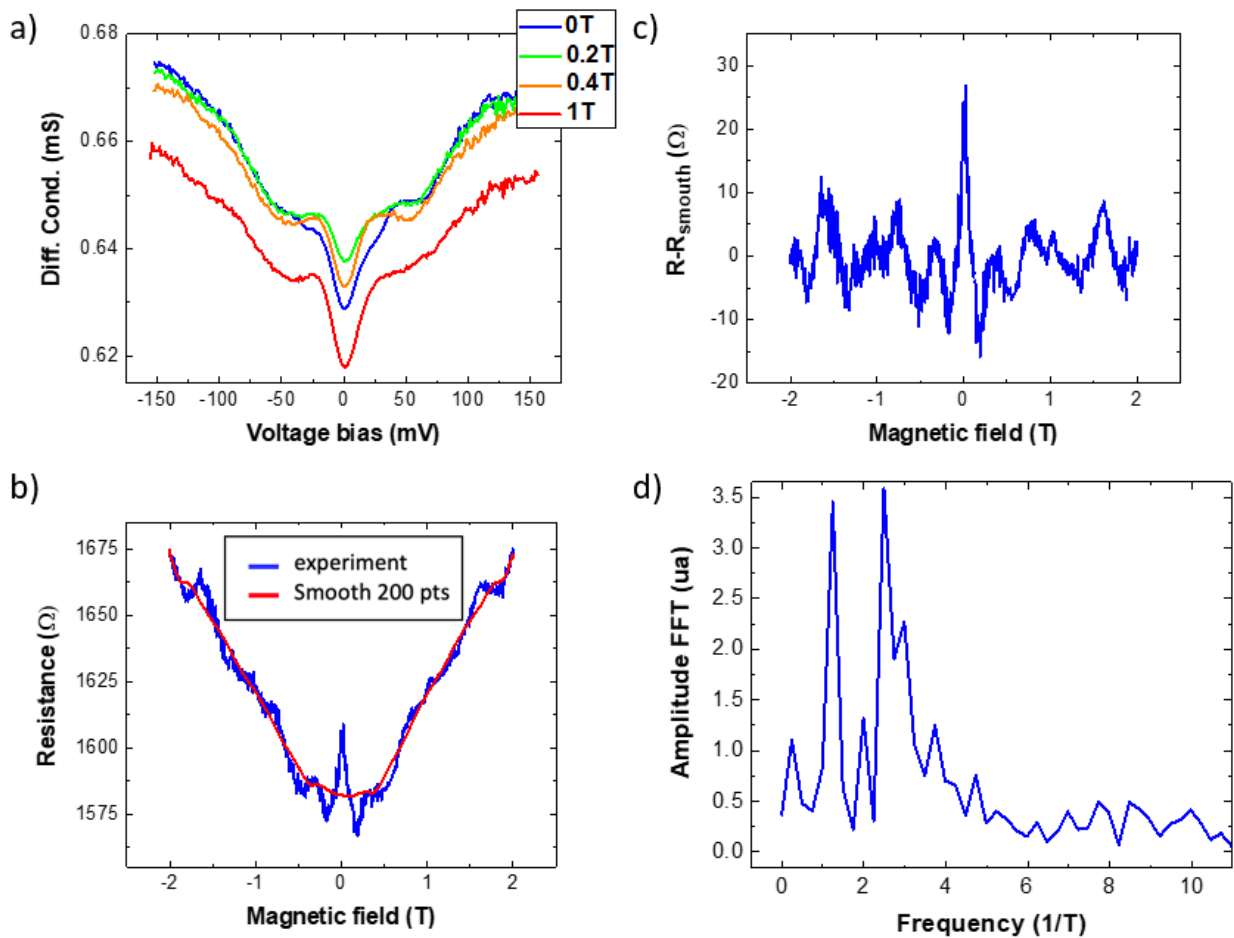


Figure 103 All these data were taken with the junction R1739BD C7U: a) Differential conductance vs voltage bias at several magnetic fields. b) Magnetoresistance at 2K (blue) and a 200-point smoothed plot of it (red). c) Difference between the magnetoresistance and its smoothed version to enhance the oscillations. d) FFT of the plot shown in c).

I have measured the type of effects described above in number of junctions. Some of them being presented below. For instance, the measurements for the junction R1123HG B3D are presented Figure 104. I first look at differential conductance spectra at different temperatures to appreciate the evolution of the dip at zero bias in the range $\delta \sim \pm 20 - 30\text{mV}$ and of the background as shown in Figure 104a.

In Figure 104b, which displays the differential conductance as a function of the voltage bias

for magnetic fields ranging from 0 to 0.9T, the magnetic field dependence shows the same behavior as for the previous junction: the background conductance decreases with increasing magnetic field, and the conductance oscillates with magnetic field around zero bias. This is better seen in the magnetoconductance displayed in Figure 104c. This figure is made from the $G(V)$ at different fields, by plotting the conductance at a fixed voltage for all the applied fields. The colormap shows the second derivative of the current with respect to the bias voltage as a function of the magnetic field. Notice that the second derivative of the current shows the oscillations even more clearly than in the magnetoconductance plot. The minima of the oscillations of the magnetoconductance (red line) correspond to the red regions of the colormap for low bias ($|V_{bias}| < 10\text{mV}$). **This colormap tells the oscillations happen for low energies below 10mV, lower than the observed gap δ .**

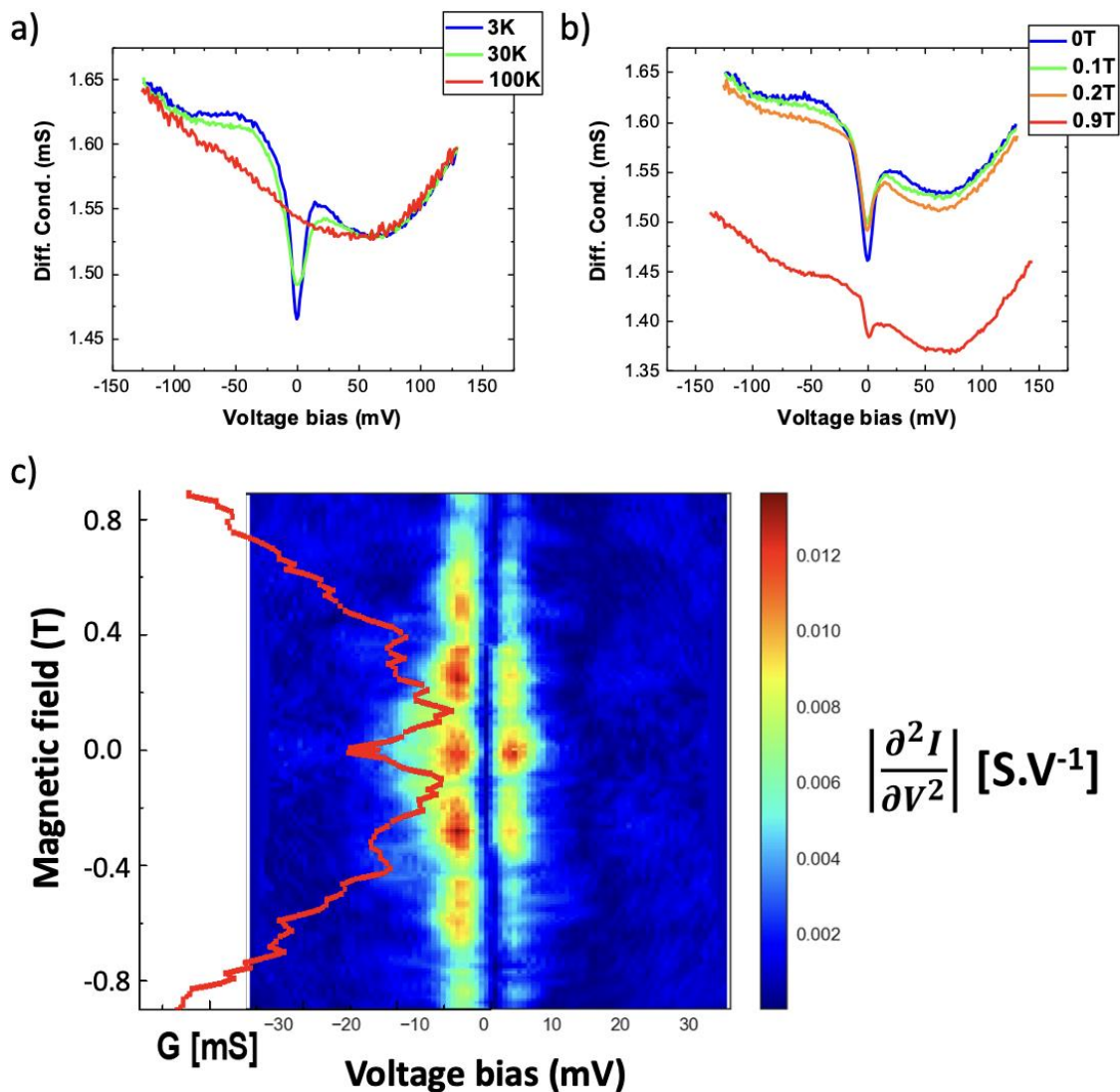


Figure 104 All these data were taken with the junction R1123HG B2D in the cryostat Garfield: a) Differential conductance against voltage bias at different temperatures. b) Same but at different magnetic field. c) Colormap of the second derivative of the current by the voltage bias with respect to the voltage bias (horizontal axis) and the magnetic field (vertical axis). Magnetoconductance oriented in order to enhance the fact that the minima of this plot correspond to the larger values of the second derivative on the colormap.

6.3.1.3 Characterization of the magnetoresistance oscillations

Further examples of magnetoresistance oscillations are shown in Figure 105 for four different samples, showing respectively the magnetoresistance as a function of the magnetic field (a) and as a function of the inverse magnetic field (b).

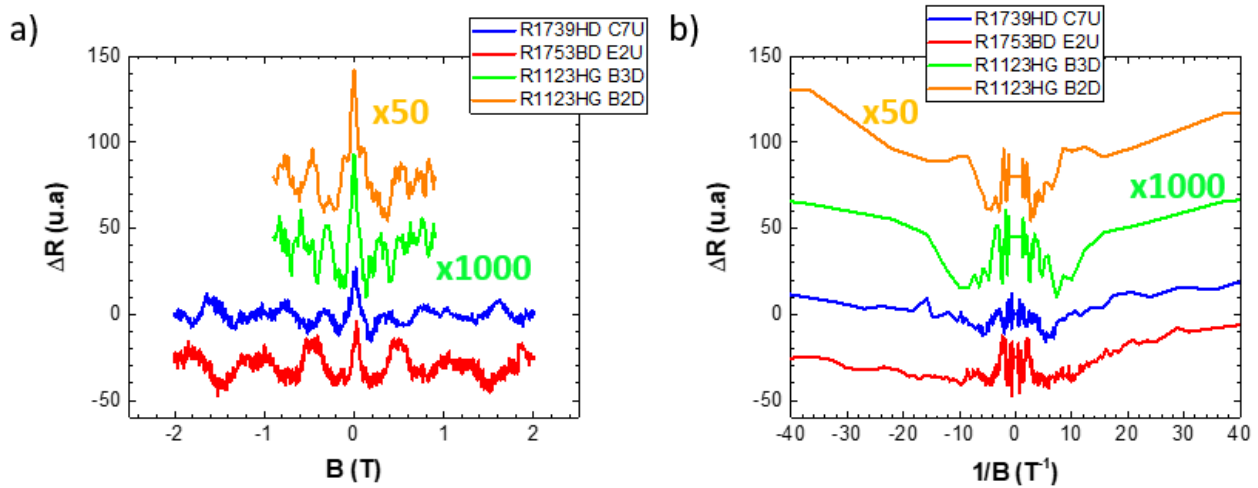


Figure 105 a) Resistance oscillations as a function of the magnetic field for four different junctions. b) Same but as a function of the inverse of the magnetic field.

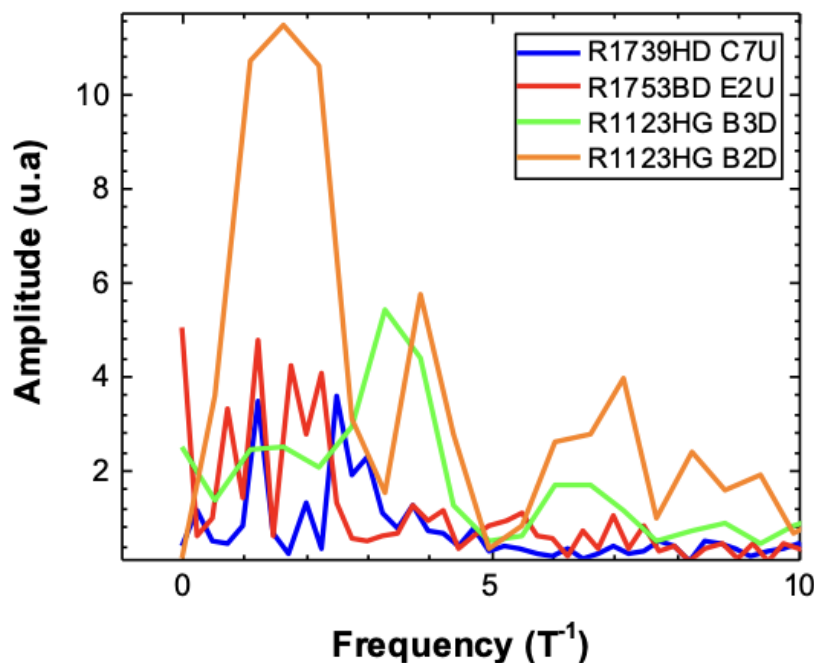


Figure 106 FFT of the magnetoresistance oscillations of the four junctions shown above.

The magnetoresistances in green and orange were multiplied respectively by 1000 and 50 for clarity. The goal of these two figures is to determine whether the oscillations are periodic with respect to the magnetic field, its inverse, or aperiodic. As we will see in the next section, this allows discriminating between oscillatory phenomena having different magnetic field

dependences. These graphs reveal that **the resistance oscillations are periodic with respect to the magnetic field** which can be further analyzed by performing the spectral analysis (Figure 106) to find the oscillation frequencies, as presented for the four same junctions. Here, I made the choice of cutting the values above $10T^{-1}$ corresponding to periods less than $0.1T$ where no major contribution is observed.

I carried out this analysis for samples of different fabrication batches, with different junctions length L and geometries (junctions as pictured in Figure 93 or double junctions as shown in Figure 102). In Figure 107, the deduced period of oscillations (from the spectral analysis) is plotted against the graphene channel length of the junctions. For the single junctions, it corresponds to the junction length L , and for the double junctions, it is the length between each superconducting electrode and the central superconducting "island".

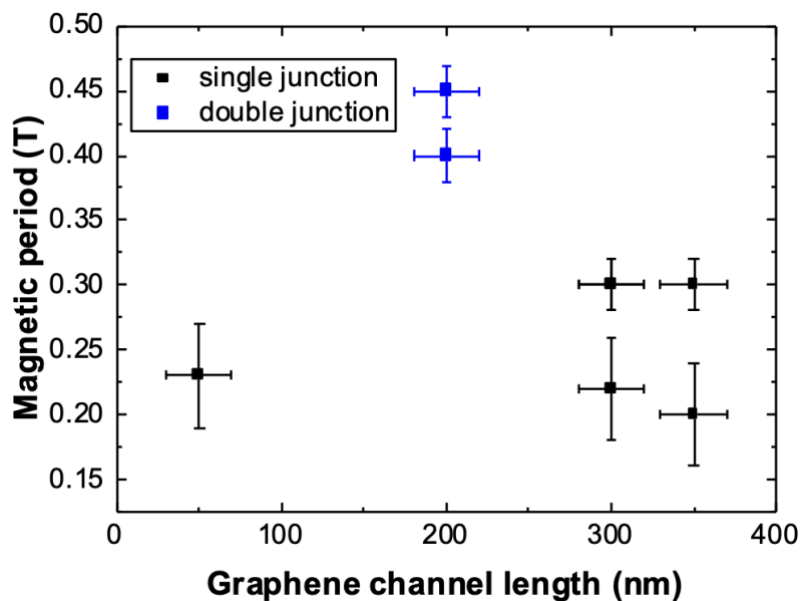


Figure 107 Period of the magnetoresistance oscillations as a function of graphene channel length. The double junctions are represented in blue. The uncertainty on the graphene channel length is about 20nm while the uncertainty on the period of oscillations mainly depends on the method of acquisition of $R(B)$ (continuous sweep or extraction of the resistance from many differential conductance spectra).

This plot does not exhibit any correlation between the magnetoresistance oscillations' period and the graphene channel length. It seems there is a variability of the oscillations' period uncorrelated to the graphene channel length.

6.3.1.4 Current and temperature dependence of the oscillations

Oscillations, especially their amplitudes, also depend on the temperature and bias current as shown in Figure 108. In Figure 108a, the temperature dependence of the magnetoresistance is presented for 4 different temperatures with the largest effect obtained for the lowest temperature (2 and 5K). While T is increased to 20K, the effect vanishes with a signal comparable to what is measured at 100K, where YBCO is not superconducting anymore. In the same way, we saw already the Figure 104 that the oscillations disappeared

when we increased the voltage bias applied to the junction. In Figure 108b, the oscillations lose amplitudes as the current amplitude is increased.

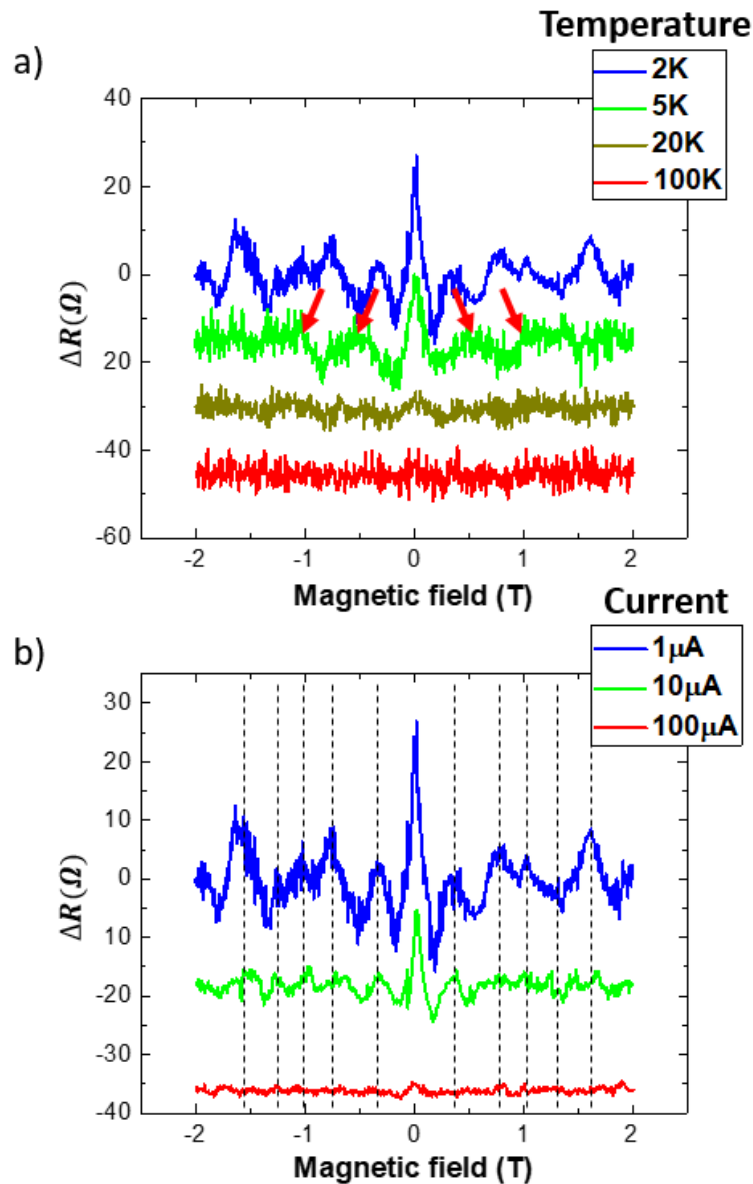


Figure 108 Magnetoconductance oscillations of the junction R1739BD C7U a) for different temperatures (shifted for clarity), b) for different bias currents (shifted). The maxima of the blue curves of each plot are highlighted by the vertical dotted lines.

In both cases, the oscillations disappear before the superconductivity of the contacts, with temperatures much lower than the superconducting temperature of the contacts (around 80K) and currents of only a few μA . In addition, in Figure 108a, there is a change in the period of oscillations between the magnetoconductance at 2K and 5K. To investigate this, I plot in Figure 109 the Fourier transform of the magnetoconductances at several temperatures. Unfortunately, the oscillations were visible only for the two lowest temperatures but the oscillations' periods are indeed different. At 2K, the peaks correspond to periods $\Delta B \sim 0.4\text{T} - 0.8\text{T}$ while at 5K, $\Delta B \sim 0.7\text{T} - 1.3\text{T}$.

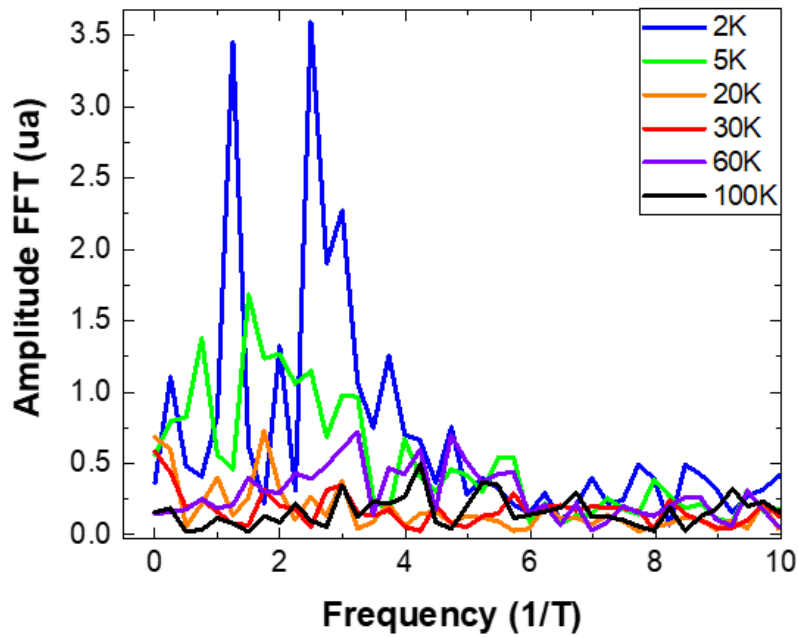


Figure 109 FFT of the magnetoresistance at different temperatures.

Both the temperature and the bias current have a strong impact on the amplitude of the oscillations. However, while the current has no impact on the period of the oscillations, the temperature changes the period in the case of the C7U junction. Further measurements of other junctions have to be carried out to clarify the dependence on the temperature.

6.3.1.5 Gate voltage dependence

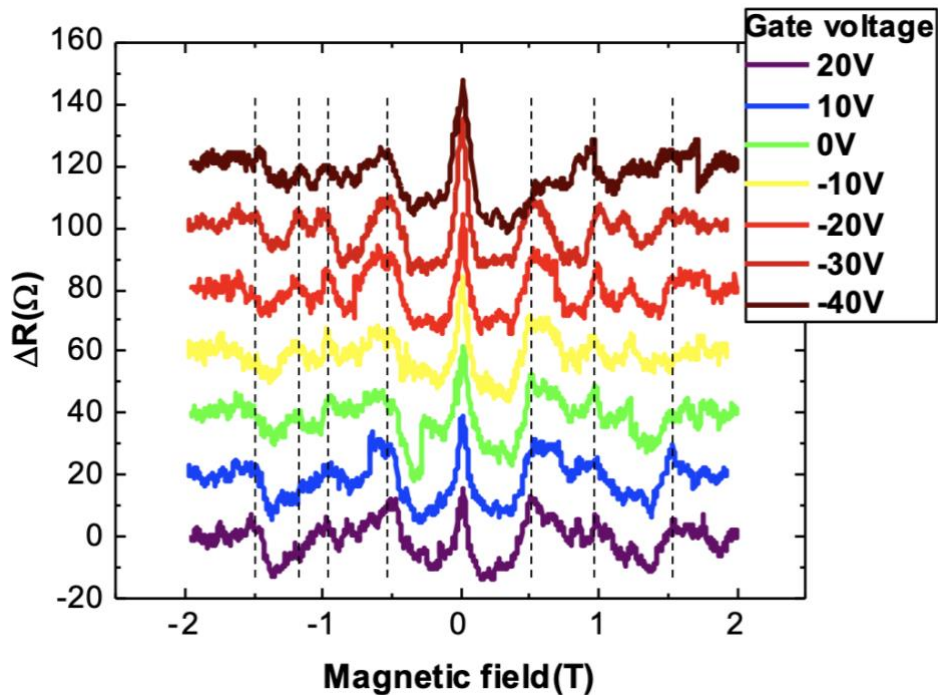


Figure 110 Magnetoresistance for different gate voltages of the junction R1753BD E2U measured at 2K (shifted for clarity).

I also measured the influence of the back gate voltage on the magnetoresistance of the junctions as presented in Figure 110 for the junction E2U. As shown by the dotted lines, the oscillations seem to occur around the same magnetic field for the different back gate voltages. Therefore, **the period of oscillation does not depend on the back gate voltage.**

For the sake of clarity, let's summarize the main experimental facts I could identify in order to discuss the physical origin of these magnetoresistance oscillations:

- They appear in junctions with an intermediate behavior between transparent and highly tunnel. The resistances of the junction are generally of the order of $1\text{k}\Omega$.
- They are periodic with respect to the magnetic field. The periods go from 0.2 to 0.45T.
- There is no clear correlation between the length of the junction and the period of oscillation.
- Their amplitudes is quickly suppressed once the temperature is increased, much faster than superconductivity. The period of oscillations also varies with the temperature.
- Their amplitudes is also suppressed when we increase the bias current on the junction.
- The oscillations are independent on the applied back gate voltage.

6.3.2 Discussion

6.3.2.1 Central features in $R(B)$

Before discussing the origins behind the oscillations, let us first discuss the central peak in the magnetoresistance, which is measured for all the junctions discussed in 6.3.1 (see Figure 105a). This feature also vanishes with temperature but decays at a much larger temperature ($\sim 40 - 60\text{K}$) than the oscillations. This peak has a different origin than the oscillations. To determine whether this phenomenon is due to superconductivity in the graphene, interfacial effects, or the transport in graphene, I realized a control experiment using CVD graphene transferred directly on a silicon oxide substrate as shown in Figure 111a. For comparison purposes, I transferred graphene atop pre-patterned contacts as done for the YBCO/graphene junctions. Figure 111b represents the magnetoresistance of this sample taken at several temperatures ranging from 5 to 50K, while sweeping the magnetic fields from -0.8 to 0.8T .

A peak of resistance is measured in this configuration (4-probes) close to zero magnetic field similar to what is measured on YBCO/graphene junctions. The peak amplitude dependence as a function of the temperature is also similar. Therefore, this magnetoresistance dependence in the case of YBCO/Graphene is probably linked to **weak localization**, an effect well described in the literature for graphene [160,219,220]. Weak localization is a quantum phenomenon that arises from scattering in disordered conductors. In such materials, electrons scatter within a characteristic length called the mean free path. The quantum nature of the electron means that it can interfere with itself and, to calculate the conductance,

it is necessary to calculate the quantum probability of all possible paths and interference terms for the electron. Magnetic field affects each possible path and interference loops differently by adding a dephasing term, eliminating interferences when averaging over disorder. The value B_{WL} of the magnetic field for which the peak disappears is of the order of $0.1T$. Since $B_{WL}l_{\phi}^2 = \phi_0$, we can deduce that the phase-coherence length of graphene is around $l_{\phi} \sim \sqrt{2 \times 10^{-15} / 0.1} \sim 140\text{nm}$ which is close to the phase-coherence length measured in CVD graphene [190].

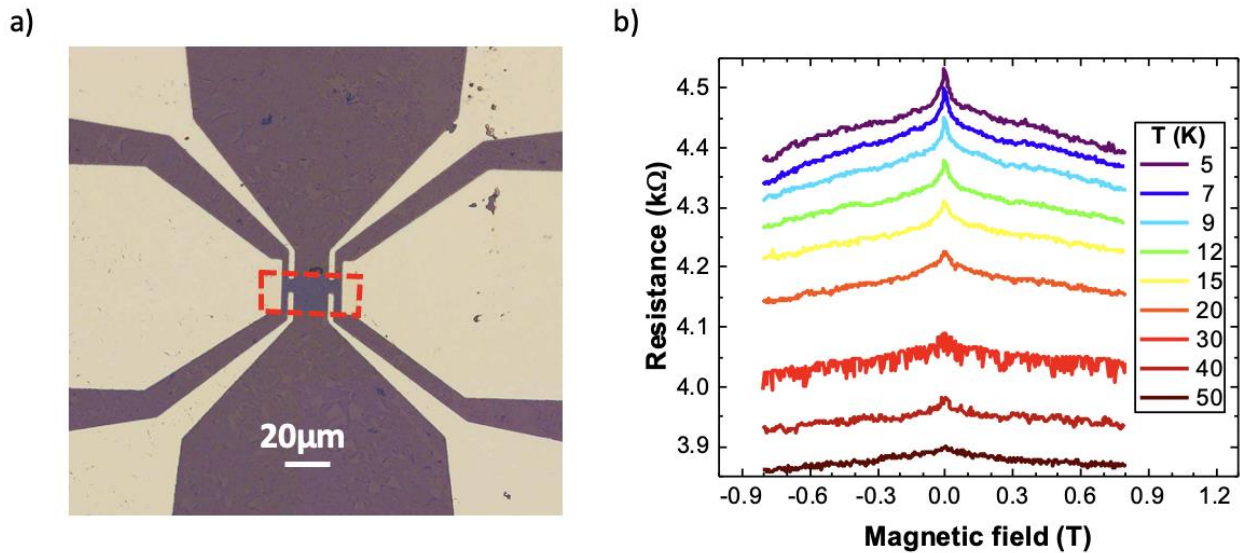


Figure 111 a) Microscope image of a device of graphene on silicon oxide contacted with gold. b) Magnetoresistance of the device at several temperatures from 5 to 50K.

On the contrary, the oscillation of the magnetoresistance described previously in the case of YBCO/Graphene junctions does not appear in this control experiment. Moreover, we can notice that the background is very different between the two kinds of samples. In the YBCO case, for all the junctions, the magnetoresistance increases with increasing magnetic field contrary to the case on silicon oxide where it slightly decreases. This is expected for the superconducting junctions as a high magnetic field destroys superconductivity and makes the resistance increase. It supports the idea that they are linked to the presence of the superconducting electrodes having an effect on either the homojunction, quantum coherent phenomena linked to the propagation in graphene, or the nature of the proximity effect.

6.3.2.2 Review of oscillatory phenomena in superconducting structures

There are many phenomena that can lead to magnetoresistance oscillations in SN or SNS structures [165]. In a very general framework, when a magnetic field is applied, two effects come into play. First, the trajectories of the charged particles are curved due to the Lorentz force, this is called cyclotron motion and is for example responsible for the Hall effect. Second, the Aharonov-Bohm effect [221] implies that the charged particles pick up a phase due to the electromagnetic field, creating measurable interference effects. In the case of SNS

junctions, Andreev and normal reflections at the interface have to be considered as well as the presence of disorder. Finally, since YBCO is a type II superconductor, the magnetic field can penetrate it through superconducting vortices. In this section, I will review some of these effects, that can originate either from flux quantization effects, from the cyclotron motion of the charge carriers, from a mixture of the two, or from the presence of superconducting vortices.

6.3.2.2.1 Flux effects

Fraunhofer oscillations

Even though the considered junctions are not in the Josephson coupling regime, I have to mention the Fraunhofer oscillations of the supercurrent [17] that have a period defined by the quantum of flux $\Phi_0 = \frac{h}{2e}$. I have described this effect in chapter 2 but I will simply remind that the magnetic flux inside the junction modulates the local supercurrent giving rise to oscillations of the total supercurrent as a function of the flux. However, this phenomenon is in fact intimately linked to the Andreev bound states since the magnetic field modifies their energy levels. As a consequence, we may expect some modulation of the conductance even in the absence of a supercurrent.

Al'tshuler-Aronov-Spivak-like (AAS) effect

This effect is related to the weak localization explained in 6.3.2.1, as it comes from the interference between time-reversal-symmetry (TRS) trajectories originating from the backscattering on impurities. At variance to the Aharonov-Bohm effect represented in Figure 112a, which results from the interference between two particles traveling around a loop enclosing magnetic flux, the Al'tshuler-Aronov-Spivak (AAS) effect (Figure 112b) [165,222] arises from the interference along a path and the time-reversed path [223]. This results in an oscillation that is periodic as a function of the magnetic flux, and twice as fast as the AB effect, that is with a period $\phi_0/2$. Notice that in metals or semiconductors, the observation of the AAS oscillation requires a loop geometry with a "hole", *i.e.* a region the particles need to circumvent as pictured in Figure 112b. In the absence of such a loop, we would only observe the magneto-resistance drop around $B = 0$ (Figure 111Figure 112b) due to weak localization. Interestingly, the AAS effect can be also observed in SNS junctions, where interference occurs between Andreev particles. Indeed, Andreev retroreflection at the SN interfaces makes the junction topologically equivalent to a loop area $W \times L$. At each SN interface, the particle can either be Andreev or normal reflected, which is respectively equivalent to the clockwise or anti-clockwise rotation in Figure 112b. In Figure 112c, the electrons are represented by a filled circle while holes are represented by hollow circles. The red and blue colors are here to stress the analogy with the usual AAS effect (direction of propagation in b). In the same way Andreev bound states (ABS) give a ϕ_0 -periodicity, the occurrence of normal reflection makes the number of round trips double and therefore the periodicity is divided by two. The resulting period of oscillation with the magnetic field is $\Phi_0/2WL$. As the magnetic field increases, time-reversal-symmetry is broken due to the Lorentz force and the oscillation amplitude therefore decays as for weak localization. A

simulation of this effect [165] is shown in Figure 112d. This effect, being related to weak localization, also presents a peak at zero magnetic field. The simulation of the probability of Andreev reflection R_{he} shows that the amplitude of the central peak and of the oscillations increases as the width W becomes large against the length L of the junction. The amplitude of the oscillations also decays as the energy increases and approaches the superconducting gap as shown in Ref. [224].

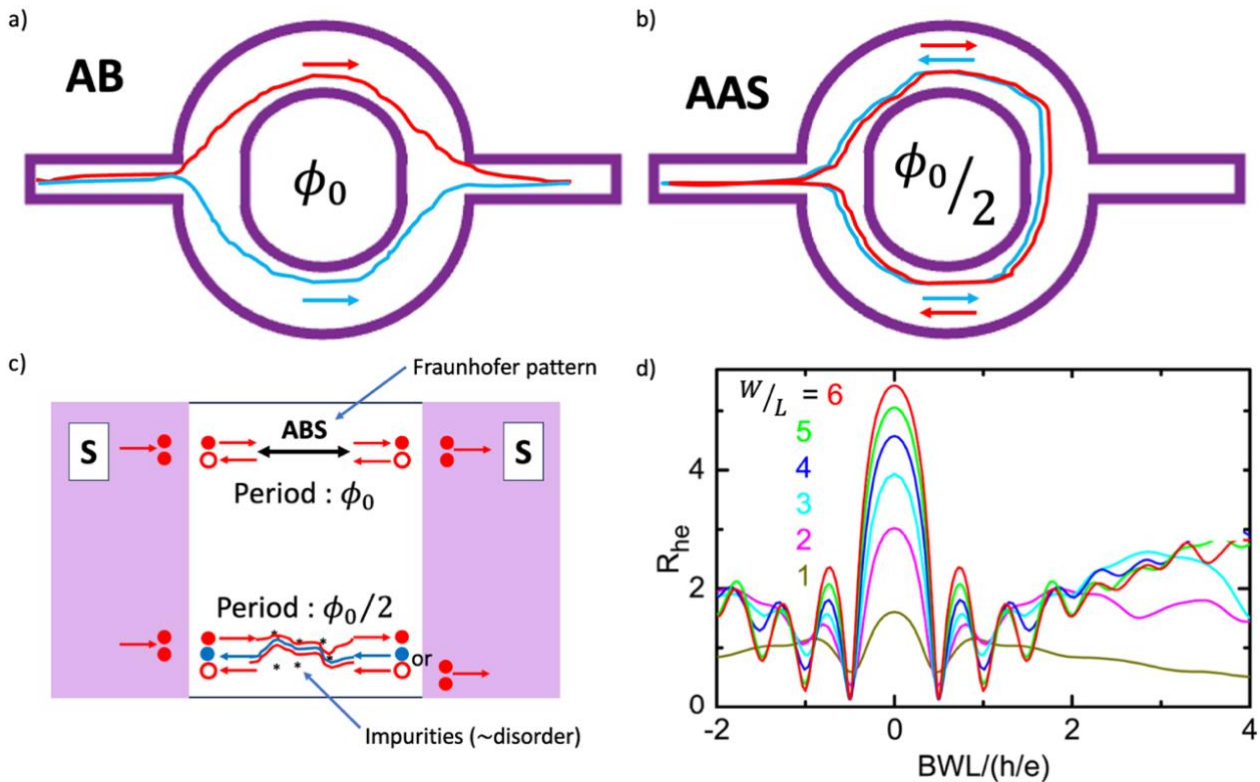


Figure 112 Comparison between a) the Aharonov-Bohm (AB) and b) the Al'tshuler-Aronov-Spivak (AAS) effects. c) Scheme of a SNS junction with on top a classical Andreev bound state (ABS) leading to Josephson effect and at the bottom the illustration of the AAS-like effect with normal and Andreev reflections. The presence of the two makes it equivalent to the AAS case in b) as the alternative between Andreev and normal reflection is the equivalent of the clock- and anti-clockwise alternative. d) Simulation of the probability of Andreev reflection with respect to the enclosed flux in the junction for 6 different width/length ratios. Figure taken from Takagaki, *J. Appl. Phys.* **128**, 024304 (2020).

6.3.2.2.2 Cyclotron motion-related effects

Andreev edge-state transport

If we consider an interface with a superconductor (both Andreev and normal reflection can occur). For interfaces with perfect transmission, only Andreev reflection happens in the presence of a large magnetic field, that is to say when the cyclotron radius R_c is smaller than the length of the interface, we observe Andreev edge-state transport along the interface with at each touching point the conversion from electron to hole or inversely by Andreev reflection [225,226]. This is depicted in Figure 113a. I already described this effect in chapter

3 but what I would like to stress here is the oscillatory behavior of the magnetoresistance. Indeed, in the presence of a strong enough magnetic field, Andreev edge channels are forming at the SN interface [227]. These transport channels are made of both holes and electrons in equal proportions because of Andreev reflection at the interface and there is no net current. However, as soon as the interface is not perfect and there is also normal reflection at the interface, oscillations in $1/B$ of the magnetoresistance start appearing [164,228]. These oscillations are shown in Figure 113b where the resistance is plotted as a function of the filling factor ($\propto 1/B$) for five different temperatures. As the magnetic field becomes larger than the second critical field of the superconductor H_{c2} the amplitude of the oscillations decreases. Indeed, contrary to the case of a SN interface where all edge channels experience Andreev reflection when the electrodes are both normal, only the inner channel is experiencing backscattering so the conductance will vary at most by one quantum of conductance (not limited in the SN case).

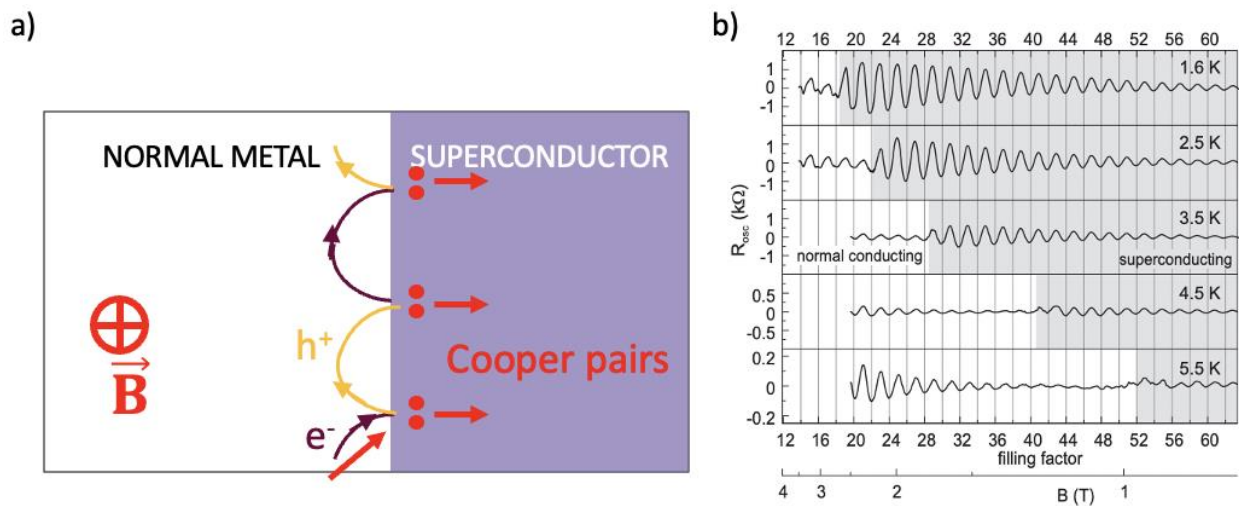


Figure 113 a) Scheme of Andreev edge transport in the case of a high magnetic field and perfect interface between a normal metal and a superconductor. b) Experimental magnetoresistance of a SN interface as a function of the filling factor ($\propto B^{-1}$) for several temperatures. Figure taken from Eroms et al., *Phys. Rev. Lett.* **95**, 107001 (2005).

Commensurability effects

Another consequence of the curvature of the electron and hole trajectories (shown in Figure 114a and b) is the potential commensurability between the cyclotron radius and a characteristic length of the system [165,229–231]. This effect only manifests when the two interfaces are perfect or almost perfect. Indeed, in that case, due to Andreev reflection and the Lorentz force, the motion of the electrons and holes in the normal region follow a guided path that makes them travel more or less distance in the resistive normal region [232]. It gives rise to oscillation of the transport coefficient when R_C matches with an integer multiple of $L/2$ and therefore an oscillation of the magnetoresistance. This effect is purely classical and periodic with $1/B$ as shown by the comparison between quantum (left) and classical (right) calculation of the transport coefficients in Figure 114. For this phenomenon to happen, the mean free path of the carriers must be a few times larger than the length of the junction to avoid any scattering during the “loop”.

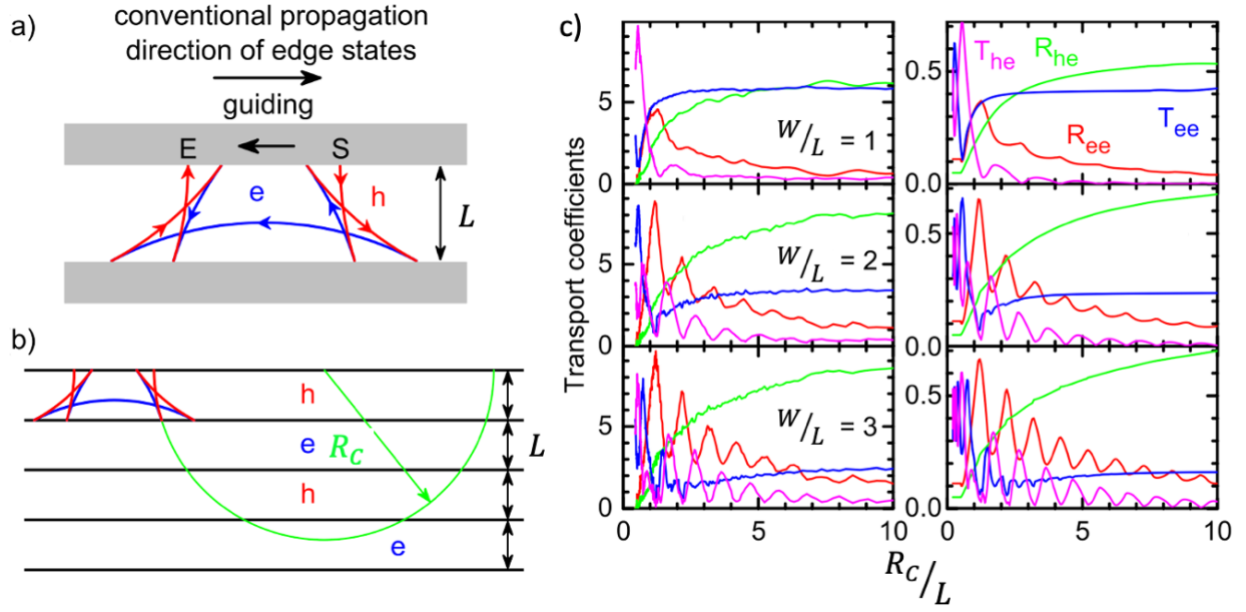


Figure 114 a) Classical Andreev trajectory in a SNS junction of length L from a hole (represented in red) at the starting point (S) to the ending point (E). The electron trajectories are represented in blue. In the presence of a magnetic field, these electron and hole trajectories are deduced from the construction in b). b) Construction of the trajectories of a) by folding the circle defined with the cyclotron radius R_c . c) (left) Quantum calculation of the transport coefficients as a function of R_c/L for different values of W/L . (right) Classical calculation of the same coefficients.

6.3.2.3 Both flux and cyclotron motion-related effect

Aharonov-Bohm (AB) effect in a single SN interface with Andreev Reflection

The next phenomenon mixes the orbital effect of the magnetic field with the magnetic phase accumulated in a loop as shown in Figure 115a and b [164,165]. It has some similarities with the Aharonov-Bohm (AB) effect pictured in Figure 112a except here it occurs at a SN interface where both Andreev reflection and normal reflection are possible. The curvature of the trajectories due to the magnetic field makes the normally reflected electron and the Andreev reflected hole goes in the same direction as shown in Figure 115a. However, this electron and hole both gain a phase at the reflection and during their motion due to the magnetic vector potential. When encountering the interface again, they can once again experience either an Andreev reflection or a normal reflection. As a consequence, in the case of only two successive reflections, there are four amplitudes (Ψ_1^e , Ψ_2^e , Ψ_3^h and Ψ_4^h) to sum in order to find the resulting conductance, as noted in Figure 115b. Ref. [164] gives an approximate formula for the case of two successive reflections on the SN interface:

$$G \approx g_0 [1 + 4|r_{ee}|^2|r_{he}|^2 p(\beta)^2 \cos(2\pi\beta - 2\theta_n)] \quad 6.4$$

Where g_0 is the normal state conductance, r_{ee} , and r_{he} are respectively the normal reflection coefficient and the Andreev reflection coefficient. θ_n is the phase shift of the normal reflection and $\beta = \frac{E_F}{\hbar\omega_c}$ with $\omega_c = \frac{|eB|}{m}$. The magnetic phase enclosed in the yellow hatched area

is:

$$\phi_B = \int_{1^{st} \text{ reflection}}^{2^{nd} \text{ reflection}} \vec{A} \cdot d\vec{l} = -\pi\beta \quad 6.5$$

Here, \vec{A} is the potential vector associated to \vec{B} . ϕ_B is the phase accumulated by each particle between the first and second reflection.

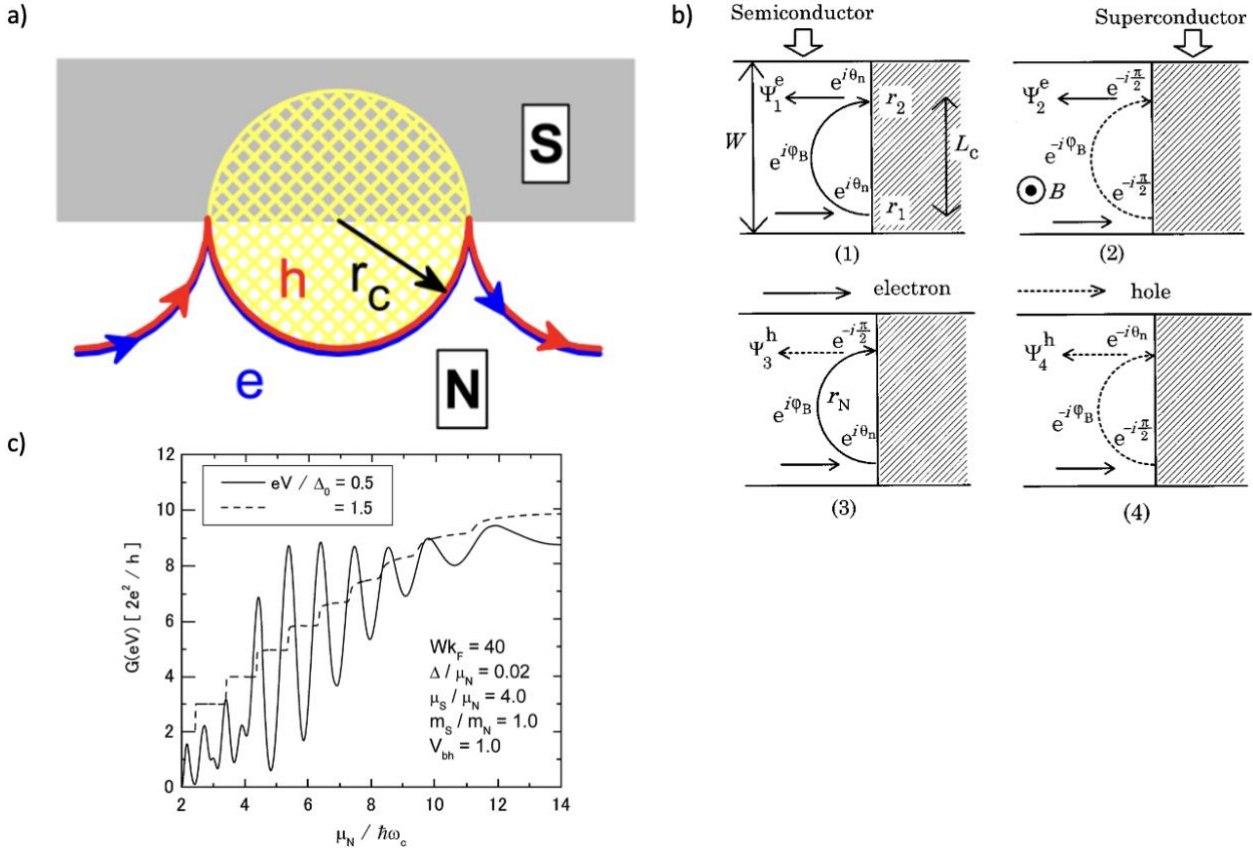


Figure 115 a) Interplay between orbital and phase effects of the magnetic field. The lines with arrows correspond to electron (red) and hole (blue) that either normal or Andreev reflects at the SN interface. The yellow-hatched region is the area where the magnetic flux is enclosed. Taken from Takagaki, *J. Appl. Phys.* **128**, 024304 (2020). b) 4 schemes describing the four interfering terms coming from an incident electron going through the SN interface depending if the first reflection is an Andreev reflection or not and the same for the second reflection. (1) two successive normal reflections (with dephasing $e^{i\theta_n}$ at each interface), (2) two successive Andreev reflections (with dephasing $e^{-i\frac{\pi}{2}}$ at each interface), (3) normal reflection and then Andreev reflection and (4) Andreev reflection and then normal reflection. c) Calculated conductance as a function of $\beta = \frac{\mu_N}{\hbar\omega_c} \propto B^{-1}$ for $eV = \Delta/2$ and $3\Delta/2$. Taken from Asano, *Phys. Rev. B*, **61** (2000).

The coefficient $p(\beta)$ is a geometrical coefficient. It is chosen to take into account that some starting positions do not lead to this interference since at least two successive reflections have to happen. Therefore, this term depends on the width W of the interface and on R_C . Since it should be equal to 1 for $W = 2R_C$ and 0 for $W = R_C$, then a linear approximation

gives $p(\beta) \approx 2 \left(1 - 4 \frac{\beta}{Wk_F}\right)$. This effect therefore oscillates with β as presented in Figure 115c, and the oscillations start when the magnetic field is sufficient to encompass one cyclotron radius in the width of the interface (here, the plot starts at $\beta = \frac{\mu_N}{\hbar\omega_c} = 2$). The field dependence of this effect, while not straightforward, can be calculated. Indeed, the area of the loop \mathcal{A} changes along with the magnetic field, roughly evolving as the square of the cyclotron radius, which is proportional to $1/B$. It then gives $\mathcal{A} \propto B^{-2}$ and $\beta \propto B^{-1}$. Therefore, the conductance evolves as $\cos(\alpha B^{-1} + cst)$ with α a constant, and the amplitude of oscillations depends on B .

6.3.2.3.1 Vortices-related effect

Effect of superconducting vortices

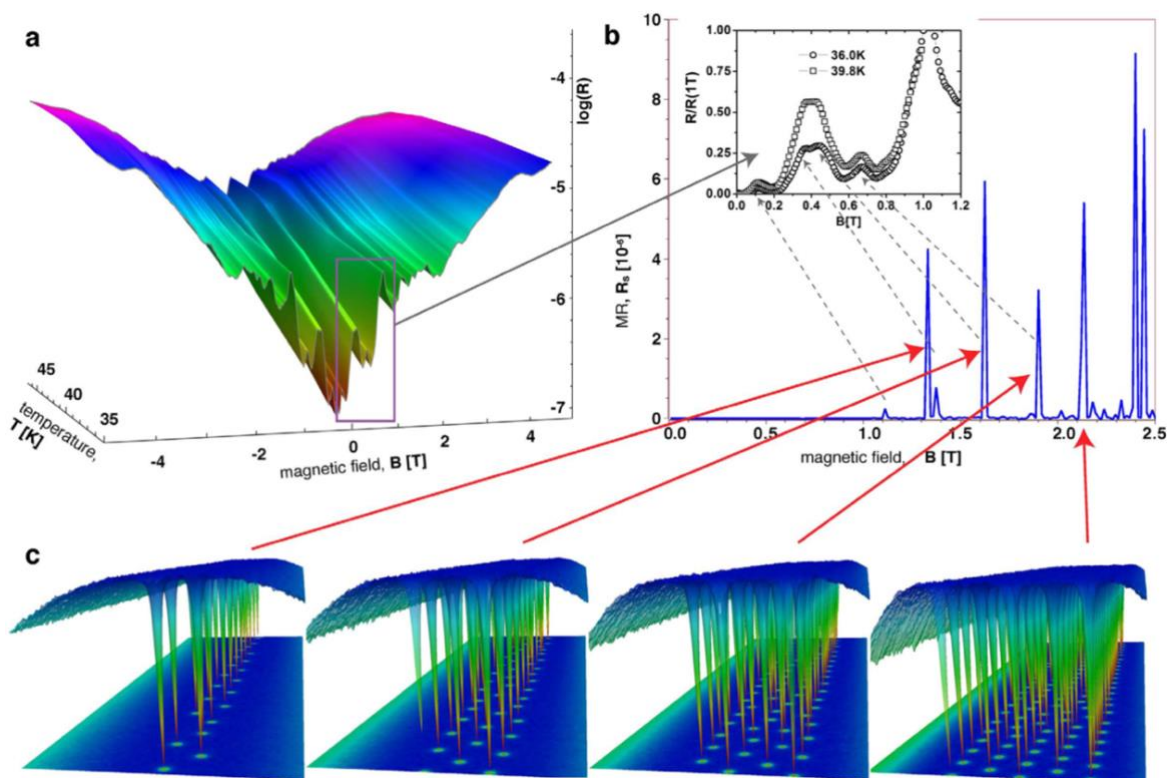


Figure 116 Taken from Papari et al., *Sci. Rep.* **6**, 38677 (2016). a) Magnetoresistance plot (resistance in logarithmic scale) as a function of temperature from 35 to 45K of a superconducting constriction of YBCO (230nm wide, 700nm long, and 150nm thick). b) Simulated magnetoresistance by micromagnetic simulation of a 2D device with a similar dimension as the experimental device. (inset: comparison with two normalized magnetoresistance at 36 and 39.8K) c) Vortex configurations at the peaks indicated with the red arrows. Each peak corresponds to the apparition of a new row of vortices before the constriction.

As for all type II superconductors, the magnetic field penetrates YBCO through **superconducting vortices**. This is also the case when stacking the superconductor in a configuration superconductor/Au/Graphene as demonstrated in Ref. [233] for Nb/Cu films.

With the current going through the junction, there will be an accumulation of vortices at the interface since it is where they enter and where the superconducting order parameter is the weakest [137]. This interface blocks the flow of vortices and, as the magnetic field grows, an increasing number of vortices accumulates. Figure 116a, from Ref. [234], presents the logarithm of the magnetoresistance of a constriction in a YBCO superconducting track (230nm wide, 700nm long, and 50nm thick) as a function of the magnetic field and the temperature. The measurement presents oscillations that are not periodic either in B or B^{-1} but depend on the vortex configuration at the interface with the constriction. Since the distance between the vortices is $\sqrt{\frac{\Phi_0}{B}}$, it results in a \sqrt{B} -dependence of the magnetoresistance. Indeed, micromagnetic simulations presented in Figure 116b and c show that the magnetoresistance peaks occur when a new row of vortices is complete. Physically, the addition of a vortex row acts like the phase transition at B_{c1} right at the moment the system overcomes the energy for creating a new row (see the vortex configurations in Figure 116c). When a row of vortices is complete, the additional vortices in the new row are more free to move which implies an increase of the magnetoresistance. As the new row gets denser, the vortices are less and less mobile and the magnetoresistance decreases. An interface could also block the vortices the same way as the constriction of ref. [234] and the vortices will accumulate on each side of the junction [137], creating magnetoresistance oscillations.

6.3.2.4 Comparison with the experimental data

I presented several phenomena that can cause an oscillating magnetoresistance from the cyclotron trajectories to the charge to flux effects or vortices. The goal of the following and last section is to confront all these phenomena in our experimental facts to discriminate the best candidates to explain the experimental data.

Let us now come back to the different possible explanations detailed above and confront the experiments. The results of the comparison are summarized in Table 5. As a reminder, experimentally, we found that the oscillations are periodic with respect to the magnetic field with a period between 0.2 and 0.4T, a period that scales with the total length L of the junction.

Andreev edge-states transport: We have seen that in the presence of a strong enough magnetic field, Andreev edge states are forming at the interface between a superconductor and a normal metal. In the presence of an imperfect interface, oscillations appear in the magnetoresistance. Therefore, this effect does not have the correct dependence on the magnetic field.

Commensurability effect: This effect is $1/B$ -periodic because oscillations occur when the cyclotron radius $R_C = \frac{E_F}{ev_F|B|}$ match with an integer multiple of the length of the junction. ($E_F \sim 100\text{meV}$ is the Fermi energy of graphene according to what we estimated from measurements performed in other works [12,14], $v_F \sim 1 \times 10^6\text{m/s}$ is the Fermi velocity of graphene). The first expected oscillation is close to what is measured since we consider here

the junction length L instead of its width W . In that case, we have $2R_C \sim L$ for $\Delta B \sim 0.2\text{T}$ with $L = 300\text{nm}$. Let alone the disagreement with the dependence in $1/B$ of the oscillations, this effect is very sensitive both to disorder and imperfection of Andreev reflection, which makes the oscillation disappear.

Aharonov-Bohm (AB) effect in a single SN interface with Andreev Reflection: This phenomenon occurs at a too-low magnetic field (around 10mT such as $R_C = W$) and has a dependence in $1/B$.

Vortices: We can exclude the contribution to superconducting vortices since the dependence is in \sqrt{B} and above all, the expected oscillation period of this effect is too small compared with the period I measured. Indeed, it is possible to compute the value of the magnetic field for the first oscillation. It happens when there is the first row full of vortices such as $\frac{W}{a_0} = W \times \sqrt{\frac{B}{\Phi_0}} = 1$. The width of my samples being $W = 10 \times 10^{-6}\text{m}$, it corresponds to $B \approx 2 \times 10^{-5}\text{T}$ which is many orders of magnitude too small compared with the period measured in our system.

All the effects above have the wrong dependence on the magnetic field and can therefore be excluded from our analysis. The two last effects present oscillations that are periodic with B and then deserve a more thorough analysis. These two effects are related to the flux enclosed in the junction area and not to the cyclotron trajectory or superconducting vortices.

Phenomenon	B -dependence	Period or first oscillation	Special requirement
Andreev edge-states transport	$\propto B^{-1}$	$\sim 0.3\text{T}$, such as $R_C < L$	
Commensurability	$\propto B^{-1}$	$\sim 10^{-2}\text{T}$ (with W) or $\sim 0.3\text{T}$ (with L)	Very sensitive to disorder and to non-perfect AR
Aharonov-Bohm like effect	$\propto B^{-1}$	$\sim 10\text{mT}$, such as $R_C = W$	
Superconducting vortices	$\propto \sqrt{B}$	$\sim 0.02\text{mT}$	
Fraunhoffern-like pattern	$\propto B$	$\sim 0.4\text{mT}$	AR on both sides
Al'tshuler-Aronov-Spivak effect	$\propto B$	$\sim 0.2\text{mT}$	Mix of AR and NR
Experiment	$\propto B$	$\sim 0.2\text{T}$	At low bias, low T

Table 5 Characteristics of the phenomena studied in the last section to simplify the interpretation as well as the experimental facts about the magnetoresistance oscillations. AR (NR) respectively means Andreev reflection (normal reflection).

Fraunhofer oscillations: I did not observe a finite critical current in my experiments, which should in principle rule out this effect. Nevertheless, even in the dissipative regime, the magnetic flux quantization effects are observable in the magneto-resistance of Josephson junctions. To know whether they explain the observed oscillations, I calculate the period with which it would be B -periodic. In my system, a raw estimation gives a period ΔB equal to:

$$\Delta B = \frac{\Phi_0}{W \times (L + 2\lambda_L^{YBCO})} \sim \frac{2 \times 10^{-15}}{10 \times 10^{-6} \times 500 \times 10^{-9}} \sim 0.4mT \quad 6.6$$

by taking the width of the junction $W = 10\mu m$, its length $L = 200nm$ and the London penetration length $\lambda_L^{YBCO} \sim 150nm$ for YBCO. It gives $(L + 2\lambda_L^{YBCO}) \sim 500nm$ for the calculation which results in a very small period $\Delta B \sim 0.4mT$ compared to the one observed in the experiment. This is far from the experimental period between 0.2 and 0.4T. Nevertheless, this larger period might come from an inhomogeneity of the local density current in the junction [235–237]. Indeed, the junctions are $10\mu m$ -wide for a length between 50 to 350nm, and the effective junction, in the sense where most of the current circulates, may have many different dimensions. For instance, it has been shown [237] that band-bending at the edge of a graphene flake, close to the Dirac point, may confine the current to the edge even at zero field. This Josephson junction exhibits a modified Fraunhofer pattern compared with the homogenous case. They deduced the distribution of the current from the critical current vs field measurement following the work of Dynes and Fulton [235]. We could try to do so with our measurement, though we only observed magnetoresistance oscillations and not a proper critical current Fraunhofer pattern. However, to carry out a correct Fourier analysis, two parameters have to be considered. The first one is the range of the measurement (here, from -2 to $2T$) which gives the spectral resolution of the FFT. The other parameter is the step of the measurement (here around $\delta B \approx 6.4mT$) which gives the range of the FFT. In our case, the step of the measurement is too large and gives a maximal spatial extent $\Delta x = \frac{\Phi_0}{\delta B \times (L + 2\lambda_L^{YBCO})} \sim 600nm$. To allow the reconstruction of the local current over the entire width $W = 10\mu m$, we should have measured every $0.1mT$, which is not possible with our experimental set-up.

Let us assume that there are one or several regions where the current circulates more easily. These regions could correspond to the edges of the graphene flake, due to band-bending as shown earlier [237]. Or to regions randomly located in other places of the junction due to the transparency of the graphene/YBCO interface being spatially inhomogeneous, which results in the proximity effect occurring locally over a reduced portion of the junction as shown in the cartoon of Figure 117. This may explain why the differential conductance is weakly tunnel. Indeed, the sheet resistance of CVD graphene is usually $R_{\square} \sim 400 - 800\Omega$ [190] which gives a resistance of the channel $R \sim R_{\square} \frac{L}{W} \sim 8 - 16\Omega \ll k\Omega$ measured for these junctions. Most of the width may not conduct current very well and explain the observed intermediate transparency. According to the observed periods $\Delta B \sim 0.2 - 0.4T$, the width w of these regions would be $w = \frac{\Phi_0}{\Delta B \times (L + 2\lambda_L^{YBCO})} \sim 20nm$ with $L \sim 200\mu m$. This size could for example correspond to the topography of the YBCO/Au film below graphene making a better electrical contact as suggested by Ref. [98], which argues that the proximity effect

induced in gold is only local due to the (100) facets of YBCO present among the mainly (001) oriented YBCO film.

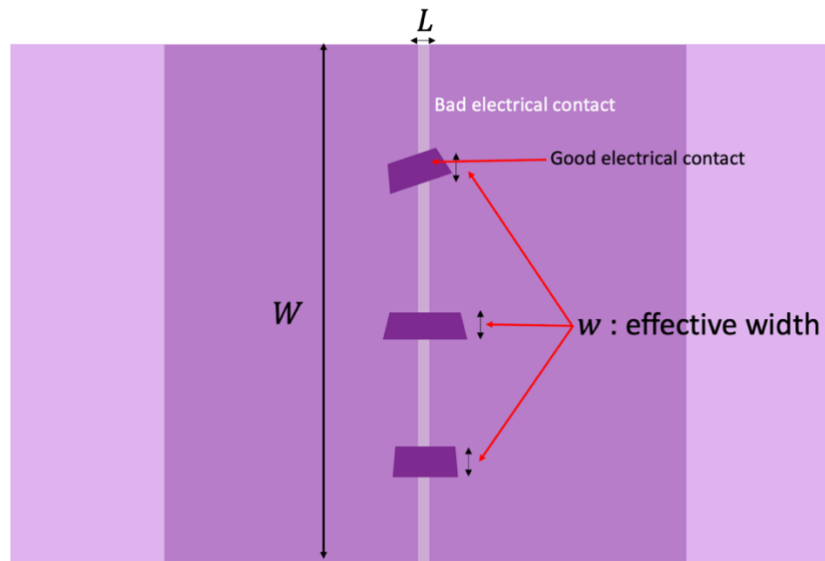


Figure 117 Scheme of a SNS junction of length L and width W . The electrical contact is tunnel over most of the width except in the deeper purple regions of width w where the current circulates with less resistance and where Andreev reflection is possible.

Before analyzing the last effect, we should keep in mind two facts. The first one is that the behavior of the resistance is opposite to what we would expect from a Fraunhofer-like effect on Cooper pairs. Indeed, in a Fraunhofer pattern, the critical current is maximal at zero field while here, the resistance is maximal at zero field. The second fact is that the hypothesis of the temperature dependence of the oscillations' period does not match the one of a Fraunhofer-like effect where the period is constant. In summary, even if we assume a spatially non-homogenous proximity effect across the YBCO/Au/graphene interfaces, the observed magnetoresistance oscillations cannot be accounted for by the Josephson effect.

Al'tshuler-Aronov-Spivak (AAS) effect: This effect also has the correct dependence in B and is also a flux-related effect like the previous one. With the dimensions of the junction, the expected period is around 0.2mT with the dimensions of the junctions, half the one of Fraunhofer oscillations. This is far from the period observed for my junctions but again, some arguments may explain the difference with the measured period. First of all, the same argument as before can apply here since the AAS effect needs Andreev reflection to occur. If there are only a few regions where Andreev reflection locally occurs, due to the YBCO/Au/graphene interface transparency being high only locally at certain spots, the typical size (w and L) of these spots as presented in Figure 117 should be considered to calculate the period of the AAS oscillations. However, this idea does not explain why the period of oscillations increases with increasing temperature (Figure 109). Indeed, the observed temperature behavior indicates that the oscillations are related to a characteristic length that decreases with temperature, making the period increase. The phase-coherence length $\xi_N = \sqrt{\frac{\hbar D}{k_B T}}$ of graphene has the same dependence on the temperature as seen in

chapter 3. Indeed, if we compute the ratios between the frequency of the peak at $2K$ and the one at $5K$ for the two first peaks of each Fourier transform, these ratios are around 1.66, very close to $\sqrt{5/2} \sim 1.58$. This is consistent with a period $\Delta B = \frac{\phi_0}{L\xi_N} \propto \sqrt{T}$. Moreover, in Ref. [238], it is said that the overall AAS resistance oscillations are obtained from the addition of the contributions of regions defined by the length of the junction L and the phase-coherence length ξ_N , as if the width was cut into pieces of side ξ_N and length L . **These arguments support the hypothesis that the Al'shuler-Aronov-Spivak effect is responsible for the magnetoresistance oscillations.** Theoretical calculations, which are beyond the scope of this experimental thesis due to time constraints, will be done soon in collaboration with colleagues to further substantiate this hypothesis.

On the experimental side, we intend to carry out more experiments to add more specific data to the theoretical model. An axis for further experiments is to vary the geometrical parameters of the junctions. It would be interesting to reduce the width of the electrode and keep varying the length of the junctions. A reduced width (ideally close to the phase-coherence length) may help to understand the dependence of the junction on the geometry of the junction. In our analysis, no correlation appeared between the period of oscillation and the length of the junctions. However, if the AAS effect is indeed responsible for the oscillations, the phase-coherence length and therefore the quality of the graphene sheet of each junction comes into play for the period which may explain the observed variability of the period.

6.4 CONCLUSIVE REMARKS

In this chapter, I started by describing the state of the art, particularly, reviewing results obtained in my lab before I started my PhD, based on large junctions to concentrate on a single YBCO/Au/Graphene interface. The study with a back gate voltage revealed the superconducting version of Klein tunneling, a relativistic effect due to the band structure of graphene. In the second part, I presented experimental results obtained by my colleagues, to whose understanding I contributed. Those results evidenced Fabry-Pérot oscillations and long-range propagation of *d-wave* Andreev pairs in graphene. Finally, the last part detailed my experiments on the magnetoresistance of YBCO/Au/graphene/Au/YBCO junctions, which revealed oscillations at low temperatures. The experimental evidence was compared to oscillating effects in the literature and allowed to retain the Al'tshuler-Aronov-Spivak effect as a likely explanation. Indeed, this effect qualitatively explains the magnetoresistance oscillations, their temperature, and bias dependence. However, to quantitatively explain the observed oscillation period, we have to consider the phase-coherence length of graphene instead of the width of the junction. Theoretical calculations beyond this analysis have to be performed to further support this hypothesis.

7 A NEW MATERIAL UNDER STUDY, MoS₂

In the previous chapter, I presented in detail the properties of YBCO/graphene junctions. For that project, we developed a whole set of experimental techniques to fabricate superconducting devices with the transfer on YBCO of CVD-grown graphene. We decided to transpose this knowledge to the study of another 2D material, MoS₂. As we have seen in chapter 2, MoS₂ is part of the transition-metal dichalcogenide family [41,59,64,239]. It is a semiconductor with a thickness-dependent gap [59] but can be tuned into a conductor with an electrostatic gate. Contrary to graphene, spin-orbit coupling (SOC) is non-negligible in MoS₂ and theory predicts that the coupling with superconductors would give rise to exotic quasiparticle [146,240,241,145].

I first started with the expertise obtained on YBCO/CVD graphene junctions to build YBCO/MoS₂ by transferring CVD-grown MoS₂ on patterned YBCO junctions. The resulting samples showed a very resistive tunnel behavior and are presented in section 7.1. To try to improve the electrical contact between YBCO and MoS₂, I then decided to change the approach to deposit MoS₂ from a transfer method to direct growth. Though the growth of MoS₂ has already been carried out in the lab on usual substrates like sapphire [60,89], growing this material on YBCO, an oxide very sensitive to the atmosphere composition and heat, was challenging. This implied optimization of the growth parameters and characterization of both YBCO and the grown MoS₂ (section 7.2). In section 7.3, I present results on the integration of this method for the fabrication of superconducting junctions YBCO/MoS₂/MoSi. These show conductance features characteristic of SIS junctions and, for those in which the MoS₂ interlayer thickness is below some limit, we could measure a finite Josephson supercurrent. These results validate the PLD approach for the fabrication of high-T_c/2D semiconductor heterostructures and devices and thus open the door to the study of high-T_c superconducting proximity effects in a vast family of materials with remarkable electronic properties.

7.1 ATTEMPTS WITH CVD MoS₂

Thanks to the expertise acquired with CVD graphene, I started this new project with high-quality CVD MoS₂ from the group of Piran Kidambi. I developed a transfer method specific to MoS₂ grown on sapphire. This method is detailed in chapter 4. After this crucial step, I characterized MoS₂ by Raman spectroscopy. In Figure 118b, the Raman spectrum of MoS₂ after the wet transfer on YBCO shows the two characteristic peaks of MoS₂ at 385cm⁻¹ and 405cm⁻¹. The spacing between the two peaks ($\approx 20\text{cm}^{-1}$) is a strong clue for monolayer MoS₂ as shown later in this chapter (see 7.2.3.1). I patterned it according to the method explained in chapter 4 to obtain devices similar to the one shown in Figure 118a. In this image, MoS₂ is barely visible since it is a monolayer but is highlighted by the red contour. After the plasma etching step, I took care to check whether the MoS₂ under the protective resist was unaffected by the in-between steps and that the MoS₂ was etched everywhere it had to be. Even if we do not always process a top gate, we covered the sample with amorphous alumina with the recipe given in chapter 4. It has been shown that it passivates

and protects TMDs [69].

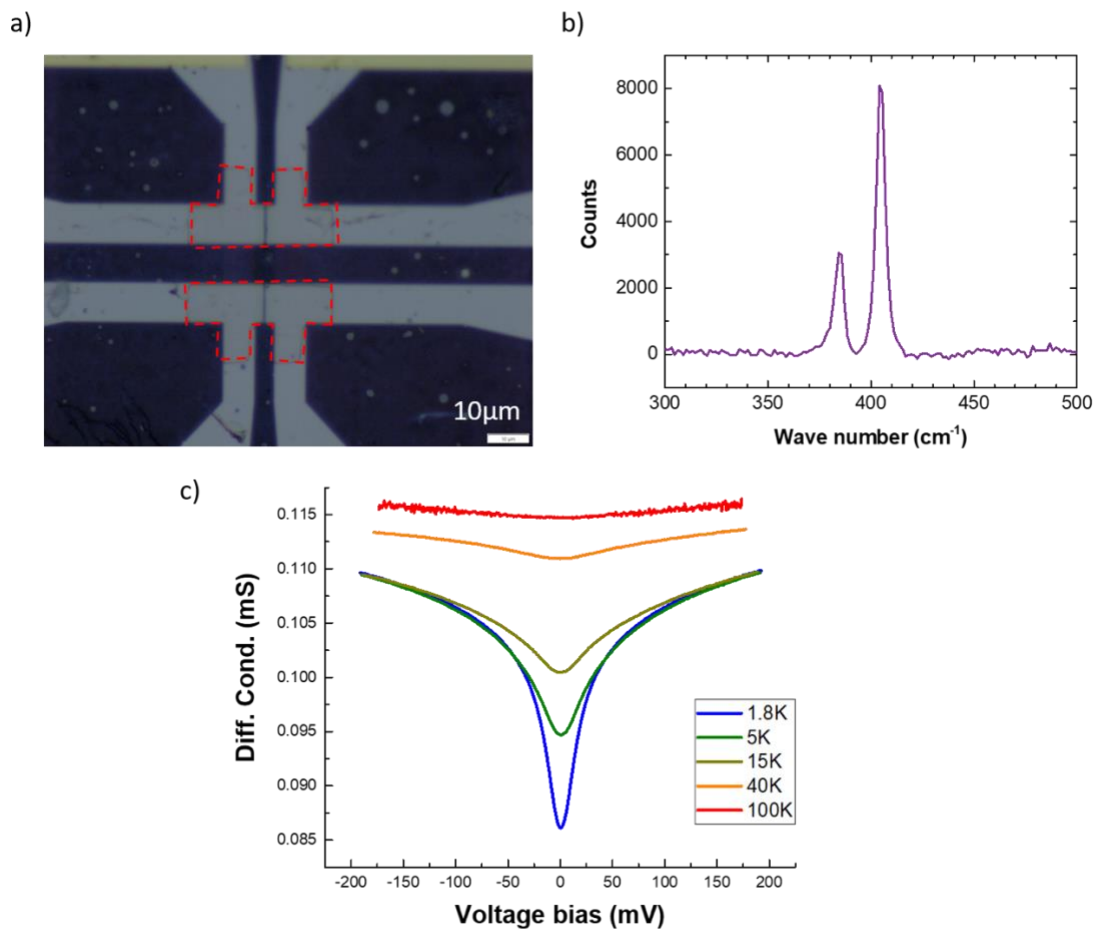


Figure 118 a) Microscope image of a device covered by patterned MoS₂ (highlighted by the red contour). b) Raman spectrum of CVD MoS₂ after the transfer on YBCO. c) Typical differential conductance measurements of a YBCO/MoS₂ junction at several temperatures.

Then, I carried out transport measurements and I obtained on average more resistive junctions than in the case of graphene. An example of a typical differential conductance measurement is shown in Figure 118c. This measurement was done in a 4-probe configuration in the delta mode of the instruments. The graph exhibits a decrease in the conductance close to zero bias indicating a tunnel behavior of the junction. This decrease is less pronounced as the temperature increases. In Figure 120a, the differential resistance of the junction at constant current ($I = 3\mu\text{A}$) is plotted against the temperature. The resistance increases a lot as the temperature gets lower. This is typical of superconducting tunnel junctions and very similar to what I computed for ref. [6] presented in chapter 3.

Similarly to what I have done with graphene, I studied the effects of both magnetic field and electrostatic gating. Concerning the magnetic field, the effect is relatively weak compared with the strong dependence on the temperature. Indeed, as seen in Figure 119b, the magnetic field increases the value of the zero bias conductance (< 1% between the one at 0 and 9T). This is also well shown by the plot of the resistance with respect to the magnetic field in Figure 120b. The resistance slightly increases until the field reaches around 5T and

then decreases again above.

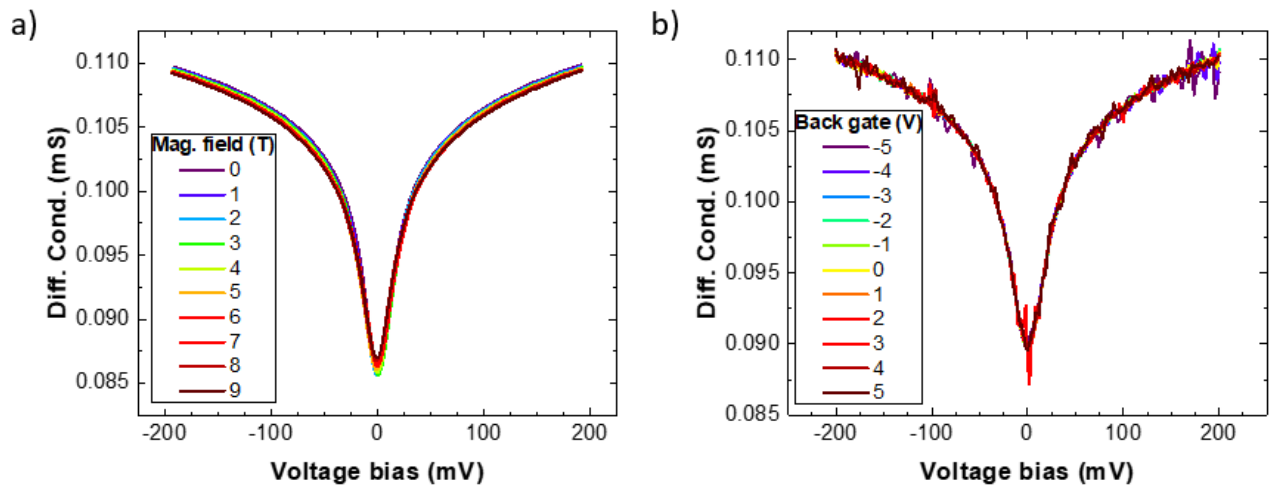


Figure 119 Differential conductance with respect to the voltage bias for a) magnetic field applied perpendicularly to the junction from 0 to 9T and b) for several back gate voltages from -5 to 5V. This second measurement was done by sourcing in voltage and not in current as all the others presented above.

I then present differential conductance spectra of the same junction measurement in a 2-probe configuration by changing the voltage applied to the back gate electrode. The result is shown in Figure 119b from -5V to +5V. There is no evolution of the conductance with the back gate voltage.

Finally, the dependence on the top gate voltage is shown in Figure 120b. The measurement was carried out in a 2-probe configuration and the top gate voltage was swept from 0 to 3V, then from 3V to -3V, and finally from -3V to 0V in order to exhibit potential hysteresis effect of the gate. This plot of the resistance as a function of the top gate voltage shows the gate voltage placed directly on top of the MoS₂ channel modulates its resistance (< 8% between -3 and 2V). The evolution is not larger because the resistance probed here is mainly made of the tunnel contact between YBCO and MoS₂. This contact resistance may not depend much on the top gate voltage. The MoS₂ channel resistance contributes to a small amount of the total resistance and the effect of the gate is then weak.

The differential conductance measurements, especially at several temperatures, tend to indicate we are in fact measuring the interface between YBCO capped by gold and MoS₂. The electrical contact has a low transparency which makes the junction have a tunnel behavior. Moreover, this low transparency does not create any proximity effect in MoS₂. Therefore, to achieve better transparency, we have to work on a better method to deposit MoS₂ on the YBCO surface. We keep trying other methods to transfer the 2D material the most efficiently with dry transfer for example but in parallel, we chose to develop a radically new method based on pulsed laser deposition directly on the superconductor as I will explain in the following.

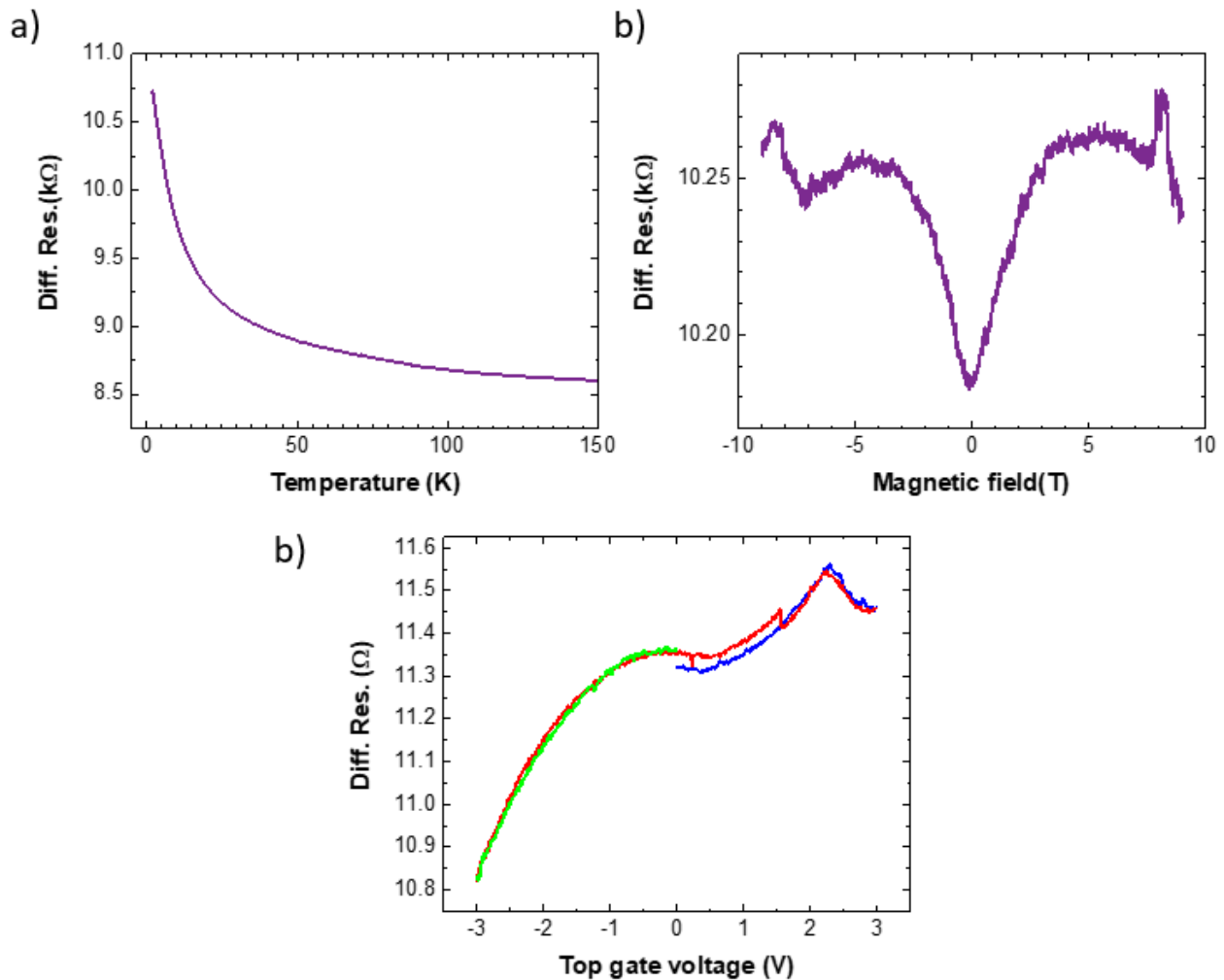


Figure 120 a) Resistance versus temperature in 4-probe configuration, b) differential resistance in 4-probe configuration versus the magnetic field, and c) differential resistance in a 2-probe measurement versus the top gate voltage.

7.2 NEW GROWTH METHOD AND CHARACTERIZATION OF THE MATERIALS

Since the transfer method presented in the previous section did not provide a good enough electrical contact between MoS_2 and YBCO, we decided to completely change the fabrication approach. Instead of transferring onto my devices a MoS_2 film that grew on a sacrificial substrate, we will grow MoS_2 directly on YBCO by pulsed laser deposition (PLD) in the wake of previous studies in the lab with this method [60,89]. This task is not trivial because is a fragile oxide that is prone to lose its oxygen atom when warmed or placed in a low-oxygen atmosphere. This loss results in a decrease of its T_c up to an insulating state if its stoichiometry changes too much. The problem is that the growth by PLD implies heating the chamber and working in a controlled atmosphere both for a good expulsion of the atoms from the target in the plasma and a correct deposition on the substrate. Following an optimization iteration of the growth parameters, Florian Godel and I developed a method to grow MoS_2 on YBCO while preserving its superconducting properties. In the following, I will first quickly present the setup we used and the initial recipe for growing MoS_2 by PLD. Then I will show the difficulties encountered and the solutions we found to preserve YBCO

superconducting properties. Finally, I will give the various characterizations of MoS₂ I carried out. The transport measurements on vertical junctions fabricated with this method will be shown in the next section.

7.2.1 Presentation of the setup

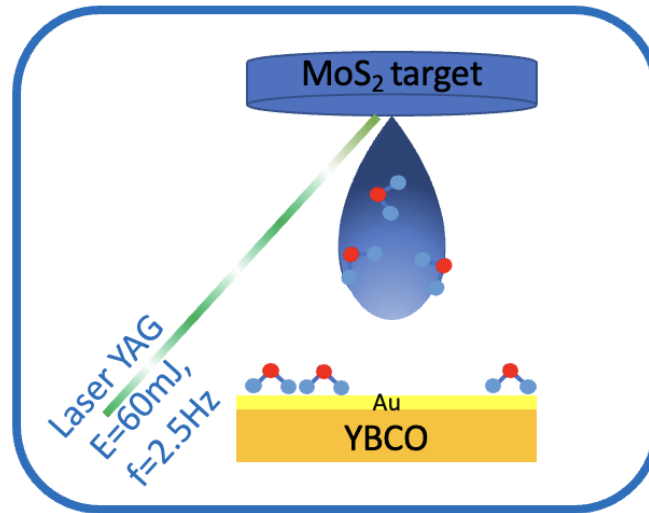


Figure 121 Simplified scheme of the PLD chamber for the growth of MoS₂ on YBCO at a growth temperature of 255°C.

I already explained pulsed laser deposition (PLD) in the chapter dedicated to the fabrication process (see chapter 4). Indeed, my YBCO films are grown by PLD. Here, I will only stress the differences between the setup previously studied and this new one depicted in Figure 121. I will describe the growth of MoS₂ on a usual substrate like SrTiO₃ (STO) or sapphire [60,89]. First, this PLD setup is equipped with a tripled frequency Nd:YAG (355nm) laser. The frequency of the laser pulses is 2.5Hz and their energy is set at 60mJ. These parameters appeared to be optimum for the quality of the growth. Indeed, the time between the pulses allows for the grown crystal to relax. In the chamber, a commercial and stoichiometric target of MoS₂ (from the company Neyco) is used. The sample holder and the target are placed 70mm apart from each other. A heater in the chamber allows for the setting of the temperature inside, allowing for the control of the growth temperature, T^{growth} , which typically ranges from 350 to 600°C and will be important in the following. This temperature is measured with a pyrometer pointed toward the substrate. During the growth, argon (Ar) is injected in the chamber at $P_{Ar} = 0.1\text{mbar}$ as background gas for the PLD plume. The duration of growth, *i.e.* the time the laser pulses on the target, determines the grown thickness. After the growth, the heater is shut down and the sample cools down inside for about one hour with $P_{Ar} = 0.1\text{mbar}$. The first experiment we tried was to grow MoS₂ in these conditions and it ended up with YBCO becoming insulating. In the following, I will present the parameters I can tune to make possible the growth of MoS₂ on YBCO without significantly deteriorating its superconducting properties.

7.2.2 Growth parameters and their effects

The first requirement for growth is to actually grow the desired material with the highest

quality possible. This point will be addressed in the next subsection. But the other requirement of my method is to preserve the superconducting properties of YBCO in order to allow a superconducting proximity effect with MoS₂, once it is grown. In this subsection, I will study the impact of three parameters -a controlled pressure of oxygen P_{O_2} , T^{growth} and the duration of growth- on the superconducting properties of YBCO by comparing resistance vs temperature measurements ($R(T)$).

7.2.2.1 Influence of the oxygen pressure in the chamber

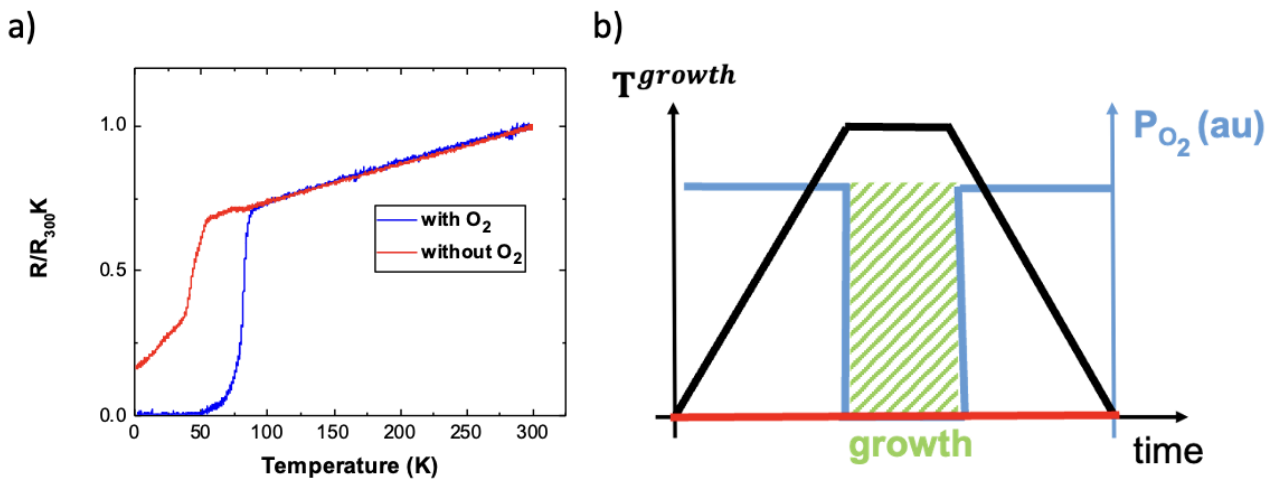


Figure 122 a) Resistance vs temperature for a process without oxygen injection in the chamber (red) and for a process with oxygen saturation before and after the growth, all the other parameters being identical ($T^{growth} = 255^{\circ}C$). b) Simplified temporal evolution the temperature inside the chamber and the pressure in oxygen for the two processes (with oxygen in blue and without in red corresponding to the plot in a).

We soon identified the problem of oxygen loss by YBCO when heated. One solution is to copy the way YBCO (and many oxides) is grown in an oxygen atmosphere. In the case of the MoS₂ growth, it is not possible to maintain a large pressure of oxygen during the whole process since oxygen atoms would be incorporated during the growth. There would be a mix of MoS₂ and MoO_x. Nevertheless, nothing prevents us from injecting oxygen in the chamber at $P_{O_2} = 300\text{mbar}$ while we are heating the chamber and cooling it down as shown with the blue line in Figure 122b. When the chamber reaches the setpoint T^{growth} , we pump the oxygen until a pressure of 0.1mbar and then inject 0.1mbar of Ar as the background gas for the deposition. This procedure is summarized in Figure 122b with (blue) or without (red) oxygen. During the growth duration represented by the hatched green region, the substrate is at T^{growth} , $P_{O_2} = 0$ and the pressure of argon is $P_{Ar} = 0.1\text{mbar}$. a compares the $R(T)$ of the samples after the two processes with (blue line) or without oxygen (red line) carried out for $T^{growth} = 255^{\circ}C$. With oxygen, a transition occurs at $\sim 80\text{K}$ with the resistance going exactly to zero. On the contrary, without any injection of oxygen during the process, the behavior remains metallic but the transition that occurs at $\sim 50\text{K}$ does not lead to a zero-resistance state. The film does not become superconducting after this process. **This shows how crucial is to maintain an oxygen-rich atmosphere in the chamber while heating it. Otherwise, a substantial part of oxygen atoms migrates out of YBCO deteriorating its**

superconducting properties.

7.2.2.2 Influence of the growth temperature

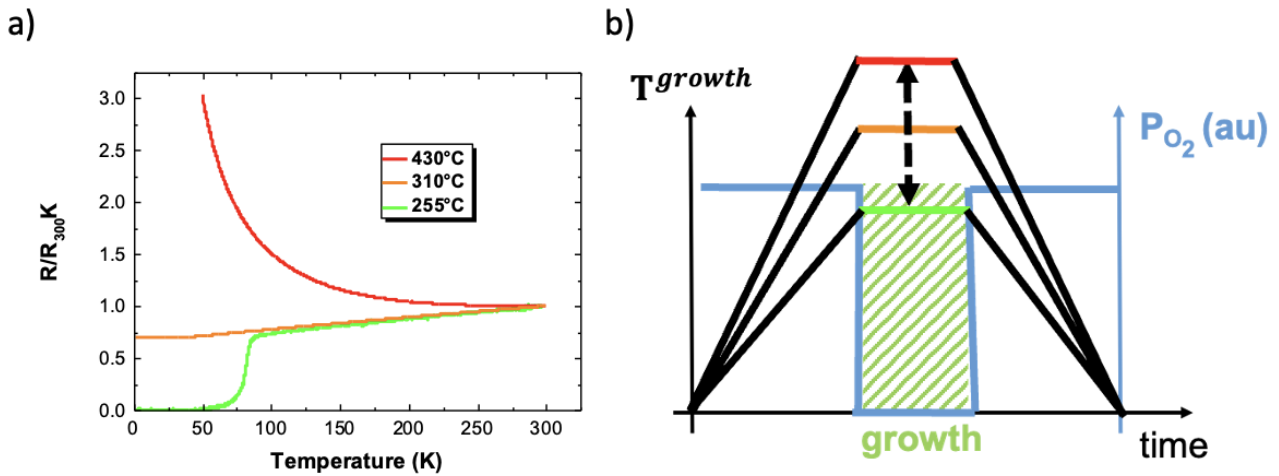


Figure 123 a) Resistance vs temperature for different T^{growth} , all the other parameters being identical. b) Simplified temporal evolution of the temperature inside the chamber and the pressure in oxygen. Only the set T^{growth} changes between these three experiments.

The substrate temperature T^{growth} usually plays a key role in the growth processes since it allows for better crystallization once the atoms are on the substrate. However, the higher the temperature, the larger the oxygen mobility in YBCO and the more easily oxygen atoms can escape from YBCO. Figure 123a shows the resistance versus temperature for different T^{growth} summarized in the recapitulative scheme in Figure 123b. All the growths shown have been made with the protocol with the injection of oxygen. Let us start with the highest $T^{growth} = 430^{\circ}\text{C}$, the resistance of a film of $5\mu\text{m} \times 5\mu\text{m}$ at ambient temperature is $5\text{k}\Omega$ and the resistance increases as the temperature is going down and diverges at temperature below 50K). This is characteristic of an insulating behavior at low temperatures. Not only the temperature made YBCO become insulating but even the 10nm-thick layer of gold on top of YBCO percolated due to the heat, resulting in an overall insulating behavior. For $T^{growth} = 310^{\circ}\text{C}$, the film behaves as a metal with a decreasing resistance when the temperature is lowered. The resistance saturates at 11.5Ω and never reaches zero which means the film never becomes superconducting. Finally, **for $T^{growth} = 255^{\circ}\text{C}$, the film still behaves as a metal for $T > 80\text{K}$ and below, a sharp transition occurs with the resistance going down quickly to zero resistance.** The presence of a tail of around 20K between the beginning and end of the transition may indicate an inhomogeneity [242] of the properties of the films with a position-dependent T_c .

7.2.2.3 Influence of the duration of growth

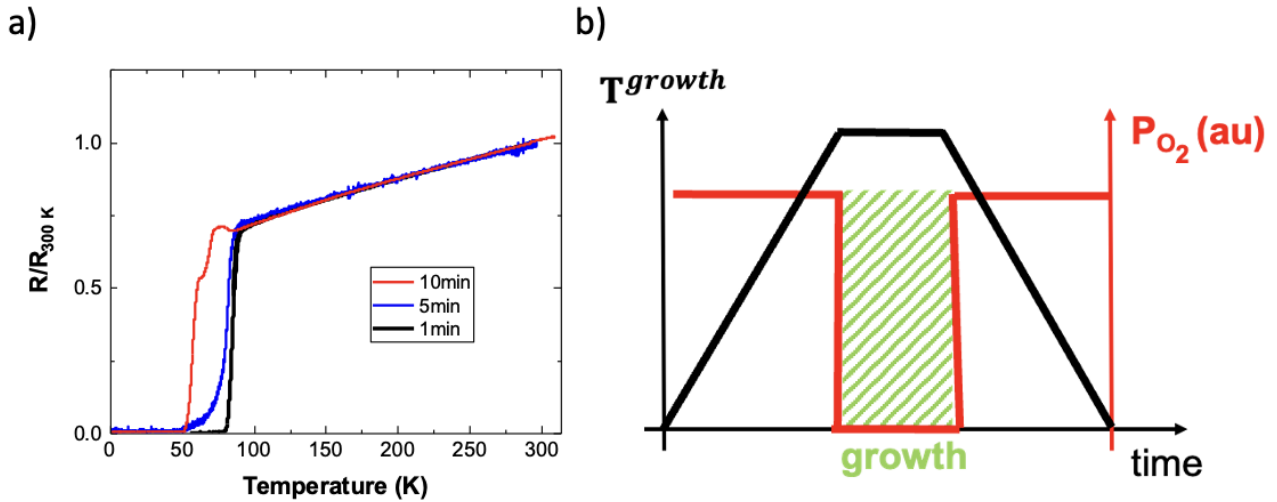


Figure 124 a) Resistance vs temperature for different durations of growth, all the other parameters being identical. b) Simplified temporal evolution of the temperature inside the chamber and the pressure in oxygen. The duration of the growth is represented by the width of the green-hatched region.

Figure 124a presents three $R(T)$ -measurements for different growth durations. For these three growths, T^{growth} is fixed at 255°C and the oxygen pressure follows the procedure explained previously and shown in Figure 124b. The three $R(T)$ show a superconducting transition but the longer the duration, the lower the critical temperature of the film. This can be understood by considering that during the growth, the superconductor is in a heated atmosphere of Ar, which is detrimental to its oxygen stoichiometry. As a consequence, the longer the superconductor stays in this atmosphere without oxygen, the more oxygen escapes from YBCO, and the lower the T_c . We have to notice that there is an incompressible time in addition to the growth duration which corresponds to the time necessary to pump the oxygen from 300mbar to 0.1mbar and then inject Ar. This takes around 5 minutes. As I will show in 7.2.3.3, the thickness of the deposited MoS_2 is linked to the duration of the growth and the shorter it is, the thinner will be MoS_2 and that's where we want to tend: high-quality few-layers MoS_2 . Now I found good growth conditions to **preserve YBCO's superconducting properties** (see Table 6), I will characterize the films I deposited.

T^{growth}	$P_{\text{O}_2}^{\text{warm-up}}$	$P_{\text{Ar}}^{\text{growth}}$	$P_{\text{O}_2}^{\text{cool}}$	Growth duration	Pumping time	Laser energy	Frequency
255°C	300mbar	10^{-1} mbar	300mbar	1-10min	~5 min	60mJ	2.5Hz

Table 6 Recap of the growth conditions for MoS_2 on YBCO to preserve YBCO and grow high-quality MoS_2 .

7.2.3 Characterization of the 2D material

After checking if YBCO is still superconducting after the growth process, my first requirement is to check the quality of the grown crystal. I used three characterization techniques: Raman

spectroscopy presented in 7.2.3.1, then X-ray photoelectron spectroscopy (XPS), and finally atomic force microscopy (AFM) in 7.2.3.3.

7.2.3.1 Raman spectroscopy

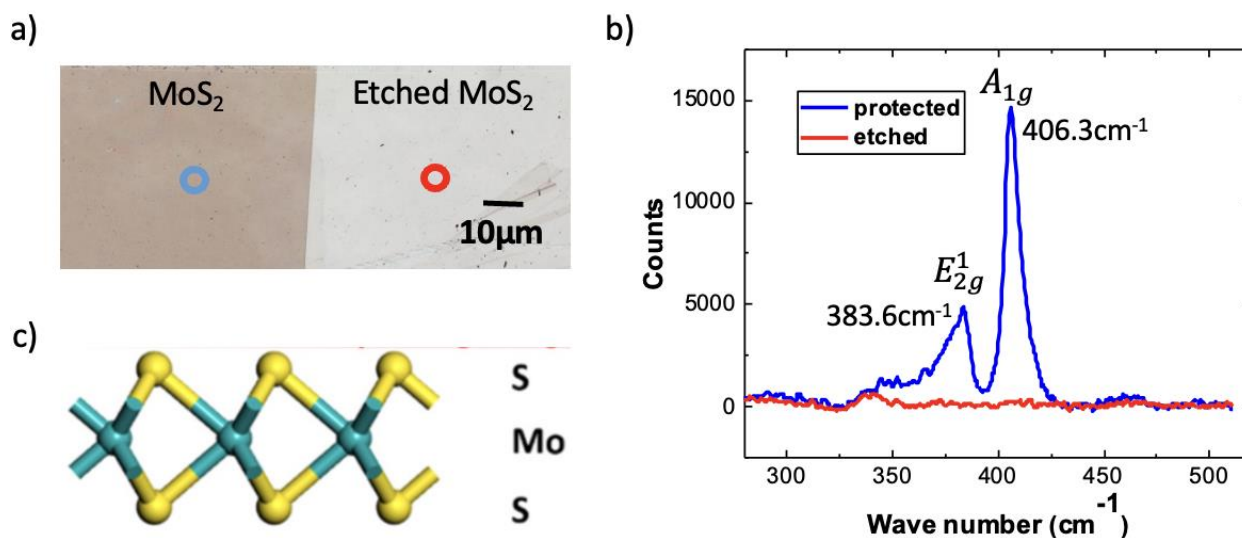


Figure 125 a) Microscope image of a step with the right side etched by an oxygen plasma, b) Raman spectra for both the etched region (red line) and protected one (blue line) and c) Schematic representation of the 2H phase of a monolayer MoS₂ (Taken from Gan et al., ACS Appl. Energy Mater., 1, 9 (2018)).

As we have seen in chapter 4, Raman spectroscopy is a very useful tool to study 2D materials since each material has a different signature. I conducted a comparative Raman study by probing two areas on each sample. In the first area (blue ring on the microscope image in Figure 125a), YBCO/Au is covered by the as-grown MoS₂. In the second area (red ring), defined by optical lithography, MoS₂ has been removed by etching with an oxygen plasma [192] (RF power at 30W with 10sccm of O₂ for 90 seconds). Raman spectra for both regions are displayed in Figure 125b. I used a green laser ($\lambda = 514\text{nm}$) at a power of 5mW for 10 seconds with a 3000l/mm grating. MoS₂ (blue) has two peaks, E_{2g}^1 at 383.6cm^{-1} and A_{1g} at 406.3cm^{-1} that are characteristic of the presence of 2H-MoS₂ [243–245], one of the phases of MoS₂ crystallographic structure shown on Figure 125c [246]. On the contrary, the red curve, corresponding to solely YBCO capped with Au (red), does not present the same **Raman signature** of MoS₂.

Raman spectroscopy also allows to estimate the **number of layers** in the few layers limit. In Figure 126, I reviewed the literature [247–253] and plotted the difference $\Delta\omega$ between the wavenumbers of the two characteristic peaks E_{2g}^1 and A_{1g} as a function of the number of layers. MoS₂ obtained and measured in different ways seems to behave always the same with Raman spectroscopy according to this plot except for the monolayer case where a variation is observed between the groups. $\Delta\omega$ first increases a lot until 6-7 layers and then reaches a plateau at the bulk value. From the Figure 125b, the difference is $\Delta\omega = (22.7 \pm 0.6)\text{cm}^{-1}$ indicating the film is a few layers thick (3-4 layers).

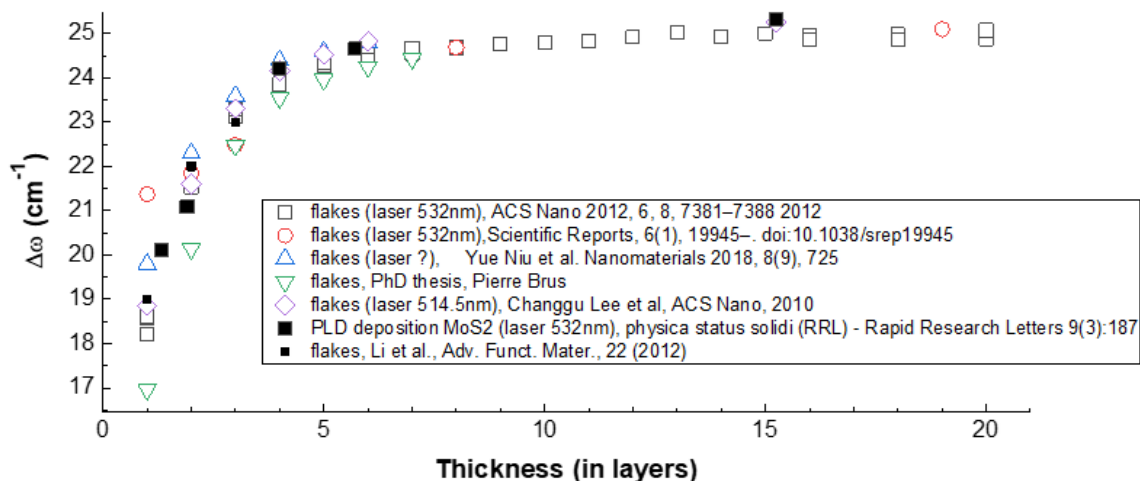


Figure 126 Difference of wave number $\Delta\omega$ (cm^{-1}) between the two characteristic peak of MoS_2 as a function of the number of layers taken from different papers in the literature.

Finally, Raman spectroscopy can be used to determine the **homogeneity** of a film by scanning the XY direction. The assumption here is that if a region is homogeneous, then the Raman spectra at different points should be very similar. To quantify the notion of similarity between spectra, I decided to choose the ratio between the intensity of the two characteristic peaks of MoS_2 : $\frac{I_{A_{1g}}}{I_{E_{2g}^1}}$ written A_{1g}/E_{2g}^1 for simplicity. This operation is done after removing the background with the software of the Raman spectrometer and fitting both peaks with Lorentzian functions. Their amplitudes are then extracted and I plotted the ratio. A colormap of this ratio as a function of the position on a $6\mu\text{m} \times 6\mu\text{m}$ grid is presented in Figure 127.

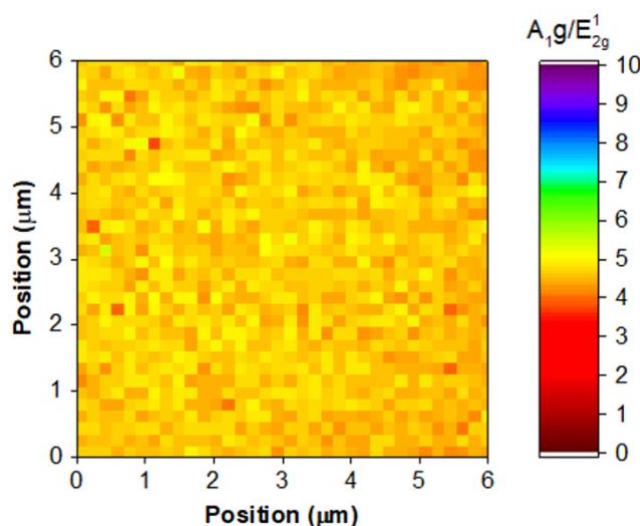


Figure 127 2D-colormap of the ratio between the intensity of the A_{1g} and E_{2g}^1 peaks on a square of $6\mu\text{m}$ side regions covered with MoS_2 .

We see on this plot that MoS_2 grew on large-scale on our sample, with a good homogeneity as the peak ratio is nearly constant over the large area we probed taking values between 4 and 5. This result indicates the successful growth of a homogeneous layer of MoS_2 on YBCO. This map shows the added value of PLD compared with CVD methods which results in islands

of flakes on the growth substrate around the seeds or other projection methods that create bubbles of material. On the contrary, this colormap demonstrates a layered growth by PLD as well as previous transmission electron microscopy (TEM) done in [89].

7.2.3.2 X-ray photoelectron spectroscopy (XPS)

After the Raman spectroscopy characterization that allowed to identify MoS_2 , and to estimate its thickness and homogeneity, we wanted to investigate the chemistry of the film. Indeed, it can happen the materials deposited are not only the ones desired, especially in the presence of oxidation. To answer this question, a convenient tool is X-ray photoelectron spectroscopy. It is a surface-sensitive experiment that allows for the detection of chemical species along with their chemical environment. An X-ray beam is sent to the sample with a given incidence, it excites electrons enough to be ejected. These electrons are collected and their kinetic energy is measured. This way, it is possible to access the atomic orbitals they come from and know the environment of the atoms since the energy levels of the atom will be modified by the presence of other atoms. The proportion of each kind of atom (**chemical species and environment**) appears as a peak in the spectroscopy.

We carried out two XPS measurements at two different incidences. The first one is given on the left of Figure 128. As shown on the inset, it corresponds to a grazing incidence, only probing the first few layers at the surface. The result of the fit shows the presence of the 3d orbital of Mo as well as the 2s orbital of S. However, an important peak corresponds to oxidized Mo (MoO_x). When we computed the proportions of Mo atoms against the one of S atoms. We found there was a deficit of Mo atoms compared with sulfur ones. So we performed the same experiment but this time with an incidence close to normal. The probed region is now deeper into the film ($\sim 5\text{nm}$) and not only the surface. The resulting spectrum has a much smaller MoO_x peak while the 3d orbital peak of Mo has a larger amplitude. This time, the computation of the ratio between the two atoms is 2.05, the expected value being 2.

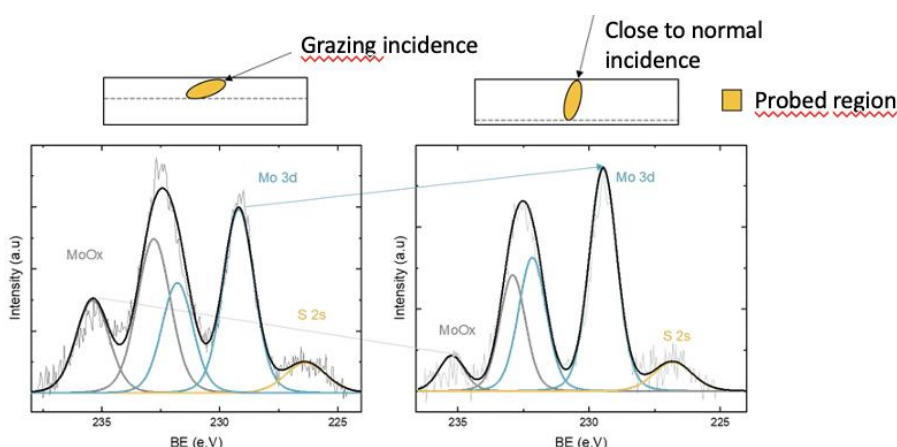


Figure 128 (left) XPS measurement at grazing incidence of a MoS_2 film grown on YBCO. (right) Same but at close to the normal incidence of a MoS_2 film grown on YBCO. Only the energy range of the molybdenum and sulfur atoms is shown for these two graphs. Each peak is fitted individually and represented with a blue (yellow) color for molybdenum (sulfur).

Though this final result shows we indeed grew MoS₂ on YBCO, the previous one suggests the presence of a molybdenum oxide layer on top of MoS₂. This may be due to the oxygen-saturated atmosphere in the chamber during the cool-down. For another batch of samples, we could try to see the effect of a cool-down without oxygen after the growth. It may also be possible to quench the sample to make it cool down very quickly and thus not have to put oxygen in the chamber.

7.2.3.3 Atomic force microscopy (AFM)

After the structural and chemical characterization, I wanted to have some information concerning the **growth rate**. Indeed, with a calibration curve, I could then easily grow a sample with the desired thickness. Therefore, I intended to do a calibration curve by only varying the duration of growth from 1 to 4 minutes. On each sample, I etched a part of the surface with the method explained in 7.2.3.1. Then I performed atomic force microscopy on these four samples to measure the step created by the etching. The path of the AFM tip is schematized by the black line in Figure 129a. The topographic profile is presented in Figure 129b. There is indeed a step between the region where MoS₂ was protected during the plasma etching and the region where it was etched. I carried out this measurement for the 4 samples and I reported the height of this step against the respective duration of growth on c.

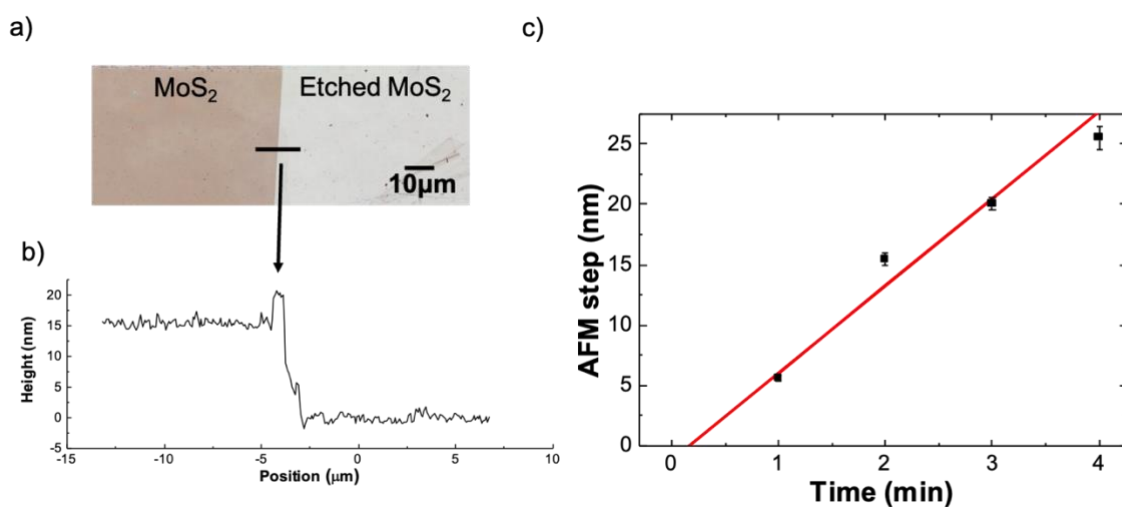


Figure 129 a) Microscope image of a step with the right side etched by an oxygen plasma. The black line corresponds to the path of the AFM tip of the measurement in b. b) 1D AFM topographic profile along the path given in a. c) AFM measurements of the step on samples as a function of their growth time (black squares). The experimental points are fitted with a linear model (red line).

I then fitted these experimental points (black squares) with a linear model (red line on the plot) which allowed me to extract a growth rate that I estimate to be (7.2 ± 0.8) nm/min, or roughly 10 layers per minute. We can compare this to the thickness I estimated earlier with the Raman spectrum. For the sample whose thickness measured with the AFM is 15 nm, the thickness of the MoS₂ film was estimated at 3 or 4 layers. Knowing that a MoS₂ layer is about

0.7nm, there is a discrepancy between the two approaches. First, the measurement of the distance between the peaks may be influenced by the nature of my substrate (YBCO/Au) which is different than the examples given in the review (mainly exfoliated MoS₂ on usual substrates like sapphire or silicon oxide). Second, the estimation of the thickness by Raman spectroscopy is limited to a few layers, typically up to 4-5 layers. Third, as suggested by the XPS measurements, a layer of oxide is forming at the surface on top of MoS₂. This layer is measured at the AFM and may also screen the Raman scattered photons. This would explain why we only estimate at 3 to 4 the number of layers of MoS₂ with the distance between the two peaks though the thickness of the film is around 15nm.

7.3 TRANSPORT MEASUREMENTS OF VERTICAL JUNCTIONS

Having successfully identified the optimal parameters for the growth of large-scale 2D MoS₂ on the surface of YBCO, while minimally affecting its superconducting characteristics, I have chosen to proceed with the integration of this methodology for the fabrication of superconducting devices. First, I will present the geometry and the materials used in these devices, and in the next two parts, I will analyze the transport measurements in two regimes, the diffusive one and the superconducting one.

7.3.1 Device fabrication

The aim here is to build superconducting vertical junctions made of YBCO as the bottom electrode and another superconductor as the top electrode with MoS₂ in between. As for the optimization process, I used YBCO grown on STO and covered *in situ* by 10nm of gold. The deposition of MoS₂ is done using the process summarized in Table 6. I chose different growth durations such as the thickness of MoS₂ will vary to aim for different regimes of superconducting coupling between the electrodes. The design of the vertical junctions is similar to the one in previous papers from our team [6,254]. The process (given in chapter 4, see also Figure 130c) consists of patterning square apertures in a resist (from 1 to 20 μ m side), making it harder, and then proceeding to another lithography to define a bigger pattern for the contacts. A microscope image after the second lithography step is given in Figure 130a where the square hole of 7.5 μ m is zoomed. Then, 100nm-thick Mo₈₀Si₂₀ (later referred to as MoSi) –an amorphous *s-wave* superconductor with a T_c^{MoSi} of ~ 7.2 K [255] but which depends on the deposition– are deposited by sputtering. Finally, 100nm of gold is sputtered to prevent MoSi from oxidation and to make the wire bonding easier. The details of the different layers are provided in Figure 130b. The lift-off of the resist removes the extra metallic layer.

With the obtained layout, it is possible to measure the junctions in a 4-probe geometry by directly wire-bonding on YBCO and the Au atop the junctions. The transport measurements carried out at low temperatures depend on the thickness of the MoS₂ layer. For thick (> 10 nm) MoS₂, I measured a tunnel barrier while for thin (~ 5 nm) MoS₂, I measured also a tunneling behavior (see 7.3.2) but with some junctions exhibiting Josephson coupling at sufficiently low current and temperature (see 7.3.3).

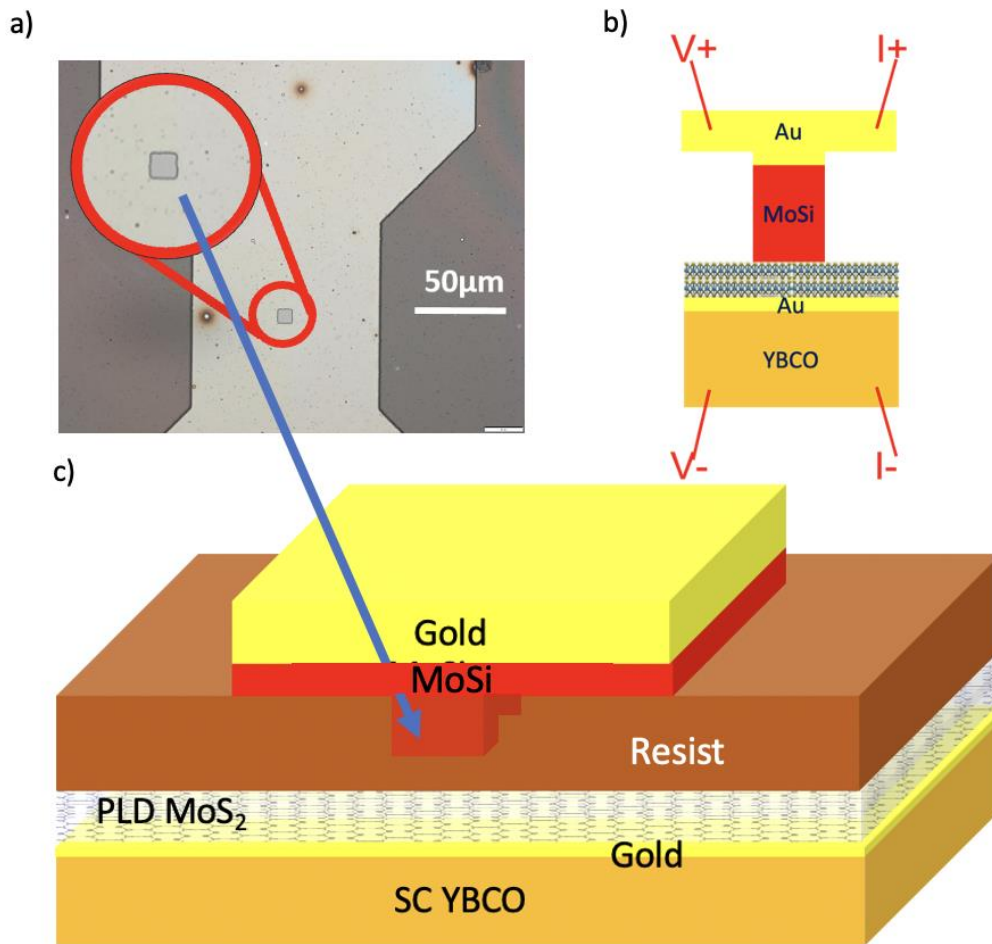


Figure 130 a) Microscope image after the second lithography step of a future vertical junction. The zoom shows a junction with the form of a square aperture. b) Details about the heterostructure with the different stacked layers. c) Side view of the vertical device.

7.3.2 Junction's differential conductance

In all the following, I present 4-probe measurements in the so-called "delta mode" of the Keithley instruments. The current is biased and the voltage is measured. Contrary to the measurements shown in this chapter or the previous ones, I chose the following unless otherwise stated, to use the current as the x-axis and not the voltage bias. Indeed, all the measured junctions present a switching between two states as a function of the injected current, so that the differential conductance is not a function of the voltage over the entire measured range. The junctions taken as examples here come from the same sample with a thin (~5nm) MoS₂ layer (1-minute growth) and are representative of the general behavior of the junctions. Their dimensions are 7.5µm × 7.5µm (R1874D D2) and 10µm × 10µm (R1874D E11). I will also compare them to a junction with a thicker MoS₂ layer (~25nm) and dimensions 14µm × 14µm (R1874A B7).

7.3.2.1 Temperature-dependent differential conductance, influence of the MoS₂ thickness

In Figure 131a, I show the differential conductance plotted against the bias current for temperatures chosen with care, and in b the voltage-current characteristics at the same

temperatures. These measurements have been carried out on the junction R1874D D2 which has a thin MoS₂ layer (~5nm).

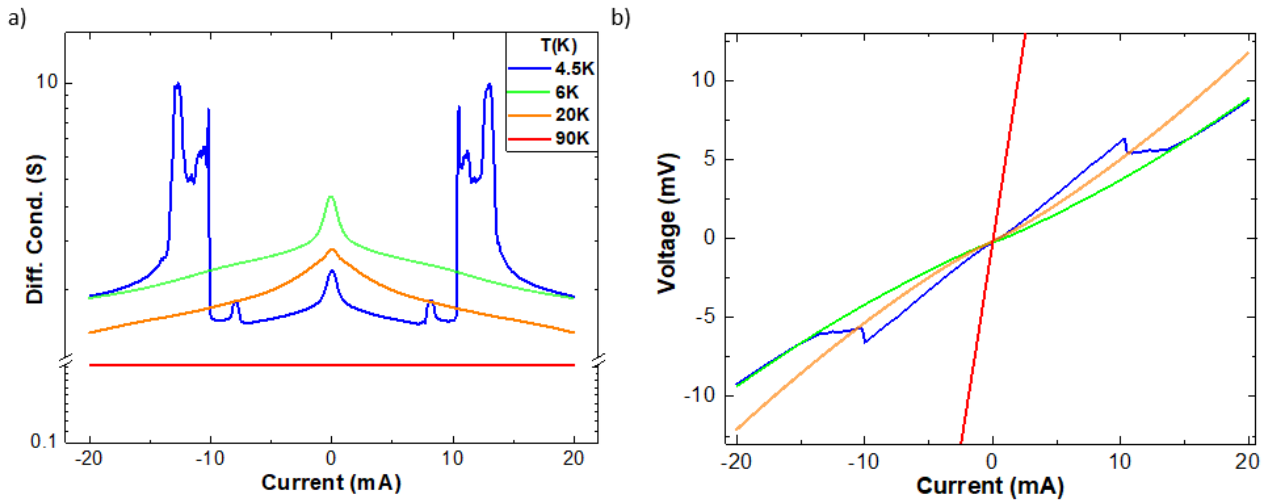


Figure 131 a) Differential conductance vs bias current of the junction R1874D D2 at different temperatures in a semi-log plot. b) Voltage-current characteristics at the same temperatures with the same color code.

At the lowest temperature, below both the superconducting transition temperature of YBCO (T_C^{YBCO}) and MoSi (T_C^{MoSi}), the differential conductance has a very rich structure. At low currents (between -10mA and 10mA), the differential conductance has a lower level ($\sim 1.5\text{S}$) than at higher currents ($\sim 1.8\text{S}$). In this region, we observe peaks at $\sim \pm 8\text{mA}$ as well as a central peak at zero bias current. Two sharp transitions occur at around $\pm 10\text{mA}$ for the first one and $\pm 14\text{mA}$ for the second one. They are also clear on the I-V curve (Figure 131b) where we can see an abrupt change in the curve's trend above a threshold current that decreases with increasing temperature. Back to the differential conductance curves in Figure 131a, we see that at 6K, just above $T_C^{MoSi} \sim 5.8\text{K}$, the differential conductance curve changes radically as compared with the one at 4.5K. The most salient feature is the enhancement of the conductance in the low current regime (between -10mA and 10mA). Notice that the conductance level at higher current is essentially the same at $T = 4.5\text{K}$ and $T = 6\text{K}$, that is, below and above T_C^{MoSi} . Notice also that at $T = 6\text{K}$ we still observe the zero-bias peak, which indicates that it is not related to superconductivity in MoSi. For an even larger temperature, still below T_C^{YBCO} , the shape remains more or less the same except the conductance at high current is lower ($\sim 1.3\text{S}$). The central peak is also less sharp. Finally, above T_C^{YBCO} , the differential conductance is featureless corresponding to an ohmic response. The overall conductance at this high temperature is much lower ($\sim 0.2\text{S}$).

Figure 132 displays the low temperature transport measurement of another junction (R1874A B7) that has a thicker MoS₂ layer ($\sim 25\text{nm}$). In this figure we focus again on the low-temperature range just below and above T_C^{MoSi} . At the lowest temperature $T = 4\text{K}$, and similarly as for the junction R1874D D2 with thinner MoS₂ in Figure 131, we observe a strong conductance decrease within a low bias range, which is followed by the peaks (here at $\sim \pm 15\text{mA}$) that precede the switching into a the high-bias regime in which the conductance is nearly the same as for $T = 6\text{K}$. However, contrary to junction R1874D D2, here, there is no

enhancement of the differential conductance at zero bias.

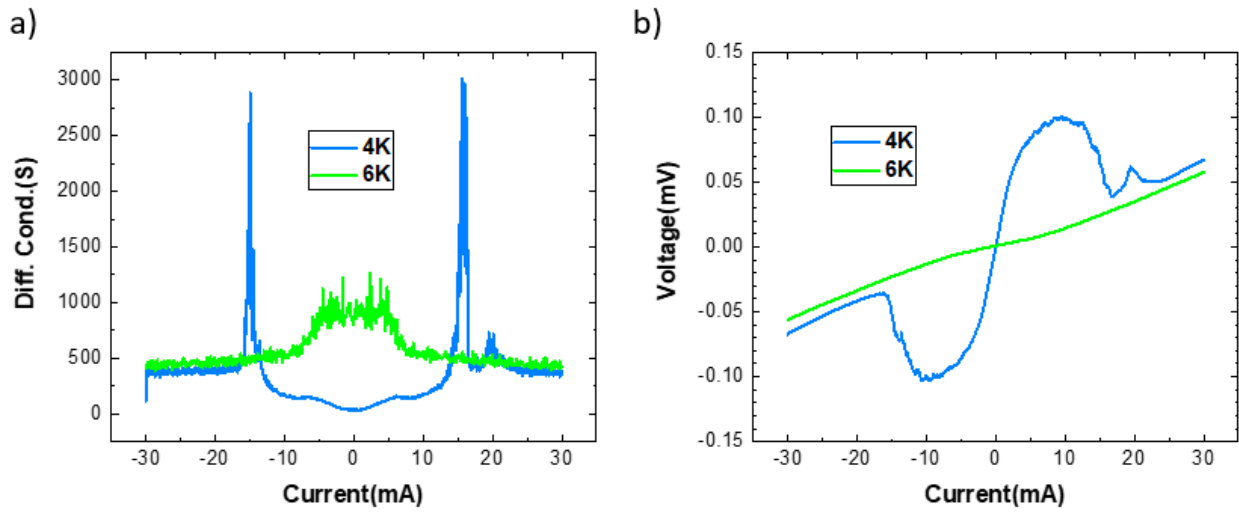


Figure 132 a) Differential conductance vs current of the junction R1874A B7 (thicker MoS₂) at two temperatures. b) Corresponding I-V characteristics.

7.3.2.2 Temperature evolution

As we started to see in the previous paragraph, the study of the transport properties of the vertical junctions revealed that all junctions share a common point, whatever the thickness of the MoS₂ layer and their resistance. To illustrate this point, I display the temperature behavior of a third junction (R1874D E11).

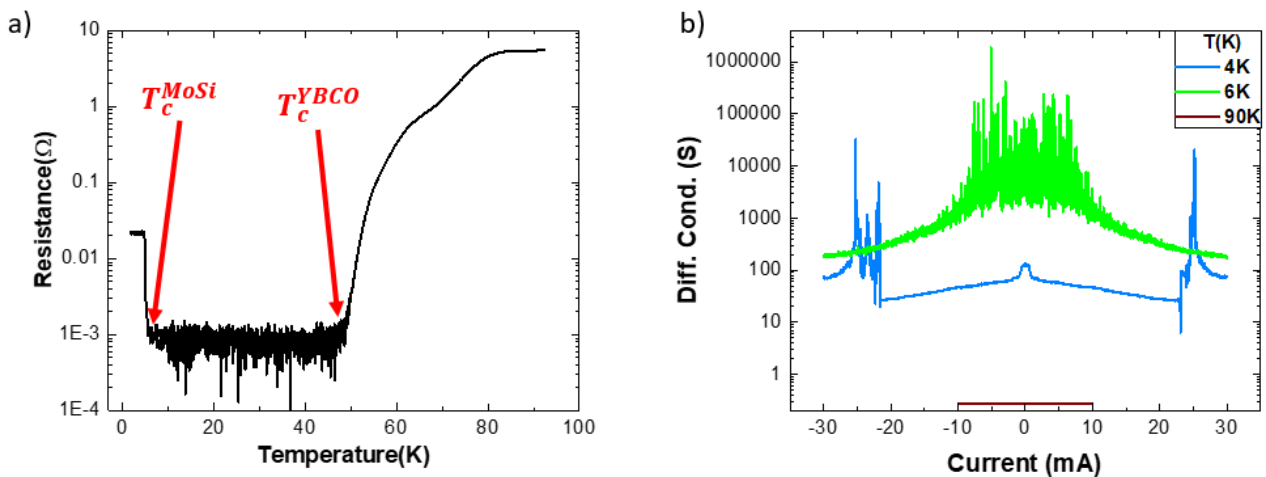


Figure 133 a) Resistance versus temperature measured at a current $I = 100\mu A$ of the junction R1874D E11. b) Differential conductance spectra at different temperatures of the same junction (semi-log plot).

In Figure 133a, I show the resistance *versus* temperature ($R(T)$) measurement of the junction. It was measured for a low bias current $I = 100\mu A$. We can see that the resistance drops below $T = 80K$, which can be attributed to the superconducting transition of the bottom electrode made of YBCO. Below T_c^{YBCO} , the resistance is very low until we reach T_c^{MoSi} . At that temperature, the resistance increases by one order of magnitude and reaches a plateau until

the lowest reachable temperature in our cryostat.

In the corresponding conductance curves in Figure 133b, we can distinguish several regimes depending on the temperature. Above 90K, the junctions have an ohmic behavior. This is shown by the flat and featureless conductance at 90K. Below 90K, the superconducting transition of YBCO occurs and the overall conductance of the devices increases gradually. In addition, a zero-bias enhancement of the conductance (a peak) appears, which is present down to the lowest temperature (see for instance $T = 6\text{K}$). Below $T_C^{Mosi} \sim 5.8\text{K}$, the conductance of the device shows a sharp conductance decrease within the low current regime. The differential conductance decreases by a factor ~ 10 . A peak remains in the differential conductance spectrum. The next subsection will describe the evolution of the spectral features at low temperatures in the presence of a magnetic field.

7.3.2.3 Magnetic field evolution

Conductance curves have also been measured at a fixed temperature 4.5K for variable magnetic fields (applied perpendicularly to the junction, that is, in-plane of the layers). A set of measurements is displayed in Figure 134a. We observe that, as the magnetic field is increased, the sharp current-induced peaks/switching mentioned above for the lowest temperature occur at smaller and smaller values of the current and end up disappearing between 0.6 and 0.8T. This trend is also visible on the I-V curves presented in Figure 134b since the abrupt change of in the $V(I)$ happens at lower current values as the field increases. We notice that the plot at 0.8T at 4.5K is very similar to the one at zero magnetic field but 6K presented earlier. They both only have the central peak as a feature and have similar conductance values. Concerning the other features of the differential conductance, the central peak remains except at 0.6T while the sharp transition peaks are only present up to 0.6T.

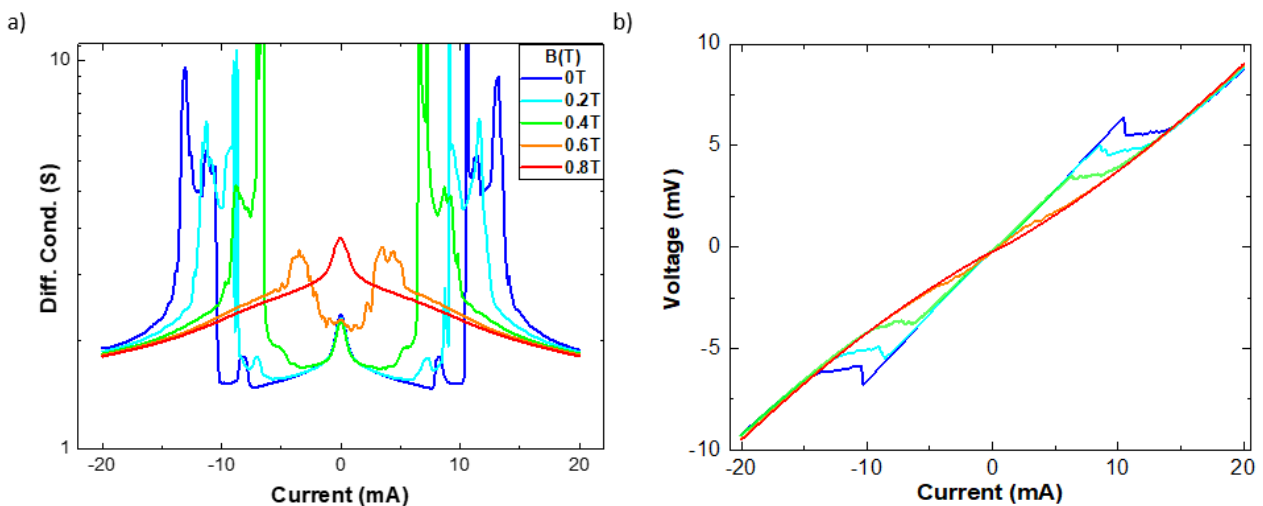


Figure 134 a) Differential conductance vs bias current of the junction at different magnetic fields in a semi-log plot. b) Voltage-current characteristics at the same magnetic field with the same color code.

7.3.2.4 Discussion

The temperature and field behavior described above allow for distinguishing what conductance features must be attributed to the onset of superconductivity in the different junction layers. At $T = 4.5\text{K}$, which is below $T_c^{\text{MoSi}} \sim 5.8\text{K}$, the most characteristic feature in comparison with the plot at 6K is the sharp conductance drop at $\pm 10\text{mA}$, accompanied by a series of peaks ($\pm 14\text{mA}$ and $\pm 10\text{mA}$ but also $\pm 8\text{mA}$). The observed conductance decrease agrees with the expected behavior when a superconducting gap forms around the Fermi level of MoSi. This behavior is consistent with electron injection into a superconductor through a contact with finite transparency. The conduction arises from a combination of Andreev reflection (AR) and electron tunneling into sub-gap quasiparticle excitations. As a result, the conductance lies between zero (expected from pure electron tunneling if the contact was not transparent) and a doubling of conductance (expected with perfect transparency, due to pure AR) as seen in chapter 3. This regime ends as the current across the junction reaches $\sim 10\text{mA}$. This corresponds to a current density $\sim 2 \times 10^{-2}\text{MA/cm}^2$, close to expected the critical current of MoSi [256]. From this, we conclude that the curve at 4.5K rejoins the curve measured at 6K just because **the current drives MoSi into the normal state**. The series of peaks ($\pm 14\text{mA}$ and $\pm 10\text{mA}$ and $\pm 8\text{mA}$) before and after the main conductance jump likely stem from small variations of the critical current over the junction area, that is, from spatial inhomogeneities of the critical current. That scenario is consistent with the behavior observed in Figure 134a, in which we see the peaks rapidly shifting towards zero current as the magnetic field is increased. An alternative scenario to explain the conductance peaks would be that they are features related to the density of states of MoSi, and particularly, that they reflect the divergence of the quasiparticle density of state near the gap edge [5]. In this scenario, again, one needs to assume a spatial inhomogeneity over the junction area, that is the gap has different sizes in the different areas yielding the various peaks observed in the conductance curves. This scenario is also consistent with the behavior under magnetic field observed in Figure 134 since the superconducting gap should be gradually suppressed as the magnetic field is increased to H_{c2} , which we estimate below $1T$ from our $G(V)$ measurements in Figure 134a. The complementary study of a MoSi film grown on a silicon oxide substrate gave $H_{c2} \approx 2T$ as the same reduced temperature T/T_c as for the measurement in Figure 134a. The lower H_{c2} inferred from the latter measurements is probably due to the fact that superconductivity in MoSi is weakened in the interfacial MoSi (this is also indicated by the lower $T_c^{\text{MoSi}} \sim 5.8\text{K}$ as compared to the films $T_c^{\text{MoSi}} \sim 7\text{K}$) due to proximity with MoS_2 .

The zero-bias conductance peak, which is observed for all $T < T_c^{\text{YBCO}}$ and is the only prominent feature for $T > T_c^{\text{MoSi}}$, must be related to superconductivity in YBCO. It is tempting to link this zero-bias peak to tunneling into the quasiparticle surface states of YBCO [119,105], a characteristic behavior of tunneling into *d-wave* superconductors that is expected when the topography of the YBCO surface makes the conductance is dominated by tunneling into the CuO planes in YBCO [105,119], as we discussed in chapter 3 when we discussed the spin-pumping experiments into YBCO [8]. The gradual peak disappearance as the temperature is increased is accompanied by a significant decrease in the overall conductance (at any of the measured current biases). This is also observed in the $R(T)$ -

measurement shown in Figure 133a. This suggests that, in addition to the tunneling between MoSi and YBCO, the measurement senses the resistance of the YBCO electrode itself for temperatures above 50K.

The arguments discussed above indicate that, at low temperatures, that are below 50K, the conductance of the junctions is dominated by tunneling between YBCO and MoSi across the intermediate Au/MoS₂ layers. However, we expect the thin Au to become superconducting by proximity (as discussed in chapters 5 and 6), and likely MoS₂ is also proximized to some extent so that the tunneling barrier is not the entire MoS₂ thickness but only a buried layer. This is indeed the scenario discussed in ref. [149], which studies Josephson junctions between MoRe (an amorphous s-wave superconductor) and a variable number of MoS₂ layers, and in which the authors argue that the first layer in contact with the superconductor is hybridized and that the barrier only comes from a layer not in contact with the superconducting electrodes, in other words the middle layer(s) of MoS₂ if the MoS₂ thickness is above three monolayers (~2nm). Because in our samples MoS₂ was directly grown by PLD on YBCO/Au, offering both an excellent quality of the VdW material and an excellent interface quality as shown in ref. [60], we expect the proximity effect on MoS₂ to be much stronger than in ref. [149] (in which experiments were based on exfoliated MoS₂).

In summary, the discussed behavior indicates that the MoS₂ layer behaves as a tunneling barrier of moderate transparency between YBCO and MoSi, which accounts for the main features discussed transport measurements: low bias conductance decreases for $T < T_C^{MoSi}$, and zero-bias peak for $T > T_C^{YBCO}$. Thus, we are dealing with SIS' junctions where I is MoS₂ behaving as a weak-link of moderate transparency. As we will see in the next subsection, this leads to Josephson coupling at sufficiently low temperature and current.

7.3.3 Josephson regime

In this subsection, I will focus on the superconducting regime observed with some junctions at low enough temperatures and currents. The junctions studied in this subsection are still on the same sample with MoS₂ grown for 1 minute and are respectively a square of 7.5 μ m side (R1874D D10) and a square of 10 μ m side (R1874D E11). They have the same behavior as the junctions shown above but reveal a critical current at low temperatures.

7.3.3.1 Low current I-V curves

In Figure 135a, the characteristic of the junction R1874D E11 at 2K exhibits a critical current $I_c \sim 200\mu$ A while it is completely absent from the characteristic at 4.5K. This behavior is also clear on the differential conductance spectra at these two temperatures. Indeed, at 2K, it has a sharp peak with a two-order magnitude increase while at 4K, there is only a small peak very similar to what we observed for instance at 4.5K.

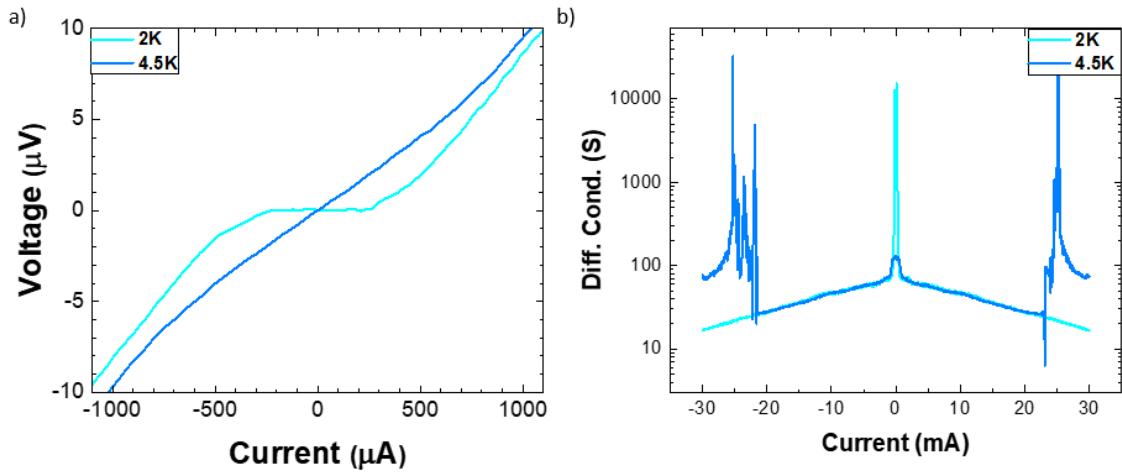


Figure 135 a) Voltage-current characteristic of the junction R1874D E11 at 2 and 4K. b) Corresponding differential conductance spectra.

7.3.3.2 Temperature evolution of the critical current

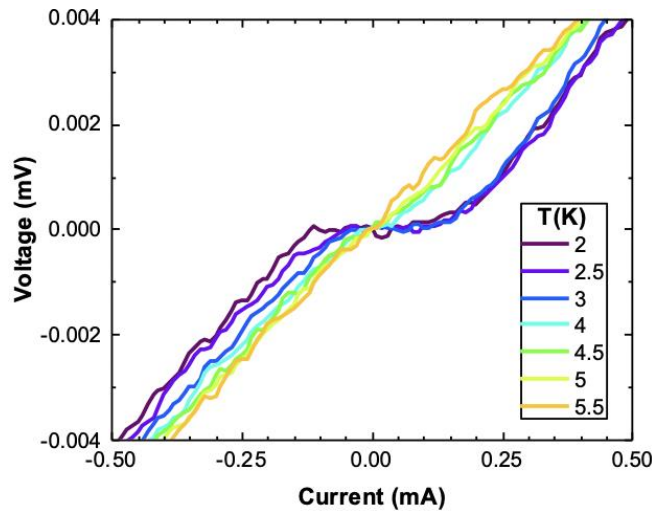


Figure 136 Current-Voltage characteristics of the junction R1874D D10 with a $10\mu\text{A}$ -step of the bias current for temperatures between 2 and 5.5K, below T_C^{MoSi} .

In Figure 136, I carried out measures of I-V curves of the junction R1874D D10 with a small step for the current ($10\mu\text{A}$) for different temperatures lower than T_C^{MoSi} . At very low currents ($< 200\mu\text{A}$), the I-V curve becomes flat for the lowest temperature plots ($T < 4\text{K}$). This behavior is reminiscent of an overdamped SIS Josephson junction. It is possible to estimate its critical current I_c for which the I-V curve remains flat. I measured it as the mean between the absolute value of the negative current at which the curve goes flat and the positive current at which it goes flat. The result as a function of the temperature is plotted in Figure 137. It allowed me to compute the $I_c R_N$ which is a figure of merit for Josephson junctions. At the lowest temperature I measured, it reaches $\sim 1\mu\text{V}$ with a critical current $I_c \sim 100\mu\text{A}$ and a normal state resistance $R_N \sim 10^{-2}\Omega$. This value has to be compared both to the value of the superconducting gap of MoSi, which has the smallest gap, and to the thermal energy. The superconducting gap of MoSi is $\frac{\Delta_{\text{MoSi}}}{e} \approx 1.14\text{meV}$ [257]. The large difference between the

$I_c R_N$ product and its expected value $\frac{\pi \Delta_{MOSi}}{2e}$ could be explained by a junction length d larger than the coherence length ξ_N . Indeed, in that case, $I_c \sim e^{-d/\xi_N}$ while the resistance only increases linearly with d . This would explain the low value of the $I_c R_N$ product. The comparison with the thermal energy, more precisely the energy of thermally activated phase-slip processes (a sudden change of the phase of 2π), is quantified through the ratio $\frac{\hbar I_c}{ek_B T}$ [17]. In our case, this ratio is around 2000, which means the impact of temperature on the IV curve is moderate. The plot of Figure 137 shows the extracted values of I_c as a function of the temperature. It decreases as the temperature increases and becomes 0 at 4K. With our experimental setup, it was not possible to measure the critical current below 2K.

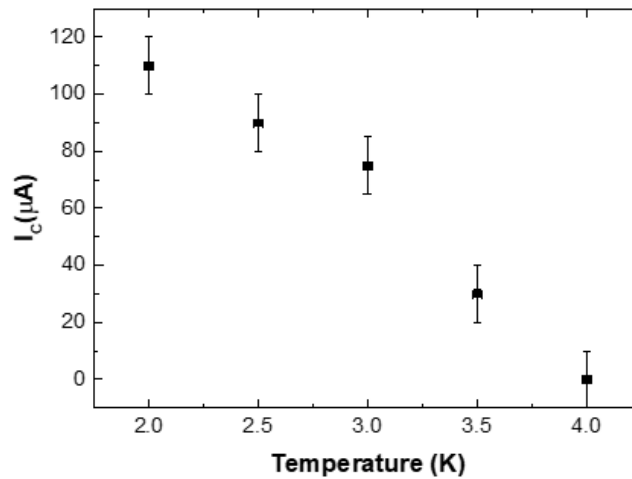


Figure 137 Critical current I_c as a function of the temperature. The uncertainty on this current is set as twice the step of the I-V curve.

7.3.3.3 Magnetic field dependence of the critical current

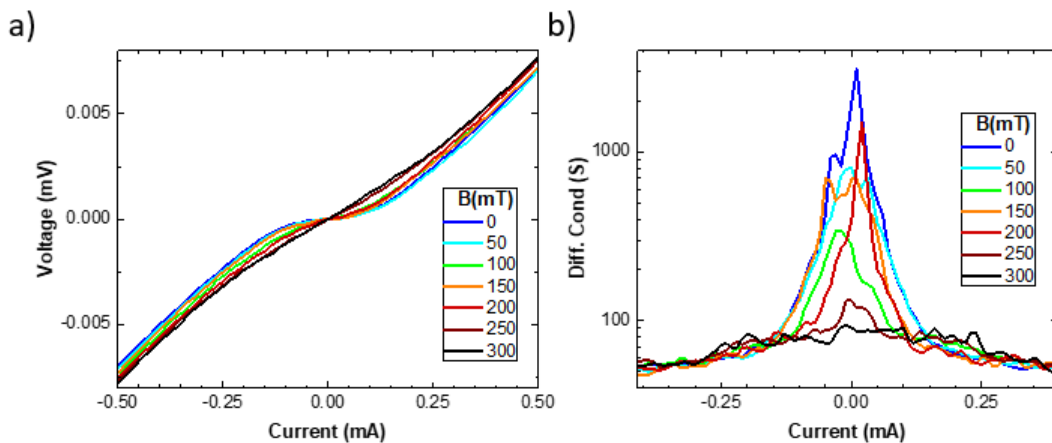


Figure 138 a) Current-Voltage characteristics at smaller currents for different magnetic fields of the junction R1874D D10. b) Corresponding differential conductance vs bias current plots (semi-log representation).

To better characterize the junction transport properties, I applied a magnetic field perpendicularly to the junction (in-plane of the layers as shown in Figure 141) and I

measured I-V curves for very small steps of the magnetic field. Some of these I-Vs and their corresponding differential conductances are plotted in Figure 138a and b. The I-V curves shown in Figure 138a exhibit a critical current I_c that depends on the value of the magnetic field. This is also visible on the differential conductance plots in Figure 138b since there is a large peak at small currents (semi-log scale). Here, it appears that both the flattening of the I-V curves and the peak in the differential conductance are strongly modulated by the magnetic field.

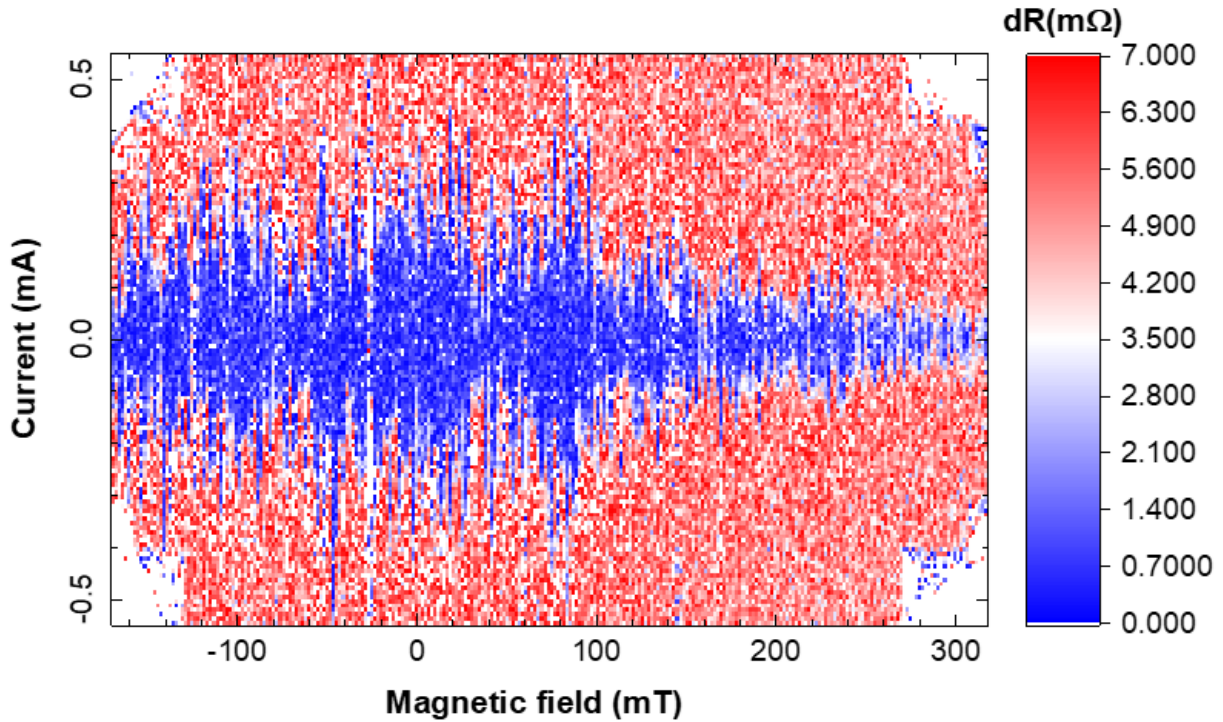


Figure 139 Colormap of the differential resistance dR as a function of the magnetic field (x-axis) and the bias current (y-axis).

To visualize the evolution of the I-V curves with the magnetic field I plot the differential resistance dR as a function of the magnetic field (x-axis) and the bias current (y-axis) as shown in Figure 139. This color plot makes visible the low differential resistance regions that is to say the regions where the I-V curves are flat. This measurement was carried out with a magnetic field step of 1mT and a current step of 10 μ A. We find again that the flat region tends to occur at smaller and smaller currents as the magnetic field is increased. Two very different kinds of oscillations are visible on this graph: very fast oscillations with a period of a few mT and much slower ones (\sim 40mT period) that modulate the faster ones. This is confirmed by the spectral analysis we performed. From the same batch of measurements presented in the colormap in Figure 139, we extracted the critical current I_c with a threshold for the differential resistance. On both sides, positive (+) and negative (-), I_c^\pm is defined as the maximum value for which the differential resistance is below the threshold. The plot shown in Figure 140 is the Fourier transform of $I_c = \frac{I_c^+ - I_c^-}{2}$. In addition to the peak at low-frequency accounting for the 40mT-periodic modulation, two peaks are visible at 210T $^{-1}$ (\sim 4.7mT), the most intense, and 470T $^{-1}$ (\sim 2.1mT) corresponding to the fast oscillations on the color map.

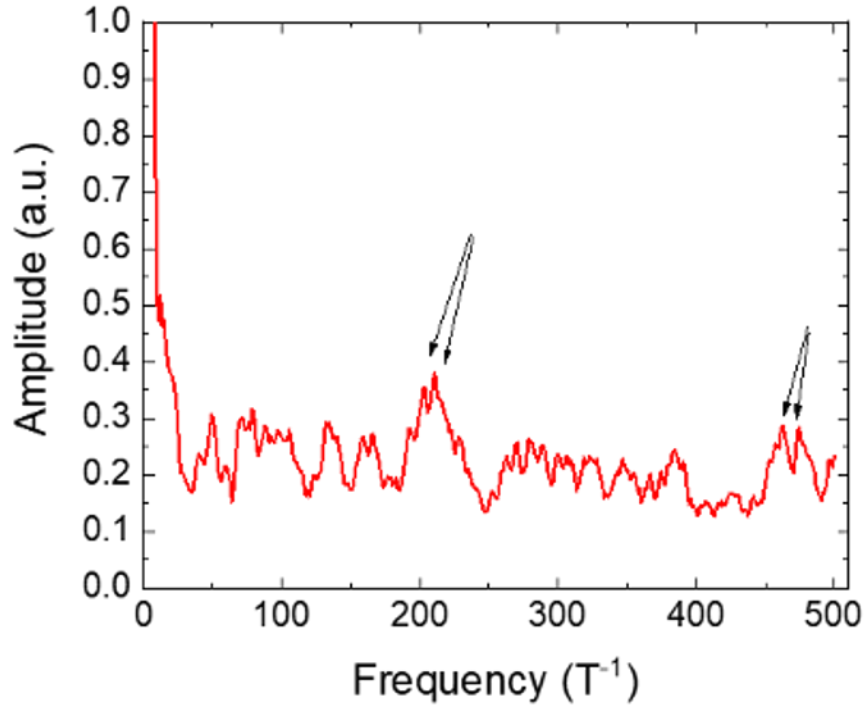


Figure 140 Fourier transform of the critical current I_c extracted from the colormap above.

7.3.3.4 Discussion

As the comparison between Figure 133a and c shows, the junction R1874D E11 which exhibits the Josephson regime at low temperatures has the same tunnel behavior in the dissipative regime as the junction R1874D C2. These junctions are therefore SIS Josephson junctions. The $I-V$ curves in Figure 135a and Figure 136 are also reminiscent of overdamped SIS Josephson junctions [17] with the onset of a critical current I_c at low temperature. In Figure 137, the plot of I_c as a function of the temperature is also compatible with the evolution of the critical current of a SIS junction [17]. Unfortunately, it was not possible to measure below 2K in our cryostat to fit it to the Ambegaokar-Baratoff formula [17].

As shown in Figure 138a and Figure 139, the application of a magnetic field perpendicularly to the junction modulates I_c . In chapter 6, we have seen this is also the case of the critical current of a Josephson junction that is modulated by the magnetic field depending on the spatial density of the current in the junction. This interplay results in an interference pattern in the critical current as the magnetic field varies. For a homogeneous density of current in a rectangular junction, the Fraunhofer pattern is a sinc function but it can be much more complicated as the density of current gets inhomogeneous in the junction. If the period of oscillations is B_0 , we deduce the surface S associated with a quantum of flux $\Phi_0 \approx 2 \times 10^{-15} \text{Wb}$:

$$S = \frac{\Phi_0}{B_0} \sim 1 \times 10^{-12} \text{m}^2 \quad 7.1$$

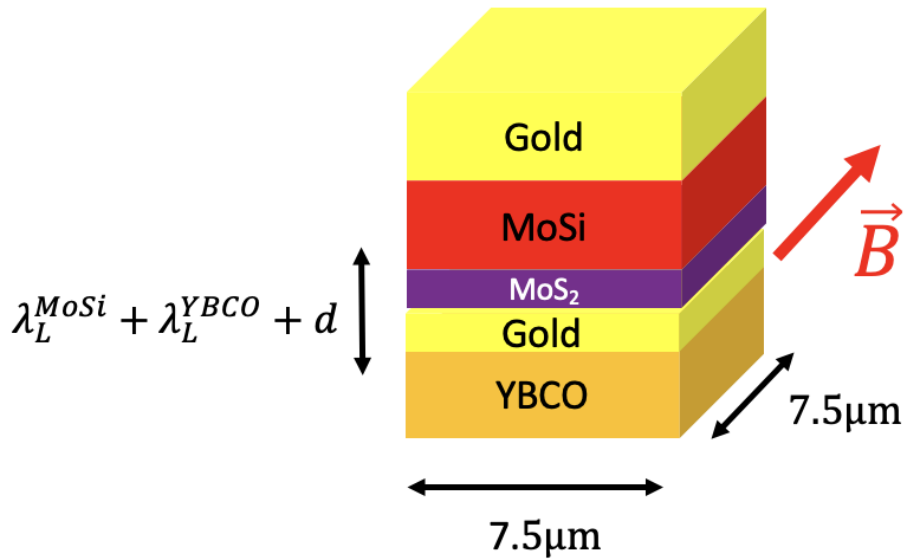


Figure 141 Scheme of the junction with the relevant lengths.

Considering the scheme in Figure 141 and making the assumption that the flow homogeneously over the whole junction width ($7.5\mu\text{m}$), as the fastest period observed $B_0 \sim 2\text{mT}$, the length associated would be equal to $\sim 130\text{nm}$. Using the second fastest period, $B_0 \sim 4.7\text{mT}$, and the same junction width, we obtain a length $\sim 53\text{nm}$. As shown on the scheme, these lengths result from the addition of the thickness of the weak link, d , and the London penetration length of YBCO and MoSi: $\lambda_L^{YBCO} \sim 150\text{nm}$ and $\lambda_L^{MoSi} \sim 500\text{nm}$ [258]. However, in our geometry, the important dimension of the superconductors is their thicknesses (50nm for YBCO and 100nm for MoSi) which are much smaller than the penetration lengths. Since we have to consider an integration path inside the superconductors (where $\vec{B} = \vec{0}$) to compute the magnetic field dependence of the critical current [17,236], $d + \lambda_L^{YBCO} + \lambda_L^{MoSi}$ is necessarily limited by the total thickness of the superconducting heterostructures, in other words $d + t_{YBCO} + t_{MoSi} \approx 165\text{nm}$ where t_{YBCO} (t_{MoSi}) corresponds respectively to the thickness of the YBCO (MoSi) film. Thus, the fastest oscillation period ($B_0 \sim 2\text{mT}$) is roughly consistent with the penetration of the magnetic flux over the whole thickness of the superconducting device and over the whole width. However, the second fastest (4.7mT) cannot be accounted for by a homogeneous current density over the whole junction's width and can only be explained if the current density is distributed over a reduced width.

Another observation of the evolution of the critical current with the magnetic field is that it does not follow a sinc function dependence as expected for a homogeneous current density in the junction. On the contrary, we can distinguish a larger period ($\sim 40\text{mT}$) modulation and the critical current remains non-zero over a large magnetic field range compared with the quick oscillations period. This can also be explained by an inhomogeneous distribution of the current density, for instance as observed for edge currents in planar devices, that creates a SQUID-like Fraunhofer pattern [136,259–261]. Suominen et al. [262] have also shown it could emerge from the Zeeman effect in semiconductor/superconductor Josephson junction. Finally, the thickness of the whole SIS junction being smaller than the sum of the penetration lengths, may influence the way the critical current is affected by the magnetic

field. For example, in Ref. [263], the authors used a single graphene as the barrier in a SIS junction made of a thin layer of titanium (the overall thickness being smaller than the penetration lengths) and observed a Fraunhofer pattern (figure 3 in the supplementary material), far from a sinc function. In our case, though we showed that both the oscillation periods and the Fraunhofer pattern cannot be explained by a homogeneous current density distribution, we cannot yet conclude on a specific distribution [235–237].

7.3.4 Overall discussion

The characterization of YBCO and MoS₂ reported in section 7.2.3 demonstrates that it is possible to obtain superconducting heterostructures with good structural and functional properties by PLD deposition of MoS₂ on YBCO protected by Au. The transport experiment of vertical YBCO/Au/MoS₂/MoSi junctions shows that these junctions behave as SIS junctions with moderate barrier strength. The thicker MoS₂ junctions do not exhibit Josephson coupling, but a finite critical current can be observed in junctions with thin MoS₂ (~5nm) at low temperatures. These junctions are usually the less resistive, the $I_c R_N$ product of our junctions being between 1μV and 4μV.

The transport experiments in the junctions reveal an excellent electrical contact between YBCO and MoS₂ since the resistances of the junctions are lower than previous studies between superconductors and exfoliated and then transferred MoS₂ [149,150]. In these two studies, they measured that the resistance normalized to the area of the junctions scales between 10 to 1000kΩ.μm² compared with our results between 1 and 100Ω.μm². The presence of pinholes in the MoS₂ layer is ruled out by various observations. First, AFM images of 10μm-side squares, the Raman spectroscopy map (shown in Figure 127) and TEM measurements from a previous study [89] show a great homogeneity of the layer. Second, the $R(T)$ measurements in Figure 133a as well as the differential conductance spectra in Figure 133b and Figure 134a demonstrate the SIS nature of the junctions. Therefore, the improved electrical contact between YBCO/Au and MoS₂ has to be attributed to the growth method by PLD which provides more transparent interfaces leading to a stronger proximity effect and also to doping of the MoS₂ as already reported [60,89]. This is discussed further below.

In subsection 7.3.2.4, the analysis of the differential conductance spectra in Figure 133a and Figure 134a suggested that the tunnel barrier may be located at the interface between MoS₂ and may become superconducting by proximity. In the study [149] with exfoliated MoS₂, the authors showed that there is a Josephson coupling between the electrodes only up to 3 layers of MoS₂ and then the behavior is strongly tunnel. They argued that the closest MoS₂ layers to the superconductor on both sides hybridize with it. With 3 layers, the one in the middle supposedly acts like a tunnel barrier. In our experiments, the thickness of MoS₂ is thicker (~5nm which corresponds to 8 layers). Nonetheless, we still measured Josephson coupling at low temperatures. This can be explained by a better electrical contact leading to an improved hybridization of the first layers of MoS₂ in contact with the YBCO/Au film. Second, as I mentioned in chapter 2, the phase diagram of MoS₂ [71] reveals that for high doping, it can become metallic and even superconducting with $T_c \sim 10K$. I recall this result

here with Figure 142. **The good coupling with the YBCO/Au film may dope MoS₂ at the point it becomes metallic and this metallicity as well as the intrinsic superconductor order at large doping may make it easier for MoS₂ to become superconducting by proximity.**

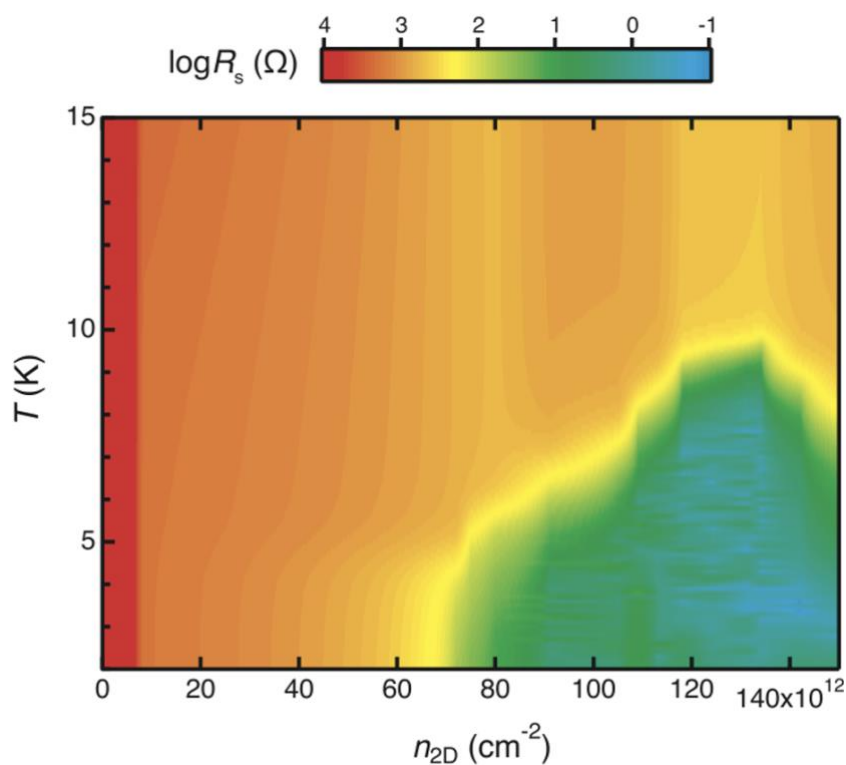


Figure 142 logarithm of the sheet resistance of MoS₂ as a function of the electron density (*x*-axis) and temperature (*y*-axis). Figure taken from Ye et al., Science **338**, 1193 (2012).

7.4 CONCLUSIVE REMARKS

In this chapter, after showing measurements with transferred CVD-grown MoS₂ in section 7.1, I presented a new method to grow large-scale 2D MoS₂ on YBCO, a high-T_c superconductor while largely preserving its superconducting properties (section 7.2). This original growth method passed the test of characterization, both of YBCO and MoS₂. I therefore decided to test the integrability of this method in a complete fabrication process of superconducting vertical junctions for transport measurements. These measurements are presented in section 7.3. The vertical YBCO/Au/MoS₂/MoSi heterostructures exhibited an SIS junction behavior we attribute to the excellent coupling between the YBCO/Au layer and MoS₂ on one side and of MoS₂ and MoSi on the other. For the sample with the thinnest MoS₂ layer (~5nm), various junctions experienced Josephson coupling with a critical current around 100μA. Some other promising directions will be given in the concluding chapter.

8 CONCLUSION

In this manuscript, I studied several systems aiming at better understanding the superconducting proximity effect between a *d-wave* superconductor and 2D materials, using transport measurements at low temperatures. I fabricated and measured devices made of YBCO, a *d-wave* superconductor combined with a thin film of gold, and Van der Waals (VdW) materials such as graphene or MoS₂. In the first section, I will recap the main results I obtained during my PhD. I will then give some perspectives on this work.

8.1 SUMMARY OF THE MAIN RESULTS

The common ground of all the studies carried out in this thesis is the coupling between a *d-wave* superconductor and another non-superconducting material. In parallel with my experimental work, I carried out numerical calculations based on the Blonder-Tinkham-Klapwijk (BTK) theory [5] very early during my PhD. This is presented in the first section. It then made it easy for me to use it for my own experimental studies involving thin metallic films (8.1.2), graphene (8.1.3), and MoS₂ (8.1.4).

8.1.1 Numerical studies within the BTK framework

The BTK theory is a useful tool to understand superconductor/normal material interfaces since it allows to compute their differential conductance with, in its simplest form, one parameter that accounts for the transparency of the interface. I used this formalism, with some modifications I implemented, on several occasions to explain experimental data from my group or collaborators.

1) The first systems I studied were vertical junctions made of YBCO and MoSi, an amorphous metal, with tunable tunneling barriers [6]. I used the BTK formalism to compute the differential conductance of an interface between a normal metal and a *d-wave* superconductor along its *c*-axis. After extracting the main parameters from fits with the BTK theory as shown in Figure 143a and b, I could simulate the temperature behavior of the system and explain the observed enhancement of the electroresistance below T_c^{YBCO} . The simulated conductances at 0 and 100mV for both the ON and OFF states are presented in Figure 143c as well as the temperature evolution of the electroresistance in the inset. The electroresistance enhancement experimentally observed can be explained by the tunneling of quasiparticles inside the superconducting gap of YBCO.

2) The following study [7] focused on transport measurements of vertical junctions made of a stack of La₅SrCu₆O₁₅ (LSCO) (top electrode), BaTiO₃ (BTO) (barrier), and La_{0.7}Sr_{0.3}MnO₃ (LSMO) (bottom electrode). The application of voltage pulses showed two distinct behavior of the differential conductance depending on the polarity. The BTK fits I performed at several temperatures in these two states allowed us to characterize their behavior as a potential emergence of a superconducting phase in LSCO and to quantify how it is affected by its electrostatic environment.

3) Finally, in the context of ferromagnet magnetoresistance (FMR) measurements with permalloy (a ferromagnet) in contact with YBCO, I could use the BTK theory to compute the interfacial properties between these two materials [8]. It allowed us to explain FMR experiments by computing the densities of quasiparticle states in YBCO for two crystallographic orientations and how it can affect the spin injection at the interface.

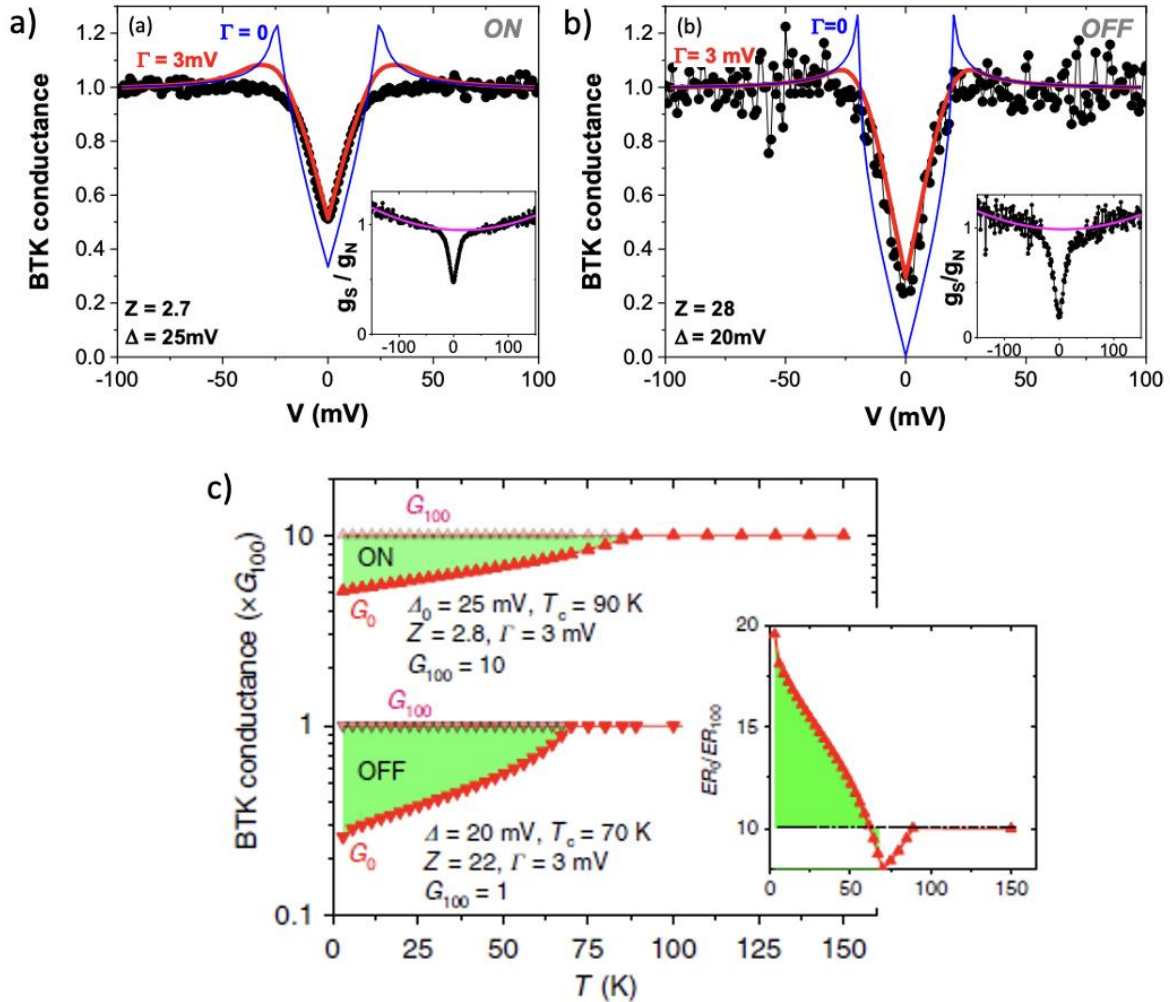


Figure 143 Numerical fits in the a) ON and b) OFF states of the junction. c) Evolution of the conductance at 0mV (G_0) and 100mV (G_{100}) for both ON and OFF states. In the inset is shown the temperature evolution of the electroresistance (ER) ratio between 0 and 100mV.

These various projects allowed me to gain an understanding of the physics at the interface between YBCO and other materials and develop BTK numerical calculation routines I will use in the following for my own studies.

8.1.2 Proximity effect between d -wave superconductor/metal thin films

In my PhD, the study of YBCO/metal junctions is a first step to characterize the propagation of d -wave superconducting correlations in a case that was, in principle, simpler than the case of graphene and MoS₂. Moreover, since a thin layer of metal has to be intercalated between graphene (or MoS₂) and YBCO to protect the YBCO surface and improve the interface transparency, it was important to first characterize the proximity effect in Au.

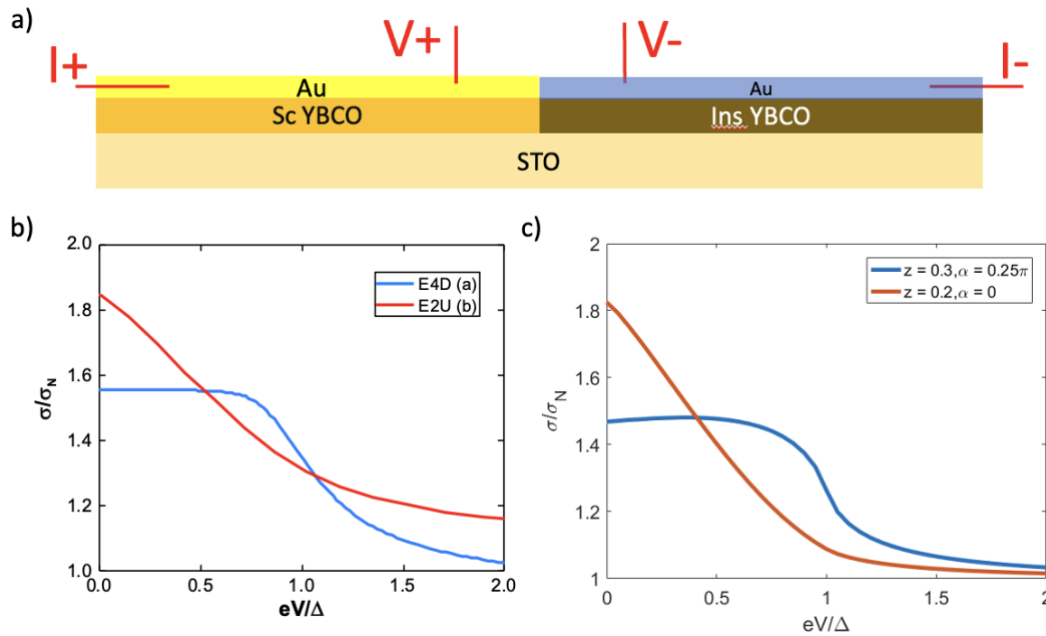


Figure 144 a) Microscope image and electrical configuration of a SN junction. b) Zoom on the SN junction. c) Side-view scheme of the SN junction with the points where the electrical measures are taken. d) Experimental differential conductance as a function of the normalized voltage for two SN junctions. e) Numerical calculations within the Usadel formalism.

In the first part, I studied SN junctions formed by a continuous thin layer of gold lying on one side (S) above the d -wave superconductor YBCO and on the other side (N) on insulating YBCO. To explain the experimental differential conductance spectra, I developed a phenomenological model based on the BTK formalism with two distinct interfaces, one s - and the over d -wave, and a metallic resistance in series. With the help of theoreticians, we developed a microscopic model, based on the Usadel formalism, which allows us to fit my measurements and reproduce the temperature dependence of the differential conductance.

I also measured SNS junctions and could analyze the measurements with the knowledge acquired from the SN junctions. Indeed, I have shown that because of the lower coherence length in gold than in graphene, the two sides of the SNS junction can be considered as independent SN junctions.

In the near future, a study of SNS junctions with a smaller length L between the electrodes may allow to observe a Josephson coupling and a critical current. Another possibility is to change the metal of the thin layer to play on the quality of the contact or the transport properties. Finally, it would be very interesting to carry out low-temperature STM measurements as in Ref. [10] on the gold both above superconducting and insulating YBCO to see the evolution of the "mini-gap" in gold. It would also be possible to pattern tunnel contacts as in Ref. [11] but the geometry would be more constrained.

Before diving into the d -wave proximity effect in 2D materials (graphene and MoS_2), I would like to stress that chapter 5 explored a very different regime than chapter 6 and 7. In the case of gold, the contact between YBCO and the layer is excellent because the growth is made *in situ*. However, compared with graphene or MoS_2 , the phase-coherence length of

gold is much lower, and coherence-related effects (such as the quantum interference I observed in graphene) are absent.

8.1.3 Proximity effect in graphene.

As we have seen in the introduction of this thesis (in chapter 2), graphene has been studied extensively with *s-wave* superconductors in the literature. However, studies with *d-wave* superconductors are scarce at the notable exception of a publication realized by my predecessor showing the first hints of the proximity effect between graphene and a *d-wave* superconductor [12]. This experimental work was completed with theoretical calculations adapted from [13], which describe well the system and the experimental measurements. Later, we demonstrated the propagation of *d-wave* Andreev pairs in CVD-grown graphene over several hundreds of nanometers [14]. It means the phase between the electron and hole from an Andreev process remains constant over the length of the junction which scales from 50 to 800nm.

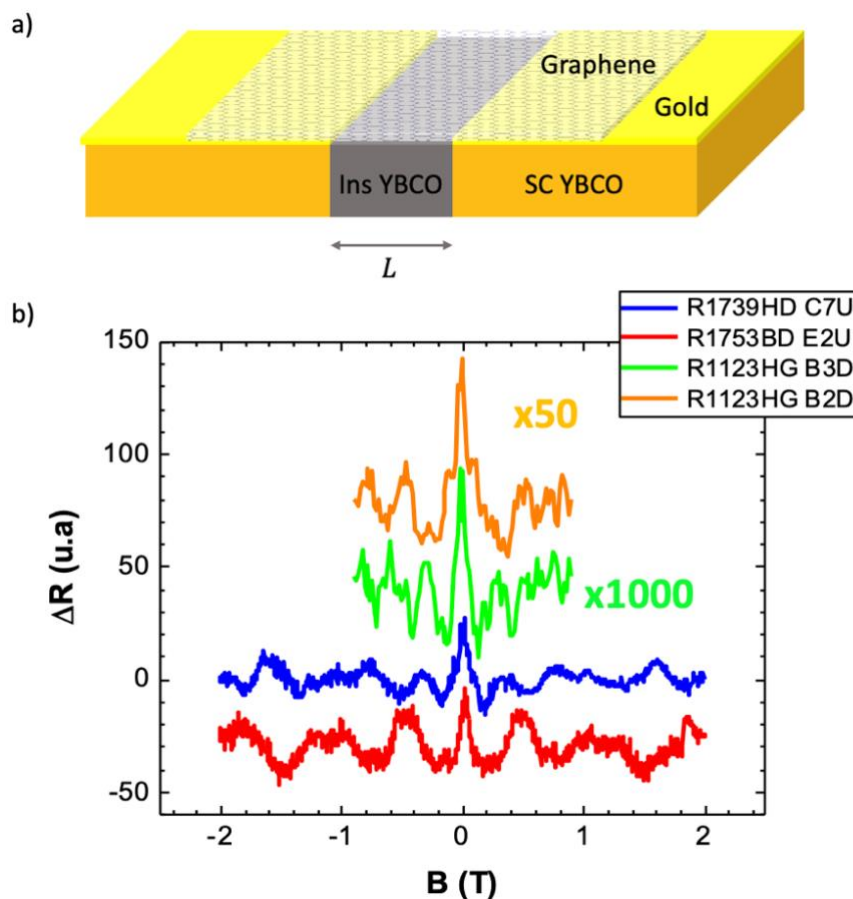


Figure 145 a) Side-view scheme of a superconducting YBCO/graphene/YBCO junctions. b) Magnetoresistance oscillations of four junctions measured on four different samples.

I subsequently studied the effect of the magnetic field on the differential conductance of YBCO/Graphene/YBCO junctions schematically represented in Figure 145a. In chapter 6, I provided an analysis of the oscillations observed in the magnetoresistance of the junctions of intermediate transparency shown in Figure 145b. The presence of a magnetoresistance peak related to weak localization around $B = 0$, and the comparison with the literature of

magnetoresistance oscillations in proximized 2D systems, led us to conclude that the observed magnetoresistance oscillations are related to the Al'tshuler-Aronov-Spivak (AAS) effect is which one of the characteristic length scales is the temperature-dependent phase-coherence length in graphene.

8.1.4 Proximity effect in MoS₂

After the study of YBCO/Graphene/YBCO junctions, we investigated the proximity effect in another 2D material, MoS₂. It was a natural candidate since this material can also be grown by chemical vapor deposition (CVD) and most of the fabrication techniques can be applied to this material. In the first stage, I attempted to fabricate devices analogous to the YBCO/Graphene/YBCO ones via wet transfer CVD MoS₂. However, the transport measurements exhibited a very resistive behavior, dictated by the contact resistance between MoS₂ and YBCO. To tackle this issue, I decided to try different approaches like the exfoliation of a parent compound (WS₂, see 8.2.1) and the development of a new growth method of MoS₂ directly on YBCO based on pulse laser deposition (PLD) (scheme in Figure 146a). As explained in chapter 7, this task is challenging because YBCO is a fragile oxide. I had to optimize the growth parameters in order to preserve YBCO's superconducting properties while growing high-quality MoS₂.

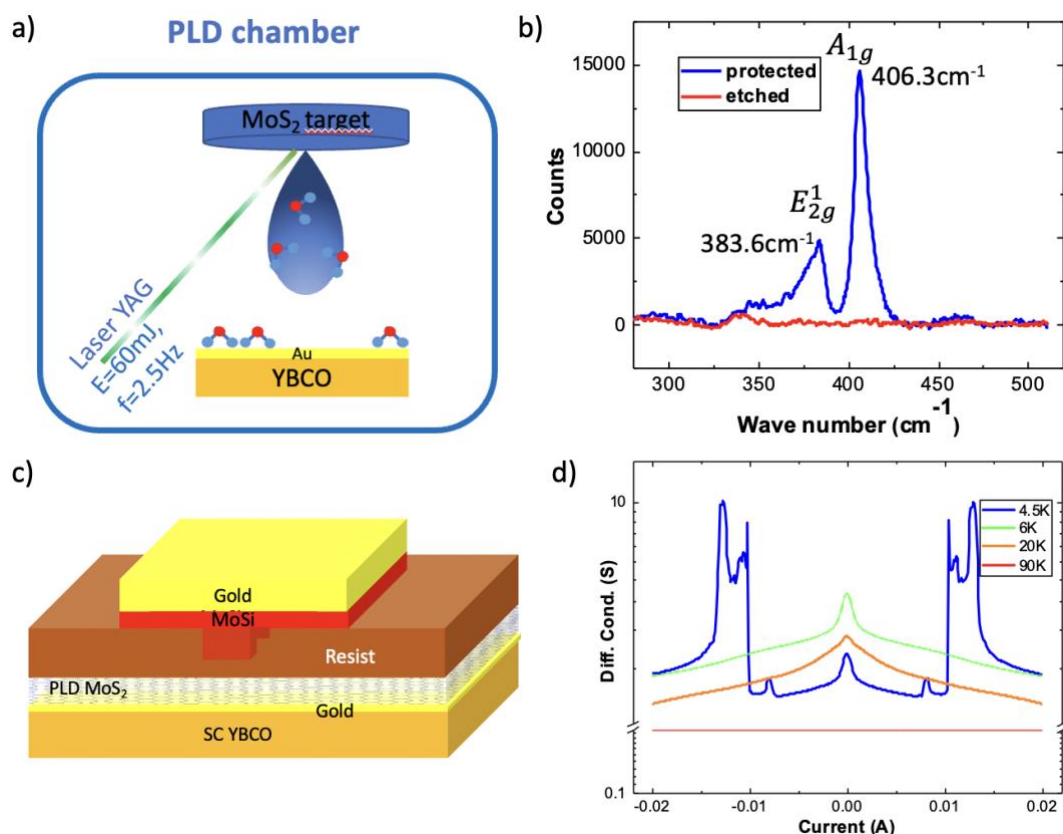


Figure 146 a) Scheme of a PLD setup to grow MoS₂ directly on YBCO/Au films. b) Raman spectra of MoS₂ grown by PLD (blue) and only the substrate (red). c) Scheme of a superconducting vertical junction with YBCO/Au (bottom electrode), MoS₂ (barrier), and MoSi (top electrode).

In chapter 7, I characterized both YBCO after the growth process and MoS₂ with for example Raman spectroscopy as shown in Figure 146b. This method allowed me to fabricate superconducting devices represented in Figure 146c, made of YBCO as the bottom electrode, MoSi (an amorphous *s-wave* superconductor) as the top electrode, while MoS₂ serves the role of a barrier in between. Electronic transport measurements exhibited a SIS behavior, whatever the thickness of the MoS₂ layer (differential conductance spectra shown in Figure 146d). For the sample with the thinnest MoS₂ layer (~5nm), some junctions experienced Josephson coupling with a critical current around 100μA.

In the near future, the goal is to fabricate planar devices made with PLD-grown MoS₂ on YBCO and to compare them to junctions made with transferred MoS₂. We are currently working on the transfer method going from a wet transfer in an alkali solution to a dry transfer process. Preliminary results obtained by Malik Ayachi show that the transfer is made easier but the contact resistance is still very large and does not allow for proximity effect yet.

8.2 BROAD PERSPECTIVES

During my PhD, there are many possibilities that I started to explore and that will be interesting to further exploit in the future. Some of these developments are detailed below.

8.2.1 Transferring Van der Waals materials

During my PhD, I had the opportunity to develop another method for transferring exfoliable Van der Waals materials and building complex 2D heterostructures. Though exfoliation only allows for flakes of a typical size of few 10μm, it is the most commonly used technique to study VdW heterostructures in the literature and allows great versatility in the choice of the used materials. It was historically the first approach to study a Van der Waals material before the development of large-scale growth methods (CVD, PLD,...) whose quality can now compete with the one encountered in crystals. The use of a transfer station, recently installed in our laboratory, strongly enlarges the spectrum of available materials we can couple with YBCO. However, for each material, some fine-tuning should be performed (polymers to be used, temperatures, peeling speed,...) to successfully transfer the structures.

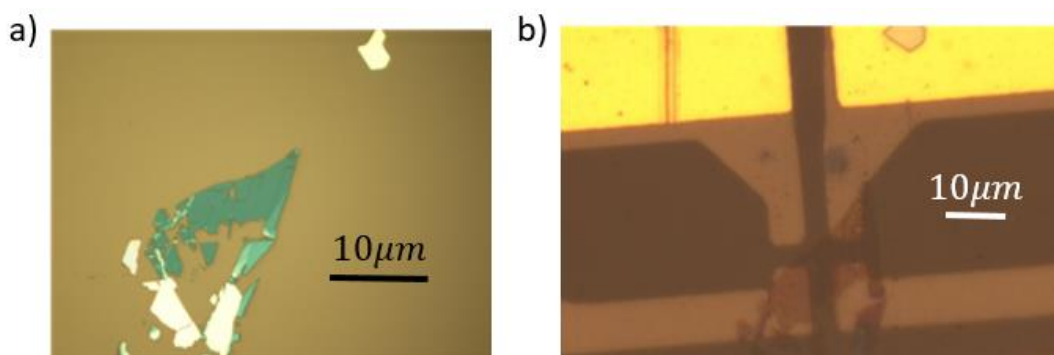


Figure 147 Microscope image of: a) a flake of tungsten disulfide (WS₂) on silicon oxide, b) the same flake after transfer onto a patterned YBCO device.

An example of VdW material transferred using the transfer station is shown in Figure 147. A

flake of WS_2 has been exfoliated and deposited on silicon oxide (SiO) (Figure 147a) as explained in chapter 4. In Figure 147b, the same flake is shown on a patterned YBCO device after picking it up from the SiO and carefully positioning it on the pre-existing superconducting electrode. In the future, this technique will need to be combined with some developments to improve the quality of the YBCO/VdW interface as the samples we realized using this technique had, so far, contact resistance too high to properly measure the devices.

8.2.2 Direct growth of VdW materials with specific properties onto YBCO

For a few years now, it has been possible to grow VdW materials by PLD. In our laboratory, the first achievements have been made with MoS_2 , WS_2 , and WSe_2 [89,264] while the growth of other materials, like black phosphorus or Fe_3GeTe_2 , is being developed. This large spectrum of materials offers multiple opportunities to study superconducting junctions with a ferromagnet or a topological insulator as a weak link. One of the qualities of this method compared with transfer methods is the improvement of the electrical contact and possibly an improved proximity effect.

A notable example of a material with great potential for our devices is NbSe_2 . This material is a transition metal dichalcogenide that has a superconducting transition at 7.2K. This material is used a lot under the form of flake (after exfoliation) to create superconducting junctions with other Van der Waals materials [134,265,115,116]. It would be then very interesting to grow this material by PLD for *in situ* processes of large-scale superconducting heterostructures. Indeed, this material being superconductor below 7.2K, electrons have an intrinsic attractive interaction that could facilitate proximity effect with YBCO even above this temperature compared with materials like graphene or MoS_2 and be an excellent weak link.

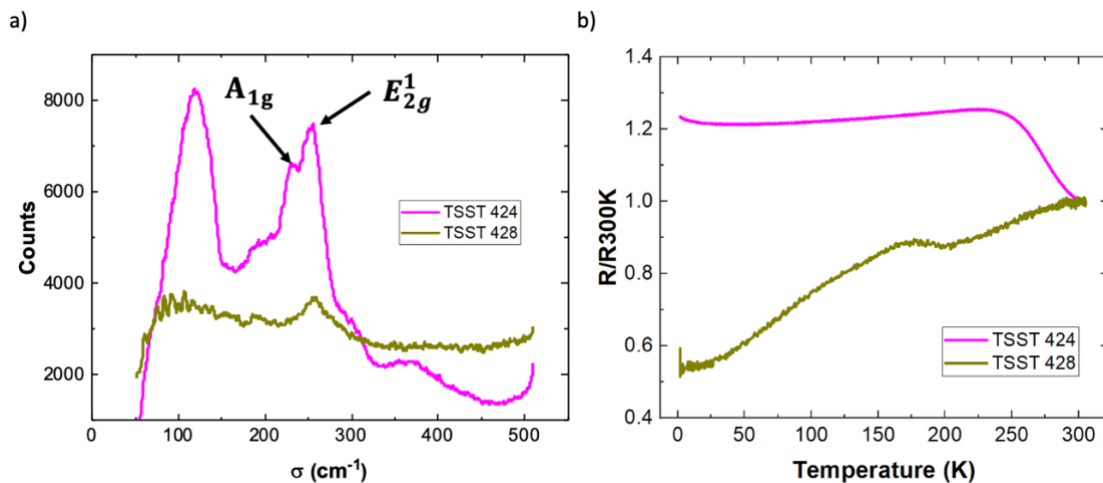


Figure 148 a) Raman spectra of two attempted growth of NbSe_2 . b) Their respective normalized resistance (at 300K) versus temperature.

In Figure 148a, I compare the Raman spectra of two attempts: TSST 424 (in magenta) and TSST 428 (in dark yellow) (the difference being the pressure in argon in the chamber, 0.1mbar for 424 and $< 10^{-5}$ mbar for 428). The spectrum of TSST 424 shows the two characteristic peaks of NbSe_2 [266], A_{1g} at 231cm^{-1} and E_{2g}^1 at 256cm^{-1} here, which gives hope for the

presence of NbSe₂. On the contrary, the sample TSST 428 only has the E_{2g}^1 peak, which means, TSST 428 is certainly not NbSe₂. One other important check we did was to measure the resistance of the films as a function of the temperature. These measurements are reported in Figure 148b for both samples. We can see that the sample TSST, though it shows the characteristic peak of NbSe₂ on the Raman spectrum, does not become superconducting at low temperatures and its resistance even slightly increases at low temperatures. While there is certainly no well-grown NbSe₂ in TSST 428, its behavior is metallic. We may have grown another material than NbSe₂.

8.3 CONCLUSIVE REMARKS

In conclusion, there are many opportunities opened by the work presented in this thesis. The study of the proximity effect between YBCO and thin metallic films offers a model system that allowed us to study a nearly ideal S/N interface in which "S" is proximitized Au and "N" is non-proximitized Au. The study of the conductance across this interface allowed to unveil the transformation from *d-wave* to *s-wave* correlation resulting from symmetry breaking and diffusive transport in Au. At variance, the study of YBCO/graphene/YBCO junctions in a magnetic field revealed a mix of Andreev and normal reflections combined with the transport in the graphene channel. This systematic study may be extended to other 2D materials. Finally, the development of a method for growing MoS₂ directly on YBCO, yielding transparent interface contacts, allowed us to obtain Josephson junctions in which MoS₂ plays the role of the weak link. This opens multiple possibilities in terms of geometry (vertical and planar devices) and material (plenty of available VdW materials with various intrinsic properties) for further studies. Despite being very interesting, I lacked time to explore all these possibilities in the timeframe of my PhD.

I hope that the work presented in this manuscript and summarized here allows the reader to access some answers to the complex physics of the proximity effect between YBCO and materials such as metals and VdW materials. I also hope it allowed for opening new possibilities in the field for future studies to further understand the longstanding problem of proximity-inducing *d-wave* superconductivity in materials. Answering these questions is an important question for the future applications of these really promising devices.

9 BIBLIOGRAPHY

- [1] H. K. Onnes, *The Superconductivity of Mercury*, Comm Phys Lab Univ (1911).
- [2] F. London, H. London, and F. A. Lindemann, *The Electromagnetic Equations of the Supraconductor*, Proc. R. Soc. Lond. Ser. - Math. Phys. Sci. **149**, 71 (1997).
- [3] V. L. Ginzburg, *On the Theory of Superconductivity*, Il Nuovo Cimento 1955-1965 **2**, 1234 (1955).
- [4] J. Bardeen, L. N. Cooper, and J. R. Schrieffer, *Theory of Superconductivity*, Phys. Rev. **108**, 1175 (1957).
- [5] G. E. Blonder, M. Tinkham, and T. M. Klapwijk, *Transition from Metallic to Tunneling Regimes in Superconducting Microconstrictions: Excess Current, Charge Imbalance, and Supercurrent Conversion*, Phys. Rev. B **25**, 4515 (1982).
- [6] V. Rouco, Seurre et al., *Quasiparticle Tunnel Electroresistance in Superconducting Junctions*, Nat. Commun. **11**, (n.d.).
- [7] F. Gallego, Seurre et al., *Ferroionic Generation of Superconductivity in a Non-Superconducting Cuprate*, **2021**, L55.005 (2021).
- [8] S. J. Carreira, Seurre, D. Sanchez-Manzano, M.-W. Yoo, K. Seurre, V. Rouco, A. Sander, J. Santamaría, A. Anane, and J. E. Villegas, *Spin Pumping in s -Wave Superconductor-Ferromagnet Hybrids*, Phys. Rev. B **104**, 144428 (2021).
- [9] P. G. DE GENNES, *Boundary Effects in Superconductors*, Rev. Mod. Phys. **36**, 225 (1964).
- [10] I. I. Gundareva, J. Martinez-Castro, F. S. Tautz, D. Grützmacher, T. Schäpers, and M. Lyatti, *Induced Superconductivity in Hybrid Au/YBa₂Cu₃O_{7-x} Electrodes on Vicinal Substrates*, arXiv:2309.14133.
- [11] S. Guéron, H. Pothier, N. O. Birge, D. Esteve, and M. H. Devoret, *Superconducting Proximity Effect Probed on a Mesoscopic Length Scale*, Phys. Rev. Lett. **77**, 3025 (1996).
- [12] D. Perconte et al., *Tunable Klein-like Tunnelling of High-Temperature Superconducting Pairs into Graphene*, Nat. Phys. **14**, 25 (2018).
- [13] J. Linder and A. Sudbo, *Tunneling Conductance in s - and d -Wave Superconductor-Graphene Junctions: Extended Blonder-Tinkham-Klapwijk Formalism*, Phys. Rev. B **77**, (2008).
- [14] D. Perconte, Seurre et al., *Long-Range Propagation and Interference of d -Wave Superconducting Pairs in Graphene*, Phys. Rev. Lett. **125**, (2020).
- [15] L. Majidi, H. Rostami, and R. Asgari, *Andreev Reflection in Monolayer MoS₂*, Phys. Rev. B **89**, 045413 (2014).
- [16] W. Meissner and R. Ochsenfeld, *Ein neuer Effekt bei Eintritt der Supraleitfähigkeit*, Naturwissenschaften **21**, 787 (1933).
- [17] M. Tinkham, *Introduction to Superconductivity*, Second (Dover, 1996).

- [18] A. A. Abrikosov, *The Magnetic Properties of Superconducting Alloys*, J. Phys. Chem. Solids **2**, 199 (1957).
- [19] L. N. Cooper, *Bound Electron Pairs in a Degenerate Fermi Gas*, Phys. Rev. **104**, 1189 (1956).
- [20] C. R. Leavens and J. P. Carbotte, *An Important Parameter in High-Temperature Superconductivity*, J. Low Temp. Phys. **14**, 195 (1974).
- [21] C. C. Tsuei and J. R. Kirtley, *Pairing Symmetry in Cuprate Superconductors*, Rev. Mod. Phys. **72**, 969 (2000).
- [22] C. Kallin, *Chiral P-Wave Order in Sr₂RuO₄*, Rep. Prog. Phys. **75**, 042501 (2012).
- [23] Y. Tsutsumi, K. Machida, T. Ohmi, and M. Ozaki, *A Spin Triplet Superconductor UPt₃*, J. Phys. Soc. Jpn. **81**, 074717 (2012).
- [24] E. Stilp et al., *Controlling the Near-Surface Superfluid Density in Underdoped YBa₂Cu₃O_{6+x} by Photo-Illumination*, Sci. Rep. **4**, 1 (2014).
- [25] R. Liang, D. A. Bonn, and W. N. Hardy, *Evaluation of $\{\mathrm{CuO}\}_2$ Plane Hole Doping in $\{\mathrm{YBa}\}_2\{\mathrm{Cu}\}_3\{\mathrm{O}\}_{6+x}$ Single Crystals*, Phys. Rev. B **73**, 180505 (2006).
- [26] C. Strunk, V. Bruyndoncx, C. V. Haesendonck, V. V. Moshchalkov, Y. Bruynseraede, and R. Jonckheere, *Nonlocality and Magnetic Flux Sensitivity of Superconducting Mesoscopic Aluminium Loops*, J. Phys. IV **06**, C3 (1996).
- [27] K. Krishana, J. M. Harris, and N. P. Ong, *Quasi-Particle Mean-Free-Path and Thermal Hall Conductivity in YBa₂Cu₃O₇*, J. Phys. Chem. Solids **56**, 1895 (1995).
- [28] C. Proust and L. Taillefer, *The Remarkable Underlying Ground States of Cuprate Superconductors*, Annu. Rev. Condens. Matter Phys. **10**, 409 (2019).
- [29] H. Thomas, A. Marian, A. Chervyakov, S. Stückrad, D. Salmieri, and C. Rubbia, *Superconducting Transmission Lines – Sustainable Electric Energy Transfer with Higher Public Acceptance?*, Renew. Sustain. Energy Rev. **55**, 59 (2016).
- [30] P. Fabbriatore, C. Priano, A. Sciutti, G. Gemme, R. Musenich, R. Parodi, F. Gömöry, and J. R. Thompson, *Flux Pinning in Bi-2212/Ag-Based Wires and Coils*, Phys. Rev. B **54**, 12543 (1996).
- [31] B. D. Josephson, *Possible New Effects in Superconducting Tunnelling*, Phys. Lett. **1**, 251 (1962).
- [32] P. W. Anderson and J. M. Rowell, *Probable Observation of the Josephson Superconducting Tunneling Effect*, Phys. Rev. Lett. **10**, 230 (1963).
- [33] D. E. McCumber, *Effect of Ac Impedance on Dc Voltage-Current Characteristics of Superconductor Weak-Link Junctions*, J. Appl. Phys. **39**, 3113 (2003).
- [34] Walther–Meissner–Institut, *Josephson Effects in Superconductors*, (2021).
- [35] J. Clarke and F. K. Wilhelm, *Superconducting Quantum Bits*, Nature **453**, (2008).
- [36] K. Sternickel and A. I. Braginski, *Biomagnetism Using SQUIDS: Status and Perspectives*,

Supercond. Sci. Technol. **19**, S160 (2006).

- [37] E. R. Pawlowski, Réseaux de SQUIDs à haute température critique pour applications dans le domaine des récepteurs hyperfréquences, phdthesis, Université Paris Saclay (COMUE), 2019.
- [38] Z. Xiong, L. Zhong, H. Wang, and X. Li, *Structural Defects, Mechanical Behaviors, and Properties of Two-Dimensional Materials*, Materials **14**, 5 (2021).
- [39] K. S. Novoselov, A. K. Geim, S. V. Morozov, D. Jiang, Y. Zhang, S. V. Dubonos, I. V. Grigorieva, and A. A. Firsov, *Electric Field Effect in Atomically Thin Carbon Films*, Science **306**, (2004).
- [40] P. R. Wallace, *The Band Theory of Graphite*, Phys. Rev. **71**, 622 (1947).
- [41] P. Avouris, T. F. Heinz, and T. Low, *2D Materials Properties and Devices* (Cambridge University Press, 2017).
- [42] A. V. Shytov, M. S. Rudner, and L. S. Levitov, *Klein Backscattering and Fabry-Pérot Interference in Graphene Heterojunctions*, Phys. Rev. Lett. **101**, (2008).
- [43] N. Stander, B. Huard, and D. Goldhaber-Gordon, *Evidence for Klein Tunneling in Graphene P-n Junctions*, Phys. Rev. Lett. **102**, (2009).
- [44] A. F. Young and P. Kim, *Quantum Interference and Klein Tunnelling in Graphene Heterojunctions*, Nat. Phys. (2009).
- [45] J.-H. Chen, C. Jang, S. Xiao, M. Ishigami, and M. S. Fuhrer, *Intrinsic and Extrinsic Performance Limits of Graphene Devices on SiO₂*, Nat. Nanotechnol. **3**, 206 (2008).
- [46] T. Knobloch et al., *The Performance Limits of Hexagonal Boron Nitride as an Insulator for Scaled CMOS Devices Based on Two-Dimensional Materials*, Nat. Electron. **4**, 2 (2021).
- [47] J. Wang, F. Ma, W. Liang, and M. Sun, *Electrical Properties and Applications of Graphene, Hexagonal Boron Nitride (h-BN), and Graphene/h-BN Heterostructures*, Mater. Today Phys. **2**, 6 (2017).
- [48] M. Yankowitz, Q. Ma, P. Jarillo-Herrero, and B. J. LeRoy, *Van Der Waals Heterostructures Combining Graphene and Hexagonal Boron Nitride*, Nat. Rev. Phys. **1**, 2 (2019).
- [49] K. I. Bolotin, K. J. Sikes, Z. Jiang, M. Klima, G. Fudenberg, J. Hone, P. Kim, and H. L. Stormer, *Ultrahigh Electron Mobility in Suspended Graphene*, Solid State Commun. **146**, 351 (2008).
- [50] K. S. Novoselov, Z. Jiang, Y. Zhang, S. V. Morozov, H. L. Stormer, U. Zeitler, J. C. Maan, G. S. Boebinger, P. Kim, and A. K. Geim, *Room-Temperature Quantum Hall Effect in Graphene*, Science **315**, 1379 (2007).
- [51] K. I. Bolotin, F. Ghahari, M. D. Shulman, H. L. Stormer, and P. Kim, *Observation of the Fractional Quantum Hall Effect in Graphene*, Nature **462**, 7270 (2009).
- [52] L. Liao, Y.-C. Lin, M. Bao, R. Cheng, J. Bai, Y. Liu, Y. Qu, K. L. Wang, Y. Huang, and X. Duan, *High-Speed Graphene Transistors with a Self-Aligned Nanowire Gate*, Nature **467**, 7313 (2010).
- [53] M. Y. Han, B. Özyilmaz, Y. Zhang, and P. Kim, *Energy Band-Gap Engineering of Graphene*

Nanoribbons, Phys. Rev. Lett. **98**, 206805 (2007).

[54] F. Xia, D. B. Farmer, Y. Lin, and P. Avouris, *Graphene Field-Effect Transistors with High On/Off Current Ratio and Large Transport Band Gap at Room Temperature*, Nano Lett. **10**, 715 (2010).

[55] F. Xia, T. Mueller, Y. Lin, A. Valdes-Garcia, and P. Avouris, *Ultrafast Graphene Photodetector*, Nat. Nanotechnol. **4**, 12 (2009).

[56] P. Seneor, B. Dlubak, M.-B. Martin, A. Anane, H. Jaffres, and A. Fert, *Spintronics with Graphene*, Mater. Res. Soc. **37**, 1245 (2012).

[57] B. Dlubak et al., *Highly Efficient Spin Transport in Epitaxial Graphene on SiC*, Nat. Phys. (2012).

[58] M. N. Baibich, J. M. Broto, A. Fert, F. N. Van Dau, F. Petroff, P. Etienne, G. Creuzet, A. Friederich, and J. Chazelas, *Giant Magnetoresistance of (001)Fe/(001)Cr Magnetic Superlattices*, Phys. Rev. Lett. **61**, 2472 (1988).

[59] X. Li and H. Zhu, *Two-Dimensional MoS₂: Properties, Preparation, and Applications*, J. Materiomics **1**, 33 (2015).

[60] F. Godel et al., *WS₂ 2D Semiconductor Down to Monolayers by Pulsed-Laser Deposition for Large-Scale Integration in Electronics and Spintronics Circuits*, ACS Appl. Nano Mater. **3**, 7908 (2020).

[61] *Recent Progress of TMD Nanomaterials: Phase Transitions and Applications*, Nanoscale (2019).

[62] Y. Tan et al., *Controllable 2H-to-1T' Phase Transition in Few-Layer MoTe₂*, Nanoscale **10**, 19964 (2018).

[63] S. Manzeli, D. Ovchinnikov, D. Pasquier, O. V. Yazyev, and A. Kis, *2D Transition Metal Dichalcogenides*, Nat. Rev. Mater. **2**, 8 (2017).

[64] *Molybdenum Disulfide, MoS₂: Theory, Structure & Applications*, <https://www.ossila.com/pages/molybdenum-disulfide-mos2>.

[65] A. Ramasubramaniam, D. Naveh, and E. Towe, *Tunable Band Gaps in Bilayer Transition-Metal Dichalcogenides*, Phys. Rev. B **84**, 205325 (2011).

[66] T. Kümmell, W. Quitsch, S. Matthis, T. Litwin, and G. Bacher, *Gate Control of Carrier Distribution in k -Space in MoS_2 Monolayer and Bilayer Crystals*, Phys. Rev. B **91**, 125305 (2015).

[67] K. Kaasbjerg, K. S. Thygesen, and K. W. Jacobsen, *Phonon-Limited Mobility in n -Type Single-Layer MoS_2 from First Principles*, Phys. Rev. B **85**, 115317 (2012).

[68] N. Ma and D. Jena, *Charge Scattering and Mobility in Atomically Thin Semiconductors*, Phys. Rev. X **4**, 011043 (2014).

[69] *Large-Scale-Compatible Stabilization of a 2D Semiconductor Platform toward Discrete Components - Brus - 2021 - Advanced Electronic Materials - Wiley Online Library*, <https://onlinelibrary-wiley-com.ezproxy.universite-paris->

saclay.fr/doi/full/10.1002/aelm.202001109.

- [70] X. Cui et al., *Multi-Terminal Transport Measurements of MoS₂ Using a van Der Waals Heterostructure Device Platform*, Nat. Nanotechnol. **10**, 6 (2015).
- [71] J. T. Ye, Y. J. Zhang, R. Akashi, M. S. Bahramy, R. Arita, and Y. Iwasa, *Superconducting Dome in a Gate-Tuned Band Insulator*, Science **338**, 1193 (2012).
- [72] C.-J. Shih, Q. H. Wang, Y. Son, Z. Jin, D. Blankshtein, and M. S. Strano, *Tuning On–Off Current Ratio and Field-Effect Mobility in a MoS₂–Graphene Heterostructure via Schottky Barrier Modulation*, ACS Nano **8**, 5790 (2014).
- [73] W. J. Yu, Y. Liu, H. Zhou, A. Yin, Z. Li, Y. Huang, and X. Duan, *Highly Efficient Gate-Tunable Photocurrent Generation in Vertical Heterostructures of Layered Materials*, Nat. Nanotechnol. **8**, 12 (2013).
- [74] Y. Hernandez et al., *High-Yield Production of Graphene by Liquid-Phase Exfoliation of Graphite*, Nat. Nanotechnol. **3**, 9 (2008).
- [75] N. Mishra, J. Boeckl, N. Motta, and F. Iacopi, *Graphene Growth on Silicon Carbide: A Review*, Phys. Status Solidi A **213**, 2277 (2016).
- [76] L. Sun, G. Yuan, L. Gao, J. Yang, M. Chhowalla, M. H. Gharahcheshmeh, K. K. Gleason, Y. S. Choi, B. H. Hong, and Z. Liu, *Chemical Vapour Deposition*, Nat. Rev. Methods Primer **1**, 1 (2021).
- [77] P. R. Kidambi, C. Ducati, B. Dlubak, D. Gardiner, R. S. Weatherup, M.-B. Martin, P. Seneor, H. Coles, and S. Hofmann, *The Parameter Space of Graphene Chemical Vapor Deposition on Polycrystalline Cu*, J. Phys. Chem. C **116**, 22492 (2012).
- [78] J. Plutnar, M. Pumera, and Z. Sofer, *The Chemistry of CVD Graphene*, J. Mater. Chem. C **6**, 6082 (2018).
- [79] A. Govind Rajan, J. H. Warner, D. Blankshtein, and M. S. Strano, *Generalized Mechanistic Model for the Chemical Vapor Deposition of 2D Transition Metal Dichalcogenide Monolayers*, ACS Nano **10**, 4330 (2016).
- [80] H. F. Liu, S. L. Wong, and D. Z. Chi, *CVD Growth of MoS₂-Based Two-Dimensional Materials*, Chem. Vap. Depos. **21**, 241 (2015).
- [81] L. Tao, K. Chen, Z. Chen, W. Chen, X. Gui, H. Chen, X. Li, and J.-B. Xu, *Centimeter-Scale CVD Growth of Highly Crystalline Single-Layer MoS₂ Film with Spatial Homogeneity and the Visualization of Grain Boundaries*, ACS Appl. Mater. Interfaces **9**, 12073 (2017).
- [82] A. T. Hoang et al., *Low-Temperature Growth of MoS₂ on Polymer and Thin Glass Substrates for Flexible Electronics*, Nat. Nanotechnol. **1** (2023).
- [83] D. Fu et al., *Molecular Beam Epitaxy of Highly Crystalline Monolayer Molybdenum Disulfide on Hexagonal Boron Nitride*, J. Am. Chem. Soc. **139**, 9392 (2017).
- [84] M. Nakano, Y. Wang, Y. Kashiwabara, H. Matsuoka, and Y. Iwasa, *Layer-by-Layer Epitaxial Growth of Scalable WSe₂ on Sapphire by Molecular Beam Epitaxy*, Nano Lett. **17**, 5595 (2017).
- [85] M. Yan et al., *High Quality Atomically Thin PtSe₂ Films Grown by Molecular Beam Epitaxy*, 2D Mater. **4**, 045015 (2017).

- [86] L. A. Walsh and C. L. Hinkle, *Van Der Waals Epitaxy: 2D Materials and Topological Insulators*, Appl. Mater. Today **9**, 504 (2017).
- [87] T. A. J. Loh, D. H. C. Chua, and A. T. S. Wee, *One-Step Synthesis of Few-Layer WS₂ by Pulsed Laser Deposition*, Sci. Rep. **5**, 1 (2015).
- [88] M. I. Serna, S. H. Yoo, S. Moreno, Y. Xi, J. P. Oviedo, H. Choi, H. N. Alshareef, M. J. Kim, M. Minary-Jolandan, and M. A. Quevedo-Lopez, *Large-Area Deposition of MoS₂ by Pulsed Laser Deposition with In Situ Thickness Control*, ACS Nano **10**, 6054 (2016).
- [89] V. Zatzko et al., *Band-Gap Landscape Engineering in Large-Scale 2D Semiconductor van Der Waals Heterostructures*, ACS Nano **15**, 7279 (2021).
- [90] J. Clarke, *The Proximity Effect Between Superconducting and Normal Thin Films in Zero Field*, J. Phys. Colloq. **29**, C2 (1968).
- [91] A. A. Golubov and M. Yu. Kupriyanov, *The Josephson Effect in SNINS and SNIS Tunnel Junctions with Finite Transparency of the SN Boundaries*, Zhurnal Eksp. Teor. Fiz. **96**, 1420 (1989).
- [92] M. Yu. Kupriyanov, *Processes in HTS Josephson Junctions*, J. Low Temp. Phys. **106**, 149 (1997).
- [93] A. A. Golubov and M. Yu. Kupriyanov, *Anomalous Proximity Effect in D-Wave Superconductors*, J. Exp. Theor. Phys. Lett. **67**, 501 (1998).
- [94] A. Kohen, G. Leibovitch, and G. Deutscher, *Andreev Reflections on $\text{Y}_1\text{C}_x\text{B}_2\text{C}_x\text{O}_7$: Evidence for an Unusual Proximity Effect*, Phys. Rev. Lett. **90**, 207005 (2003).
- [95] Y. Tanaka, Yu. V. Nazarov, and S. Kashiwaya, *Circuit Theory of Unconventional Superconductor Junctions*, Phys. Rev. Lett. **90**, 167003 (2003).
- [96] Y. Tanuma, Y. Tanaka, and S. Kashiwaya, *Proximity Effect on the Interface of Normal Metal/d-Wave Superconductors*, Phys. C Supercond. **412–414**, 319 (2004).
- [97] Y. Tanaka, Yu. V. Nazarov, A. A. Golubov, and S. Kashiwaya, *Theory of Charge Transport in Diffusive Normal Metal/Unconventional Singlet Superconductor Contacts*, Phys. Rev. B **69**, 144519 (2004).
- [98] A. Sharoni, I. Asulin, G. Koren, and O. Millo, *Proximity Effect in Gold-Coated YBa₂Cu₃O₇ Films Studied by Scanning Tunneling Spectroscopy*, Phys. Rev. Lett. **92**, (2004).
- [99] T. Löfwander, *Proximity Effect in Normal Metal--High- T_c Superconductor Contacts*, Phys. Rev. B **70**, 094518 (2004).
- [100] W.-J. Li, S.-P. Chao, and T.-K. Lee, *Theoretical Study of Large Proximity-Induced d -Wave-like Pairing from a d -Wave Superconductor*, Phys. Rev. B **93**, 035140 (2016).
- [101] D. A. Wollman, D. J. Van Harlingen, J. Giapintzakis, and D. M. Ginsberg, *Evidence for $d_{x^2-y^2}$ Pairing from the Magnetic Field Modulation of YBa₂Cu₃O₇-Pb Josephson Junctions*, Phys. Rev. Lett. **74**, 797 (1995).

- [102] K. A. Kouznetsov et al., *c -Axis Josephson Tunneling between $\text{YBa}_2\text{Cu}_3\text{O}_{7-\delta}$ and Pb: Direct Evidence for Mixed Order Parameter Symmetry in a High- T_c Superconductor*, Phys. Rev. Lett. **79**, 3050 (1997).
- [103] J. R. Kirtley, C. C. Tsuei, Ariando, C. J. M. Verwijs, S. Harkema, and H. Hilgenkamp, *Angle-Resolved Phase-Sensitive Determination of the in-Plane Gap Symmetry in $\text{YBa}_2\text{Cu}_3\text{O}_{7-\delta}$* , Nat. Phys. **2**, 3 (2006).
- [104] I. Giaever and K. Megerle, *Study of Superconductors by Electron Tunneling*, Phys. Rev. **122**, 1101 (1961).
- [105] S. Kashiwaya, Y. Tanaka, M. Koyanagi, and K. Kajimura, *Theory for Tunneling Spectroscopy of Anisotropic Superconductors*, Phys. Rev. B **53**, (1996).
- [106] V. V. Khanin, D. V. Shuvaev, O. V. Snigirev, E. S. Soldatov, A. S. Trifonov, I. I. Vengrus, M. Yu. Kupriyanov, G. Yu. Shubnyi, and A. N. Zherikhin, *Detection of the Proximity Effect in Au/YBCO Bilayers at 77 K with the Aid of a Low-Temperature Scanning Tunneling Microscope*, J. Exp. Theor. Phys. Lett. **63**, 1041 (1996).
- [107] W. L. McMillan, *Tunneling Model of the Superconducting Proximity Effect*, Phys. Rev. **175**, 537 (1968).
- [108] V. T. Volkov, P. H. C. Magnée, B. J. van Wees, and T. M. Klapwijk, *Proximity and Josephson Effects in Superconductor-Two-Dimensional Electron Gas Planar Junctions*, Phys. C **242**, 261 (1994).
- [109] N. B. Kopnin and A. S. Melnikov, *Proximity-Induced Superconductivity in Two-Dimensional Electronic Systems*, Phys. Rev. B **84**, (2011).
- [110] N. B. Kopnin, A. S. Mel'nikov, I. A. Sadovskyy, and V. M. Vinokur, *Weak Links in Proximity-Superconducting Two-Dimensional Electron Systems*, Phys. Rev. B **89**, 081402 (2014).
- [111] I. I. Soloviev, S. V. Bakurskiy, V. I. Ruzhickiy, N. V. Klenov, M. Yu. Kupriyanov, A. A. Golubov, O. V. Skryabina, and V. S. Stolyarov, *Miniaturization of Josephson Junctions for Digital Superconducting Circuits*, Phys. Rev. Appl. **16**, 044060 (2021).
- [112] V. Ruzhickiy, S. Bakurskiy, M. Kupriyanov, N. Klenov, I. Soloviev, V. Stolyarov, and A. Golubov, *Contribution of Processes in SN Electrodes to the Transport Properties of SN-N-NS Josephson Junctions*, Nanomaterials **13**, 12 (2023).
- [113] M. Kjaergaard, H. J. Suominen, M. P. Nowak, A. R. Akhmerov, J. Shabani, C. J. Palmstrøm, F. Nichele, and C. M. Marcus, *Transparent Semiconductor-Superconductor Interface and Induced Gap in an Epitaxial Heterostructure Josephson Junction*, Phys. Rev. Appl. **7**, 034029 (2017).
- [114] W. Mayer et al., *Superconducting Proximity Effect in InAsSb Surface Quantum Wells with In Situ Al Contacts*, ACS Appl. Electron. Mater. **2**, 2351 (2020).
- [115] R. Moriya, N. Yabuki, and T. Machida, *Superconducting Proximity Effect in a NbSe₂/Graphene van Der Waals Junction*, Phys. Rev. B **101**, (2020).
- [116] J. Li, H.-B. Leng, H. Fu, K. Watanabe, T. Taniguchi, X. Liu, C.-X. Liu, and J. Zhu, *Superconducting Proximity Effect in a Transparent van Der Waals Superconductor-Metal Junction*,

Phys. Rev. B **101**, 195405 (2020).

[117] Y. Takane and R. Ando, *Superconducting Proximity Effect on a Two-Dimensional Dirac Electron System*, J. Phys. Soc. Jpn. **83**, 014706 (2014).

[118] A. A. Golubov and M. Yu. Kupriyanov, *Surface Electron Scattering in D-Wave Superconductors*, J. Exp. Theor. Phys. Lett. **69**, 262 (1999).

[119] S. Kashiwaya, Y. Tanaka, M. Koyanagi, H. Takashima, and K. Kajimura, *Origin of Zero-Bias Conductance Peaks in High-T_c Superconductors*, Phys. Rev. B **51**, (1995).

[120] C. W. J. Beenakker, *Specular Andreev Reflection in Graphene*, Phys. Rev. Lett. **97**, (2006).

[121] S. Bhattacharjee and K. Sengupta, *Tunneling Conductance of Graphene NIS Junctions*, Phys. Rev. Lett. **97**, 217001 (2006).

[122] C. W. J. Beenakker, *Colloquium : Andreev Reflection and Klein Tunneling in Graphene*, Rev. Mod. Phys. **80**, 1337 (2008).

[123] C. W. J. Beenakker, A. R. Akhmerov, P. Recher, and J. Tworzydło, *Correspondence between Andreev Reflection and Klein Tunneling in Bipolar Graphene*, Phys. Rev. B **77**, 075409 (2008).

[124] M. Titov and C. W. J. Beenakker, *Josephson Effect in Ballistic Graphene*, Phys. Rev. B **74**, 041401 (2006).

[125] S. Bhattacharjee and K. Sengupta, *Tunneling Conductance of Graphene NIS Junctions*, Phys. Rev. Lett. **97**, (2006).

[126] I. I. Mazin and M. D. Johannes, *A Critical Assessment of the Superconducting Pairing Symmetry in $\text{NaxCoO}_2 \cdot y\text{H}_2\text{O}$* , Nat. Phys. **1**, 2 (2005).

[127] H. B. Heersche, P. Jarillo-Herrero, J. B. Oostinga, L. M. K. Vandersypen, and A. F. Morpurgo, *Bipolar Supercurrent in Graphene*, Nature **446**, (2007).

[128] X. Du, I. Skachko, and E. Y. Andrei, *Josephson Current and Multiple Andreev Reflections in Graphene SNS Junctions*, Phys. Rev. B **77**, 184507 (2008).

[129] C. Ojeda-Aristizabal, M. Ferrier, S. Guéron, and H. Bouchiat, *Tuning the Proximity Effect in a Superconductor-Graphene-Superconductor Junction*, Phys. Rev. B **79**, (2009).

[130] T. Li, J. Gallop, L. Hao, and E. Romans, *Ballistic Josephson Junctions Based on CVD Graphene*, Supercond. Sci. Technol. **31**, (2018).

[131] B. Jouault et al., *Josephson Coupling in Junctions Made of Monolayer Graphene Grown on SiC*, J. Supercond. Nov. Magn. **29**, 1145 (2016).

[132] I. V. Borzenets et al., *Ballistic Graphene Josephson Junctions from the Short to the Long Junction Regimes*, Phys. Rev. Lett. **117**, (2016).

[133] V. E. Calado, S. Goswami, G. Nanda, M. Diez, A. R. Akhmerov, K. Watanabe, T. Taniguchi, T. M. Klapwijk, and L. M. K. Vandersypen, *Ballistic Josephson Junctions in Edge-Contacted Graphene*, Nat. Nanotechnol. **10**, 9 (2015).

[134] D. K. Efetov et al., *Specular Interband Andreev Reflections at van Der Waals Interfaces*

between Graphene and NbSe₂, Nat. Phys. **12**, 4 (2016).

[135] T. Dvir, A. Zalic, E. H. Fyhn, M. Amundsen, T. Taniguchi, K. Watanabe, J. Linder, and H. Steinberg, *Planar Graphene-NbSe₂ Josephson Junctions in a Parallel Magnetic Field*, Phys. Rev. B **103**, 115401 (2021).

[136] F. Amet and G. Finkelstein, *Supercurrent in the Quantum Hall Regime*, Science **352**, 966 (2016).

[137] P. Kumaravadivel, S. Mills, and X. Du, *Magnetic Field Suppression of Andreev Conductance at Superconductor-Graphene Interface*, 2D Mater. **4**, (2017).

[138] Q. J. Sun, H. S. Wang, H. M. Wang, L. W. Deng, Z. W. Hu, B. Gao, Q. Li, and X. M. Xie, *Electronic Transport Transition at Graphene/YBa₂Cu₃O_{7-δ} Junction*, Appl. Phys. Lett. **104**, 102602 (2014).

[139] A. Di Bernardo et al., *P-Wave Triggered Superconductivity in Single-Layer Graphene on an Electron-Doped Oxide Superconductor*, Nat. Commun. **8**, 1 (2017).

[140] Y. Wu, H. Xiao, Q. Li, X. Li, Z. Li, G. Mu, D. Jiang, T. Hu, and X. M. Xie, *The Transport Properties in Graphene/Single-Unit-Cell Cuprates van Der Waals Heterostructure*, Supercond. Sci. Technol. **32**, 085007 (2019).

[141] S. Jois, J. L. Lado, G. Gu, Q. Li, and J. U. Lee, *Andreev Reflection and Klein Tunneling in High-Temperature Superconductor-Graphene Junctions*, Phys. Rev. Lett. **130**, 156201 (2023).

[142] M. Khezerlou and H. Goudarzi, *Transport Properties of Spin-Triplet Superconducting Monolayer MoS₂*, Phys. Rev. B **93**, 115406 (2016).

[143] H. Goudarzi, M. Khezerlou, and S. F. Ebadzadeh, *Andreev Reflection and Subgap Conductance in Monolayer MoS₂ Ferromagnet/s and d-Wave Superconductor Junction*, Superlattices Microstruct. **93**, 73 (2016).

[144] S. F. Ebadzadeh, H. Goudarzi, and M. Khezerlou, *Superconductivity and Magnetic Exchange Field Coexistence in Monolayer MoS₂*, Phys. E Low-Dimens. Syst. Nanostructures **125**, 114388 (2021).

[145] C. Triola, D. M. Badiane, A. V. Balatsky, and E. Rossi, *General Conditions for Proximity-Induced Odd-Frequency Superconductivity in Two-Dimensional Electronic Systems*, Phys. Rev. Lett. **116**, 257001 (2016).

[146] L. Fu, C. L. Kane, and E. J. Mele, *Topological Insulators in Three Dimensions*, Phys. Rev. Lett. **98**, 106803 (2007).

[147] J. D. Sau, S. Tewari, R. M. Lutchyn, T. D. Stanescu, and S. Das Sarma, *Non-Abelian Quantum Order in Spin-Orbit-Coupled Semiconductors: Search for Topological Majorana Particles in Solid-State Systems*, Phys. Rev. B **82**, 214509 (2010).

[148] D. J. Trainer, B. Wang, F. Bobba, N. Samuelson, X. Xi, J. Zasadzinski, J. Nieminen, A. Bansil, and M. Iavarone, *Proximity-Induced Superconductivity in Monolayer MoS₂*, ACS Nano **14**, 2718 (2020).

[149] J. O. Island, G. A. Steele, H. S. J. van der Zant, and A. Castellanos-Gomez, *Thickness*

- Dependent Interlayer Transport in Vertical MoS₂ Josephson Junctions*, 2D Mater. **3**, 031002 (2016).
- [150] M. Ramezani, I. C. Sampaio, K. Watanabe, T. Taniguchi, C. Schönenberger, and A. Baumgartner, *Superconducting Contacts to a Monolayer Semiconductor*, Nano Lett. **21**, 5614 (2021).
- [151] A. Seredinski, E. G. Arnault, V. Z. Costa, L. Zhao, T. F. Q. Larson, K. Watanabe, T. Taniguchi, F. Amet, A. K. M. Newaz, and G. Finkelstein, *One-Dimensional Edge Contact to Encapsulated MoS₂ with a Superconductor*, AIP Adv. **11**, 045312 (2021).
- [152] L. Wang et al., *One-Dimensional Electrical Contact to a Two-Dimensional Material*, Science **342**, 614 (2013).
- [153] M. S. Choi, N. Ali, T. D. Ngo, H. Choi, B. Oh, H. Yang, and W. J. Yoo, *Recent Progress in 1D Contacts for 2D-Material-Based Devices*, Adv. Mater. **34**, 2202408 (2022).
- [154] S. M. Freake and C. J. Adkins, *Excitation Spectrum Induced by the Proximity Effect between Copper and Superconducting Lead*, Phys. Lett. A **29**, 382 (1969).
- [155] T. M. Klapwijk, *Proximity Effect From an Andreev Perspective T. M.*, J. Supercond. **17**, (2004).
- [156] B. Pannetier and H. Courtois, *Andreev Reflection and Proximity Effect*, J. Low Temp. Phys. **118**, (2000).
- [157] P. G. D. Gennes, *Superconductivity Of Metals And Alloys* (CRC Press, Boca Raton, 2019).
- [158] M. J. M. de Jong and C. W. J. Beenakker, *Andreev Reflection in Ferromagnet-Superconductor Junctions*, Phys. Rev. Lett. **74**, 1657 (1995).
- [159] S. Uchida, T. Habe, and Y. Asano, *Andreev Reflection in Weyl Semimetals*, J. Phys. Soc. Jpn. **83**, 064711 (2014).
- [160] Y. Nazarov and Y. Blanter, *Quantum Transport : Introduction to Nanoscience* (Cambridge University Press, 2009).
- [161] M. Kupka, *Current-Voltage Characteristic and Differential Conductance of a Point Contact and Planar Tunnel Contact between an Ordinary Metal and Superconductor in Realistic Three-Dimensional Geometry: Comparison with a One-Dimensional Case*, Phys. C Supercond. **281**, 91 (1997).
- [162] N. A. Mortensen, K. Flensberg, and A.-P. Jauho, *Angle Dependence of Andreev Scattering at Semiconductor--Superconductor Interfaces*, Phys. Rev. B **59**, 10176 (1999).
- [163] M. Kupka, *Modification of the Blonder, Tinkham and Klapwijk Expressions for Andreev and Normal Reflection Coefficients Due to a Finite-Thickness Barrier at the Normal Metal-Superconductor Interface*, Phys. C **221**, (1994).
- [164] Y. Asano, *Magnetoconductance Oscillations in Ballistic Semiconductor-Superconductor Junctions*, Phys. Rev. B **61**, 1732 (2000).
- [165] Y. Takagaki, *Effects of Disorder on Magnetotransport Oscillations in a Two-Dimensional Electron Gas Terminated by Superconductors*, J. Appl. Phys. **128**, (2020).
- [166] B. J. van Wees, P. de Vries, P. Magnée, and T. M. Klapwijk, *Excess Conductance of*

Superconductor-Semiconductor Interfaces Due to Phase Conjugation between Electrons and Holes, Phys. Rev. Lett. **69**, 510 (1992).

[167] J. Y. T. Wei, *Directional Tunneling and Andreev Reflection on YBa₂Cu₃O_{7.2}d Single Crystals: Predominance of d-Wave Pairing Symmetry Verified with the Generalized Blonder, Tinkham, and Klapwijk Theory*, Phys. Rev. Lett. **81**, (1998).

[168] V. Rouco, Seurre et al., *Quasiparticle Tunnel Electroresistance in Superconducting Junctions*, Nat. Commun. **11**, 1 (2020).

[169] W. F. Brinckman, R. C. Dynes, and J. M. Rowell, *Tunneling Conductance of Asymmetrical Barriers*, J. Appl. Phys. **41**, 1915 (1970).

[170] R. C. Dynes, V. Narayanamurti, and J. P. Garno, *Direct Measurement of Quasiparticle-Lifetime Broadening in a Strong-Coupled Superconductor*, Phys. Rev. Lett. **41**, 1509 (1978).

[171] A. Plecenik, M. Grajcar, and S. Benacka, *Finite-Quasiparticle-Lifetime Effects in the Differential Conductance of Bi₂Sr_zCaCu_{20y}/Au Junctions*, Phys. Rev. B **49**, (1994).

[172] W. K. Park, J. L. Sarrao, J. D. Thompson, and L. H. Greene, *Andreev Reflection in Heavy-Fermion Superconductors and Order Parameter Symmetry in CeCoIn₅*, Phys. Rev. Lett. **100**, (2008).

[173] T. Mamiya, K. Hattori, H. Shibayama, K. Iwahashi, T. Kusakabe, and K. Adachi, *Electrical Resistivity of Nonsuperconducting La₄BaCu₅O₁₃ and La₅SrCu₆O₁₅-Based Compounds down to the mK Temperature Range*, Phys. B Condens. Matter **194–196**, 1523 (1994).

[174] C. Kittel, *On the Theory of Ferromagnetic Resonance Absorption*, Phys. Rev. **73**, 155 (1948).

[175] T. L. Gilbert, *A Phenomenological Theory of Damping in Ferromagnetic Materials*, IEEE Trans. Magn. **40**, 3443 (2004).

[176] M. A. Silaev, *Large Enhancement of Spin Pumping Due to the Surface Bound States in Normal Metal--Superconductor Structures*, Phys. Rev. B **102**, 180502 (2020).

[177] X. Du, I. Skachko, and E. Y. Andrei, *Josephson Current and Multiple Andreev Reflections in Graphene SNS Junctions*, Phys. Rev. B **77**, (2008).

[178] R. Bernard, *Dynamique Des Réseaux de Vortex Dans Des Films Minces Supraconducteurs à Haute Température Critique En Vue de l'optimisation d'un Transformateur à Flux de Vortex*, These de doctorat, Paris 11, 2006.

[179] R. E. Hage, *The Effects of Electric Field, Illumination and Their Interplay on the Transport Properties of Cuprate Superconductor Thin Films and Heterostructures*, phdthesis, Université Paris-Saclay, 2021.

[180] D. Perconte, *Proximity Effect between a High Temperature Superconductor and Graphene*, Pierre and Marie Curie University, 2018.

[181] F. Giubileo and A. Di Bartolomeo, *The Role of Contact Resistance in Graphene Field-Effect Devices*, Prog. Surf. Sci. **92**, 143 (2017).

[182] C. E. Malec and D. Davidović, *Electronic Properties of Au-Graphene Contacts*, Phys. Rev. B **84**, 033407 (2011).

- [183] T. Li, J. Gallop, L. Hao, and E. Romans, *Ballistic Josephson Junctions Based on CVD Graphene*, *Supercond. Sci. Technol.* **31**, 045004 (2018).
- [184] I. V. Borzenets, Y. Shimazaki, G. F. Jones, M. F. Craciun, S. Russo, M. Yamamoto, and S. Tarucha, *High Efficiency CVD Graphene-Lead (Pb) Cooper Pair Splitter*, *Sci. Rep.* **6**, 1 (2016).
- [185] A. N. Broers, A. C. F. Hoole, and J. M. Ryan, *Electron Beam Lithography—Resolution Limits*, *Microelectron. Eng.* **32**, 131 (1996).
- [186] G. J. Clark, A. D. Marwick, F. Legoues, R. B. Laibowitz, R. Koch, and P. Madakson, *Radiation Effects in Thin Films of High Tc Superconductors*, *Nucl. Instrum. Methods Phys. Res. Sect. B Beam Interact. Mater. At.* **32**, 405 (1988).
- [187] J. Lesueur, P. Nedellec, H. Bernas, J. P. Burger, and L. Dumoulin, *Depairing-like Variation of Tc in YBa₂Cu₃O_{7-δ}*, *Phys. C Supercond.* **167**, 1 (1990).
- [188] J. Trastoy, V. Rouco, C. Ulysse, R. Bernard, G. Faini, J. Lesueur, J. Briatico, and J. E. Villegas, *Nanostructuring of High-TC Superconductors via Masked Ion Irradiation for Efficient Ordered Vortex Pinning*, *Phys. C Supercond. Its Appl.* **506**, 195 (2014).
- [189] I. Swiecicki, C. Ulysse, T. Wolf, R. Bernard, N. Bergeal, J. Briatico, G. Faini, J. Lesueur, and J. E. Villegas, *Strong Field-Matching Effects in Superconducting YBa₂Cu₃O_{7-δ} Films with Vortex Energy Landscapes Engineered via Masked Ion Irradiation*, *Phys. Rev. B* **85**, 224502 (2012).
- [190] P. R. Kidambi, C. Ducati, B. Dlubak, D. Gardiner, R. S. Weatherup, M.-B. Martin, P. Seneor, H. Coles, and S. Hofmann, *The Parameter Space of Graphene CVD on Polycrystalline Cu*, *J. Phys. Chem. C* (2012).
- [191] S. Ullah, X. Yang, H. Q. Ta, M. Hasan, A. Bachmatiuk, K. Tokarska, B. Trzebicka, L. Fu, and M. H. Rummeli, *Graphene Transfer Methods: A Review*, *Nano Res.* **14**, 3756 (2021).
- [192] T. He, Z. Wang, F. Zhong, H. Fang, P. Wang, and W. Hu, *Etching Techniques in 2D Materials*, *Adv. Mater. Technol.* **4**, 1900064 (2019).
- [193] J. Robertson, *High Dielectric Constant Oxides*, *Eur. Phys. J. Appl. Phys.* **28**, 3 (2004).
- [194] J. Antula, *Temperature Dependence of Dielectric Constant of Al₂O₃*, *Phys. Lett. A* **25**, 308 (1967).
- [195] S. M. George, *Atomic Layer Deposition: An Overview*, *Chem. Rev.* **110**, 111 (2010).
- [196] J.-U. Lee and H. Cheong, *Resonance Raman Effects in Transition Metal Dichalcogenides*, *J. Raman Spectrosc.* **49**, 66 (2018).
- [197] N. Briggs et al., *A Roadmap for Electronic Grade 2D Materials*, *2D Mater.* **6**, 022001 (2019).
- [198] A. Berkdemir et al., *Identification of Individual and Few Layers of WS₂ Using Raman Spectroscopy*, *Sci. Rep.* **3**, 1 (2013).
- [199] A. C. Ferrari et al., *Raman Spectrum of Graphene and Graphene Layers*, *Phys. Rev. Lett.* **97**, 187401 (2006).
- [200] K. Instruments, *Model 2182 and 2182A Nanovoltmeter User's Manual*, (n.d.).

- [201] M. Grove, R. Dittmann, M. Bode, M. Siegel, and A. I. Braginski, *Current Transport across YBa₂Cu₃O₇-Au Interfaces*, Appl. Phys. Lett. **69**, 696 (1996).
- [202] Z. W. Dong, P. Hadley, and J. E. Mooij, *High I_cR_n Products and Hysteretic Behavior of YBCO/Au/YBCO Josephson Junctions*, Phys. C Supercond. **235–240**, 3243 (1994).
- [203] G. Grissonnannache et al., *Direct Measurement of the Upper Critical Field in Cuprate Superconductors*, Nat. Commun. (2014).
- [204] K. Fuchs, *The Conductivity of Thin Metallic Films According to the Electron Theory of Metals*, Math. Proc. Camb. Philos. Soc. **34**, 100 (1938).
- [205] *Frontiers | Optical Properties of Gold After Intense Short-Pulse Excitations*, <https://www.frontiersin.org/articles/10.3389/fphy.2022.856817/full>.
- [206] D. Gall, *Electron Mean Free Path in Elemental Metals*, J. Appl. Phys. **119**, 085101 (2016).
- [207] X. Palermo, Proximity and Flux Pinning Effects in Superconductor-Ferromagnet Hybrids, phdthesis, Université Paris Saclay (COMUE), 2019.
- [208] Y. V. Nazarov, *Novel Circuit Theory of Andreev Reflection*, Superlattices Microstruct. **25**, 1221 (1999).
- [209] W. Belzig, F. K. Wilhelm, C. Bruder, G. Schön, and A. D. Zaikin, *Quasiclassical Green's Function Approach to Mesoscopic Superconductivity*, Superlattices Microstruct. **25**, 1251 (1999).
- [210] H. Le Sueur, Développement d'un AFM-STM Pour La Spectroscopie Électronique Haute Résolution de Nanocircuits : Application à l'effet de Proximité Supraconducteur, These de doctorat, Paris 6, 2007.
- [211] G. Eilenberger, *Transformation of Gorkov's Equation for Type II Superconductors into Transport-like Equations.*, Z Phys **214** 195-213 (1968).
- [212] K. D. Usadel, *Generalized Diffusion Equation for Superconducting Alloys*, Phys. Rev. Lett. **25**, 507 (1970).
- [213] P. Charlat, H. Courtois, Ph. Gandit, D. Mailly, A. F. Volkov, and B. Pannetier, *Resistive Transport in a Mesoscopic Proximity Superconductor*, Czechoslov. J. Phys. **46**, 3107 (1996).
- [214] Y. Wu, H. Xiao, Q. Li, X. Li, Z. Li, G. Mu, D. Jiang, T. Hu, and X. M. Xie, *The Transport Properties in Graphene/Single-Unit-Cell Cuprates van Der Waals Heterostructure*, Supercond. Sci. Technol. **32**, (2019).
- [215] M. Ben Shalom, A. K. Geim, and J. R. Prance, *Quantum Oscillations of the Critical Current and High-Field Superconducting Proximity in Ballistic Graphene*, Nat. Phys. **2**, (2016).
- [216] B. Huard, J. A. Sulpizio, N. Stander, K. Todd, B. Yang, and D. Goldhaber-Gordon, *Transport Measurements Across a Tunable Potential Barrier in Graphene*, Phys. Rev. Lett. **98**, (2007).
- [217] E. H. Hwang and S. Das Sarma, *Acoustic Phonon Scattering Limited Carrier Mobility in Two-Dimensional Extrinsic Graphene*, Phys. Rev. B **77**, 115449 (2008).
- [218] T. Shen, Y. Q. Wu, M. A. Capano, L. P. Rokhinson, L. W. Engel, and P. D. Ye, *Magnetoconductance Oscillations in Graphene Antidot Arrays*, Appl. Phys. Lett. **93**, 122102 (2008).

- [219] M. Hilke, M. Massicote, E. Whiteway, and V. Yu, *Weak Localization in Graphene: Theory, Simulations, and Experiments*, Sci. World J. **2014**, (2014).
- [220] R. Somphonsane et al., *Universal Scaling of Weak Localization in Graphene Due to Bias-Induced Dispersion Decoherence*, Sci. Rep. **10**, (2020).
- [221] Y. Aharonov and D. Bohm, *Significance of Electromagnetic Potentials in the Quantum Theory*, Phys. Rev. **115**, 485 (1959).
- [222] L. Al'tshuler, *Mesoscopic Fluctuations in a Superconductor-Normal Metal-Superconductor Junction*, (1987).
- [223] B. Altshuler, A. Aronov, and B. Spivak, *The Aaronov-Bohm Effect in Disordered Conductors*, JETP Lett **33**, 94 (1981).
- [224] Y. Asano and T. Kato, *Andreev Reflection and Cyclotron Motion of a Quasiparticle in High Magnetic Fields*, J. Phys. Soc. Jpn. **69**, 1125 (2000).
- [225] Y. Takagaki, *Transport Properties of Semiconductor-Superconductor Junctions in Quantizing Magnetic Fields*, Phys. Rev. B **57**, 4009 (1998).
- [226] T. Akazaki, H. Yamaguchi, J. Nitta, and H. Takayanagi, *Superconductor-Semiconductor-Superconductor Junctions Using NbN*, Supercond. Sci. Technol. **12**, 901 (1999).
- [227] J. Eroms, D. Weiss, J. D. Boeck, G. Borghs, and U. Zülicke, *Andreev Reflection at High Magnetic Fields: Evidence for Electron and Hole Transport in Edge States*, Phys. Rev. Lett. **95**, 107001 (2005).
- [228] H. Hoppe, U. Zülicke, and G. Schön, *Andreev Reflection in Strong Magnetic Fields*, Phys. Rev. Lett. **84**, 1804 (2000).
- [229] J. Eroms, M. Tolkiehn, D. Weiss, U. Rössler, J. D. Boeck, and G. Borghs, *Commensurability Effects in Andreev Antidot Billiards*, Europhys. Lett. **58**, 569 (2002).
- [230] P. Rakyta, A. Kormányos, Z. Kaufmann, and J. Cserti, *Andreev Edge Channels and Magnetic Focusing in Normal-Superconductor Systems: A Semiclassical Analysis*, Phys. Rev. B **76**, 064516 (2007).
- [231] Y. Takagaki, *Commensurability and Quantum Interference Magnetotransport Oscillations in a Two-Dimensional Electron Gas Sandwiched by Superconductors*, J. Phys. Condens. Matter **31**, 485301 (2019).
- [232] R. R. Gerhardts, D. Weiss, and K. v. Klitzing, *Novel Magnetoresistance Oscillations in a Periodically Modulated Two-Dimensional Electron Gas*, Phys. Rev. Lett. **62**, 1173 (1989).
- [233] V. S. Stolyarov, T. Cren, C. Brun, I. A. Golovchanskiy, O. V. Skryabina, D. I. Kasatonov, M. M. Khapayev, M. Y. Kupriyanov, A. A. Golubov, and D. Roditchev, *Expansion of a Superconducting Vortex Core into a Diffusive Metal*, Nat. Commun. **9**, (June2018).
- [234] G. P. Papari, A. Glatz, F. Carillo, D. Stornaiuolo, D. Massarotti, V. Rouco, L. Longobardi, F. Beltram, V. M. Vinokur, and F. Tafuri, *Geometrical Vortex Lattice Pinning and Melting in YBaCuO Submicron Bridges*, Sci. Rep. **6**, 1 (2016).
- [235] R. C. Dynes and T. A. Fulton, *Supercurrent Density Distribution in Josephson Junctions*,

Phys. Rev. B **3**, 3015 (1971).

[236] A. Barone and G. Paterno, *Physics and Applications of the Josephson Effect* (John Wiley & sons, 1982).

[237] M. T. Allen, O. Shtanko, I. C. Fulga, A. R. Akhmerov, K. Watanabe, T. Taniguchi, P. Jarillo-Herrero, L. S. Levitov, and A. Yacoby, *Spatially Resolved Edge Currents and Guided-Wave Electronic States in Graphene*, Nat. Phys. **12**, 2 (2016).

[238] B. L. Al'tshuler and B. Z. Spivak, *Mesoscopic Fluctuations in a Superconductor-Normal Metal-Superconductor Junction*, Zh. Eksp. Teor. Fiz **92**, 609 (1987).

[239] K. F. Mak, C. Lee, J. Hone, J. Shan, and T. F. Heinz, *Atomically Thin MoS₂ : A New Direct-Gap Semiconductor*, Phys. Rev. Lett. **105**, 136805 (2010).

[240] J. D. Sau, R. M. Lutchyn, S. Tewari, and S. Das Sarma, *Generic New Platform for Topological Quantum Computation Using Semiconductor Heterostructures*, Phys. Rev. Lett. **104**, 040502 (2010).

[241] G. Xu, J. Wang, B. Yan, and X.-L. Qi, *Topological Superconductivity at the Edge of Transition-Metal Dichalcogenides*, Phys. Rev. B **90**, 100505 (2014).

[242] M. Kakihana, L. Börjesson, S. Eriksson, and P. Svedlindh, *Fabrication and Characterization of Highly Pure and Homogeneous YBa₂Cu₃O₇ Superconductors from Sol-gel Derived Powders*, J. Appl. Phys. **69**, 867 (1991).

[243] S. Hussain et al., *Strain-Induced Hierarchical Ripples in MoS₂ Layers Investigated by Atomic Force Microscopy*, Appl. Phys. Lett. **117**, 153102 (2020).

[244] N. H. Attanayake, A. C. Thenuwara, A. Patra, Y. V. Aulin, T. M. Tran, H. Chakraborty, E. Borguet, M. L. Klein, J. P. Perdew, and D. R. Strongin, *Effect of Intercalated Metals on the Electrocatalytic Activity of 1T-MoS₂ for the Hydrogen Evolution Reaction*, ACS Energy Lett. **3**, 7 (2018).

[245] S. J. R. Tan et al., *Temperature- and Phase-Dependent Phonon Renormalization in 1T'-MoS₂*, ACS Nano **12**, 5051 (2018).

[246] X. Gan, L. Y. S. Lee, K. Wong, T. W. Lo, K. H. Ho, D. Y. Lei, and H. Zhao, *2H/1T Phase Transition of Multilayer MoS₂ by Electrochemical Incorporation of S Vacancies*, ACS Appl. Energy Mater. **1**, 4754 (2018).

[247] C. Lee, H. Yan, L. E. Brus, T. F. Heinz, J. Hone, and S. Ryu, *Anomalous Lattice Vibrations of Single- and Few-Layer MoS₂*, ACS Nano **4**, 2695 (2010).

[248] S.-L. Li, H. Miyazaki, H. Song, H. Kuramochi, S. Nakaharai, and K. Tsukagoshi, *Quantitative Raman Spectrum and Reliable Thickness Identification for Atomic Layers on Insulating Substrates*, ACS Nano **6**, 7381 (2012).

[249] H. Li, Q. Zhang, C. C. R. Yap, B. K. Tay, T. H. T. Edwin, A. Olivier, and D. Baillargeat, *From Bulk to Monolayer MoS₂: Evolution of Raman Scattering*, Adv. Funct. Mater. **22**, 1385 (2012).

[250] Y.-T. Ho et al., *Layered MoS₂ Grown on c -Sapphire by Pulsed Laser Deposition*, Phys. Status Solidi RRL – Rapid Res. Lett. **9**, 187 (2015).

[251] S. Xiao, P. Xiao, X. Zhang, D. Yan, X. Gu, F. Qin, Z. Ni, Z. J. Han, and K. (Ken) Ostrikov,

Atomic-Layer Soft Plasma Etching of MoS₂, Sci. Rep. **6**, 1 (2016).

[252] Y. Niu et al., *Thickness-Dependent Differential Reflectance Spectra of Monolayer and Few-Layer MoS₂, MoSe₂, WS₂ and WSe₂*, Nanomaterials **8**, 9 (2018).

[253] P. Brus, *Stabilisation Grande Surface de Semi-Conducteurs Bidimensionnels Pour Une Intégration Dans Des Composants Discrets*, These de doctorat, université Paris-Saclay, 2021.

[254] R. El Hage et al., *Bimodal Ionic Photomemristor Based on a High-Temperature Oxide Superconductor/Semiconductor Junction*, Nat. Commun. **14**, 1 (2023).

[255] S. Kubo, *Superconducting Properties of Amorphous MoX (X=Si, Ge) Alloy Films for Abrikosov Vortex Memory*, J. Appl. Phys. **63**, 2033 (1988).

[256] A. E. Lita, V. B. Verma, R. D. Horansky, J. M. Shainline, R. P. Mirin, and S. Nam, *Materials Development for High Efficiency Superconducting Nanowire Single-Photon Detectors*, MRS Online Proc. Libr. **1807**, 1 (2015).

[257] A. Banerjee, L. J. Baker, A. Doye, M. Nord, R. M. Heath, K. Erotokritou, D. Bosworth, Z. H. Barber, I. MacLaren, and R. H. Hadfield, *Characterisation of Amorphous Molybdenum Silicide (MoSi) Superconducting Thin Films and Nanowires*, Supercond. Sci. Technol. **30**, 084010 (2017).

[258] L. Ceccarelli, D. Vasyukov, M. Wyss, G. Romagnoli, N. Rossi, L. Moser, and M. Poggio, *Imaging Pinning and Expulsion of Individual Superconducting Vortices in Amorphous MoSi Thin Films*, Phys. Rev. B **100**, 104504 (2019).

[259] B. Baxevanis, V. P. Ostroukh, and C. W. J. Beenakker, *Even-Odd Flux Quanta Effect in the Fraunhofer Oscillations of an Edge-Channel Josephson Junction*, Phys. Rev. B **91**, 041409 (2015).

[260] A. Kononov, G. Abulizi, K. Qu, J. Yan, D. Mandrus, K. Watanabe, T. Taniguchi, and C. Schönenberger, *One-Dimensional Edge Transport in Few-Layer WTe₂*, Nano Lett. **20**, 4228 (2020).

[261] S. Hart, H. Ren, T. Wagner, P. Leubner, M. Mühlbauer, C. Brüne, H. Buhmann, L. W. Molenkamp, and A. Yacoby, *Induced Superconductivity in the Quantum Spin Hall Edge*, Nat. Phys. **10**, 9 (2014).

[262] H. J. Suominen, J. Danon, M. Kjaergaard, K. Flensberg, J. Shabani, C. J. Palmstrøm, F. Nichele, and C. M. Marcus, *Anomalous Fraunhofer Interference in Epitaxial Superconductor-Semiconductor Josephson Junctions*, Phys. Rev. B **95**, 035307 (2017).

[263] G.-H. Lee, S. Kim, S.-H. Jhi, and H.-J. Lee, *Ultimately Short Ballistic Vertical Graphene Josephson Junctions*, Nat. Commun. **6**, 1 (2015).

[264] F. Godel et al., *WS₂ 2D Semiconductor Down to Monolayers by Pulsed-Laser Deposition for Large-Scale Integration in Electronics and Spintronics Circuits*, ACS Appl. Nano Mater. **3**, 7908 (2020).

[265] C. Huang et al., *Inducing Strong Superconductivity in WTe₂ by a Proximity Effect*, ACS Nano **12**, 7185 (2018).

[266] G. J. Orchin et al., *Niobium Diselenide Superconducting Photodetectors*, Appl. Phys. Lett. **114**, 251103 (2019).

10 APPENDIX

10.1 LITHOGRAPHY RECIPES

10.1.1 Electronic lithography

10.1.1.1 First step: definition of the contact pads and alignment marks

Step number	Step	Technical details
1	Pre-bake of the substrate	Hot plate: 100°C during 2 minutes
2	PMMA A5 (500nm-thick)	Spin-coating 4000rpm/30 seconds
3	Bake	Hot plate: 100°C during 2 minutes
4	Exposure in Raith EBG5200	100kV
5	Development	45 seconds in MIBK/IPA (1:3)
6	Cleaning/drying	IPA and N ₂ -dryer

10.1.1.2 Second step: definition of the superconducting tracks/junctions

Step number	Step	Technical details
1	Pre-bake of the substrate	Hot plate: 100°C during 2 minutes
2	PMMA A7 (600nm-thick)	Spin-coating 4000rpm/30 seconds
3	Bake	Hot plate: 100°C during 2 minutes
4	Exposure in Raith EBG5200	100kV
5	Development	45 seconds in MIBK/IPA (1:3)
6	Cleaning/drying	IPA and N ₂ -dryer

10.1.1.3 Third step: definition of the top gate

Step number	Step	Technical details
1	Pre-bake of the substrate	Hot plate: 100°C during 2 minutes
2	PMMA A5 (500nm-thick)	Spin-coating 4000rpm/30 seconds
3	Bake	Hot plate: 100°C during 2 minutes
4	Exposure in Raith EBG5200	100kV
5	Development	45 seconds in MIBK/IPA (1:3)
6	Cleaning/drying	IPA and N ₂ -dryer

10.1.2 Optical lithography

Step number	Step	Technical details
-------------	------	-------------------

1	SPR 700 1.0	Spin-coating 4000rpm/30 seconds
2	Bake	Hot plate: 95°C during 1 minute
3	Exposure	UV light. 10 seconds with the MJB3 optical masker and for the maskless lithography (Smartprint): 1.6s (x10 magnification), 6.4s (x5) and 160s (x1)
4	Development	MF319 30 seconds
5	Cleaning and drying	Water and then N ₂ -assisted drying

10.2 NUMERICAL CALCULATION

The following code allows me to compute the differential conductance spectra of the metallic SN junctions with the BTK-inspired model I described in chapter 5. It is written with the programming language Julia which allowed me to compute integrals much faster than with Python.

```

using Plots
#The first time you use a package like Plots, you have to install the same way
#you do with python "pip install ...", here the instruction in the command
line of your editor is:
#"using Pkg"
#"Pkg.add("Package Name") "
using QuadGK
using HCubature
using Interpolations
using DataFrames
using CSV

#If you want to import the experimental data to compare with the simulations
#I will send you the normalized files, tell me if I forgot...
#rep = "/Users/kevinseurre/Mon Drive/CNRS-Thales/Rapports, papiers,
présentations/Papiers/metal junctions/experiments/"
rep = "/Users/kevinseurre/Mon Drive/CNRS-Thales/Rapports, papiers,
présentations/Papiers/metal junctions/experiments/"
file = string(rep, "E4D_norm.csv")
data = DataFrame(CSV.File(file))
Voltage = data[:,1]
Cond = data[:,2]

function sym(x)

```

```
#I will only compute the conductance for V>0 and then I use the symetry for V<0
```

```
n = length(x)
x_ = reverse(x)
final_x = vcat(x_,x)
return final_x
```

```
end
```

```
function antisym(x)
#same but mostly for the x-axis
n = length(x)
x_ = -reverse(x)
final_x = vcat(x_,x)
return final_x
```

```
end
```

```
function look_for_y(x,y,x0)
#return the value of y(x closest to x0)
l = abs.(x .- x0)
i = argmin(l)
return y[i]
```

```
end
```

```
e = 1.6e-19
kb = 1.38e-23
```

```
function FermiDirac_dim(x::Any,t)
#Here I decompose in 2 because otherwise, it returns errors because numbers are too small if I remember well.
x = x
if e*x/kb/t < 30
    1 / (exp(e*x/(kb*t)) + 1)
else
    exp(-e*x/(kb*t)) / (exp(-e*x/(kb*t)) + 1)
end
```

```
end
```

```
function Deriv_FermiDirac_dim(x::Any,t)
#Same
x = x
if e*x/kb/t < 30
    return -1/t * exp(e*x/(kb*t)) / (exp(e*x/(kb*t)) + 1)^2
else
    return -1/t * exp(-e*x/(kb*t)) / (exp(-e*x/(kb*t)) + 1)^2
end
```

```
end
```

```
function Delta_t(t::Any,Delta,tc,b)
#This is the function to reproduce the evolution of the gap. It is usually the form taken to interpolate the real Delta(t)
return Delta*tanh(b*sqrt((tc/t) -1))
```

```
end
```

```

function sigma_dim_ang(x::Any,Delta,Z0,Gamma,θ,alpha,beta)
    #Here the BTK core of the whole code.
    if x < 0
        x = -x
    end
    #This line is quite debatable but nothing exists but for us, it may not be
    too much of a concern
    #you know that in order to smooth the BTK simulations, we use a
    phenomenological Gamma factor.
    #In s-wave, it is just a constant Gamma but this constant in d-wave may
    have the same symetry. We said that in 2 papers already.
    #Anyway, if Gamma=0, we don't have to bother.
    x = x + im*Gamma #*cos(2*(alpha-θ))
    Delta_p = Delta*cos(2*(alpha-θ))
    Delta_m = Delta*cos(2*(alpha+θ))
    #I just apply Tanaka formula
    Omega_p = x/abs(Delta_p) - sqrt((x/abs(Delta_p))^2-1+0*im)
    Omega_m = x/abs(Delta_m) - sqrt((x/abs(Delta_m))^2-1+0*im)
    num = 16*(1+abs(Omega_p)^2)*cos(θ)^4 + 4*(Z0^2)*(1-
abs(Omega_p*Omega_m)^2)*cos(θ)^2
    den = abs(4*cos(θ)^2 + (Z0^2)*(1-
Omega_p*Omega_m*Delta_m/Delta_p*abs(Delta_p)/abs(Delta_m)))^2
    num/den
end

function sigma_dim(x::Any,Delta,Z0,Gamma,t,alpha,beta)
    #Here I integrate over the direction of the incident particles. The
    exponential term stems for the tunneling cone in some problems
    #But here, I do not use i. The tunneling cone is relevant for thin
    insulating tunnel barrier.
    h(θ) = sigma_dim_ang.(x,Delta,Z0,Gamma,θ,alpha,beta) #*exp(-θ^2/beta^2)
    integral, err = quadgk(θ -> h(θ), -π/2, π/2)
    integral
end

function fit_function(x::Any,Delta,Z0,Gamma,t,alpha,beta,tc,b)
    if t==0
        f(θ) = sigma_dim_ang.(x,Delta,Z0,Gamma,θ,alpha,beta) #*exp(-
θ^2/beta^2)
        integral, err = quadgk(θ -> f(θ), -π/2, π/2)
        return integral
    else
        #First compute the gap and then inject it into the BTK formula and
        then convolute with Fermi-Dirac.
        new_Delta = Delta_t(t,Delta,tc,b)
        g(E) = -sigma_dim_ang.(E,new_Delta,Z0,Gamma,t,alpha,beta) *
Deriv_FermiDirac_dim.(E-x,t)
        integral,err = quadgk(E -> g(E),x-200e-3,x+200e-3)
        return integral
    end
end

function IV_SN(v,G_SN,Delta,Z0,Gamma,t,alpha,beta,tc,b)
    #Integrate G(V) to find I(V)
    I = Float64[]
    new_Delta = Delta_t(t,Delta,tc,b)
    f(x) = sigma_dim_ang.(x[2],new_Delta,Z0,Gamma,x[1],alpha,beta) #*exp(-
x[1]^2/beta^2)

```

```

i = 0
I_ = 0
volt_ = 0
v_max = maximum(v)
G_max = fit_function(v_max,new_Delta,Z0,Gamma,0,alpha,beta,tc,b) / G_SN
for volt in v
    a = [-pi/2,volt_]
    b = [pi/2,volt]
    integral,err = hcubature(x -> f(x), a, b)
    new_I = integral/G_max
    I_ = I_ + new_I
    push!(I,I_)
    volt_ = volt
    i = i + 1
end
return I
end

function sigma_dim_ang_s_wave(x::Any,Delta,Z0,Gamma,theta,alpha,beta)
    #Here the BTK core of the whole code.
    if x < 0
        x = -x
    end
    #This line is quite debatable but nothing exists but for us, it may not be
    too much of a concern
    #you know that in order to smooth the BTK simulations, we use a
    phenomenological Gamma factor.
    #In s-wave, it is just a constant Gamma but this constant in d-wave may
    have the same symetry. We said that in 2 papers already.
    #Anyway, if Gamma=0, we don't have to bother.
    x = x + im*Gamma
    Delta_p = Delta
    Delta_m = Delta
    #I just apply Tanaka formula
    Omega_p = x/abs(Delta_p) - sqrt((x/abs(Delta_p))^2-1+0*im)
    Omega_m = x/abs(Delta_m) - sqrt((x/abs(Delta_m))^2-1+0*im)
    num = 16*(1+abs(Omega_p)^2)*cos(theta)^4 + 4*(Z0^2)*(1-
abs(Omega_p*Omega_m)^2)*cos(theta)^2
    den = abs(4*cos(theta)^2 + (Z0^2)*(1-
Omega_p*Omega_m*Delta_m/Delta_p*abs(Delta_p)/abs(Delta_m)))^2
    num/den
end

function sigma_dim_s_wave(x::Any,Delta,Z0,Gamma,t,alpha,beta)
    #Here I integrate over the direction of the incident particles. The
    exponential term stems for the tunneling cone in some problems
    #But here, I do not use i. The tunneling cone is relevant for thin
    insulating tunnel barrier.
    h(theta) = sigma_dim_ang_s_wave.(x,Delta,Z0,Gamma,theta,alpha,beta) #*exp(-
theta^2/beta^2)
    integral, err = quadgk(theta -> h(theta), -pi/2, pi/2)
    integral
end

function fit_function_s_wave(x::Any,Delta,Z0,Gamma,t,alpha,beta,tc,b)
    if t==0

```

```

    f( $\theta$ ) = sigma_dim_ang_s_wave.(x,Delta,Z0,Gamma, $\theta$ ,alpha,beta) #*exp(-
 $\theta^2$ /beta^2)
    integral, err = quadgk( $\theta$  -> f( $\theta$ ), - $\pi$ /2,  $\pi$ /2)
    return integral
else
    #First compute the gap and then inject it into the BTK formula and
    then convolute with Fermi-Dirac.
    new_Delta = Delta_t(t,Delta,tc,b)
    g(E) = -sigma_dim_ang_s_wave.(E,new_Delta,Z0,Gamma,t,alpha,beta) *
    Deriv_FermiDirac_dim.(E-x,t)
    integral,err = quadgk(E -> g(E),x-80e-3,x+80e-3)
    return integral
end
end

function IV_SN_s_wave(v,G_SN,Delta,Z0,Gamma,t,alpha,beta,tc,b)
    #Integrate G(V) to find I(V)
    I = Float64[]
    new_Delta = Delta_t(t,Delta,tc,b)
    f(x) = sigma_dim_ang_s_wave.(x[2],new_Delta,Z0,Gamma,x[1],alpha,beta)
    #*exp(-x[1]^2/beta^2)
    i = 0
    I_ = 0
    volt_ = 0
    v_max = maximum(v)
    G_max = fit_function_s_wave(v_max,new_Delta,Z0,Gamma,0,alpha,beta,tc,b) /
    G_SN
    for volt in v
        a = [- $\pi$ /2,volt_]
        b = [ $\pi$ /2,volt]
        integral,err = hcubature(x -> f(x), a, b)
        new_I = integral/G_max
        I_ = I_ + new_I
        push!(I,I_)
        volt_ = volt
        i = i + 1
    end
    return I
end

function G_metal_Ch(v::Any,G_metal)
    #This takes into account a heating effect on the metal leading to a lower
    conductance (for the background). But here, I set alpha=0.
    return G_metal
end

function IV_metal_Ch(v::Any,G_metal)
    I = G_metal.* v
    return I
end

function
simul_Mag(G_SN,G_s_wave,G_metal,param_Z,param_s_wave,I_max,N_points,tc,b)
#Here I use all the functions created. I first compute a first guess for the
    voltage for both the resistor in series and the junction
    v_SN = range(0.0000001/G_SN, stop=I_max/G_SN, length = N_points) #V
    v_s_wave = range(0.0000001/G_s_wave, stop=I_max/G_s_wave, length =
    N_points) #V

```

```

    v_metal = range(0.0000001/G_metal, stop=I_max/G_metal, length = N_points)
#V
#Then I compute the corresponding I(V)
    i_SN =
IV_SN(v_SN,G_SN,param_SN[1],param_SN[2],param_SN[3],param_SN[4],param_SN[5],pa
ram_SN[6],tc,b)
    i_s_wave =
IV_SN_s_wave(v_s_wave,G_s_wave,param_s_wave[1],param_s_wave[2],param_s_wave[3]
,param_s_wave[4],param_s_wave[5],param_s_wave[6],tc,b)
    i_metal = IV_metal_Ch.(v_metal,G_metal)
#I interpolate I(V)
    V_SN = LinearInterpolation(i_SN,v_SN)
    V_s_wave = LinearInterpolation(i_s_wave,v_s_wave)
    V_metal = LinearInterpolation(i_metal,v_metal)
#I define my final current list.
    I_max = min(maximum(i_SN),maximum(i_s_wave),maximum(i_metal))
    I_0_max = max(minimum(i_SN),minimum(i_s_wave),minimum(i_metal))
    I = range(I_0_max,I_max,length = 5*N_points)
#For this current list, I compute the corresponding voltage for both
    v_SN = V_SN.(I)
    v_s_wave = V_s_wave.(I)
    v_metal = V_metal.(I)

    v_SN_max = maximum(v_SN)
    v_s_wave_max = maximum(v_s_wave)
    v_metal_max = maximum(v_metal)
#I sum the voltages since they are in series
    V = v_SN .+ v_s_wave .+ v_metal
#I compute the G(V) for both
    g_SN =
fit_function.(v_SN,param_SN[1],param_SN[2],param_SN[3],param_SN[4],param_SN[5]
,param_SN[6],tc,b)
    g_s_wave =
fit_function_s_wave.(v_s_wave,param_s_wave[1],param_s_wave[2],param_s_wave[3],
param_s_wave[4],param_s_wave[5],param_s_wave[6],tc,b)
    g_metal = G_metal_Ch(v_metal,G_metal)

    g_SN_max =
fit_function(v_SN_max,param_SN[1],param_SN[2],param_SN[3],param_SN[4],param_SN
[5],param_SN[6],tc,b)
    g_s_wave_max =
fit_function_s_wave.(v_s_wave_max,param_s_wave[1],param_s_wave[2],param_s_wave
[3],param_s_wave[4],param_s_wave[5],param_s_wave[6],tc,b)
#The result of BTK is normalized to 1 but here the integration doesn't give
one because of missing prefactors
#So I normalize by the value of G at large V
#Then I multiply by the physical conductance to compute Gtot
    cond_SN = g_SN /g_SN_max * G_SN
    cond_s_wave = g_s_wave/g_s_wave_max * G_s_wave
#I compute Gtot
    G_tot = 1 ./ (1 ./ cond_SN .+ 1 ./ cond_s_wave .+ 1 ./ g_metal)

    return V,G_tot,I,cond_SN
end

```

```

#An example with the SN junction E4D (a)

```

```

I_max = 1.5e-2 #A
N_points = 50
T = 0
Tc = 60
b = 1.5
param_SN = [ 25e-3 , 0.001 , 0.5e-3 , T , π*0 , 0.01 ]
param_s_wave = [ 22e-3 , 0 , 0.5e-3 , T , 0 , 0.01 ]

G_total = 0.08
ratio_s_wave = 8
ratio_metal = 2.5
G_SN = (1+ratio_s_wave+ratio_metal)*G_total #S

G_s_wave = G_SN/ratio_s_wave
G_metal = G_SN/ratio_metal

Gexpected = 1/((1/G_SN)+(1/G_s_wave)+(1/G_metal))

V,G_tot,I,cond_SN =
simul_Mag(G_SN,G_s_wave,G_metal,param_SN,param_s_wave,I_max,N_points,Tc,b)

V = antisym(V)
I = antisym(I)
G_tot = sym(G_tot)
G_norm = G_tot ./ G_tot[1]
cond_SN = sym(cond_SN)
plot(V*1e3,G_norm,label="Rs_w/RSN=$(ratio_s_wave),Rm/RSN=$(ratio_metal)")
xlabel! ("V [mV]")
ylabel! ("G")

```